Towards testing Bell's inequality using atoms correlated in momentum

Almazbek Imanaliev

NNT : 2016SACL0003

THESE DE DOCTORAT
DE L'UNIVERSITE PARIS-SACLAY,
préparée à
L'INSTITUT D'OPTIQUE GRADUATE SCHOOL

ÉCOLE DOCTORALE N°572
Ondes et Matière (EDOM)

Spécialité de doctorat : Physique

Par

Almazbek Imanaliev

Towards testing Bell's inequality using atoms correlated in momentum

Thèse présentée et soutenue à Palaiseau, le 30 mars 2016 :

Composition du Jury :

M. T. Coudreau	Président	Université Paris VII
M. B. Laburthe-Tolra	Rapporteur	Université de Paris XIII
M. F. Pereira Dos Santos	Rapporteur	SYRTE
Mme L. Pruvost	Examinatrice	Université Paris-Sud
M. D. Boiron	Directeur de thèse	Institut d'Optique
M. A. Aspect	Invité	Institut d'Optique

Declaration of Authorship

I declare that this thesis is a presentation of my original research work unless otherwise stated with due reference to the literature and acknowledgement of collaborative research and discussions.

We must abandon the world view advocated by Einstein, sometimes referred to as 'local realism'. One might ask which of the ideas leading to the Bell inequalities should be abandoned: locality or realism? For our part, it seems difficult to understand these two notions as being independent. How could one conceive of independent physical realities for two spatially separated systems but which were nevertheless able to remain in contact via an instantaneous, superluminal interaction? ***It is our view that the nonlocality of quantum mechanics, often presented as the conclusion to be drawn from the violation of the Bell inequalities, represents a negation of the whole local realist view of the world.***

Grynberg, Aspect & Fabre 2010, p.432 [62]

Acknowledgements

Searching a short term project for a one month internship, I went to see Chris Westbrook hoping that he might have one in his group - atomic optics group of Charles Fabry laboratory. Chris kindly accepted me in his office and described the observation of the superradiance phenomenon with the "helium" experiment. I appreciated a lot the explanation of Chris with enthusiasm and I liked the subject which involved atoms, photons, quantum physics and more. Thanks to Chris, I could get the internship on the statistical analysis of the superradiance which was my first step in the cold atom experiments domain. I would like to thank Chris who made possible for me to do a PhD following the internship in his group. Although his administrative responsibilities, Chris could find time to see us to discuss physics and gave his point of view which contributed a lot to my understanding of physics.

I feel very lucky for having met and having been supervised by Denis Boiron. He is a very good pedagogue and indeed had a great impact in my personal advancement of physics. Denis visits experiment in the morning and late in the afternoon each day. I was pleased to see my supervisor two times per day during which I enjoyed discussing confronting problems, new ideas and even experimenting till late hours. I have a good souvenir of having passed several hours on changing the mirror of one of the MOT beams although initially we thought that it should be done in few minutes. I appreciated Denis' personal traits and his nice humor. I would like to express my gratitude to Denis not only for supervising and teaching me but also supporting me through three years.

I had a pleasure to work with Marc Cheneau who joined our group in 2012. He is a very talented scientist and I admired his analytical reasoning and his strong knowledge in physics. Indeed, I learned a lot from him both experiments and theory and I appreciated his invaluable advices. He backed us up not only in the laboratory but in the soccer tournament between different laboratories on the Saclay. I wish you all the best with your new experiment.

I would like to thank our 'spiritual leader' Alain Aspect. I am very happy that I could work on the PhD thesis subject-Bell's inequality test, of our leader in his own group. During writing my thesis, I benefited a lot from his works which I admired for its simplicity and pedagogical approach. I was honored by his partipication in my thesis defense.

Of course, experiments is the team work and each member of team progresses based on the accomplished works by the earlier colleagues. I would like to thank Marie Bonneau and Josselin Ruaudel for their contribution whom I met at the beginning of my PhD. I worked two years with Raphael Lopes and I thank him for having me introduced to the experimental physics and coming to my thesis despite the long journey from London. You are hardworking student and I wish you success in your scientific career. I enjoyed

a lot to work with Pierre Dussarrat, a cheerful and intelligent guy. He helped me a lot in realizing many tests on the Bragg pulse and taught me french phrases which I find useful in my daily life in France. I am sure that with Maxime Perrier, new PhD student in our team, the experiment is in good hands, and the test of the non-locality will be demonstrated successfully.

Besides the science, I had a great three years with my colleagues in the Charles Fabry laboratory: Guilhem, Amaudric, Qeuntin, Hugo, Lorenzo, Cecile, Vincent, Aisling, Bess, Laurianne, Lynn, Samuel, Ralf, Kilian, Jeremie, Rockson, Valentin, Henning. Whether it is summer school of les Houches or YAO, soccer tournament, partys or just our daily life in the laboratories, I have good memories with you.

Moreover I would like to thank permanent members of the atom optics group and quantum optics: Isabelle Bouchoule, Thomas Bourdel, David Clement, Vincent Josse, Laurent Sanchez-Palencia, Antoine Browaeys, Yvan Sortais, Thierry Lahaye for the discussions and loans of material. My gratitudes are to Andre Villing, Fred Moron, Andre Guilbaud, and Patrick Roth, Florence Nogrette for their technical assistance. I would like to thank also reporters who accepted reading my thesis. Last but not the least, I would like to thank people who supported me, my family, my friends.

Physical Constants

Speed of light in vacuum	c	=	$2.997\ 924\ 58\ \times\ 10^{8}$ m s^{-1}
Atomic mass constant	m_u	=	$1.660\ 539\ 040\ \times\ 10^{-27}$ kg
Boltzmann constant	k_B	=	$1.380\ 648\ 52\ \times\ 10^{-23}$ J K^{-1}
Electric constant	ε_0	=	$8.854\ 187\ 817...\ \times\ 10^{-12}$ F m^{-1}
Electron mass	m_e	=	$9.109\ 383\ 56\ \times\ 10^{-31}$ kg
Elementary charge	e	=	$1.602\ 176\ 6208\ \times\ 10^{-19}$ C
Magnetic constant	μ_0	=	$12.566\ 370\ 614...\ \times\ 10^{-7}$ N A^{-2}
Planck constant	h	=	$6.626\ 070\ 040\ \times\ 10^{-34}$ J s
Planck constant over 2π	$\hbar$	=	$1.054\ 571\ 800\ \times\ 10^{-34}$ J s
Bohr radius	a_0	=	$0.529\ 177\ 210\ 67\ \times\ 10^{-10}$ m
Bohr magneton	μ_B	=	$927.400\ 9994\ \times\ 10^{-26}$ J T^{-1}
Fine-structure constant	α	=	$7.297\ 352\ 5664\ \times\ 10^{-3}$
Proton mass	m_p	=	$1.672\ 621\ 898\ \times\ 10^{-27}$ kg
Nuclear magneton	μ_N	=	$5.050\ 783\ 699\ \times\ 10^{-27}$ J T^{-1}

Contents

Introduction

In the quantum formalism, the strong correlations between independent measurements on each particle of an entangled pair can be revealed despite the long separation between them. Thus, it opposes the relativistic causality principle in which any communication between particles can not propagate faster than the speed of the light. For this reason, three physicists Albert Einstein, Boris Podolsky, and Nathan Rosen (EPR), questioning the completeness of the formalism of quantum mechanics in their famous paper [47] in 1935, proposed to introduce a reasonable, "local realist", description of the world in which each particle carries together, locally, all the properties that produces the results of any measurement. The collection of these properties make up the particle's physical reality. However, the developer of the "Copenhagen interpretation" of the quantum theory, Niels Bohr strongly opposed to the proposal putting forward that one can no longer speak of the individual properties of each particle in an entangled state [16].

Most physicists paid little attention to the debate between Bohr and Einstein believing that it merely affects one's interpretation of the quantum formalism and not the ability of the quantum physics to correctly predict the results of the measurements. But in 1964, John Stewart Bell, a theorist at CERN, changed the nature of the debate by showing the controversial predictions of local realism against those of standard quantum physics in measuring the correlations between particles of the entangled pair [10, 11]. He came up with the inequalities, now known as the Bell's inequalities, which sets limits on the predicted correlations for any local realist formalism while these limits are passed under some measurement settings for quantum mechanics. Then, it suddenly became possible to put an end to the debate by performing the correlation measurement.

In the following decades, experimentalists have realized many tests [23] reporting the violation of the Bell's inequalities and thus showing the completeness of the quantum formalism. But these tests, having at least one "loophole", leaves always a room for a local realist interpretation unless one makes a supplementary hypothesis [36]. The loopholes can be categorized under two categories: the "locality loophole" [7, 144] and the "detection loophole" [34, 52]. The first one is related to the fact that the measurement on one particle might not be totally independent of the measurement of the other

particle of the pair, a requirement to derive the Bell's inequalities. The second one is related to the imperfect detection efficiencies which registers a fraction of the emitted pairs which might not be a "fair sample", another requirement to test the Bell's inequalities. Freshly, three teams independently [53, 66, 131] have finalized decades of experimental efforts by simultaneously closing two loopholes and confirming that we must definitely renounce to local realism.

Besides testing quantum mechanics, the demonstrations of the quantum nonlocality open new doors of applications on top of already existing ones in the field of quantum information and quantum cryptography [1, 27, 39]. An example of such a new potential door would be the Bell's inequality test with momentum-correlated massive particles which would allow to extend fundamental tests of quantum mechanics into domains of gravitational fields through the direct coupling with particle mass [109]. The massive particle experiments of the quantum nonlocality [66, 70, 83, 95, 123, 125, 135, 149], performed so far, exploited internal degrees of freedom of particles but never external degrees of freedom. Therefore we are motivated to demonstrate the quantum nonlocality for a momentum-correlated atomic pair following closely the scheme [117] for photons. The important ingredients of such scheme is the momentum-correlated pair, coherent control of the pair, and the correlation measurements.

- The ability to create nonclassical sources is at the heart of the experimental advancements of quantum physics. The cold atoms community is in the developing stage of nonclassical pair creation and manipulation compared to the mature quantum optics community. Nevertheless, several promising results were already obtained in the atomic community concerning the creation of atomic pairs correlated with internal degrees of freedom [19, 59, 91] as well as with external degrees of freedom [25, 57, 79, 110, 119]. Such atomic sources can provide more degrees of freedom (internal, external, bosonic and fermionic) and strong non-linearity for quantum information in contrast to the optical sources. In our group, three methods of the atomic pair creation have been explored [18, 75, 110] by demonstrating their nonclassical correlations [81]. Among three methods, the dynamical instability of Bose-Einstein condensate in a moving optical lattice [18] produces our atomic pair entangled in momentum. This method offers a possibility to tune the population and the momentum of particles in a pair.

- The coherent control of the atomic pair in the proposed scheme is realized through the Bragg diffraction [94] of atoms from an optical periodic potential. By controlling the duration of the optical standing wave one can obtain either an atomic mirror ($\pi-$pulse) or an atomic beamsplitter ($\pi/2-$pulse). In addition, the selectivity of the Bragg pulse in momenta can play a role of the filter, while the phase of the standing wave can be used to imprint a phase on the atoms. The parameters

of the Bragg pulse can be controlled to a very good degree and it is a vital element in realizing atom interferometers [12]. We have demonstrated the two particle interference effect [88] for our atomic pair with an atomic beamsplitter made of the $\pi/2-$pulse. Obtaining non-classical interference effect with massive particles, we were able to characterize and manipulate them coherently. It has opened an opportunity for us to test the Bell's inequality with massive particles correlated in external degrees of freedom.

- Another important point is the ability to measure correlations of the particles. The correlation studies, developed by Glauber [54], is at the heart in studying quantum effects such as the bunching of bosonic particles (the Hanbury Brown and Twiss effect [64]), the two-particle interference effect (the Hong-Ou-Mandel effect [71]), and the non-locality of entanglement (the violation of Bell's inequality [8]). To carry out the correlation measurements, the detection at single atomic level is desirable. Today, several single atom resolved imaging techniques exist such as fluorescence imaging of trapped atoms in the lattice or in an array of tweezers [9, 132, 145], or again fluorescence resonance imaging with light sheet [26], or the single atom momentum resolved electronic detection of the metastable helium atoms by the micro-channel plate (MCP) detector [127] which we employ in our group.

Thus, we employ the necessary elements of the scheme for the Bell's inequality test with massive particles correlated in external degrees of freedom and we can hope to perform the experiment.

Manuscript organisation

During my first year of thesis work, we performed the correlation measurement on the collective emission, and I have participated actively on the analysis (in which I have worked also during my internship before starting my PhD) as well as in the realisation and acquiring practical skills on the experiment. During the second year of thesis work, we performed the atomic Hong-Ou-Mandel experiment with my senior experimental partner Raphael Lopes. I was actively involved in building the setup of the Bragg beams and running the experiment. During my last year of thesis work ($\sim$ 8 months), with junior experimental partner Pierre Dussarrat, we have prepared the scheme for the atomic Bell's inequality test. At this stage, the important issues we have tackled with was finding a suitable scheme which allows to control the phase of the atomic interferometers (important for Bell's inequality test) and preparing the Bragg beams to satisfy the selectivity and the phase control.

This manuscript is organized as follows:

Chapter 1. We will define the correlation function and discuss its meaning for the first and second order correlations. We will present the collective radiation (the superradiance effect [43]) from the Bose-Einstein condensate [89] and its second order coherence measurement. The superradiance can generate atom-field entanglement [38] or atom-atom entanglement [24, 113, 114]. The latter one can be revealed by the correlation measurement on the atoms and it is interesting topic for us to investigate in the future.

Chapter 2. The theory of the Bell's inequality will be discussed together with the scheme to be adopted for the test of the quantum nonlocality with helium atoms. The underlying theory of the pair production, the Bragg diffraction is visited. We conclude by presenting the estimation of the quantum prediction for our potential experiment.

Chapter 3. This chapter is entirely devoted to the experimental tests and preparations for the Bell's inequality test. The characterization of the condensate and the characterization of the resulting pair from loading the condensate in the moving lattice will be presented. The tests on the Bragg pulse, namely on its selectivity and phase are found in this chapter.

Chapter 4. Finally, we present the HOM experiment (two-particle interference) performed with the helium atoms and its result exceeding the classical threshold. The theoretical description with estimations for dip and width of the HOM signal is shown.

Chapter 1

Second-order coherence of superradiance from Bose-Einstein condensate

The milestone experiments such as the bunching of bosonic particles (the Hanbury Brown and Twiss effect [64]), the two-particle interference effect (the Hong-Ou-Mandel effect [71]), and the non-locality of entanglement (the violation of Bell's inequality [8]) have demonstrated fascinating features of quantum mechanics making it the successful theory in accurately describing the microscopic world over the classical mechanics. Moreover, advancements in understanding these fundamental laws of nature revolutionized technology creating new domains of applications in precision interferometry [112], quantum information [21, 48] etc. The quantum optics community has been the frontier in demonstrating the aforementioned experiments but with the realisation of the first Bose-Einstein condensate in 1995 [2, 42], the atomic optics community is catching up very rapidly and extending the validity of quantum theory for neutral atoms as well. In our group, we are interested in such quantum experiments with matter waves and the correlation studies, developed by Glauber [54], is the essential tool for us in studying such quantum effects and its importance should be stressed. It was developed initially in the framework of quantum optics but applies generally to any quantum field. In the first section of this chapter, we will define the correlation functions which will appear all over in this manuscript and discuss its importance in demonstrating quantum effects. Next, in the second section, we will present the mechanism of collective radiation (the superradiance effect [43]) from the Bose-Einstein condensate [89]. We measured the second order correlation of this collective phenomenon during my first year of thesis work. In addition to being an excellent example of the application of the correlation theory, this experiment was the direct demonstration of a density fluctuation of radiation from

an a priori complex process. In the last section, the measurement result of the second order coherence of the superradiance from a coherent source will be presented.

1.1 Correlations and coherence

1.1.1 Definition of correlation function

Let $\hat{\Psi}(\vec{r}) = \sum_i \phi_i(\vec{r})\hat{a}_i$ be the quantum field operator where $\hat{a}_i$ is an annihilation operator of a particle with wave function $\phi_i(\vec{r})$, $\vec{r}$ referring to a considered coordinate (depending on the situation it may refer to a position, momentum or frequency) and where $\{\phi_i(\vec{r})\}$ is an orthonormal basis. The correlation function of $\hat{\Psi}(\vec{r})$ of order n is defined as

$$G^{(n)}(\vec{r}_1,\dots,\vec{r}_n,\vec{r}_{n+1},\dots,\vec{r}_{2n}) = \langle\hat{\Psi}^\dagger(\vec{r}_1)\dots\hat{\Psi}^\dagger(\vec{r}_n)\hat{\Psi}(\vec{r}_{n+1})\dots\hat{\Psi}(\vec{r}_{2n})\rangle \tag{1.1a}$$

$$= \mathrm{Tr}\Big[\hat{\rho}\hat{\Psi}^\dagger(\vec{r}_1)\dots\hat{\Psi}^\dagger(\vec{r}_n)\hat{\Psi}(\vec{r}_{n+1})\dots\hat{\Psi}(\vec{r}_{2n})\Big]. \tag{1.1b}$$

If $\forall i, \vec{r}_{n+i} = \vec{r}_i$, the correlation function can be expressed in terms of number operator, or equally an intensity of field $\hat{N}(\vec{r}) = |\hat{\Psi}(\vec{r})|^2$ as

$$G^{(n)}(\vec{r}_1,\dots,\vec{r}_n) = \langle: \hat{N}(\vec{r}_1)\dots\hat{N}(\vec{r}_n) :\rangle \tag{1.2}$$

where the notation $\langle: \dots :\rangle$ designates normal ordering, i.e. creation operators ordered on the left of annihilation operators.

The normalised correlation function is obtained by normalising $G^{(n)}$ with the mean intensity of field $\langle\hat{N}(\vec{r})\rangle$ which is nothing but the first order correlation function $G^{(1)}(\vec{r},\vec{r})$ at $\vec{r}$:

$$g^{(n)}(\vec{r}_1,\dots,\vec{r}_n,\vec{r}_{n+1},\dots,\vec{r}_{2n}) = \frac{G^{(n)}(\vec{r}_1,\dots,\vec{r}_n,\vec{r}_{n+1},\dots,\vec{r}_{2n})}{\sqrt{G^{(1)}(\vec{r}_1,\vec{r}_1)\dots G^{(1)}(\vec{r}_{2n},\vec{r}_{2n})}}. \tag{1.3}$$

We are interested in the first ($n = 1$) and second ($n = 2$) order correlations which will be discussed in detail in the following.

1.1.2 First order correlation function: phase coherence

The first order normalized correlation function is given by

$$g^{(1)}(\vec{r}_1,\vec{r}_2) = \frac{\langle\hat{\Psi}^\dagger(\vec{r}_1)\hat{\Psi}(\vec{r}_2)\rangle}{\sqrt{\langle\hat{N}(\vec{r}_1)\rangle\langle\hat{N}(\vec{r}_2)\rangle}} \tag{1.4}$$

and it quantifies the phase coherence of a field and its amplitude $|g^{(1)}|$ is equal to the contrast of interference of fields at $\vec{r}_1$ and $\vec{r}_2$.

Coherent state. Consider a coherent state $|\alpha\rangle$ which is an eigenstate of $\hat{a}_i$ and which is expressed as a function of the Fock state $|p\rangle$ where p is a number of particles

in the mode ϕ_i. It is given by

$$|\alpha\rangle = e^{-\frac{1}{2}|\alpha|^2} \sum_{p=0}^{\infty} \frac{\alpha^p}{p!} |p\rangle \tag{1.5}$$

and it describes an ideal monomode laser (i.e. with infinitely thin spectral width) of intensity $I = |\alpha|^2$. In the framework of atom optics, the equivalent system is the Bose-Einstein condensate (in the mean-field approximation where all atoms are assumed to be in the same state) whose mean atom number is $\langle \hat{N} \rangle = |\alpha|^2$. For this state, we find a maximal contrast, i.e. $|g^{(1)}(\vec{r}_1, \vec{r}_2)| = 1$, $\forall \vec{r}_1, \vec{r}_2$ meaning that the field does not show any phase fluctuation which is what we expect from an ideal laser.

Incoherent state. For an incoherent state of a field which shows phase fluctuations we do not expect a flat contrast of an interference as a function of $\vec{r}_1$ and $\vec{r}_2$, in fact it is a bell shaped function with a characteristic coherence length. To illustrate this point, consider a thermal light which is described by a statistical mixture with the density operator

$$\hat{\rho} = \prod_i (1 - \exp\{-\hbar\omega_i / k_B T\}) \sum_{n_i} \exp\{-n\hbar\omega_i\} |n_i\rangle\langle n_i| \tag{1.6}$$

where T is the temperature of source and $\hbar\omega_i$ is the energy and n_i is the number of photons in the mode ϕ_i. If we assume that the distribution of ω_i is given by the Gaussian spectrum (e.g. spectrum of an emission from the Doppler broadened source) for the thermal light,

$$\mathcal{F}(\omega_i) = \frac{1}{\sqrt{2\pi}\Delta\omega} e^{-(\omega_i - \bar{\omega})^2 / 2\Delta\omega^2} \tag{1.7}$$

where $\bar{\omega}$ is the central frequency of the spectrum and $\Delta\omega$ its standard deviation, then one can show that [90]

$$g^{(1)}(\tau) = \frac{\mathrm{Tr}[\hat{\rho}\hat{\Psi}^\dagger(\vec{t_1})\hat{\Psi}(\vec{t_2})]}{\sqrt{\mathrm{Tr}[\hat{\rho}\hat{\Psi}^\dagger(\vec{t_1})\hat{\Psi}(\vec{t_1})]\mathrm{Tr}[\hat{\rho}\hat{\Psi}^\dagger(\vec{t_2})\hat{\Psi}(\vec{t_2})]}} = \exp\{-\imath\bar{\omega}\tau - \frac{1}{2}(\Delta\omega)^2\tau^2\} \tag{1.8}$$

with $\tau = t_1 - t_2$. Thus the contrast, $|g^{(1)}(\tau)|$, is not a flat function, in fact, it is a Gaussian function of τ with the temporal coherence length $\tau_0 = \frac{1}{\Delta\omega}$, proportional to the inverse of the spectrum width while for an ideal laser ($\Delta\omega \to 0$), the coherence length is infinite with a contrast of 1 confirming the result stated before.

The interference experiments carried out with matter waves demonstrates nicely a drop of contrast of fringes when the coherent source is replaced by the thermal source due to the finite coherence length of thermal cloud [15]. This observation is shown in the figure 1.1 where matter-wave beams, emitted from two spatially separated regions of a trapped Bose gas, are made interfere. (in (a) from coherent source, in (b) from source

just below the critical temperature T_c, in (c) from thermal cloud at the temperature above T_c).

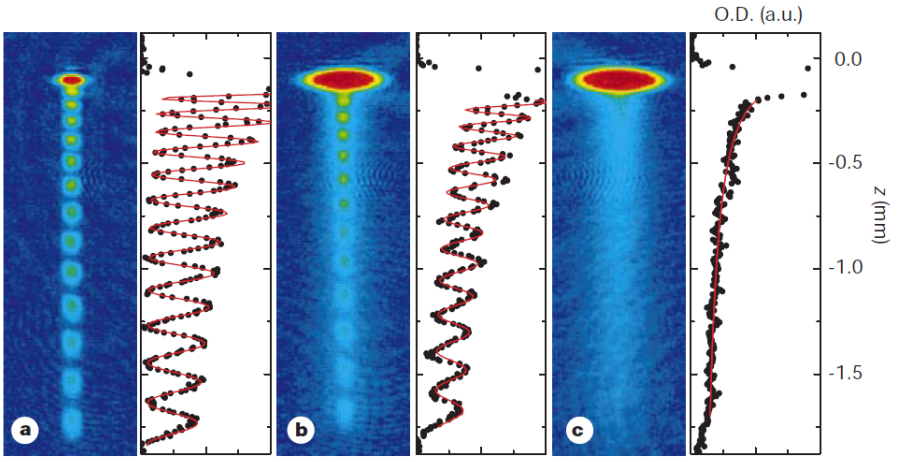

FIGURE 1.1: Interference of matter-wave beams from two spatially separated regions of a trapped Bose gas at temperatures: (a) well below critical the temperature T_c, (b) just below T_c, and (c) above T_c (figure extracted from [15])

In the following, the two coherence lengths, spatial and temporal, will be discussed with classical fields in detail.

Temporal coherence length. Consider a complex electric field $E(t)$ with fixed polarization entering in one of the input arm of the Mach-Zehnder interferometer in a perfect plane parallel form as it is shown in Figure 1.2. A Mach-Zehnder interferometer

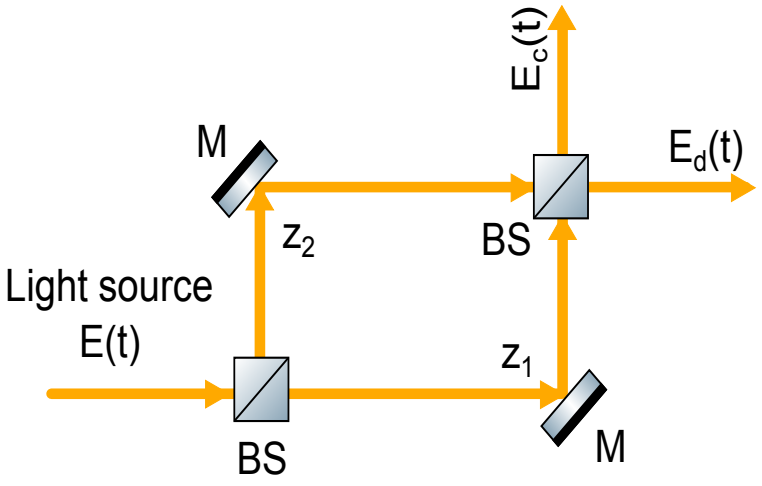

FIGURE 1.2: Mach-Zehnder Interferometer

is made up of two lossless optical beamsplitters with transmission and reflection coefficients given by t_s and r_s respectively. The fields after the first beamsplitter ($t_s E(t)$

"horizontally" and $r_s E(t)$ "vertically" in the figure 1.2) travel different paths z_1 and z_2. So the field at the output d at instant t is given by:

$$E_d(t) = r_s t_s E(t - \frac{z_1}{c}) + t_s r_s E(t - \frac{z_2}{c}). \tag{1.9}$$

which we will write

$$E_d(t, \tau) = r_s t_s E(t') + t_s r_s E(t' + \tau) \tag{1.10}$$

with $t' = t - \frac{z_1}{c}$ and $\tau = \frac{z_1 - z_2}{c}$. We will consider the average intensity $\langle I_d(\tau)\rangle = \varepsilon_0 c \frac{1}{t_{obs}} \int_{t_{obs}} dt |E_d(t,\tau)|^2$ over an observation time t_{obs} which can be accessed directly in an experiment. It is expressed in terms of the input field as

$$\begin{aligned}
\langle I_d(\tau)\rangle &= \varepsilon_0 c \langle |E_d(t)|^2 \rangle && \text{(1.11a)}\\
&= \varepsilon_0 c |r_s|^2 |t_s|^2 \Big(\langle |E(t')|^2 \rangle + \langle |E(t'+\tau)|^2 \rangle + 2\mathrm{Re}\big[\langle E^*(t') E(t'+\tau)\rangle\big] \Big) && \text{(1.11b)}\\
&= 2|r_s|^2 |t_s|^2 \langle I \rangle \Big(1 + \mathrm{Re}\big[\frac{\langle E^*(t') E(t'+\tau)\rangle}{\langle E^*(t') E(t')\rangle} \big] \Big) && \text{(1.11c)}\\
&= 2|r_s|^2 |t_s|^2 \langle I \rangle \Big(1 + \mathrm{Re}\big[g^{(1)}(\tau) \big] \Big) && \text{(1.11d)}
\end{aligned}$$

with stationary input intensity $\langle I\rangle = \varepsilon_0 c \langle |E(t')^2| \rangle = \varepsilon_0 c \langle |E(t'+\tau)^2| \rangle$. Thus the Mach-Zehnder fringes are characterized by the real part of $g^{(1)}(\tau)$ with $|g^{(1)}(\tau)|$ contrast of fringes. For example, taking the result in (1.8), we have

$$\langle I_d(\tau)\rangle = 2|r_s|^2 |t_s|^2 \langle I \rangle \Big(1 + e^{-\frac{1}{2}(\Delta\omega)^2 \tau^2} \cos(\bar{\omega}\tau) \Big) \tag{1.12}$$

for which the contrast is higher for longer temporal coherence length $\tau_0 = \frac{1}{\Delta\omega}$ or equivalently spectrally finer distribution. In fact, the relation between these two is given by the *Wiener-Khintchine theorem* [92]:

$$g^{(1)}(\tau) = \frac{1}{\sqrt{2\pi}} \int_{-\infty}^{\infty} \mathrm{d}\omega \mathcal{F}(\omega) e^{-\imath\omega\tau}. \tag{1.13}$$

where $\mathcal{F}(\omega)$ spectral distribution of an emission. Thus, we can see how the temporal coherence length is related inversely with the spectral width. Conversely, we have

$$\mathcal{F}(\omega) = \frac{1}{2\pi} \int_{-\infty}^{\infty} d\tau g^{(1)}(\tau) e^{\imath\omega\tau}. \tag{1.14}$$

The relation in (1.13) can be easily established for the case where the electric field is modeled as a sum of contribution of an emission of N emitters of source with identical polarization and with parallel propagation direction:

$$E(t) = E_0 \sum_{i=1}^{N} \exp(-\imath\omega_i t + \imath\phi_i) \tag{1.15}$$

where E_0 the amplitude, ϕ_i the phase and ω_i the frequency of the electric field of ith emitter. The $g^{(1)}$ is then equal to

$$g^{(1)}(\tau) = \frac{\langle E^*(t)E(t+\tau)\rangle}{\langle E^*(t)E(t)\rangle} \tag{1.16a}$$

$$= \frac{E_0^2 \sum_{i,j=1}^{N} \langle \exp\{\imath\omega_i t - \imath\phi_i - \imath\omega_j(t+\tau) + \imath\phi_j\}\rangle}{E_0^2 \sum_{i,j=1}^{N} \langle \exp\{\imath\omega_i t - \imath\phi_i - \imath\omega_j(t) + \imath\phi_j\}\rangle} \tag{1.16b}$$

$$= \sum_{i=1}^{N} \exp(-\imath\omega_i\tau) \tag{1.16c}$$

where to write the last line we used the fact that the terms $i \neq j$ average to zero due to the random phase distribution of an emission of independent emitters. Then, the last line can be written in a form (1.13) by converting the sum to the integral $\sum_i^N \to \int_{-\infty}^{\infty} \mathrm{d}\omega \mathcal{F}(\omega)$.

Spatial coherence length. Let us consider an incoherent, quasi-monochromatic (centered at wavelength λ) extended source σ. The first order spatial correlation of the

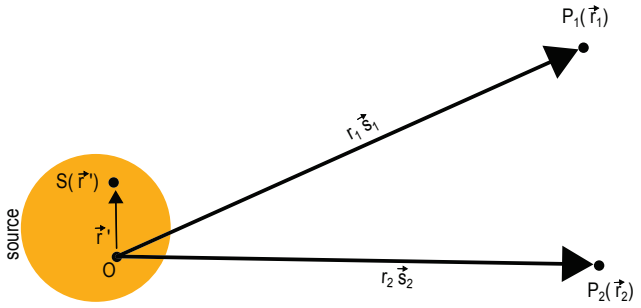

FIGURE 1.3: The fields at $P_1(\vec{r}_1)$ and $P_2(\vec{r}_2)$ emitted by an incoherent, quasi-monochromatic, extended source.

fields at points $P_1(\vec{r}_1)$ and $P_2(\vec{r}_2)$, which are situated in the far-zone of the source as shown in the figure 1.3, is given by [93]

$$g^{(1)}(\vec{r}_1 - \vec{r}_2) = e^{\imath k(r_2 - r_1)} \frac{\int_\sigma I(\vec{r}') e^{-\imath\bar{k}(\vec{s}_2 - \vec{s}_1)\cdot\vec{r}'} \,\mathrm{d}^2\vec{r}'}{\int_\sigma I(\vec{r}')\,\mathrm{d}^2\vec{r}'} \tag{1.17}$$

where $k = \frac{2\pi}{\lambda}$ and $I(\vec{r}')$ the intensity across the source, and $\vec{s}_{1,2}$ the unit vectors pointing from the origin O taken in the source region σ to the field points $P_{1,2}$, i.e. $\vec{r}_1 = r_1\vec{s}_1$ and $\vec{r}_2 = r_2\vec{s}_2$. We see that the spatial first-order correlation is given in terms of the Fourier transform of the intensity $I(\vec{r}')$ across the source and it is referred as the *van Cittert-Zernike theorem*. As an example of the theorem, consider the circular source σ, of radius a, centered at O and of uniform intensity $I(\vec{r}')$ =const. Also, we take $r_1 = r_2 = r$. Then $g^{(1)}$ is reduced to the similar integral that appears in the theory of Fraunhofer diffraction

at a circular aperture [93] and one finds that

$$g^{(1)}(\vec{r}_1 - \vec{r}_2) = \frac{2J_1(k\frac{a}{r}d_{12})}{k\frac{a}{r}d_{12}} \tag{1.18}$$

where J_1 is the Bessel function of the first kind and first order and d_{12} is the distance between points $P_1(\vec{r}_1)$ and $P_2(\vec{r}_2)$. The spatial first-order correlation function decreases from the value 1 for $d_{12} = 0$ to the value 0.88 for

$$d_{12} = 0.16\lambda r/a \tag{1.19}$$

defining the spatial coherence length for this particular case. In fact, by measuring this coherence length one can obtain the angular radius r/a of the source.

1.1.3 Second order correlation function: intensity coherence

The second order normalized correlation function is defined generally as

$$g^{(2)}(\vec{r}_1, \vec{r}_2, \vec{r}_3, \vec{r}_4) = \frac{\langle \hat{\Psi}^\dagger(\vec{r}_1)\hat{\Psi}^\dagger(\vec{r}_2)\hat{\Psi}(\vec{r}_3)\hat{\Psi}(\vec{r}_4)\rangle}{\sqrt{\langle \hat{N}(\vec{r}_1)\rangle\langle \hat{N}(\vec{r}_2)\rangle\langle \hat{N}(\vec{r}_3)\rangle\langle \hat{N}(\vec{r}_4)\rangle}}. \tag{1.20}$$

For $\vec{r}_1 = \vec{r}_3$ and $\vec{r}_2 = \vec{r}_4$, it reduces to

$$g^{(2)}(\vec{r}_1, \vec{r}_2) = \frac{\langle : \hat{N}(\vec{r}_1)\hat{N}(\vec{r}_2) : \rangle}{\langle \hat{N}(\vec{r}_1)\rangle\langle \hat{N}(\vec{r}_2)\rangle} \tag{1.21}$$

which quantifies the intensity fluctuation of field or equivalently corresponds to the joint probability of detecting a particle at $\vec{r}_1$ knowing that another one is at $\vec{r}_2$ if the corpuscular aspect of a field is invoked.

Measuring coherence length from $g^{(2)}$. In case of incoherent ensemble, by measuring $g^{(2)}$, one can access its coherence length (valid only for incoherent source). To illustrate, considering an incoherent ensemble such as the one described by the density operator in (1.6), one can establish the relation [90] between the first and second order correlations:

$$g^{(2)}(\tau) = 1 + |g^{(1)}(\tau)|^2 \tag{1.22a}$$

$$= 1 + \exp\{-(\Delta\omega)^2\tau^2\} \tag{1.22b}$$

Thus the characteristic width of $g^{(2)}(\tau)$ is that of $g^{(1)}(\tau)$ divided by a factor $\frac{1}{\sqrt{2}}$. Looking at the intensity correlation rather than the field correlation in determining coherence length has a practical advantage of being more stable to external effects. It is for this reason R. Hanbury Brown and R. Twiss looked at the intensity correlation to measure the angular size of the Sirius star [65]. The phase correlation did not allow precise

measurement of the angular size of the star due to the turbulence in the atmosphere which introduces aberrations to the phase of the field by varying the refractive index of air.

The bunching effect. An interesting point of the second order correlation is the interpretation of its amplitude. From the equation (1.22b), we see that the amplitude of the $g^{(2)}(\tau)$ function is greater for smaller value of τ and it reaches its maximum value for $\tau = 0$. This behaviour represents the intensity fluctuation of the field and can be understood easily with classical fields. An extended incoherent light source produces a speckle pattern when it is seen on the screen as shown in the figure 1.4. Then, intensity

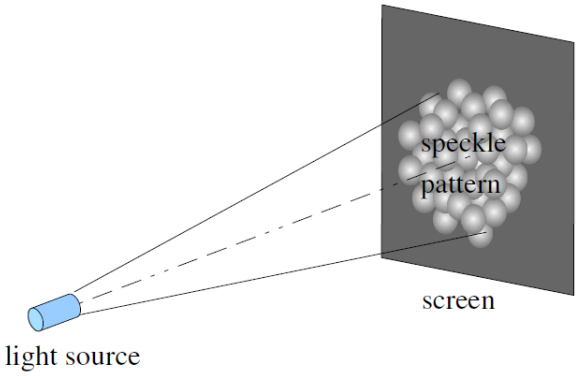

FIGURE 1.4: The speckle pattern produced by a spatially incoherent light source (figure extracted from [127]).

correlation measurement is essentially a speckle measurement whose characteristic size is of the order of the spatial coherence and whose characteristic time at which this pattern evolves is of the order of the time coherence. For most sources, the evolution is sufficiently quick compared to the detector integration time, that the speckle averages to a homogeneously lighted screen. On the other hand, for the coherent state in (1.5), one has

$$g^{(2)}(\vec{r}_1, \vec{r}_2) = 1. \tag{1.23}$$

implying an absence of intensity fluctuation $\forall \vec{r}_1, \vec{r}_2$. So far, we discussed the interpretation of the behaviour of $g^{(2)}$ amplitude with classical fields but the interpretation with the corpuscular aspect of the quantum field is more surprising. We see an enhanced joint probability of detection of photons from an incoherent source for the smaller spatial or temporal intervals. Why these photons from independent sources show such bunching effect? Consider a photon is detected at the detector $D1$ and another one is detected at the detector $D2$. They are emitted from two independent points A and B of the source shown in the figure 1.5. There are four processes that contribute to the detection of two photons (see figure 1.5.a: either two photons arrive on the same detector (first two

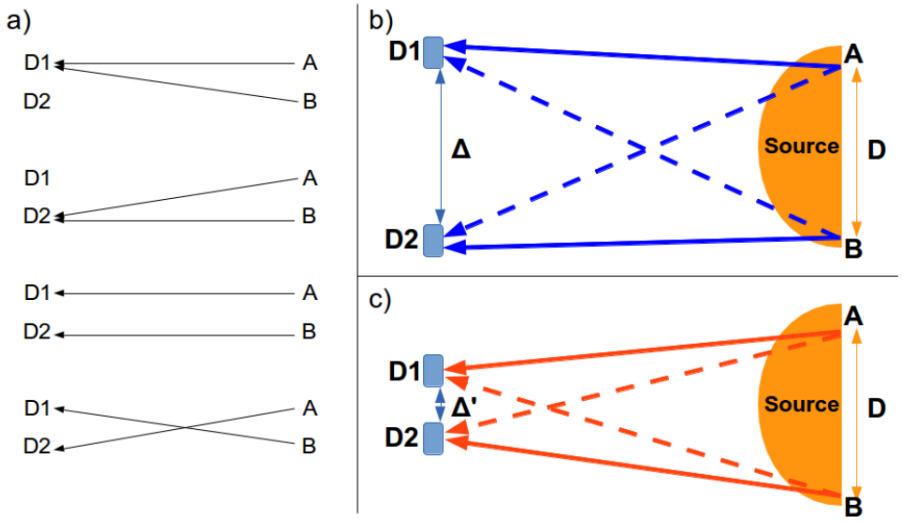

FIGURE 1.5: (a) Four processes contributing to the detection of two photons. Only last two lead to the joint detection whose amplitudes interfere due to the indistinguishability of these two processes. (b) When the distance Δ between the detectors is large, the phase difference between the two processes, which interfere, is large. (c) For smaller distance, the two processes have similar phases and interfere constructively resulting in the enhanced joint detection. (figure extracted from [124])

processes), or two photons arrive on the separate detectors (last two processes)). In this case, it is impossible to distinguish the last two processes and they will interfere. The quantum state on the detector can be written as

$$|\psi\rangle = \frac{1}{2}\left(e^{\imath\phi_1}|2_{D1}, 0_{D2}\rangle + e^{\imath\phi_2}|0_{D1}, 2_{D2}\rangle + (1 + e^{\imath\Phi})|1_{D1}, 1_{D2}\rangle\right). \tag{1.24}$$

The phase difference Φ between two processes that interfere depends on the optical path differences of two possibilities. Assuming that the distance L between the source and the detectors is very large compared to the size of the source D_S, the phase difference between two processes for two point sources separated by $D \leq D_S$ and for two detectors separated by Δ is

$$\Phi \approx \frac{2\pi D\Delta}{\lambda L} \tag{1.25}$$

where λ is the wavelength of two emitted photons. The joint probability of detecting a photon at each detector is given by

$$P(\Delta) = \langle 1, 1|\hat{N}_1\hat{N}_2|1, 1\rangle \tag{1.26a}$$

$$= P_{D1}P_{D2}(1 + \cos(\frac{2\pi D}{\lambda L}\Delta)) \tag{1.26b}$$

where P_{D1} and P_{D2} are the probabilities of detection of $D1$ and $D2$. The second order normalized correlation function is then obtained by normalizing this probability by

$P_{D1}P_{D2}$:

$$g^{(2)}(\Delta) = 1 + \cos(\frac{2\pi D}{\lambda L}\Delta). \tag{1.27}$$

So we observe a modulation whose period depends on the angular separation of two point sources D/L. To account for all set of possible points A and B, we need to integrate over the source which averages to 1 for larger separations while for separation between the detectors smaller than the spatial coherence length, $\Delta < \frac{\lambda L}{D_S}$, it produces the bell shaped function with maximum amplitude equal to 2. This demonstrates the bunching effect of two photons but more generally of bosons. If we realize the same experiment with fermions, we obtain the inverse effect due to the Pauli principle: while we approach two detectors, $g^{(2)}$ will decrease. The measurements of the second order correlation for fermionic particles and bosonic particles were carried out in our group with the collaboration of the group of V. Wassen in Amsterdam [76, 128] some years ago before I joined the group and as we can see from the result of the measurement (see figure 1.6) the expected behaviour (bunching for bosons and antibunching for fermions) was observed.

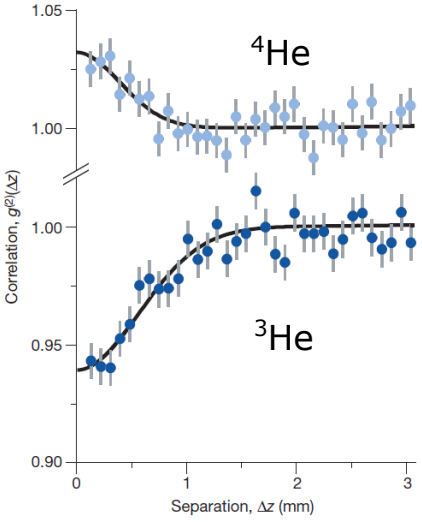

FIGURE 1.6: **Second order correlation function measurement for two isotopes of helium.** Helium 4 is a boson and we observe an enhancement of the joint probability of detection for small separations while for Helium 3 being a fermion, we observe decrease of the correlation function for the similar separations.(figure is extracted from [76, 128])

Finally, by looking an intensity correlation function it is possible to reveal the quantum effects deviating from the classical results which does not happen for the first-order correlation function. Single photon anti-correlation is one of the example of the quantum effects for which classical counterparts do not exist. We can measure the second-order correlation function of a single photon with the setup shown in the figure

1.7 where a photon is entering from the port 1 of a beamsplitter and the intensity correlations are measured with the help of detectors at the output ports 3 and 4. So the

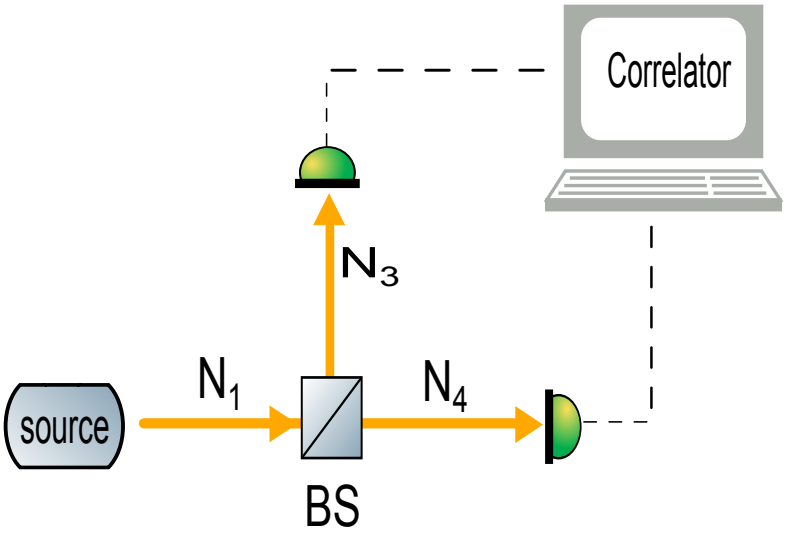

FIGURE 1.7: An experimental setup to measure the intensity correlation of a single photon source.

second order correlation at the output ports can be related to the input port 1:

$$g^{(2)}_{3,4} = \frac{\langle : \hat{N}_3 \hat{N}_4 : \rangle}{\langle \hat{N}_3 \rangle \langle \hat{N}_4 \rangle} \tag{1.28a}$$

$$= \frac{\langle \hat{N}_1 (\hat{N}_1 - 1) \rangle}{\langle \hat{N}_1 \rangle^2} \tag{1.28b}$$

from which it is clear that if a single photon is sent to the beamsplitter, the $g^{(2)}_{3,4}$ diminishes while for a classical field we expect non-null intensity at the outputs of the $50:50$ beamsplitter for whatever small value of the input intensity. In the experiment [55], this quantum effect was measured with the mentioned setup. The single-photon inputs are obtained from the cascade emission in which two pair photons are emitted in two different directions. One of them is directly detected and its signal is used to operate an electronic gate that activates a measurement of the correlation function with the other photon of the pair. However, "parasite" photons may enter the apparatus during the correlation measurement time. So, they measured the second-order correlation as a function of average number of photons received by the gate detector which has the same integration time with the ones at the output of the beamsplitter in 1.7. Their experimental result is shown in the figure 1.8 where the second-order correlation function is plotted as a function of average number of photons at the gate detector which is equivalent to number of photons at the input 1 of the beamsplitter in the figure 1.7. When the integration time is decreased to ensure having a single photon at the input,

the second-order correlation function indeed drops to zero as it is expected. Other ex-

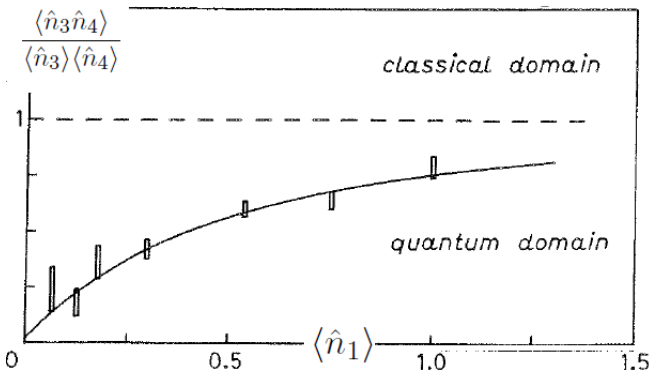

FIGURE 1.8: The measured second order correlation between two outputs of the beamsplitter as a function of mean input photon number sent to the one of the input of the beamsplitter. (figure extracted from [55])

amples of quantum effects revealed through the intensity correlation are the subject of the Chapter 2 and 4.

Next, we are going to discuss the superradiance process from the Bose-Einstein condensate for which we have measured the second-order correlation.

1.2 Superradiance from the Bose-Einsten condensate

Dicke calculated the radiation rate of a spontaneous emission by a collection of two-level atoms in his seminal paper [43] in 1954. He considered the entire sample of N atoms as a single quantum system and he found that the atoms prepared in the excited state can cooperatively decay into the ground state at a rate $\Gamma \propto N\Gamma_0$ much faster than the independent atom emission rate Γ_0. The emission intensity $I = N\Gamma\hbar\omega_0$ with ω_0 frequency of the emission, is thereby collectively enhanced by N^2 with respect to the emission intensity of independent emitters which is proportional to N.

The mechanism behind this collective spontaneous emission dubbed as 'superradiance' depends on the size of the sample [43, 61, 108]. For atoms localized in a subwavelength region $|r| < \lambda_0$, the phase coherence between atomic dipoles builds up and thus they emit in phase due to the indistinguishability of the dipoles in the spontaneous emission process of an atomic system. On the other hand, for a spatially extended sample $|r| \gg \lambda_0$, the superradiant emission is associated with the classical constructive interference of the radiation field produced by scattering sites in the phase matched direction which is related to the sample geometry. Therefore, depending upon the relative spatial phases of the atoms, the radiation into a particular mode could be enhanced (superradiance) or suppressed (subradiance) for a spatially extended sample. Superradiance has

been observed in many systems; hot gases, cold gases, solids and even planetary and astrophysical environments [84]. Early experimental works [51, 60, 122, 136] were carried out on atomic or molecular vapors. But more recently, renewed interest was sparked in the subject using the Bose-Einsten condensate gas after the pioneering experiment [72].

In this section, I discuss briefly superradiance from a small sample $|r| < \lambda_0$ (Dicke's formalism) to introduce the subject and then I will present a Raman superradiance from the Bose-Einstein condensate [129, 148] which we observed also in our experiment.

1.2.1 Superradiance from a sub-wavelength sample

We consider an ensemble of N two-level atoms at positions $\vec{r}_i$ with $i = 1, \ldots, N$. The excited state $|e\rangle$ is separated by an energy of $\hbar\omega_0$ from the ground state $|g\rangle$. We write the atom-light Hamiltonian in the interaction picture for the stationary atoms (in the electric dipole approximation) as

$$\begin{aligned}\hat{H}_{Dicke} = &\sum_{j}^{N} \frac{1}{2}\hbar\omega_0(|e\rangle_j\ {}_j\langle e| - |g\rangle_j\ {}_j\langle g|) + \sum_{\vec{k}} \hbar\omega_{\vec{k}}\hat{a}^{\dagger}_{\vec{k}}\hat{a}_{\vec{k}} \\ &+ \sum_{\vec{k}} \left(\hbar g_{\vec{k}}\hat{a}_{\vec{k}} \sum_{j}^{N} e^{\imath(\vec{k}\cdot\vec{r}_j - (\omega_k - \omega_0)t)}|e\rangle_j\ {}_j\langle g| + \text{h.c.}\right)\end{aligned} \tag{1.29}$$

where $|e\rangle_j$ ($|g\rangle_j$) is the j^{th} atom in the state $|e\rangle$ ($|g\rangle$), $\hat{a}_{\vec{k}}$, $\hat{a}^{\dagger}_{\vec{k}}$ are the mode operators of light for wave-vector $\vec{k}$ and $\hbar g_{\vec{k}} = \imath\sqrt{\frac{\hbar c k d_0^2}{2\epsilon_0 \mathcal{V}}}\vec{\epsilon}_\gamma \cdot \vec{\epsilon}_a$ is the single-atom single photon coupling constant, $\epsilon_{\gamma,a}$ are the polarization vectors of the photon and the atomic dipole, and $\mathcal{V}$ is the quantization volume.

There are two consequences of considering atoms in a small volume compared to λ_0: firstly the atomic states are symmetrized since the atoms are indistinguishable under emission process and secondly the N radiators behave as a point-like dipole resulting from the sum of the N individual dipoles.

Collective dipole operator. If we assume the sub-wavelength condition

$$e^{\imath\vec{k}\cdot\vec{r}_j} \simeq e^{\imath\vec{k}\cdot\vec{r}_0} \tag{1.30}$$

we can define collective lowering and raising operators

$$\hat{D}^{-} = \sum_{i}^{N} e^{\imath\vec{k}\cdot\vec{r}_j}|g\rangle_j\ {}_j\langle e| \simeq \sum_{j}^{N} e^{\imath\vec{k}\cdot\vec{r}_0}|g\rangle_j\ {}_j\langle e| \tag{1.31}$$

$$\hat{D}^{+} = \sum_{j}^{N} e^{\imath\vec{k}\cdot\vec{r}_j}|e\rangle_j\ {}_j\langle g| \simeq \sum_{j}^{N} e^{\imath\vec{k}\cdot\vec{r}_0}|e\rangle_j\ {}_j\langle g| \tag{1.32}$$

and the collective diagonal operator

$$\hat{D}_z = \sum_j^N \frac{1}{2}(|e\rangle_j\ {}_j\langle e| - |g\rangle_j\ {}_j\langle g|). \tag{1.33}$$

These collective operators obey the commutation relations

$$[\hat{D}^+, \hat{D}^-] = 2\hat{D}_z \tag{1.34a}$$

$$[\hat{D}_z, \hat{D}^\pm] = \pm\hat{D}^\pm. \tag{1.34b}$$

In addition, we define the operator

$$\hat{D}^2 = \frac{1}{2}(\hat{D}^+\hat{D}^- + \hat{D}^-\hat{D}^+) + \hat{D}_z. \tag{1.35}$$

These operators can be used to define the collective electric dipole operator

$$\mathcal{D} = \sum_j^N \mathcal{D}_j = (\hat{D}^+ + \hat{D}^-)\vec{\epsilon}_\gamma \cdot \vec{\epsilon}_a \tag{1.36}$$

which is written as a sum of the jth atom dipole operator $\mathcal{D}_j = (|e\rangle_j\ {}_j\langle g| + |g\rangle_j\ {}_j\langle e|)\vec{\epsilon}_\gamma \cdot \vec{\epsilon}_a$. The fact that we can add up the individual dipole operators demonstrates the phase coherence between the emitters.

Collective symmetric states. Since the coupling of the atoms to the radiation field is symmetrical with respect to the exchange of any two atoms in the system, the atomic system evolution must remain in the space invariant by all atomic permutations. The elements of this space are given by the collective symmetric states $|JM\rangle$ which are defined by [43]

$$|JM\rangle = \sqrt{\frac{(J+M)!}{N!(J-M)!}}\left(\hat{D}^-\right)^{(J-M)}|e, e, e \ldots e\rangle \tag{1.37}$$

with $-J \leq M \leq J$ and $J = N/2$. The $|JM\rangle$ state represents the fully symmetrical state in which $J + M$ atoms are in the upper level $|e\rangle$ and $J - M$ in the lower level $|g\rangle$. The $|JM\rangle$ states are defined as the eigenstates of $\hat{D}_z$ and $\hat{D}^2$:

$$\hat{D}_z|JM\rangle = M|JM\rangle \tag{1.38}$$

$$\hat{D}^2|JM\rangle = J(J+1)|JM\rangle \tag{1.39}$$

and we have relations

$$\hat{D}^\pm|JM\rangle = \sqrt{(J \mp M)(J \pm M + 1)}|JM \pm 1\rangle. \tag{1.40}$$

System evolution. We assume that all atoms are prepared at time $t = 0$ in the

upper level $|\Psi(t=0)\rangle = |e\dots e\rangle$. We suppose that all the atoms are motionless and the subsequent evolution of the system is only due to the coupling of the atoms to the radiation field (all other causes of evolution are neglected). Under these assumptions, the atomic system evolution simply appears as a cascade emission down a 'ladder' of $2J+1 = N+1$ equidistant levels (see figure 1.9). As the atomic system cascades down,

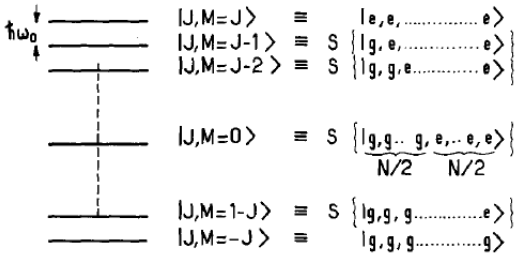

FIGURE 1.9: The 'ladder' of $N+1$ symmetrical states $|JM\rangle$; the atomic system starts at time $t=0$ from the $|e,e,e\dots e\rangle$ state and cascades down to the $|g,g,g\dots g\rangle$ state.(figure extracted from [61])

the rate of a photon emission [63]

$$\Gamma = \Gamma_0 \langle \hat{D}^+ \hat{D}^- \rangle = \Gamma_0 (J+M)(J-M+1) \tag{1.41}$$

changes depending on the value of M. For a fully excited state $M=J$ we have $\Gamma = N\Gamma_0$ and it increases to $\Gamma = \frac{1}{2}N(\frac{1}{2}N+1)\Gamma_0$ when the system reaches the half-deexcited state (M=0). As a result, we understand that the rate of photon emission strongly increases when the system cascades down the ladder of $|JM\rangle$ states and it looses energy with a maximum rate of emission proportional to N^2 obtained for $M=0$. Finally, when the system ends up in the $M=-J$ level, the rate of photon emission vanishes and the emission terminates.

In order to calculate the intensity of the emission, we solve the equations of motion. The Dicke Hamiltonian, which is given in terms of the collective operators by

$$\hat{H}_{Dicke} = \hbar\omega_0 \hat{D}_z + \sum_{\vec{k}} \hbar\omega_{\vec{k}} \hat{a}^\dagger_{\vec{k}} \hat{a}_{\vec{k}} + \sum_{\vec{k}} \left(\hbar g_{\vec{k}} \hat{a}_{\vec{k}} e^{-\imath(\omega_k - \omega_0)t} \hat{D}^+ + \text{h.c.} \right), \tag{1.42}$$

commutes with the operator $\hat{D}^2$, then $\langle \hat{D}^2 \rangle$ is a constant of motion. On the other hand, $[\hat{D}_z, \hat{H}_{Dicke}] \neq 0$ involving the cascade emission. Using the commutation relations (1.34), one can write the equation of motion for the operators $\hat{D}_z$ and $\hat{D}^-$:

$$\begin{aligned} \frac{\mathrm{d}}{\mathrm{d}t}\langle \hat{D}_z \rangle &= -\Gamma_0 \langle \hat{D}^+ \hat{D}^- \rangle \\ \frac{\mathrm{d}}{\mathrm{d}t}\langle \hat{D}^- \rangle &= -\Gamma_0 \langle \hat{D}_z \hat{D}^+ \rangle. \end{aligned} \tag{1.43}$$

In the semi-classical approximation (i.e. taking operators as $c-$numbers), we find the superradiant emission intensity [33]

$$I = -\Gamma_0 \frac{\mathrm{d}}{\mathrm{d}t}\langle \hat{D}_z \rangle = \frac{N^2\Gamma_0}{4}\mathrm{sech}^2\Big(\frac{N\Gamma_0}{2}(t-t_d)\Big) \tag{1.44}$$

with t_d the delay time resulting from calculation. In the figure 1.10, we compare the intensity profile of the superradiant emission for three different values of the number of radiators $N = 5, 10, 15$ and we see that as the number of radiators increase the emission takes place in the shorter time showing the enhanced emission rate.

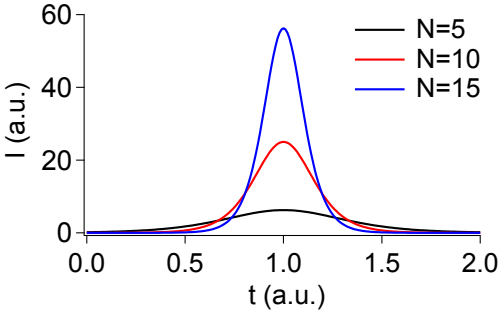

FIGURE 1.10: The intensity profile of the superradiant pulse for three different values of number of radiators N. The enhanced emission rate as a function of N is evident.

1.2.2 Raman superradiance from the Bose-Einstein condensate

We are going to consider the collective spontaneous emission from a coherent atomic source. There are three main differences compared to the classic example of Dicke superradiance from sub-wavelength sample which we have presented in 1.2.1. They are:

1. the size of the sample is larger than the pump field $r \gg \lambda$,
2. the initial state of atoms is not the excited, they are excited by the optical pump pulse
3. atoms are in motion getting recoiled or kicked whenever it emits or absorbs a photon.

Nevertheless, as we are going to see we find the same gain of the superradiation process.

1.2.2.1 Experimental configuration

The shematics of experimental setup is illustrated in Fig. 1.11(a). First a BEC (see 3.2.1 for the BEC of the metastable helium atom) is illuminated by a near-resonant laser pulse after which it emits in 4π direction, absorbing photons from an incident pulse. The advantage of using a BEC is due to two reasons; firstly, it is a source free

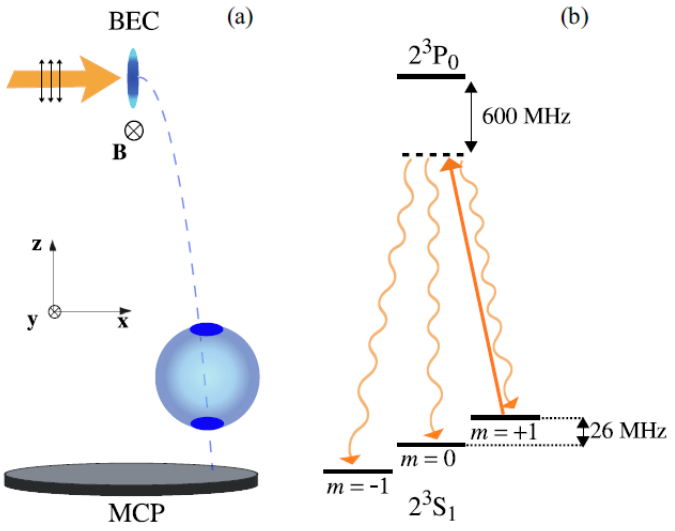

FIGURE 1.11: (a) Sketch of the experiment, (b) Atomic level scheme

from Doppler broadening and secondly, it provides optically dense medium which can be controlled easily in the experiment by letting the BEC expand after releasing it from the trap for a duration τ before applying the laser pulse. Initially the BEC is prepared in the $2^3S_1, m = 1$ state confined in a crossed dipole trap with frequencies of 1300 Hz in the x and y directions and 130 Hz in the (vertical) z direction. The dipole trap wavelength is 1.5 μm. The atom number is approximately 50000, and the temperature of the remaining cloud is 140 nK. A $9 - G$ magnetic field along the y axis defines a quantization axis. By absorbing σ^- photon from a laser pulse of 2.4 W/cm^2 tuned 600 MHz to the red of the $2^3S_1 \rightarrow 2^3P_0$ transition at $\lambda = 1083$ nm with natural linewidth 1.6 MHz, pulse length 5 μs and linear polarization relative to z axis, atoms are excited to 2^3P_0 state. The corresponding Rabi frequency of the coupling is 56 MHz. From there, it can decay with equal branching ratios to three sublevels of the ground state as shown in Fig. 1.11(b). During the pulse, less than 10% of the atoms are pumped into each of these states. We detect (see Appendix D for the electronic detection of the metastable helium) only atoms scattered to the magnetic field insensitive $m = 0$ state and the rest is swept away by strong magnetic field gradient in the experiment. So, these atoms are undergoing the Raman spontaneous emission meaning that the initial internal state ($m = 1$) is not same as the final state ($m = 0$). The atoms which fall in the $m = 0$ sublevel after emitting a single photon, get recoiled and are distributed in momentum on a sphere with radius of unit recoil momentum $k_{rec} = 2\pi/\lambda$ because of momentum conservation. For these atoms multiple scattering is not allowed in principle since they are not coupled with incident light pulse because of polarization selection rules.

In what follows we are going to look at the theory by considering only atoms making transition from $m = 1$ to $m = 0$ state, in the perturbative regime (no BEC depletion)

by following closely [38, 100].

1.2.3 Theory of Raman superradiance

We start by writing the Hamiltonian of an atom-light system whose transition is shown in the figure 1.12 where the classical pump field couples the macroscopically occupied state $|g\rangle$ to the excited state $|e\rangle$. The atoms in the excited state then decay to the state $|c\rangle$ by spontaneously emitting a photon at frequency $\omega_{\vec{k}}$. Note that we consider here a simplified picture by considering the spontaneous emission between $|e\rangle$ and $|c\rangle$ which is different from the experimental configuration where atoms allowed to decay to three substates $m = 0$, $m = +1$ and $m = -1$ competing with each other. In the perturbative regime where the BEC is far from depletion, the competition between different substates is not important and the simplified picture is assumed to describe well the process. So,

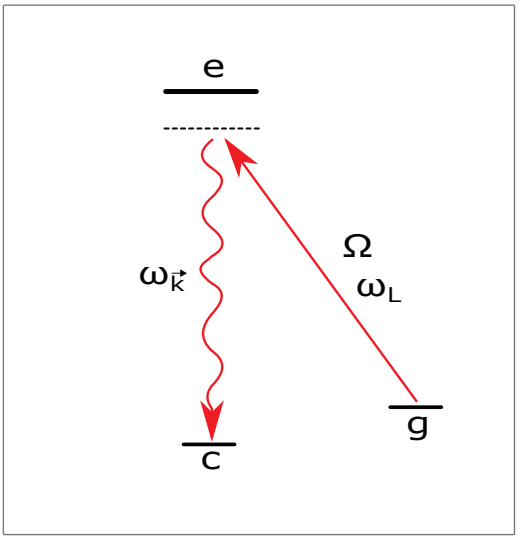

FIGURE 1.12: Atomic transition scheme for the atoms which are pumped by the coherent field with frequency ω_L from the ground state $|g\rangle$ to the excited state $|e\rangle$. The atoms in the excited state then spontaneosly decay into the state $|c\rangle$ by spontaneously emitting a photon at frequency $\omega_{\vec{k}}$.

the total Hamiltonian in the interaction picture is

$$\begin{aligned}\hat{H} = &\sum_{\alpha=g,e,c}\int \mathrm{d}\vec{r} \quad \hat{\psi}^{\dagger}_{\alpha}(\vec{r},t)\Big[-\frac{\hbar^2}{2m}\bigtriangledown^2\Big]\hat{\psi}_{\alpha}(\vec{r},t) + \int \mathrm{d}\vec{r} \quad \hbar\omega_{eg}\hat{\psi}^{\dagger}_{e}\hat{\psi}_{g} + \int \mathrm{d}\vec{k} \quad \hbar\omega_{\vec{k}}\hat{b}^{\dagger}_{\vec{k}}\hat{b}_{\vec{k}} \\ &- \int \mathrm{d}\vec{r} \quad \frac{\hbar\Omega}{2\Delta}\vec{\psi}^{+}_{e}(\vec{r},t)\hat{\psi}_{g}(\vec{r},t)e^{\imath(\vec{k}_L\cdot\vec{r}-\omega_L t)} + \text{h.c.} \\ &- \imath\int \mathrm{d}\vec{r}\int \mathrm{d}\vec{k} \quad g_{\vec{k}}\hat{b}^{\dagger}_{\vec{k}}(t)\hat{\psi}_{e}(\vec{r},t)\hat{\psi}^{\dagger}_{c}(\vec{r},t)e^{-\imath(\vec{k}\cdot\vec{r}-\omega_{\vec{k}}t)} + \text{h.c.}\end{aligned} \tag{1.45}$$

where

- 1. line is the sum of the free atomic hamiltonian and the free radiation hamiltonian with $\hat{\psi}_\alpha(\vec{r},t)$, $\hat{b}_{\vec{k}}(t)$ boson annihilation operators satisfying standard bosonic commutation relations.
- 2. line is the atom-light coupling between the states $|e\rangle$ and $|g\rangle$,
- 3. term is the atom-light coupling between the states $|e\rangle$ and $|c\rangle$ with coupling constant $g_{\vec{k}} = \sqrt{\frac{\omega_{\vec{k}}}{2\hbar\epsilon_0(2\pi)^3}}\hat{\epsilon}_{\vec{k}} \cdot \vec{d}_{e,g}$.

Experimentally, the pump laser is detuned far enough from the atomic resonance $\Delta = \omega_{eg} - \omega_p = 600$ MHz that the excited state population remains negligible, a condition which requires $\Delta \gg \gamma_{eg} = 1.6$ MHz, where γ_{eg} is the natural width of the atomic transition between the states $|e\rangle$ and $|g\rangle$. In this regime, we can formally eliminate the excited state atomic field operator. From the Heisenberg equation for $\hat{\psi}_e$ and dropping the kinetic term, we have

$$\hat{\psi}_e(\vec{r},t) \approx -\frac{\hbar\Omega}{2\Delta}\hat{\psi}_g(\vec{r},t)e^{\imath(\vec{k}_L\cdot\vec{r}-\omega_L t)} + \frac{\imath}{\Delta}\int \mathrm{d}\vec{k} g_{\vec{k}}\hat{b}_{\vec{k}}(t)\hat{\psi}_c(\vec{r},t)e^{-\imath(\vec{k}\cdot\vec{r}-\omega_{\vec{k}}t)}.$$

By substituting the expression (1.46) into the equation (1.45) and neglecting the small light shifts proportional to $|\Omega|^2$ and $|g_{\vec{k}}|^2\hat{b}^\dagger_{\vec{k}}\hat{b}_{\vec{k}}$, we obtain the following effective Hamiltonian:

$$\begin{aligned}\hat{H}_{eff} = &\sum_{\alpha=g,c}\int \mathrm{d}\vec{r} \quad \hat{\psi}^\dagger_\alpha(\vec{r},t)\Big[-\frac{\hbar^2}{2m}\bigtriangledown^2\Big]\hat{\psi}_\alpha(\vec{r},t) + \int \mathrm{d}\vec{k} \quad \hbar\omega_{\vec{k}}\hat{b}^\dagger_{\vec{k}}(t)\hat{b}_{\vec{k}}(t)\\ &+\imath\hbar\int \mathrm{d}\vec{r}\int \mathrm{d}\vec{k} \quad \frac{\Omega}{2\Delta}g_{\vec{k}}\hat{b}^\dagger_{\vec{k}}\hat{\psi}^\dagger_c(\vec{r},t)\hat{\psi}_g(\vec{r},t)e^{\imath((\vec{k}_L-\vec{k})\cdot\vec{r}-(\omega_L-\omega_{\vec{k}})t)}\end{aligned} \tag{1.46}$$

Next, as the number of atoms N in the condensate is very large and it is far from getting depleted, we neglect its density fluctuation and treat it as a c-number (see subsection 3.2.1.3):

$$\hat{\psi}_g(\vec{r},t) \approx \sqrt{N}\varphi_0(\vec{r}) \tag{1.47}$$

with φ_0 the condensate wave function. On the other hand, from momentum conservation we know that the atoms which undergo spontaneous emission get recoiled by $\vec{q} = \vec{k}_L - \vec{k}$. This suggests us to expand the scattered atomic field operator in terms of momentum states:

$$\hat{\psi}_c(\vec{r},t) = \int \mathrm{d}\vec{q} \quad \sqrt{N}\varphi_0(\vec{r})e^{\imath(\vec{q}\cdot\vec{r}-\omega_{\vec{q}}t)}\hat{c}_{\vec{q}}(t) \tag{1.48}$$

where $\omega_{\vec{q}} = \frac{|\vec{q}|^2}{2m}$. Then the effective Hamiltonian in (1.46) takes the form

$$\begin{aligned}\hat{H}_{eff} = &\int \mathrm{d}\vec{q} \quad \hbar\omega_{\vec{q}}\hat{c}^\dagger_{\vec{q}}(t)\hat{c}_{\vec{q}}(t) + \int \mathrm{d}\vec{k} \quad \hbar\omega_{\vec{k}}\hat{b}^\dagger_{\vec{k}}(t)\hat{b}_{\vec{k}}(t)\\ &+\imath\hbar\int \mathrm{d}\vec{q}\int \mathrm{d}\vec{k} \quad N\frac{\Omega}{2\Delta}g_{\vec{k}}\rho_0(\vec{k}_L-\vec{k}-\vec{q})e^{-\imath(\omega_L-\omega_{\vec{k}}-\omega_{\vec{q}})t}\hat{b}^\dagger_{\vec{k}}(t)\hat{c}^\dagger_{\vec{q}}(t)\end{aligned} \tag{1.49}$$

where we neglected relatively small energy coming from the spatial inhomogeneity of $\varphi_0(\vec{r})$ and where

$$\rho_0(\vec{k}_L - \vec{k} - \vec{q}) = \int \mathrm{d}\vec{r} \quad |\varphi_0|^2 e^{\imath(\vec{k}_L - \vec{k} - \vec{q})\cdot\vec{r}} \tag{1.50}$$

is the Fourier transform of the ground state density distribution centered at $\vec{k} = \vec{k}_L - \vec{q}$. We recognize that the Hamiltonian in the expression (1.49), is the one of the Optical Parametric Amplifier (OPA) (see 2.2.3.3). In fact, one can look at the superradiance from BEC as a Four Wave Mixing process (FWM), where a matter wave (BEC) and a coherent wave (pump) is mixed producing scattered atoms with emitted field. When the BEC and the pump is treated classically, the FWM becomes equivalent to the OPA process. Thus, the resulting state is the entangled state between scattered atoms with emitted field.

We can write the Heisenber equation for $\hat{b}_{\vec{k}} \to \hat{b}_{\vec{k}} e^{-\omega_k t}$:

$$\dot{\hat{b}}_{\vec{k}}(t) = -\imath\hbar \int \mathrm{d}\vec{q} \quad N\frac{\Omega}{2\Delta} g_{\vec{k}} \rho_0(\vec{k}_L - \vec{k} - \vec{q}) e^{-\imath(\omega_L - \omega_{\vec{k}} - \omega_{\vec{q}})t} \hat{c}^\dagger_{\vec{q}}(t) \tag{1.51}$$

In the perturbative approach (small number of scattered atom), we assume that $\hat{b}_{\vec{k}}(t)$, $\hat{c}_{\vec{q}}(t)$ and $\rho_0(\vec{k}_L - \vec{k} - \vec{q})$ vary slowly compared to $e^{-\imath(\omega_L - \omega_{\vec{k}} - \omega_{\vec{q}})t}$. Keeping this in mind, the integration of (1.51) gives a solution:

$$\hat{b}_{\vec{k}}(t) = -\imath\hbar \int \mathrm{d}\vec{q} \quad N\frac{\Omega}{2\Delta} g_{\vec{k}} \rho_0(\vec{k}_L - \vec{k} - \vec{q}) \delta_t(\omega_L - \omega_{\vec{k}} - \omega_{\vec{q}}) \hat{c}^\dagger_{\vec{q}}(t) \tag{1.52}$$

where δ_t is a function converging to a delta function for $t \to \infty$. As we can see, the emitted field amplitude is proportional to N and thus the intensity will be proportional to N^2 characterizing superradiance behaviour. Here, the collective enhancement is manifested not by the coherence of the emitting dipoles, but by the coherence between a BEC and the scattered matter wave where the memory of previous scattering events, stored in the matter-wave interference fringes, thus enhancing the rate of Raman scattering.

In the experiment we detect the scattered atoms and it can be shown that the rate of the scattering process is given by [100]

$$\frac{\mathrm{d}\langle \hat{c}^\dagger_{\vec{q}} \hat{c}_{\vec{q}} \rangle(t)}{\mathrm{d}t} \propto N^2 \int \mathrm{d}\vec{k} \quad |g_{\vec{k}}|^2 |\rho_0(\vec{k}_L - \vec{k} - \vec{q})|^2 \delta(\omega_L - \omega_{\vec{k}}). \tag{1.53}$$

As we see there is a contribution of dipole term $|g_{\vec{k}}|^2 \propto \sin^2\theta$ where θ is the angle with respect to the dipole axis and the contribution $|\rho_0(\vec{k}_L - \vec{k} - \vec{q})|^2$ coming from the condensate. This function determines the "phase matching" condition of the superradiant emission. For the anisotropic condensate the rate is high along the long axis of the condensate and the modes in this axis are privileged (so-called 'end-fire' mode [72]) while for the isotropic case we do not have privileged direction. In anisotropic case, the

matter wave is efficiently constructed along the highest optical density, thus scattering is efficient in this direction. In the experiment by expanding the condensate we change its anisotropy and the density leading to the modification of the gain of the superradiant process.

1.2.4 Experimental observation of superradiance

In the experiment, atoms fall on the detector after a long time of flight, and we essentially detect the momentum of the atoms. Two dimensional cuts in yz-plane of such momentum sphere distribution is illustratred in Fig. 1.13 for two values of duration: $\tau = 500\mu s$ (left panel) and $\tau \approx 0\mu s$ (right panel). τ is an expansion time of the BEC after release from dipole trap, it is an experimental button to control density and anisotropy of the BEC (see section 3.2.1.3). Every point here represents a single atom. In left panel, the BEC's density is low enough that we see only ordinary Raman scattering which is a well known spontaneous emission process. On the other hand, for an optically dense BEC in the right panel, the emission rate is enhanced resulting in a high gain of emission compared to ordinary Raman scattering. Total number of atoms in the right panel is increased by a factor ~ 5 compared to the left panel although the only difference between them is the density of the BEC. This is a clear signature of the superradiance process. Furthermore, we see a strong signal on top and bottom poles of yz cut of the momentum sphere in right panel corresponding to the end-fire modes. To compare, we

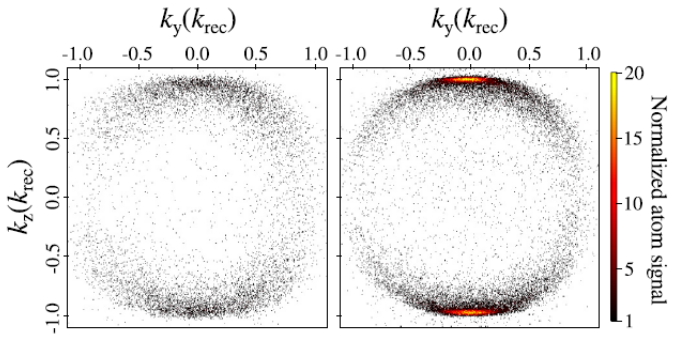

FIGURE 1.13: Average 2D momentum distribution of scattered atoms in yz plane: left panel $\tau = 500\mu s$, right panel $\tau = 0\mu s$

plot the polar distribution of the yz plane of the right panel in Fig. 1.14. Three plots are shown, corresponding to three different values of τ. For $\tau = 500\mu s$ where the optical density is quite low, we see a characteristic $\sin^2(\theta)$ dipole emission pattern with $\theta = 0, \pi$ corresponding to the orientation of the dipole along y axis. By increasing the density, we can see clearly how superradiance peaks rise indicating the high gain of the superradiant emission. To estimate theoretically the amount of the scattered atoms we need to

study the decoherence effects due to the Doppler and mean field broadenings [72] which reduces total number of the scattered atoms. Since our aim was to measure the second order correlation, we have not look at the decoherence effects and we moved directly to the second-order correlation measurements.

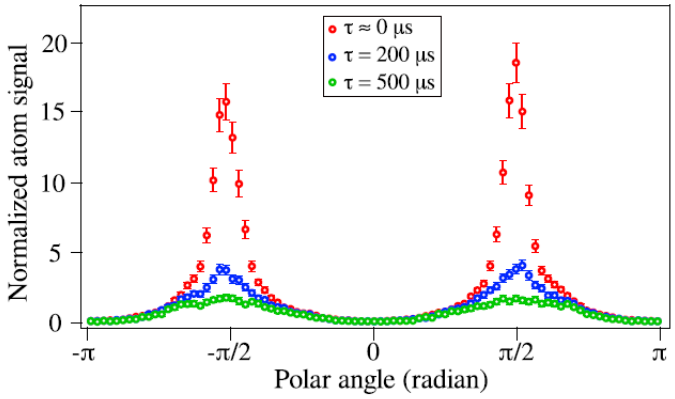

FIGURE 1.14: Angular distribution of scattered atoms in the yz plane for different values of delay τ before the excitation pulse

1.3 Measurement of the second order correlation of superradiant peaks

The second-order correlation function is done by counting atoms as a function of their momentum in three dimension. By measuring the $g^{(2)}$ function, not only we get information on the source but also on the emission as long as every single photon emission corresponds to a recoiled atom. Hence, we are also measuring indirectly the second-order correlation function of the scattered light resolved in transverse and longitudinal momentum as well as in polarization. So, why we would like to measure $g^{(2)}$ function. Well, first of all, to our knowledge nobody has measured directly the second-order correlation function of a superradiant emission in free space from the coherent source. Secondly, it is not so obvious what will be the result of this function for such a complex process. The theory we considered before is the simplified one since we did not give full account of the process (refer to [61] for a "complete" theory). On one hand, one can say that it is just an ordinary spontaneous emission since the process is initiated by vacuum and therefore the statistics is thermal. On the other hand, the high gain of superradiance might suggest a process similar to that of a laser where stimulated emission occurs and thus it is a coherent source. Taking advantage of the capability of our experimental setup, we have decided to measure the second order correlation function on superradiant atomic source and see experimentally what is the true answer.

The result of the measurement of the normalized second-order correlation function for $\tau \approx 0$ of Fig. 1.13 is presented in Fig. 1.15 along z and y axes as a function of momentum separation (see section 3.2.2 of Chapter 3 for experimental correlation measurement). The atoms in the endfire modes are considered to be superradiant and those away from the endfire modes are considered as spontaneously emitting atoms. The

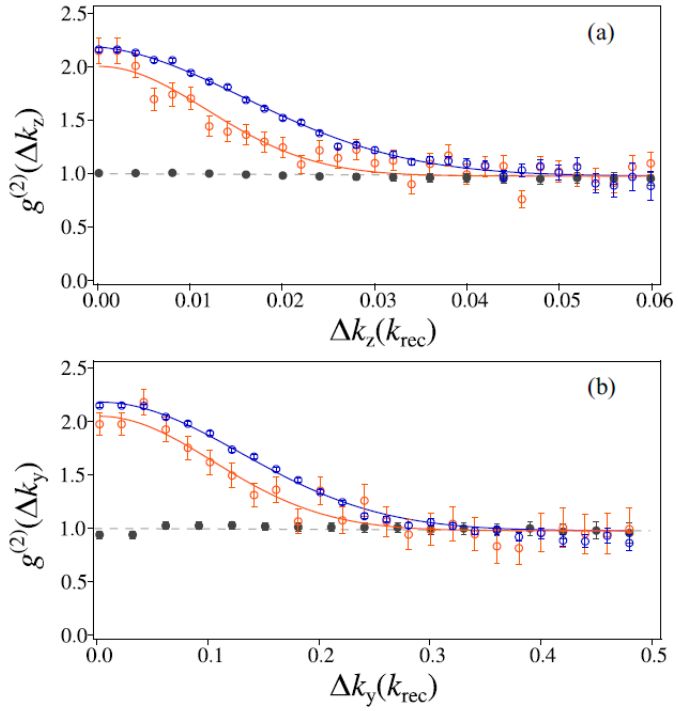

FIGURE 1.15: Correlation functions along the (a) z and (b) y axis for $\tau \approx 0$: darker (blue) circles - superradiant peaks (defined by $|k_z| > 0.95k_{rec}$), lighter (orange) circles - atoms from the scattering sphere away from the superradiant peaks (defined by $|k_z| < 0.92k_{rec}$). Solid lines are Gaussian fits constrained to approach unity at large separation. Filled gray circles correspond to a fraction of the initial condensate transferred to the $m = 0$ state via a stimulated Raman transfer. The dashed gray line shows unity. Error bars denote the 68% confidence interval

result shows that for both superradiant and spontaneously emitting atoms the correlation function at zero separation produces a value close to 2. This signifies clearly that the atoms undergoing a superradiant process have statistics comparable to that of a thermal sample despite strong amplified emission in the endfire modes. This type of statistics has been observed experimentally on Rydberg atoms coupled to a millimeter-wave cavity [115] showing thermal mode occupation, also an experiment in a cold atomic vapor in free space [56] observed a nonflat second-order correlation function. To exemplify the difference between stimulated and superradiant emission, we have measured a correlation function of a stimulated Raman scattering by applying the excitation beam together with another beam polarized parallel to the magnetic field inducing a stimulated Raman transition. The π-polarized beam is detuned by the Zeeman shift (25 MHz) with respect

to the σ-polarized beam. The laser intensities were adjusted to transfer a similar number of atoms to the $m = 0$ state as in the superradiance experiment. The normalized correlation functions in this situation, shown in Fig. 1.15, are very nearly flat and equal to unity as we expect for a BEC [68, 101, 128]. So it is in clear contrast with the second-order correlation of superradiant atoms having a thermal statistics behaviour.

1.4 Conclusion

In concusion, we have discussed first-order and second-order coherence properties of chaotic versus coherent sample. The superradiance emission from Bose-Einstein condensate and its measurement of second-order coherence is presented. We found that superradiance, even in the presence of strong gain, shows a correlation function close to that of a thermal state, just as for ordinary spontaneous emission. An interesting extension of the techniques used here is to examine enough superradiant Rayleigh scattering of a light pulse short enough and strong enough to populate oppositely directed modes [130]. It has been predicted that the modes propagating in opposite directions are entangled [24, 113, 114]. We should be able to reveal such entanglement with a similar measurement technique in the future.

Second-order coherence of superradiance from a Bose-Einstein condensate

R. Lopes, A. Imanaliev, M. Bonneau,* J. Ruaudel,† M. Cheneau, D. Boiron, and C. I. Westbrook‡
Laboratoire Charles Fabry, Institut d'Optique–CNRS–Université Paris-Sud, 2 avenue Augustin Fresnel, 91127 Palaiseau, France
(Received 23 December 2013; published 16 July 2014)

We have measured the two-particle correlation function of atoms from a Bose-Einstein condensate participating in a superradiance process, which directly reflects the second-order coherence of the emitted light. We compare this correlation function with that of atoms undergoing stimulated emission. Whereas the stimulated process produces correlations resembling those of a coherent state, we find that superradiance, even in the presence of strong gain, shows a correlation function close to that of a thermal state, just as for ordinary spontaneous emission.

DOI: 10.1103/PhysRevA.90.013615 PACS number(s): 03.75.Kk, 42.50.Lc, 67.10.Jn

Ever since the publication of Dicke's 1954 paper [1], the problem of the collective emission of radiation has occupied many researchers in the fields of light scattering, lasers, and quantum optics. Collective emission is characterized by a rate of emission which is strongly modified compared to that of individual atoms [2]. It occurs in many different contexts: hot gases, cold gases, solids and even planetary and astrophysical environments [3]. The case of an enhanced rate of emission, originally dubbed superradiance, is closely connected to stimulated emission and gain and, as such, resembles laser emission [4]. Lasers are typically characterized by high phase coherence but also by a stable intensity, corresponding to a Poissonian noise, or a flat second-order correlation function [5]. Here we present measurements showing that the coherence properties of superradiance, when it occurs in an ultracold gas and despite strong amplified emission, are much closer to those of a thermal state, with super-Poissonian-intensity noise.

Research has shown that the details of collective emission depend on many parameters such as the pumping configuration, dephasing and relaxation processes, sample geometry, presence of a cavity, etc., and, as a result, a complex nomenclature has evolved including the terms superradiance, superfluorescence, amplified spontaneous emission, mirrorless lasing, and random lasing [2,4,6–9], the distinctions among which we do not attempt to summarize here. The problem has recently seen renewed interest in the field of cold atoms [10–25]. This is partly because cold atoms provide a reproducible, easily characterized ensemble in which Doppler broadening effects are small and relaxation is generally limited to spontaneous emission. Most cold-atom experiments differ in an important way from the archetypal situation first envisioned by Dicke: instead of creating an ensemble of excited atoms at a well-defined time and then allowing this ensemble to evolve freely, the sample is typically pumped during a period long compared to the relaxation time and emission lasts essentially only as long as the pumping. The authors of Ref. [10], however, have argued that there is a close analogy to the Dicke problem, and we follow them in designating this process superradiance.

In the literature on superradiance there has been relatively little discussion about the coherence and correlation properties of the light. The theoretical treatments we are aware of show that the coherence of collective emission can be quite complicated but does not resemble that of a laser [2,13,20,26–28]. These results, however, were obtained for simple models that do not include all parameters relevant to laboratory experiments. Experimentally, a study performed on Rydberg atoms coupled to a millimeter-wave cavity [29] showed a thermal mode occupation, and an experiment in a cold atomic vapor in free space [24] observed a nonflat second-order correlation function. In the present work, we show that even if the initial atomic state is a Bose-Einstein condensate (BEC), the second-order correlation function looks thermal rather than coherent.

Such behavior, which may seem counterintuitive, can be understood by describing superradiance as a four-wave mixing process between two matter waves and two electromagnetic waves. The initial state consists of a condensate, a coherent optical pump beam, and empty modes for the scattered atoms and the scattered photons. If we make the approximation that the condensate and the pump beam are not depleted and can be treated as classical fields, the matter-radiation interaction Hamiltonian is given by

$$\hat{H} = \sum_i [\chi_i \, \hat{a}^\dagger_{\mathrm{at},i} \, \hat{a}^\dagger_{\mathrm{ph},i} + \chi_i^* \, \hat{a}_{\mathrm{at},i} \, \hat{a}_{\mathrm{ph},i}], \tag{1}$$

where $\hat{a}^\dagger_{\mathrm{at},i}$ ($\hat{a}_{\mathrm{at},i}$) and $\hat{a}^\dagger_{\mathrm{ph},i}$ ($\hat{a}_{\mathrm{ph},i}$) denote atom and photon creation (annihilation) operators for a specific pair of momenta i fixed by energy and momentum conservation and χ_i is a coupling constant. Textbooks [30] show that, starting from an input vacuum state, this Hamiltonian leads to a product of two-mode squeezed states. When one traces over one of the two modes, $\alpha = \{\mathrm{at},i\}$ or $\{\mathrm{ph},i\}$, the remaining mode β has a thermal occupation with a normalized two-particle or second-order correlator

$$\frac{\langle \hat{a}^\dagger_\beta \, \hat{a}^\dagger_\beta \, \hat{a}_\beta \, \hat{a}_\beta \rangle}{\langle \hat{a}^\dagger_\beta \, \hat{a}_\beta \rangle^2} = 2, \tag{2}$$

whereas it is unity for a laser. The problem has also been treated for four-wave mixing of matter waves [31]. We emphasize

*Current address: Vienna Center for Quantum Science and Technology, Atominstitut, TU Wien, Stadionallee 2, 1020 Vienna, Austria.
†Current address: Laboratoire Kastler Brossel, Université Pierre et Marie Curie–École normale supérieure–CNRS, 4 place Jussieu, 75005 Paris, France.
‡christoph.westbrook@institutoptique.fr

that, when starting from initially empty modes, the occupation remains thermal *regardless* of the gain.

In the experiment, we start from initially nearly motionless atoms of a BEC and observe their recoil upon photon emission. To the extent that each recoil corresponds to the emission of a single photon, we can obtain essentially the same information about the radiation from such measurements as by observing it directly. In doing this, we are following the approach pioneered in experiments such as [10] and [29] and followed by many others, which uses highly developed atom detection and imaging techniques to glean most of the experimental information about the process. We are able to make time-integrated measurements of the emission, resolved in transverse and longitudinal momentum as well as in polarization, and reconstruct the two-particle correlation function of the recoiling atoms or, equivalently, the second-order correlation function of the scattered light. We show that in the configuration of our experiment, the second-order correlation is close to that of a thermal sample and very different from the correlation properties of the initial, condensed atomic state.

We use helium in the $2\,^3S_1$, $m = 1$ state confined in a crossed dipole trap [see Fig. 1(a)] with frequencies of 1300 Hz in the x and y directions and 130 Hz in the (vertical) z direction. The dipole trap wavelength is 1.5 μm. The atom number is approximately 50 000, and the temperature of the remaining thermal cloud 140 nK. A 9-G magnetic field along the y axis defines a quantization axis. After producing the condensate, we irradiate it with a laser pulse of 2.4 W/cm^2 tuned 600 MHz to the red of the $2\,^3S_1 \rightarrow 2\,^3P_0$ transition at $\lambda = 1083$ nm and with natural linewidth 1.6 MHz. The excitation beam propagates

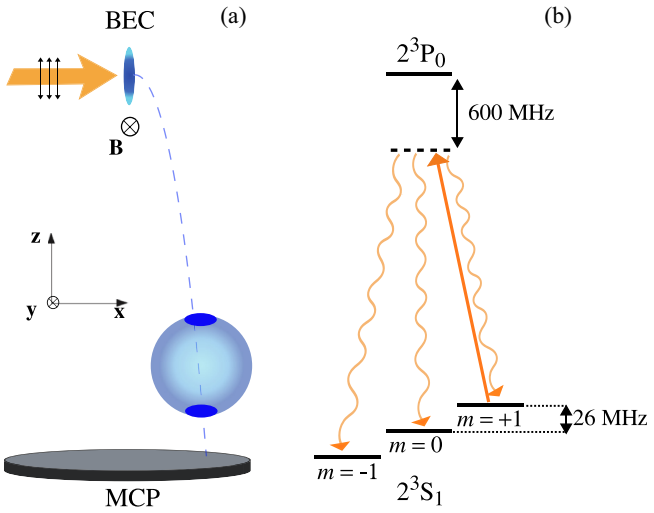

FIG. 1. (Color online) (a) Sketch of the experiment. A 9-G magnetic field **B** applied along the y axis defines the quantization axis. The excitation beam propagates with an angle of 10° (not shown) relative to the x axis and its polarization is linear, with the same angle relative to the z axis. After emission, the atoms fall 46 cm to a position-sensitive microchannel plate (MCP). The atom cloud forms a sphere with enhanced occupation of the endfire modes. (b) Atomic level scheme. The atoms, initially in the $2\,^3S_1$, $m = +1$ state, are excited to the $2\,^3P_0$ state. From there, they can decay with equal branching ratios to the three sublevels of the ground state. We detect only the atoms which scatter into the $m = 0$ state.

with an angle of 10° relative to the x axis and its polarization is linear, with the same angle relative to the z axis [see Fig. 1(a)]. The pulse length is 5 μs and it is applied with a delay τ after switching off the trap. The expansion of the cloud during this delay is a convenient way to vary both the optical density and the anisotropy of the sample at constant atom number. The absorption dipole matrix element is of the σ^- form and thus one-half of the laser intensity is coupled to the atomic transition corresponding to a Rabi frequency of 56 MHz. The excited atoms decay with equal branching ratios to the three ground states. During the pulse, less than 10% of the atoms are pumped into each of these states. Because of the polarization selection rules, the atoms which are pumped into the $m = 0$ state cannot reabsorb light from the excitation laser. By focusing on these atoms, we study the regime of "Raman superradiance" [15,32], by which we mean that an absorption and emission cycle is accompanied by a change in the internal state of the atom. When the trap is switched off, the atoms fall toward a microchannel plate detector which detects individual atoms with three-dimensional imaging capability and a 10% to 20% quantum efficiency [33]. A magnetic-field gradient is applied to sweep away all atoms except those scattered into the $m = 0$ magnetic sublevel. The average time of flight to the detector is 310 ms and is long enough that the atoms' positions at the detector reflect the atomic momenta after interaction with the excitation laser. Conservation of momentum then requires that these atoms lie on a sphere with a radius equal to the recoil momentum $k_{\rm rec} = 2\pi/\lambda$. Any additional scattering of light, whether from imperfect polarization of the excitation laser or from multiple scattering by the atoms, will result in the atoms lying outside the sphere. We see no significant signal from such events, but in order to completely eliminate the possibility of multiple scattering we restrict our analysis of the data to the spherical shell with inner radius $0.8\,k_{\rm rec}$ and outer radius $1.2\,k_{\rm rec}$.

We excite atoms in an elongated BEC in such a way that an allowed emission dipole can radiate along the long axis. In an anisotropic source, collective emission builds up more efficiently in the directions of highest optical thickness. Superradiance is therefore expected to occur along the long axis of the BEC, in so-called "endfire" modes [10,34]. An important parameter, then, is the Fresnel number of the sample [2], $F = 2R_\perp^2/\lambda R_z$, where $R_\perp$ and R_z are the horizontal and vertical Thomas-Fermi radii of the condensate. The Fresnel number distinguishes between the diffraction limited ($F < 1$) and the multimode superradiance regimes ($F > 1$). In our case, $R_\perp \approx 5$ μm and $R_z \approx 50$ μm, yielding a Fresnel number of about unity.

Typical cuts through the atomic momentum distribution in the yz plane are shown in Fig. 2, for $\tau = 500$ μs (left) and $\tau \approx 0$ (right). In both cases, the spherical shell with radius $1\,k_{\rm rec}$ appears clearly. For the short delay, when the atomic sample remains dense and anisotropic, we observe strong scattering in the endfire modes at the top and bottom poles of the sphere. In addition to this change in the profile of the distribution, we measure an increase in the *total number* of atoms on the sphere by a factor of ~5 from $\tau = 500$ μs to $\tau \approx 0$. Because each atom has scattered a single photon, this increase directly reflects an increase in the rate of emission in the sample and therefore demonstrates the collective nature

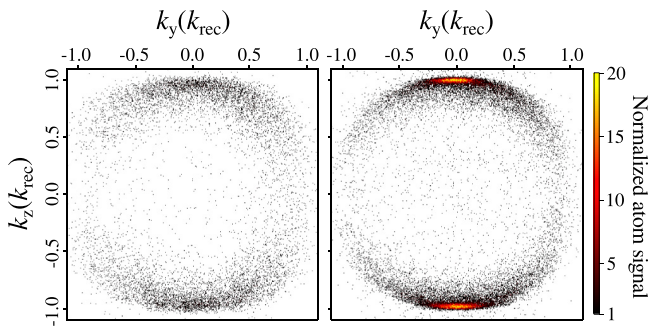

FIG. 2. (Color online) Momentum distribution of scattered atoms in the yz plane (containing the emission dipole). Both panels show the distribution in the yz plane, integrated between $k_x = \pm 0.1\, k_{rec}$ and summed over 100 shots. See the Supplemental Information for a cut in the xz plane [35]. Left: Excitation laser applied 500 μs after the trap switch-off. Only the radiation pattern for a y-polarized dipole is visible. Right: Excitation laser applied immediately after the trap switch-off. Strong superradiance is visible in the vertical, endfire modes.

of the scattering process. At long delays, the condensate has expanded sufficiently that the optical thickness and anisotropy have fallen dramatically, suppressing the collective scattering. By looking at the number of scattered atoms in the x direction (perpendicular to the plane in Fig. 2), we have verified that, away from the endfire modes, the rate of emission varies by less than 10% for different delays [35].

To see the distribution in a more quantitative way, we show in Fig. 3 an angular plot of the atom distribution in the yz plane. Data are shown for three delays τ before application of the

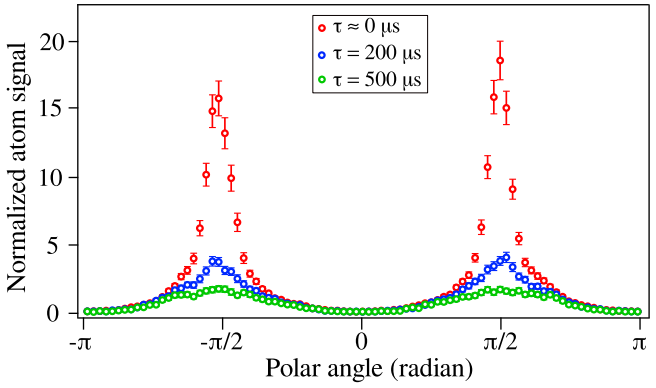

FIG. 3. (Color online) Angular distribution of scattered atoms in the yz plane (containing the emission dipole) for different values of the delay τ before the excitation pulse. From bottom to top: light-gray (green) circles correspond to $\tau = 500$ μs; dark-gray (blue) circles, to $\tau = 200$ μs; and light-gray (red) circles, to $\tau = 0$ μs. Data for $\tau = 0$ and 500 μs are the same as those shown in Fig. 2. Images were integrated along the x axis between $\pm 0.1\, k_{rec}$, and only atoms lying inside a shell with inner radius $0.8\, k_{rec}$ and outer radius $1.2\, k_{rec}$ were taken into account. The delays $\tau = 0$, 200, and 500 μs correspond to peak densities of $\approx$8, 2, and 0.4×10^{18} m^{-3} and to aspect ratios of 10, 5, and 2.5, respectively. The endfire modes are located at $\pm\pi/2$. The half-width at half-maximum of the highest peak is 0.14 rad. Error bars are shown, denoting the 68% confidence interval.

excitation pulse. For the 500-μs delay, the angular distribution follows the well-known "$\sin^2\theta$" linear dipole emission pattern, with the angles $\theta = 0$ and π corresponding to the orientation of the dipole along the y axis [35]. For the 200-μs delay, the superradiant peaks are already visible at the top of the dipole emission profile. For the shortest delay, the half-width of the superradiant peaks is $0.14\, k_{rec}$, or 0.14 rad, consistent with the diffraction angle and the aspect ratio of the source. In the vertical direction, the superradiant peaks are 10 times narrower than in the horizontal direction [35].

In the strongly superradiant case, we observe large and uncorrelated fluctuations of the heights of the two superradiant peaks on a shot-to-shot basis. These fluctuations directly reflect the fluctuations of the population of the superradiant modes. We investigate these fluctuations further by measuring the normalized two-particle correlation function of the scattered atoms, defined as

$$g^{(2)}(\Delta\mathbf{k}) = \frac{\langle : \hat{n}(\mathbf{k})\hat{n}(\mathbf{k}+\Delta\mathbf{k}) : \rangle}{\langle \hat{n}(\mathbf{k}) \rangle \, \langle \hat{n}(\mathbf{k}+\Delta\mathbf{k}) \rangle}. \tag{3}$$

Here, $\hat{n}$ is the atomic density and : : denotes normal ordering. In practice, this function is obtained from a histogram of pair separations $\Delta\mathbf{k}$ normalized to the autoconvolution of the average particle momentum distribution [36,37]. Figure 4 shows the experimentally measured correlation functions integrated over the momentum along two of three axes, both

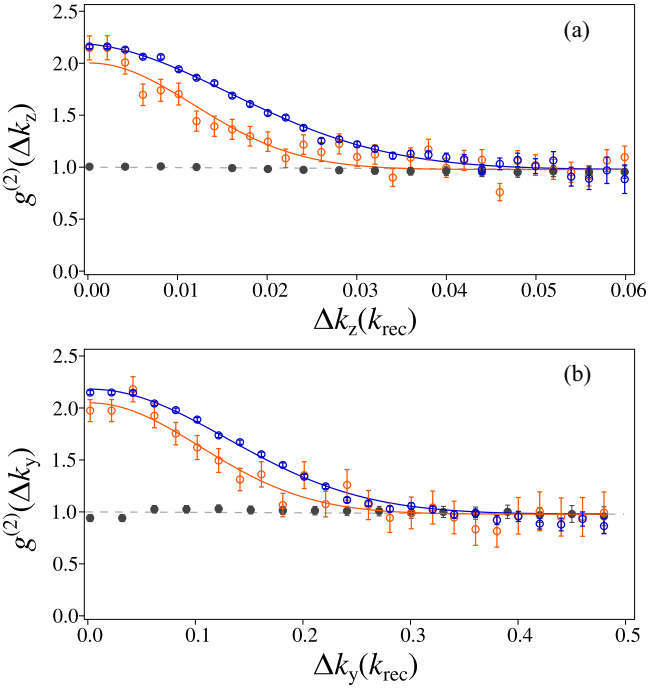

FIG. 4. (Color online) Correlation functions along the (a) z and (b) y axis for $\tau \approx 0$. Darker (blue) circles correspond to superradiant peaks (defined by $|k_z| > 0.95\, k_{rec}$). Lighter (orange) circles correspond to atoms from the scattering sphere away from the superradiant peaks (defined by $|k_z| < 0.92\, k_{rec}$). Solid lines are Gaussian fits constrained to approach unity at large separation. Filled gray circles correspond to a fraction of the initial condensate transferred to the $m = 0$ state via a stimulated Raman transfer. The dashed gray line shows unity. Error bars denote the 68% confidence interval.

for the superradiant peaks and on the scattering sphere away from the peaks [35].

We see that in both cases the correlation function at zero separation reaches a value close to 2. This shows clearly that, despite strong amplified emission in the endfire modes, the atoms undergoing a superradiant process have statistics comparable to that of a thermal sample. As emphasized in the introductory section, these large fluctuations can be simply understood by modeling the superradiant emission as a four-wave mixing process; they arise from the fact that the emission is triggered by spontaneous emission. For the superradiant peaks, the correlation actually is slightly larger than 2. Similar behavior has appeared in some models [20,38], but these models may not be directly applicable to our situation.

Figure 4 also shows that the correlation widths of the superradiant modes are somewhat broader than those of the atoms scattered in other modes. The effect is a factor of about 1.5 in the vertical direction and about 1.25 in the horizontal direction [35]. The broadening indicates that the effective source size for superradiance is slightly smaller than that for spontaneous scattering. A decreased vertical source size for superradiance is consistent with the observations in Refs. [39] and [40], which showed that the superradiant emission is concentrated near the ends of the sample. In the horizontal direction, one also expects a slightly reduced source size relative to the atom cloud since the gain is higher in the center, where the density is higher. The fact that the correlation widths are close to the widths of the momentum distribution [35] indicates that the superradiant peaks are almost single mode as expected for samples with a Fresnel number close to unity [2].

The spontaneous superradiant scattering process should be contrasted with stimulated Raman scattering. In terms of the model described by Hamiltonian (1), stimulated Raman scattering corresponds to seeding one of the photon modes with a coherent state. In this case, vacuum fluctuations do not initiate the scattering process, and the resulting mode occupation is not thermal but coherent. To study stimulated scattering, we applied the excitation beam together with another beam polarized parallel to the magnetic field and detuned by the Zeeman shift (25 MHz) with respect to the σ-polarized beam, inducing a stimulated Raman transition. The laser intensities were adjusted to transfer a similar number of atoms to the $m = 0$ state as in the superradiance experiment. The normalized correlation functions in this situation, shown in Fig. 4, are very nearly flat and equal to unity as we expect for a BEC [36,41,42]. The complementary experiment, seeding the *atomic* mode with a coherent state has also been observed to produce a coherent amplified matter wave [43,44]. As a side remark, we have also observed that the superradiant atom peaks are 2.8 times narrower in the vertical direction than the vertical width of the transferred condensate [35]. We attribute this to a longitudinal gain narrowing effect [27].

We also investigated the influence of several other experimental parameters on the second-order coherence of the superradiant emission: We have excited the atomic sample with a longer and stronger pulse (10 μs, 3.2 W/cm^2), so that the initial condensate was entirely depleted. We have explored the Rayleigh scattering regime, in which the atoms scatter back to their initial internal state. We also changed the longitudinal confinement frequency of the BEC to 7 Hz, leading to a much higher aspect ratio. These different configurations led to two-particle correlation functions which were very similar to the one discussed above. We believe that similar fluctuations will occur in superradiance from a thermal cloud provided that the gain in the medium is large enough. We were unable to confirm this experimentally in our system, precisely because of the vastly reduced optical density. However, noncoherent intensity fluctuations have been observed using magneto-optically trapped atoms [24]. This seems to confirm our interpretation that the large fluctuations of the superradiant mode occupation is an intrinsic property of superradiant emission, reflecting the seeding by spontaneous emission. The only way to suppress these fluctuations would be to restrict the number of scattering modes to one by means of a cavity and to saturate the gain by completely depleting the atomic cloud. The occupation of the superradiant mode would then simply reflect that of the initial atomic sample.

An interesting extension of the techniques used here is to examine superradiant Rayleigh scattering of a light pulse short enough and strong enough to populate oppositely directed modes [45]. It has been predicted [13,14,46] that the modes propagating in opposite directions are entangled, similar to those produced in atomic four-wave mixing [47–49]. A similar measurement technique should be able to reveal them.

We acknowledge fruitful discussions with A. Browaeys, J.-J. Greffet, and P. Pillet. This work was supported by the IFRAF institute, the Triangle de la Physique, the LABEX PALM, the ANR-ProQuP project, and the ERC Quantatop (Grant No. 267 775). J.R. was supported by the DGA; R.L., by FCT scholarship SFRH/BD/74352/2010.

[1] R. H. Dicke, Phys. Rev. **93**, 99 (1954).
[2] M. Gross and S. Haroche, Phys. Rep. **93**, 301 (1982).
[3] V. Letokhov and S. Johansson, *Astrophysical Lasers* (Oxford University Press, New York, 2008).
[4] A. E. Siegman, *Lasers* (University Science Books, Mill Valley, CA, 1986).
[5] R. Loudon, *The Quantum Theory of Light* (Oxford University Press, Oxford, 2000).
[6] N. Rehler and J. Eberly, Phys. Rev. A **3**, 1735 (1971).
[7] L. Allen and G. Peters, Phys. Rev. A **8**, 2031 (1973).
[8] R. Bonifacio and L. Lugiato, Phys. Rev. A **11**, 1507 (1975).
[9] J. MacGillivray and M. Feld, Phys. Rev. A **14**, 1169 (1976).
[10] S. Inouye, A. P. Chikkatur, D. M. Stamper-Kurn, J. Stenger, D. E. Pritchard, and W. Ketterle, Science **285**, 571 (1999).
[11] M. G. Moore, O. Zobay, and P. Meystre, Phys. Rev. A **60**, 1491 (1999).
[12] Ö. E. Müstecaplioglu and L. You, Phys. Rev. A **62**, 063615 (2000).
[13] N. Piovella, M. Cola, and R. Bonifacio, Phys. Rev. A **67**, 013817 (2003).

[14] H. Pu, W. Zhang, and P. Meystre, Phys. Rev. Lett. **91**, 150407 (2003).
[15] Y. Yoshikawa, T. Sugiura, Y. Torii, and T. Kuga, Phys. Rev. A **69**, 041603 (2004).
[16] N. Bar-Gill, E. E. Rowen, and N. Davidson, Phys. Rev. A **76**, 043603 (2007).
[17] T. Wang, S. F. Yelin, R. Côté, E. E. Eyler, S. M. Farooqi, P. L. Gould, M. Koštrun, D. Tong, and D. Vrinceanu, Phys. Rev. A **75**, 033802 (2007).
[18] E. Paradis, B. Barrett, A. Kumarakrishnan, R. Zhang, and G. Raithel, Phys. Rev. A **77**, 043419 (2008).
[19] A. Hilliard, F. Kaminski, R. le Targat, C. Olausson, E. S. Polzik, and J. H. Müller, Phys. Rev. A **78**, 051403 (2008).
[20] D. Meiser and M. J. Holland, Phys. Rev. A **81**, 063827 (2010).
[21] L. Deng, E. W. Hagley, Q. Cao, X. Wang, X. Luo, R. Wang, M. G. Payne, F. Yang, X. Zhou, X. Chen *et al.*, Phys. Rev. Lett. **105**, 220404 (2010).
[22] T. Vogt, B. Lu, X. X. Liu, X. Xu, X. Zhou, and X. Chen, Phys. Rev. A **83**, 053603 (2011).
[23] J. G. Bohnet, Z. Chen, J. M. Weiner, D. Meiser, M. J. Holland, and J. K. Thompson, Nature **484**, 78 (2012).
[24] J. A. Greenberg and D. J. Gauthier, Phys. Rev. A **86**, 013823 (2012).
[25] Q. Baudouin, N. Mercadier, V. Guarrera, W. Guerin, and R. Kaiser, Nat. Phys. **9**, 357 (2013).
[26] F. Haake and R. J. Glauber, Phys. Rev. A **5**, 1457 (1972).
[27] M. G. Moore and P. Meystre, Phys. Rev. Lett. **83**, 5202 (1999).
[28] V. V. Temnov and U. Woggon, Opt. Express **17**, 5774 (2009).
[29] J.-M. Raimond, P. Goy, M. Gross, C. Fabre, and S. Haroche, Phys. Rev. Lett. **49**, 1924 (1982).
[30] C. C. Gerry and P. Knight, *Introductory Quantum Optics* (Cambridge University Press, Cambridge, 2005).
[31] K. Mølmer, A. Perrin, V. Krachmalnicoff, V. Leung, D. Boiron, A. Aspect, and C. I. Westbrook, Phys. Rev. A **77**, 033601 (2008).
[32] D. Schneble, G. K. Campbell, E. W. Streed, M. Boyd, D. E. Pritchard, and W. Ketterle, Phys. Rev. A **69**, 041601 (2004).
[33] J.-C. Jaskula, M. Bonneau, G. B. Partridge, V. Krachmalnicoff, P. Deuar, K. V. Kheruntsyan, A. Aspect, D. Boiron, and C. I. Westbrook, Phys. Rev. Lett. **105**, 190402 (2010).
[34] R. H. Dicke, in *Quantum Electronics; Proceedings of the Third International Congress, Paris.*, edited by P. Grivet and N. Bloembergen (Columbia University Press, New York, 1964).
[35] See Supplemental Material at http://link.aps.org/supplemental/10.1103/PhysRevA.90.013615 for the atomic distribution in the xz plane, details on the calculation of the correlation functions, and a table summarizing the widths of the momentum distributions and correlation functions.
[36] M. Schellekens, R. Hoppeler, A. Perrin, J. V. Gomes, D. Boiron, A. Aspect, and C. I. Westbrook, Science **310**, 648 (2005).
[37] K. V. Kheruntsyan, J.-C. Jaskula, P. Deuar, M. Bonneau, G. B. Partridge, J. Ruaudel, R. Lopes, D. Boiron, and C. I. Westbrook, Phys. Rev. Lett. **108**, 260401 (2012).
[38] T. Wasak, J. Chwedeńczuk, P. Ziń, and M. Trippenbach, Phys. Rev. A **86**, 043621 (2012).
[39] O. Zobay and G. M. Nikolopoulos, Phys. Rev. A **73**, 013620 (2006).
[40] L. E. Sadler, J. M. Higbie, S. R. Leslie, M. Vengalattore, and D. M. Stamper-Kurn, Phys. Rev. Lett. **98**, 110401 (2007).
[41] A. Öttl, S. Ritter, M. Köhl, and T. Esslinger, Phys. Rev. Lett. **95**, 090404 (2005).
[42] S. S. Hodgman, R. G. Dall, A. G. Manning, K. G. H. Baldwin, and A. G. Truscott, Science **331**, 1046 (2011).
[43] S. Inouye, T. Pfau, S. Gupta, A. P. Chikkatur, A. Gorlitz, D. E. Pritchard, and W. Ketterle, Nature **402**, 641 (1999).
[44] M. Kozuma, Y. Suzuki, Y. Torii, T. Sugiura, T. Kuga, E. Hagley, and L. Deng, Science **286**, 2309 (1999).
[45] D. Schneble, Y. Torii, M. Boyd, E. W. Streed, D. E. Pritchard, and W. Ketterle, Science **300**, 475 (2003).
[46] L. F. Buchmann, G. M. Nikolopoulos, O. Zobay, and P. Lambropoulos, Phys. Rev. A **81**, 031606 (2010).
[47] W. RuGway, S. S. Hodgman, R. G. Dall, M. T. Johnsson, and A. G. Truscott, Phys. Rev. Lett. **107**, 075301 (2011).
[48] R. Bucker, J. Grond, S. Manz, T. Berrada, T. Betz, C. Koller, U. Hohenester, T. Schumm, A. Perrin, and J. Schmiedmayer, Nat. Phys. **7**, 608 (2011).
[49] M. Bonneau, J. Ruaudel, R. Lopes, J.-C. Jaskula, A. Aspect, D. Boiron, and C. I. Westbrook, Phys. Rev. A **87**, 061603 (2013).

Chapter 2

Bell's inequality test with massive particles: theory

In this chapter, the theory of the Bell's inequality test with momentum correlated particles will be presented. By following closely [62], we first state the problem raised by Einstein, Podolsky and Nathan (EPR)[47] who did not accept the idea that a measurement on one particle in an entangled pair could affect the state of the other-distant-particle, and concluded that quantum formalism is not a complete theory and should be replaced by 'local realist' theories. Then we derive the Bell's inequality which allows to test experimentally the predictions of local realism against those of quantum physics. Next, various experiments of Bell's inequality test will be discussed shortly and the equivalence of the experimental schemes with sources entangled in internal degrees of freedom and in external degrees of freedom will be demonstrated. Then we present our experimental scheme for the Bell's inequality test with momentum entangled helium atoms. The theories of the pair production and the Bragg pulse which are the main ingredients of this scheme will be investigated. Finally, we conclude with the evaluation of the prediction of the quantum mechanics for our atomic source and experimental scheme.

2.1 Bell's theorem

2.1.1 Joint measurements of polarization correlated photon pairs

We consider a pair of photons ν_1 and ν_2 emitted simultaneously along directions **-z** and **+z** respectively (see Fig. 2.1). The only unspecified degree of freedom is the polarization of each photon. The polarization properties of a pair are described by a state $|\psi\rangle$ in the space

$$\mathcal{E} = \mathcal{E}_1 \otimes \mathcal{E}_2 \tag{2.1}$$

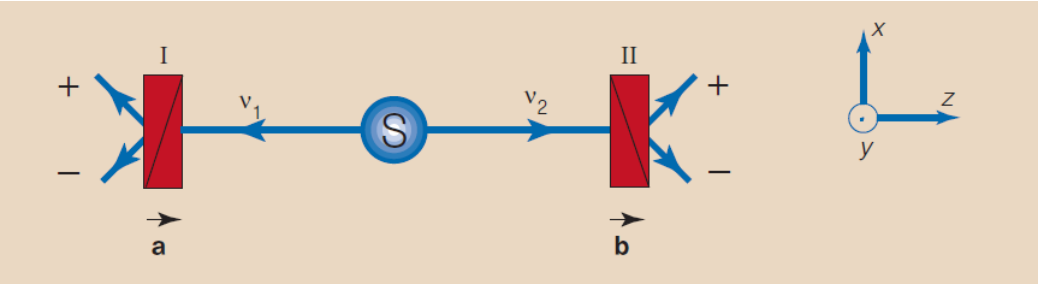

FIGURE 2.1: The polarization of photons, ν_1 and ν_2 is analysed by the linear polarizers I and II, which are oriented along $\vec{a}$ and $\vec{b}$ respectively perpendicular to the z axis. Each measurement has two possible outcomes, + or −, and one can measure the probabilities of single or joint measurements at various orientations $\vec{a}$ and $\vec{b}$. The figure is taken from [6].

which is the tensor product of the two-dimensional spaces $\mathcal{E}_1 = \{|x_1\rangle; |y_1\rangle\}$ and $\mathcal{E}_2 = \{|x_2\rangle; |y_2\rangle\}$ representing the polarizations of photon ν_1 and photon ν_2 respectively. Here $|x\rangle$ and $|y\rangle$ are basis along the axis shown in the figure 2.1. So the space $\mathcal{E}$ is four-dimensional and its basis is given by the four kets,

$$\mathcal{E} = \{|x_1, x_2\rangle; |x_1, y_2\rangle; |y_1, x_2\rangle; |y_1, y_2\rangle\}. \tag{2.2}$$

Polarization measurements can be realized using polarizers I and II, oriented along the selected directions **a** and **b** (which make angles of $\theta_{\mathbf{a}}$ and $\theta_{\mathbf{b}}$ with respect to the x-axis). Each polarizer has two output ports marked as + and −, such that if the photon $\nu_1(\nu_2)$ is polarized parallel to **a**(**b**) then it will go for sure via port + while photons with perpendicular polarization to **a**(**b**) will go via port −. The + port state $|+_{\theta_{\mathbf{a,b}}}\rangle$, and − port state $|-_{\theta_{\mathbf{a,b}}}\rangle$ of the polarizers I and II are expressed relative to the basis $\{|x\rangle, |y\rangle\}$ as,

$$|+_{\theta_{\mathbf{a,b}}}\rangle = \cos\theta_{\mathbf{a,b}}|x\rangle + \sin\theta_{\mathbf{a,b}}|y\rangle, \tag{2.3}$$

$$|-_{\theta_{\mathbf{a,b}}}\rangle = -\sin\theta_{\mathbf{a,b}}|x\rangle + \cos\theta_{\mathbf{a,b}}|y\rangle. \tag{2.4}$$

The outcome of a joint measurement on two photons of the same pair can result in one out of four possibilities $(+,+)$, $(+,-)$, $(-,+)$ and $(-,-)$. The corresponding probabilities are

$$P_{+,+}(\mathbf{a},\mathbf{b}) = |\langle +_{\theta_{\mathbf{a}}}, +_{\theta_{\mathbf{b}}}|\psi\rangle|^2 \tag{2.5}$$

$$P_{+,-}(\mathbf{a},\mathbf{b}) = |\langle +_{\theta_{\mathbf{a}}}, -_{\theta_{\mathbf{b}}}|\psi\rangle|^2 \tag{2.6}$$

and so on.

2.1.2 Polarization correlation of EPR pairs

Imagine photon pairs in the state

$$|\psi_{EPR}\rangle = \frac{1}{\sqrt{2}}(|x,x\rangle + |y,y\rangle) \tag{2.7}$$

The special nature of this state is that we cannot attribute a distinct polarization neither to photon ν_1 nor to photon ν_2 in contrast to state such as $|x,y\rangle$ which tells us clearly that a photon ν_1 is polarized along x direction whereas a photon ν_2 is polarized along y direction. The EPR state is in the configuration space where two particles are described globally, and it is less intuitive than the description in real space.

The probabilities of joint detections for the EPR state $|\psi_{EPR}\rangle$ can be easily calculated when the polarizers I and II are oriented along $\mathbf{a}$ and $\mathbf{b}$, respectively, making angles $\theta_{\mathbf{a}}$ and $\theta_{\mathbf{b}}$ with the x axis. For instance, using (2.3), (2.5), and (2.7) the probability of detecting both particles at ports $(+,+)$ is given by

$$P_{+,+}(\mathbf{a},\mathbf{b}) = |\langle +_{\theta_{\mathbf{a}}}, +_{\theta_{\mathbf{b}}}|\psi\rangle|^2 = \frac{1}{2}\cos^2(\theta_{\mathbf{a}} - \theta_{\mathbf{b}}). \tag{2.8}$$

Similarly, the other three joint detection probabilities are

$$P_{-,-}(\mathbf{a},\mathbf{b}) = \frac{1}{2}\cos^2(\theta_{\mathbf{a}} - \theta_{\mathbf{b}}), \tag{2.9}$$

$$P_{+,-}(\mathbf{a},\mathbf{b}) = P_{-,+}(\mathbf{a},\mathbf{b}) = \frac{1}{2}\sin^2(\theta_{\mathbf{a}} - \theta_{\mathbf{b}}). \tag{2.10}$$

We note that these probabilities depend only on the difference between two angles $\theta_{\mathbf{a}} - \theta_{\mathbf{b}}$ which is the angle between the two polarizers.

The probability of having the photon ν_1 at $+$ port, without taking care of ν_2, is

$$P_+(\mathbf{a}) = P_{+,+}(\mathbf{a},\mathbf{b}) + P_{+,-}(\mathbf{a},\mathbf{b}) = \frac{1}{2}. \tag{2.11}$$

Similarly, the other single detection probabilities are

$$P_-(\mathbf{a}) = \frac{1}{2}, \tag{2.12}$$

$$P_+(\mathbf{b}) = P_-(\mathbf{b}) = \frac{1}{2}. \tag{2.13}$$

For both photons it turns out that we have equal probability of detecting at $+$ and $-$ if each photon is considered separately. Consequently, in the EPR state, each photon taken independently manifests itself as unpolarized. Nevertheless, there is a strong correlation between the polarizations of ν_1 and ν_2. To demonstrate this correlation, we look at the

correlation coefficient between random variables $\mathcal{A}(\mathbf{a})$ and $\mathcal{B}(\mathbf{b})$, defined by [107]

$$E(\mathbf{a},\mathbf{b}) = \frac{\overline{\mathcal{A}(\mathbf{a})\cdot\mathcal{B}(\mathbf{b})} - \overline{\mathcal{A}(\mathbf{a})}\cdot\overline{\mathcal{B}(\mathbf{b})}}{\left(\overline{\mathcal{A}^2(\mathbf{a})} - \overline{\mathcal{A}(\mathbf{a})}^2\right)^{1/2}\cdot\left(\overline{\mathcal{B}^2(\mathbf{b})} - \overline{\mathcal{B}(\mathbf{b})}^2\right)^{1/2}} \tag{2.14}$$

where a bar over the top denotes a statistical average. The correlation coefficient takes a value between $+1$ and -1 where $+1$(-1) indicates the perfect correlation (anticorrelation), and 0 indicates no correlation between $\mathcal{A}(\mathbf{a})$ and $\mathcal{B}(\mathbf{b})$. We will use this definition to evaluate both the predictions of the quantum mechanics and the local hidden variable theories that will come later.

We can choose such that the random variables $\mathcal{A}(\mathbf{a})$ and $\mathcal{B}(\mathbf{b})$ represent the measurement results. Specifically, the random variable $\mathcal{A}(\mathbf{a})$ represents the outcome of measurement of the polarizer I, oriented along $\mathbf{a}$, and it can only assume the values $+1$ or -1. Same is true for $\mathcal{B}(\mathbf{b})$ which stands for the outcome of measurement of the polarizer II, oriented along $\mathbf{b}$. From (2.11), (2.12), and (2.13) we imply the probabilities of outcomes:

$$\mathcal{P}[\mathcal{A}(\mathbf{a}) = +1] = \mathcal{P}[\mathcal{A}(\mathbf{a}) = -1] = \frac{1}{2}, \tag{2.15}$$

$$\mathcal{P}[\mathcal{B}(\mathbf{b}) = +1] = \mathcal{P}[\mathcal{B}(\mathbf{b}) = -1] = \frac{1}{2}. \tag{2.16}$$

We now calculate the correlation coefficient in (2.14) for the measurement results given by the quantum theoretical predictions in relation to the EPR pair, as specified in (2.8)-(2.10). The statistical averages of $\mathcal{A}(\mathbf{a})$ and $\mathcal{B}(\mathbf{b})$ are

$$\overline{\mathcal{A}(\mathbf{a})} = (+1)\cdot\mathcal{P}[\mathcal{A}(\mathbf{a}) = +1] + (-1)\cdot\mathcal{P}[\mathcal{A}(\mathbf{a}) = -1] = 0, \tag{2.17}$$

$$\overline{\mathcal{B}(\mathbf{b})} = (+1)\cdot\mathcal{P}[\mathcal{B}(\mathbf{b}) = +1] + (-1)\cdot\mathcal{P}[\mathcal{B}(\mathbf{a}) = -1] = 0. \tag{2.18}$$

Similarly, we have

$$\overline{\mathcal{A}^2(\mathbf{a})} = (+1)^2\cdot\mathcal{P}[\mathcal{A}(\mathbf{a}) = +1] + (-1)^2\cdot\mathcal{P}[\mathcal{A}(\mathbf{a}) = -1] = 1, \tag{2.19}$$

$$\overline{\mathcal{B}^2(\mathbf{b})} = (+1)^2\cdot\mathcal{P}[\mathcal{B}(\mathbf{b}) = +1] + (-1)^2\cdot\mathcal{P}[\mathcal{B}(\mathbf{a}) = -1] = 1, \tag{2.20}$$

and

$$\overline{\mathcal{A}(\mathbf{a})\cdot\mathcal{B}(\mathbf{b})} = P_{+,+}(\mathbf{a},\mathbf{b}) + P_{-,-}(\mathbf{a},\mathbf{b}) - P_{+,-}(\mathbf{a},\mathbf{b}) - P_{-,+}(\mathbf{a},\mathbf{b}) \tag{2.21}$$

$$= \cos 2(\theta_{\mathbf{a}} - \theta_{\mathbf{b}}). \tag{2.22}$$

Hence, we find the correlation coefficient predicted by quantum mechanics:

$$E_{QM}(\mathbf{a},\mathbf{b}) = \overline{\mathcal{A}(\mathbf{a})\cdot\mathcal{B}(\mathbf{b})} = \cos 2(\theta_{\mathbf{a}} - \theta_{\mathbf{b}}). \tag{2.23}$$

When polarizers are aligned in the same direction, i.e. $\theta_{\mathbf{a}} - \theta_{\mathbf{b}} = 0$, we find the correlation coefficient to be equal to unity suggesting a perfect correlation between two measurements. We can thus be confident to find $+1(-1)$ for ν_2 whenever we find $+1(-1)$ for ν_1, when the polarizers have the same orientations.

2.1.3 The idea of local hidden variable theories

We have seen that there is a strong correlation between the polarizations of EPR pairs. As long as no measurement is made, there is an equal probability of finding $+1$ or -1 for each photon. But as soon as a first measurement has been made and has produced a result, for example, $+1$ along $\mathbf{a}$ for ν_1, its twin photon ν_2 is projected instantaneously into an identical polarization state as of the first one since $\frac{1}{\sqrt{2}}(|x,x\rangle + |y,y\rangle) = \frac{1}{\sqrt{2}}(|+\theta,+\theta\rangle + |-\theta,-\theta\rangle)$, $\forall\theta$. This is true whatever the distance between the two particles is, even for the distance which is greater than $c|t_1 - t_2|$ where c is speed of light, t_1 and t_2 are the instants of measurements made by polarizer I and II. This picture does not fit in the relativistic causality principle, which forbids any information from travelling faster than the speed of light. Therefore, the quantum picture seemed to be incomplete, and to be replaced with a better one. This idea was put forward in the EPR paper [47] which has lead several authors and in particular David Bohm to develop local models which we are going to discuss next.

The strong polarization correlations of the EPR pairs is rather its intrinsic property and actually it is what we measure experimentally. The model which can potentially replace the formalism of quantum mechanics should be able to predict the same correlations found for a photon pair and also satisfy the relativistic causality at the same time. A toy model we can imagine could be that half of the pairs are produced from the beginning with a common polarization in the x direction, and the other half with a polarization in the y direction . When the polarizers are oriented in the x direction, we recover the same results predicted by quantum mechanics in this configuration, i.e.

$$P_{++} = P_{--} = \frac{1}{2}, \tag{2.24}$$

$$P_{+-} = P_{-+} = 0. \tag{2.25}$$

In this picture not all pairs are identical, for each pair of photons an additional variable is prescribed during their creation. This variable is referred as the hidden variable and it may be different from one pair generation to another. To account for all orientations of the polarizers, an improved model can be developed. For instance, we suppose that the polarization of a particular pair is well defined from the outset and it has an angle λ with respect to x axis in the plane perpendicular to z axis. The orientation of the polarization changes from one pair to another, and λ can be chosen as a random variable with uniform

probability between 0 and 2π which is characterized by a probability density function

$$\rho(\lambda) = \frac{1}{2\pi}. \tag{2.26}$$

The outcomes of the measurements by polarizer I and II, which make angles θ_a and θ_b respectively with the x axis, can be defined as

$$A(\lambda, \mathbf{a}) = \text{sign}\left\{\cos 2(\theta_{\mathbf{a}} - \lambda)\right\}, \tag{2.27}$$

$$B(\lambda, \mathbf{b}) = \text{sign}\left\{\cos 2(\theta_{\mathbf{b}} - \lambda)\right\} \tag{2.28}$$

where sign-function equals $+1$ or -1 depending on the sign of the cos-function. With this model it is easy to find the predictions similar to ones in quantum mechanics for the EPR pairs. For example, the single detection probability of finding $+1$ by polarizer I is

$$P_+(\mathbf{a}) = \int_{\theta_{\mathbf{a}}-\pi/4}^{\theta_{\mathbf{a}}+\pi/4} \mathrm{d}\lambda\rho(\lambda) + \int_{\theta_{\mathbf{a}}+\pi-\pi/4}^{\theta_{\mathbf{a}}+\pi+\pi/4} \mathrm{d}\lambda\rho(\lambda) = \frac{1}{2}. \tag{2.29}$$

In fact, all the single detection probabilities are equal to $\frac{1}{2}$(compare with (2.15),(2.16)). In addition, the correlation coefficient predicted by this local hidden variable theory (LHVT) from (2.14) is

$$E_{LHVT}(\mathbf{a}, \mathbf{b}) = \int_0^{2\pi} \mathrm{d}\lambda\rho(\lambda)A(\lambda, \mathbf{a}) \cdot B(\lambda, \mathbf{b}) = 1 - 4\frac{|\theta_{\mathbf{a}} - \theta_{\mathbf{b}}|}{\pi} \tag{2.30}$$

where

$$-\frac{\pi}{2} \leq \theta_{\mathbf{a}} - \theta_{\mathbf{b}} \leq \frac{\pi}{2}. \tag{2.31}$$

In the figure 2.2, we compare the correlation coefficients (2.23) and (2.30) as a function of an angle between the polarizers I and II. They match exactly at angles $0°$, $\pm 45°$ and $\pm 90°$, and stay close for other intermediate angles. One may wonder whether it is possible to improve the form of (2.26) to be able to match exactly the two curves. The answer is provided by Bell's theorem and it is negative!

2.1.4 Bell's inequalities

The derivation of the Bell's inequalities is quite general and it applies to not only the model we discussed before but to all kinds of local hidden variable theories [10]. Broadly speaking, by introducing a parameter λ which describes the polarization of a photons of the same pair and which is random from one run to another, we would like to account for the polarization correlations of a pair. The probability density $\rho(\lambda)$ is taken as positive

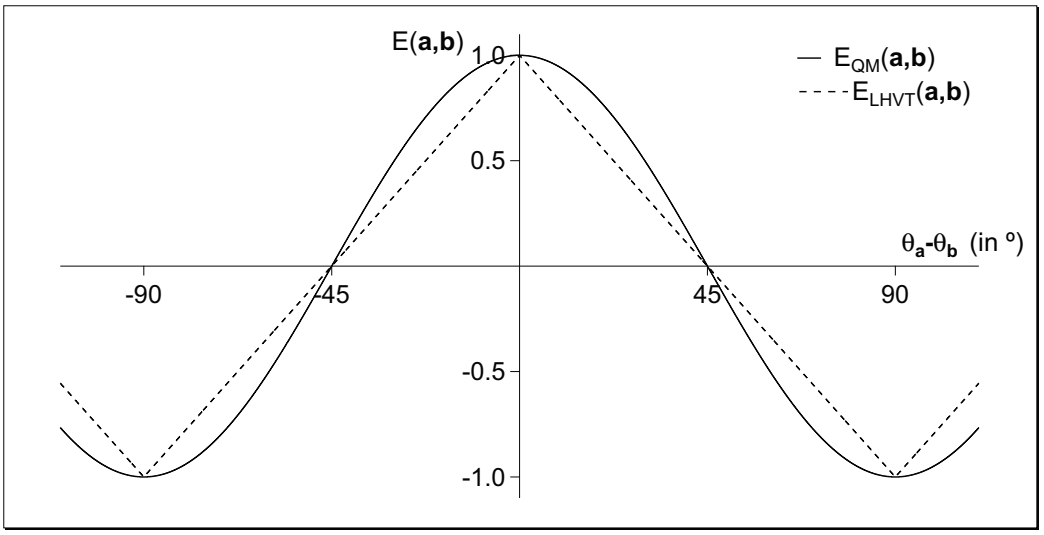

FIGURE 2.2: Polarization correlation coefficient as a function of the angle between the polarizers I and II. Comparison between the two theoretical polarization coefficients: predicted by the quantum mechanics (solid line) and the local hidden variable theory (dashed line) described in the text. We can see that they produce same results when two polarizers are perpendicular, parallel and at 45° to each other, and stay close at intermediate angles.

and definite probability, i.e.

$$\rho(\lambda) \geq 0, \tag{2.32}$$

$$\int \mathrm{d}\lambda \rho(\lambda) = 1. \tag{2.33}$$

Moreover, the outcomes of the measurements from polarizer I and II for a given pair with the common parameter λ, can exclusively assume values $+1$ or -1:

$$|\mathcal{A}(\lambda, \mathbf{a})| = |\mathcal{B}(\lambda, \mathbf{b})| = 1. \tag{2.34}$$

The probability of getting $+1$ and -1 are assumed to be equal, i.e.

$$\int \mathrm{d}\lambda \rho(\lambda) \mathcal{A}(\lambda, \mathbf{a}) = \int \mathrm{d}\lambda \rho(\lambda) \mathcal{B}(\lambda, \mathbf{b}) = 0. \tag{2.35}$$

From (2.34) and (2.35), we have $\overline{\mathcal{A}(\lambda, \mathbf{a})} = \overline{\mathcal{B}(\lambda, \mathbf{b})} = 0$ and $\overline{\mathcal{A}^2(\lambda, \mathbf{a})} = \overline{\mathcal{B}^2(\lambda, \mathbf{b})} = 1$.

In the light of these assumptions for the hidden variable model, the correlation coefficient defined in (2.14) reduces to

$$E_{LHVT}(\mathbf{a}, \mathbf{b}) = \overline{\mathcal{A}(\lambda, \mathbf{a}) \cdot \mathcal{B}(\lambda, \mathbf{b})} = \int \mathrm{d}\lambda \rho(\lambda) \mathcal{A}(\lambda, \mathbf{a}) \mathcal{B}(\lambda, \mathbf{b}). \tag{2.36}$$

To prove the Bell's inequalities, consider the quantity

$$s(\lambda, \mathbf{a}, \mathbf{a}', \mathbf{b}, \mathbf{b}') = \mathcal{A}(\lambda, \mathbf{a}) \cdot \mathcal{B}(\lambda, \mathbf{b}) - \mathcal{A}(\lambda, \mathbf{a}) \cdot \mathcal{B}(\lambda, \mathbf{b}') \tag{2.37}$$

$$+\mathcal{A}(\lambda, \mathbf{a}') \cdot \mathcal{B}(\lambda, \mathbf{b}) + \mathcal{A}(\lambda, \mathbf{a}') \cdot \mathcal{B}(\lambda, \mathbf{b}'). \tag{2.38}$$

It can be factorized in a form

$$s(\lambda, \mathbf{a}, \mathbf{a}', \mathbf{b}, \mathbf{b}') = \mathcal{A}(\lambda, \mathbf{a})\Big(\mathcal{B}(\lambda, \mathbf{b}) - \mathcal{B}(\lambda, \mathbf{b}')\Big) \tag{2.39}$$

$$+\mathcal{A}(\lambda, \mathbf{a}')\Big(\mathcal{B}(\lambda, \mathbf{b}) + \mathcal{B}(\lambda, \mathbf{b}')\Big). \tag{2.40}$$

Since, $\mathcal{B}(\lambda, \mathbf{b}) = \mathcal{B}(\lambda, \mathbf{b}')$ or $\mathcal{B}(\lambda, \mathbf{b}) = -\mathcal{B}(\lambda, \mathbf{b}')$ from (2.34), we can see that this quantity amounts to

$$s(\lambda, \mathbf{a}, \mathbf{a}', \mathbf{b}, \mathbf{b}') = \pm 2, \tag{2.41}$$

whatever the value of λ. If the quantity (2.41) is averaged over λ, it will be lying between -2 and $+2$:

$$-2 \leq \int \mathrm{d}\lambda \rho(\lambda) s(\lambda, \mathbf{a}, \mathbf{a}', \mathbf{b}, \mathbf{b}') \leq 2 \tag{2.42}$$

We can define a parameter S which is known as the Clauser-Horn-Shimony-Holt (CHSH) parameter after their discoveries [77]:

$$S(\mathbf{a}, \mathbf{a}', \mathbf{b}, \mathbf{b}') = \int \mathrm{d}\lambda \rho(\lambda) s(\lambda, \mathbf{a}, \mathbf{a}', \mathbf{b}, \mathbf{b}') \tag{2.43}$$

$$= E(\mathbf{a}, \mathbf{b}) - E(\mathbf{a}, \mathbf{b}') + E(\mathbf{a}', \mathbf{b}) + E(\mathbf{a}', \mathbf{b}') \tag{2.44}$$

where (2.36) is used for the second line of the definition. As we can see the CHSH parameter is bounded by the inequality (2.42):

$$-2 \leq S_{LHVT}(\mathbf{a}, \mathbf{a}', \mathbf{b}, \mathbf{b}') \leq 2 \tag{2.45}$$

according to the inequality (2.42). This is the Bell's inequality stated for the local hidden variable theories compatible with (2.32)-(2.35). But on the other hand, the S parameter deduced from quantum mechanics can violate the mentioned inequality for the certain set of angles. To demonstrate it, we will calculate the CHSH parameter defined in (2.44) using the correlation coefficient given by (2.23) for the following four sets of angles: $\{\theta_{\mathbf{a}} - \theta_{\mathbf{b}} = \frac{\pi}{8}, \theta_{\mathbf{a}} - \theta_{\mathbf{b}'} = \frac{3\pi}{8}, \theta_{\mathbf{a}'} - \theta_{\mathbf{b}} = -\frac{\pi}{8}, \theta_{\mathbf{a}'} - \theta_{\mathbf{b}'} = \frac{\pi}{8}\}$. The result is

$$S_{QM}(\mathbf{a}, \mathbf{a}', \mathbf{b}, \mathbf{b}') = 2\sqrt{2} = 2.828\ldots \tag{2.46}$$

It turns out that the quantum prediction of the S parameter for the EPR state can exceed considerably the upper bound set by the Bell's inequality and thereby contradicts with the results found by using the LHVT. This result is very surprising because the

conceptually easier and intuitive local models fail to reproduce same predictions of the quantum mechanics. *Finally, we have a single parameter to be measured in a suitable experiment in order to put the end to the debate between Einstein and Bohr.*

2.1.5 The experimental violation of Bell's inequality

Since the publication of the Clauser-Horne-Shimony-Holt paper [77] in 1969 which framed the Bell's inequalities in a suitable form for real experiments, there has been generations of experiments which have been tended to get more closer to the ideal scheme to test the Bell's inequalities (see for the references [5, 23]). The first generation of the experiment was carried out in the early 1970 using photon pairs generated by a decay cascaded down from a calcium atom [36]. Most results were satisfactory with quantum mechanics but the experimental set-up imperfections such as the low efficiency of the light sources and in particular, the use of single-channel polarizers giving access to only the + outcome, made these experiments extremely difficult and far from the ideal thought experiment. In the early 1980s, the second generation of the experiment was realized [8] making profit of the progress in laser physics which allowed to have a highly efficient source of pairs of correlated photons and utilizing two-channel polarizers as suggested in the ideal EPR *gedanken* scheme. It produced unambiguous violation of the Bell's inequalities by tens of standard deviations, $S_{expt} = 2.697 \pm 0.015$, [8] and an impressive agreement with the quantum mechanics was recorded (calculated quantum prediction for this experiment is $S_{expt} = 2.70 \pm 0.05$). In the late 1980s, a third generation of tests were launched with sources of photon pairs based on nonlinear optical effects [102, 104, 133, 138, 139]. With such a source the experiments were taken one step further by allowing the large separation of several tens of kilometres between two correlated photons and choosing the orientation of each polarizer in a strictly random way during the time of flight of the photons from the source [7, 144]. Indeed, then the measurement of each polarizer was totally independent of each other, which is the locality hypothesis pointed out by Bell. If there is a possible exchange between two polarizers, it is possible to reconcile the quantum mechanical and the local hidden variable theory results. So it is absolutely necessary to avoid such a loophole. There is another loophole due to the limited efficiency of the detectors which was eliminated in the experiment using the efficient detection of ions instead of photons [123]. The goal of the third generation and later experiments was to close the loopholes to demonstrate the loophole-free violation of the Bell' inequality which has not only a foundational importance in understanding the nature but also has a critical importance in device-independent quantum security protocols [1].

2.1.6 Loopholes in the experimental Bell's inequality tests

Detection loophole. In real experiments there are losses either between the source and the detector or losses resulting from the detector itself which has non-unit efficiency. So, there are three measurement outcomes instead of two; $+1$, -1 and the 'no-click' outcome, denoted as $\varnothing$. In general, such 'inconclusive' data is simply discarded and only 'valid' ± 1 measurement outcomes are considered to evaluate the Bell's expression. Such approach is approved only under the assumption of 'fair sampling' meaning that the selected set of data are the representative of the whole ensemble. However, more generally, this fair-sampling assumption fails in situations where 'no click' outcome $\varnothing$ depends on the choice of measurement [35, 106] and one should take into account 'no click' events. When 'no click' events are treated, the Bell's inequality violation becomes possible only with detectors having efficiency η above a certain threshold η^*. For the EPR state we can estimate the threshold efficiency as follows. When both detectors click, which happens with probability η^2, the CHSH parameter equals to $S = 2\sqrt{2}$ (maximum quantum mechanical value). When only one detector clicks, the outcomes are completely uncorrelated leading to $S = 0$. Finally, when no detectors click, which happens with probability $(1-\eta)^2$, the outputs are always same ('no click' for both sides) achieving the local bound $S = 2$. The entire data of the experiment must violate the Bell's inequality:

$$\eta^2 2\sqrt{2} + (1-\eta)^2 2 > 2 \tag{2.47}$$

which gives the threshold value of the detector efficiency:

$$\eta > \eta^* = \frac{2}{1+\sqrt{2}} \approx 82.8\%. \tag{2.48}$$

On the other hand, for the partially entangled state of the form $|\psi_\theta\rangle = \cos(\theta)|x,x\rangle + \sin(\theta)|y,y\rangle$ (in particular in the limit of a product state $\theta \to 0$) it was discovered [45] that the threshold limit of the detector efficiency can be lowered to $\eta \to \frac{2}{3} \sim 0.66\%$. It is a remarkable result showing that sometimes less entanglement can lead to more nonlocality.

Locality loophole. In deriving the Bell's inequality it was assumed that the two measurement sites do not communicate which seems well justified if the two sites are sufficiently separated so that the measurement duration is shorter than the time taken by a signal traveling at the speed of light, to travel from one site to the other. In addition to the condition that two measurement sites must be space-like separated, the measurement settings must be totally independent from the other side and especially they should not be correlated with the hidden variables λ. These

requirements are mathematically written as

$$\mathcal{A}(\lambda, \mathbf{a}, \mathbf{b}) = \mathcal{A}(\lambda, \mathbf{a}) \text{ and } \mathcal{B}(\lambda, \mathbf{a}, \mathbf{b}) = \mathcal{B}(\lambda, \mathbf{a}) \tag{2.49}$$

and

$$\rho(\lambda, \mathbf{a}, \mathbf{b}) = \rho(\lambda). \tag{2.50}$$

Failure to satisfy these conditions is known as the locality loophole and experimentally it is closed by using two independent random number generators to control the measurement settings and by separating the two measurement sites by a large distance.

Loophole-free Bell's inequality tests. Closing two loopholes together in one experiment has been achieved only in 2015, since the introduction of Bell's findings in 1964 by three research teams led by Ronald Hanson at Delft University of Technology in the Netherlands [66], Anton Zeilinger at the University of Vienna, Austria [53], and Lynden Shalm at NIST in Boulder, Colorado [131]. Three teams have independently confirmed that the local realism should be definitely given up. The teams at Vienna and NIST based their experiments on the scheme in the figure 2.1 using the entangled photons that are separated by 30 meters in Vienna experiment and more than 100 meters in the Boulder experiment. The alignment of the polarizers are chosen by the independent random number generators. The overall detector efficiencies were about 75%. The Delft team on the other hand used different scheme with the entanglement system which consists of two nitrogen vacancies (NV) centers, each located in a different lab. In each NV center, an electron spin is associated with an emitted photon, which is sent to a common detection station located between the labs housing the NV centers. Mixing the two photons on a beam splitter and detecting them in coincidence entangles the electron spins on the remote NV centers. In cases when the coincidence signal is detected, the researchers then keep the measurements of the correlations between the spin components and compare the resulting correlations to Bell's inequalities. The detection loophole is closed because for each entangling signal there is a result for the two spin-component measurements. The impressive distance between the two labs (1.3 km) allows the measurement directions of the spin components to be chosen independently of the entangling event, thus closing the locality loophole.

Each discovery pave the way to quite remarkable new prospects. The fact that we understand more now the properties of quantum correlation has given birth to new applications such as quantum cryptography, quantum computing, quantum teleportation etc ([23] and references therein). As we have discussed, the demonstrations of violations of Bell's inequalities have been performed with massless photons, but in only a few using

massive particles [66, 70, 83, 95, 123, 125, 135, 149]. Moreover, these massive particle experiments have been up to now limited to the spin correlation of pairs exploiting internal degrees of freedom of particles but never external degrees of freedom such as translational momentum of the type originally considered by Einstein, Podolsky and Rosen. Such momentum state Bell's inequality test would allow to extend fundamental tests of quantum mechanics into domains of gravitational fields through the direct coupling with particle mass [109]. Therefore we are motivated to demonstrate a Bell's inequality violation for a momentum-correlated atomic pair produced from the dynamical instability of Bose-Einstein condensate in a moving optical lattice [18]. Before focusing on our experimental setup, the scheme of the experiment for a momentum correlated pair will be presented and it will be shown that such scheme can be exactly mapped to the spin-wise correlated pairs scheme that we have discussed so far.

2.2 The Bell's inequality test with helium atoms correlated in momentum space

2.2.1 The equivalence between schemes using external and internal degrees of freedom for the Bell's inequality test

The Bell's inequality test can also be demonstrated using a pair correlated in momentum and indeed such experiment has been realized using two-color photon pairs from the parametric down conversion within the birefringent crystal by J. G. Rarity and P. R. Tapster [117]. In what follows, the setup of this kind will be described and the one to one correspondence with the joint measurements of the spin correlated pairs will be shown.

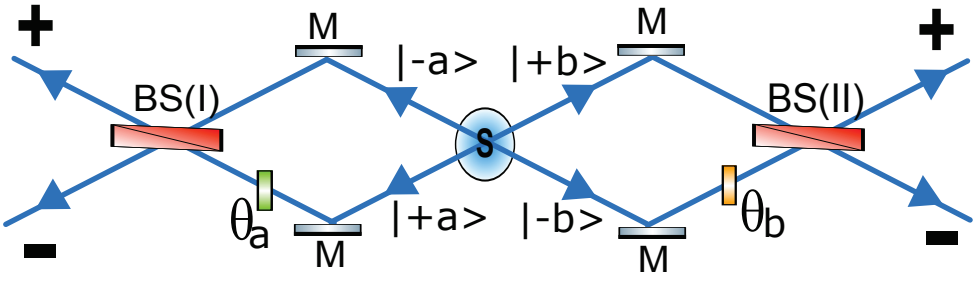

FIGURE 2.3: The Bell's inequality test scheme in momentum space. The momentum conjugate pair a and b is produced by a source in the EPR state in momentum space: $|\psi_{EPR}\rangle = \frac{1}{\sqrt{2}}(|+a,+b\rangle + |-a,-b\rangle)$. The basis for particle a, emitted to the left in the figure, is $\mathcal{E}_a = \{|+a\rangle;|-a\rangle\}$ and for particle b, emitted to the right, is $\mathcal{E}_b = \{|+b\rangle;|-b\rangle\}$. These four states are shown explicitly by four paths in the figure. Each particle is detected at either $+$ or $-$ port after the beamsplitters I and II depending on the angle between two paths $\theta_a - \theta_b$. We find one to one correspondence with the setup of the polarization correlated photons (see Fig. 2.1) in terms of joint measurements (see text).

In figure 2.3, the source is producing conjugate particles, a emitted to the left and b emitted to the right. The momentum of these particles are strongly correlated and they are in the EPR state in momentum space,

$$|\psi_{EPR}\rangle = \frac{1}{\sqrt{2}}(|+a,+b\rangle + |-a,-b\rangle) \tag{2.51}$$

where the momentum bases are $\mathcal{E}_a = \{|+a\rangle;|-a\rangle\}$ for particle a and $\mathcal{E}_b = \{|+b\rangle;|-b\rangle\}$ for particle b. So, the momentum basis for a pair is given in four dimensional space by

$$\mathcal{E} = \{|+a,+b\rangle;|-a,-b\rangle;|+a,-b\rangle;|-a,b\rangle\}. \tag{2.52}$$

We introduce phase shifts of θ_a and θ_b on one of the arms of each direction before superposing on the identical symmetric $50:50$ beamsplitters. The input and output states are related through beamsplitter matrix for a:

$$\begin{pmatrix} |+\theta_a\rangle \\ |-\theta_a\rangle \end{pmatrix} = \frac{1}{\sqrt{2}} \begin{pmatrix} 1 & \imath \\ \imath & 1 \end{pmatrix} \begin{pmatrix} \exp(\imath\theta_a)|+a\rangle \\ |-a\rangle \end{pmatrix} \tag{2.53}$$

and for b:

$$\begin{pmatrix} |+\theta_b\rangle \\ |-\theta_b\rangle \end{pmatrix} = \frac{1}{\sqrt{2}} \begin{pmatrix} 1 & \imath \\ \imath & 1 \end{pmatrix} \begin{pmatrix} \exp(\imath\theta_b)|-b\rangle \\ |+b\rangle \end{pmatrix} \tag{2.54}$$

as shown in figure 2.4. This way we define the measurement basis $|\pm\theta_{a,b}\rangle$ which is the analogue of (2.3) and (2.4). Joint measurement probabilities are given as before

$$P_{\pm,\pm}(\theta_{\mathbf{a}},\theta_{\mathbf{b}}) = |\langle\pm_{\theta_{\mathbf{a}}},\pm_{\theta_{\mathbf{b}}}|\psi_{EPR}\rangle|^2 \tag{2.55}$$

By using (2.53), (2.54) and (2.51) it is easy to show that

$$P_{+,+}(\theta_{\mathbf{a}},\theta_{\mathbf{b}}) = P_{-,-}(\theta_{\mathbf{a}},\theta_{\mathbf{b}}) = \frac{1}{2}\cos^2(\frac{\theta_a-\theta_b}{2}) \tag{2.56}$$

$$P_{+,-}(\theta_{\mathbf{a}},\theta_{\mathbf{b}}) = P_{-,+}(\theta_{\mathbf{a}},\theta_{\mathbf{b}}) = \frac{1}{2}\sin^2(\frac{\theta_a-\theta_b}{2}) \tag{2.57}$$

Thus we recover, up to a factor 2 of the argument of cos-funtion, the same correlation coefficient with the EPR state in momentum space for quantum prediction as in (2.23)

$$\begin{aligned} E_{QM}(\theta_{\mathbf{a}},\theta_{\mathbf{b}}) &= \overline{\mathcal{A}(\lambda,\mathbf{a})\cdot\mathcal{B}(\lambda,\mathbf{b})} = \sum_{\mathcal{A},\mathcal{B}} P_{\mathcal{A},\mathcal{B}}(\theta_{\mathbf{a}},\theta_{\mathbf{b}})\mathcal{A}(\theta_{\mathbf{a}})\cdot\mathcal{B}(\theta_{\mathbf{b}}) \\ &= P_{+,+}(\theta_{\mathbf{a}},\theta_{\mathbf{b}}) + P_{-,-}(\theta_{\mathbf{a}},\theta_{\mathbf{b}}) - P_{+,-}(\theta_{\mathbf{a}},\theta_{\mathbf{b}}) - P_{-,+}(\theta_{\mathbf{a}},\theta_{\mathbf{b}}) \\ &= \cos(\theta_{\mathbf{a}}-\theta_{\mathbf{b}}). \end{aligned} \tag{2.58}$$

On the other hand, the correlation coefficient predicted by the local hidden variable theories can be written in a form

$$E_{LHVT}(\theta_{\mathbf{a}},\theta_{\mathbf{b}}) = \overline{\mathcal{A}(\lambda,\theta_{\mathbf{a}})\cdot\mathcal{B}(\lambda,\theta_{\mathbf{b}})} = \int \mathrm{d}\lambda\rho(\lambda)A(\lambda,\theta_{\mathbf{a}})B(\lambda,\theta_{\mathbf{b}}). \tag{2.59}$$

because the conditions given by (2.32)-(2.35) are indeed satisfied with the current scheme, thus enabling to realize the Bell's inequality test with external degrees of freedom.

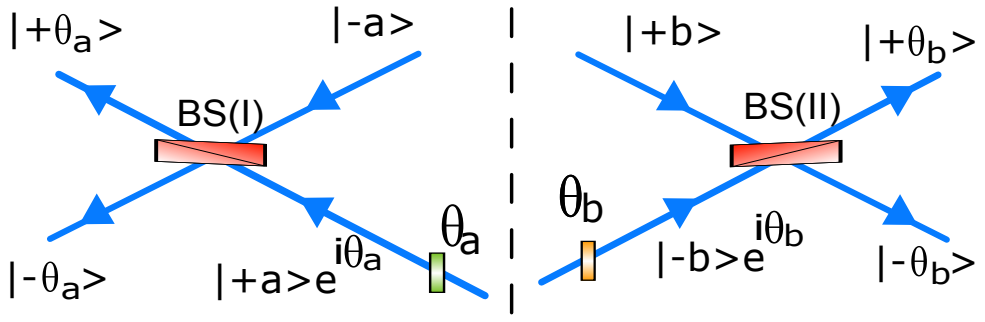

FIGURE 2.4: Input output relations of a symmetric beamsplitter for particles a and b

The more general calculation can be carried out using the second quantization quantum formalism. To evaluate the correlation coefficient we need to estimate joint probabilities $P_{\pm,\pm}(\theta_{\mathbf{a}},\theta_{\mathbf{b}})$ which are written in terms of coincidence counts $C_{\pm,\pm}(\theta_{\mathbf{a}},\theta_{\mathbf{b}})$ that are accessible directly in the experiment:

$$P_{\pm,\pm}(\theta_{\mathbf{a}},\theta_{\mathbf{b}}) = \frac{C_{\pm,\pm}(\theta_{\mathbf{a}},\theta_{\mathbf{b}})}{C_{+,+}(\theta_{\mathbf{a}},\theta_{\mathbf{b}}) + C_{-,-}(\theta_{\mathbf{a}},\theta_{\mathbf{b}}) + C_{+,-}(\theta_{\mathbf{a}},\theta_{\mathbf{b}}) + C_{-,+}(\theta_{\mathbf{a}},\theta_{\mathbf{b}})}. \tag{2.60}$$

The coincidence count can be written as

$$C_{\pm,\pm}(\theta_{\mathbf{a}},\theta_{\mathbf{b}}) = \frac{1}{\triangle T}\int_{-\triangle T/2}^{\triangle T/2} \eta_a\eta_b\langle\hat{\Psi}^{(+)}_{\pm a}(t_a)\hat{\Psi}^{(+)}_{\pm b}(t_b+\tau)\hat{\Psi}^{(-)}_{\pm b}(t_b+\tau)\hat{\Psi}^{(-)}_{\pm a}(t_a)\rangle\,\mathrm{d}\tau \tag{2.61}$$

where $\triangle T$ is finite coincidence gate time, η_a and η_b are detector efficiencies, τ is the time difference and $t_{a,b}$ is the time of detection, and $\hat{\Psi}^{(\pm)}_{\pm a,b}$ is the particle creation/annihilation operator. The evaluation of this parameter depends on the type of state used, the details of set up, etc. For two-color photons, the found result is as follows (see [117] for calculation):

$$C_{\pm,\pm}(\theta_{\mathbf{a}},\theta_{\mathbf{b}}) = C_0(R^2+T^2)\Big[1+(-1)^{\pm1\pm1}V\cos\Big(\theta_a-\theta_b+(\omega_a-\omega_b)\frac{\delta x}{c}\Big)\exp\Big(-\frac{(\delta x')^2}{\sigma^2}\Big)\Big]$$

where C_0 is a constant related to detector efficiencies and coincidence counting before

the beamsplitter, $V = 2RT/(R^2+T^2)$ is a visibility which is unity for $50:50$ beamsplitter ($R = T = 0.5$), c is the speed of light, $\omega_{a,b}$ frequencies of photons, δx is the gross path-length difference between left and right interferometers, σ is the spectral width of the photons, and $\delta x' = \delta x - c(\theta_a/\omega_a - \theta_b/\omega_b)$. Normally the photon "coherence" σ covers many optical cycles while phase delays are less than one cycle and the approximation $\delta x \approx \delta x'$ can be made. The coincidence count as a function of gross path-legth difference δx shows a cosinusoidal oscillation within a Gaussian envelope of width σ. This behaviour namely the quantum beating phenomenon has already been observed in [103, 118]. Near zero path-length difference the exponential term becomes unity. Then we find the same joint measurements formally equivalent to those for a polarization correlated photon pairs.

The goal of the rest of the chapter is going to be the calculation of the coincidence count in the case of the Bell's inequality test experiment using external degrees of freedom of massive particles which is the Helium atoms in our case.

2.2.2 The proposed scheme of the Bell's inequality test with the helium atoms

To realize the Bell's inequality test with the massive particles correlated between external degrees of freedom, we should be able to create an atomic source and manipulate it. In our case, we create a pair of atoms a and b in a conjugate multimode momentum state which is the result of the process of dynamical instability when atoms are loaded in an optical lattice (section 2.2.3.2). This method has been proven to be efficient and the nonclassical properties of this source has already been demonstrated in our group [18]. The output state of a pair of atoms can be put in the EPR state $|\psi_{EPR}\rangle = \frac{1}{\sqrt{2}}(|1_{k_{b+}}, 1_{k_{a-}}\rangle + |1_{k_{b-}}, 1_{k_{a+}}\rangle)$ by isolating two conjugate modes, $\{k_{b+}; k_{a-}\}$ and $\{k_{b-}; k_{a+}\}$, with the help of aperture (A) as shown in figure 2.5. We should also ensure to have a pair of atom at a time to obtain such a state. The next step is to make interfere the non-conjugate modes, $\{k_{b+}; k_{a+}\}$ and $\{k_{b-}; k_{a-}\}$, on the two separate beamsplitters and measure the coincidence counting between outputs of distinct interferometers as a function of phases θ_+ and θ_- introduced on the interferometers of $+$ modes and $-$ modes respectively. The manipulating elements: aperture, mirror, beamsplitter and phase plate are all realized using bragg pulses obtained from superposition of two optical beams (section 2.2.4). The last step is to look at the coincidences $C_{++}(\theta_+, \theta_-) = C_{D1,D3}$, $C_{--}(\theta_+, \theta_-) = C_{D2,D4}$, $C_{+-}(\theta_+, \theta_-) = C_{D1,D4}$ and $C_{-+}(\theta_+, \theta_-) = C_{D2,D3}$ which correspond to coincidence counts between detectors of separate interferometers to estimate the correlation coefficient as a function of angles θ_+ and θ_-. In the next two sections the pair creation method and bragg pulse will be described in detail. The last section is devoted to the estimation of the correlation coefficient for our experimental setup.

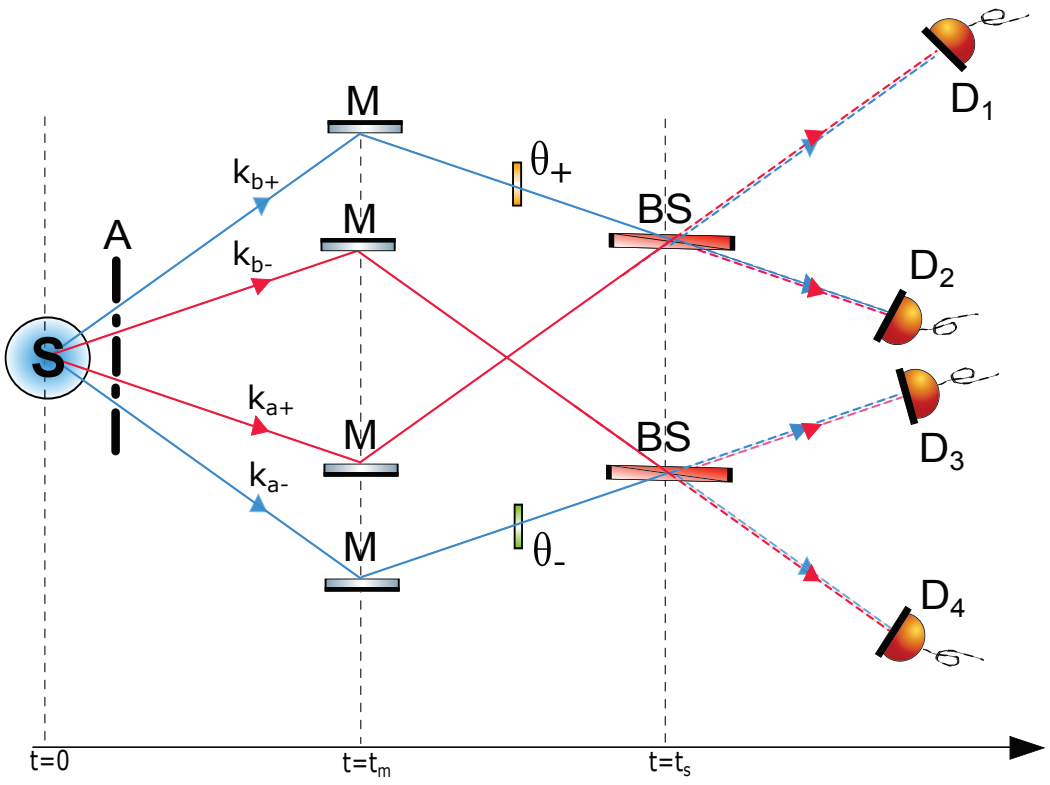

FIGURE 2.5: **Schematics of the Bell's inequality test experiment using a pair of helium atoms correlated in momentum space** A pair of helium atoms, a and b, are emitted in a conjugate multimode momentum state by the source (S) at time $t = 0$. Two pair of conjugate modes, $\{k_{b+}; k_{a-}\}$ (shown in blue) and $\{k_{b-}; k_{a+}\}$ (shown in red) are selected by the aperture (A). The non-conjugate modes $\{k_{b+}; k_{a+}\}$ and $\{k_{b-}; k_{a-}\}$ are then made to interfere on two different beamsplitters (BS) at time $t = t_s$ with the help of mirrors (M) applied at $t = t_m$. Two distinct phases θ_+ and θ_- are introduced for each interferometer, $+$ and $-$ respectively. Finally, the atoms are detected after a time of flight and the coincidence counting is made between outputs of separate interferometers.

2.2.3 The atomic pair creation

2.2.3.1 The dynamical instability

In order to get full insight of the physics of the atomic pair creation process, the summary of the work by Biao Wu and Qian Niu [146, 147] who studied the effect of the lattice on the stability of the condensate in one dimension will be presented. Later, we will focus on the state of the resulting pair considering the nondepleted condensate regime.

Most of the photon pair creation processes necessitate a nonlinear medium. On the contrary, we do not need an intermediate medium for the atoms, since the nonlinearity is created through the strong interaction of the atoms between each other. We consider a system of Bose-Einstein condensate (BEC) of helium atoms in an optical lattice and look at the dynamical instability resulting from it. Using a BEC provides us with high density of atoms and with a well defined momentum. The BEC can be considered atomic

analog of a laser source in optics. The system is governed by the following Hamiltonian:

$$\hat{H} = \hat{H}_0 + \hat{H}_{int} = \int \mathrm{d}\vec{r} \quad \hat{\Psi}^\dagger \Big[-\frac{\hbar^2\nabla^2}{2m} + V(\vec{r},t)\Big]\hat{\Psi} + \frac{g}{2}\int \mathrm{d}\vec{r} \quad \hat{\Psi}^\dagger\hat{\Psi}^\dagger\hat{\Psi}\hat{\Psi} \tag{2.62}$$

where $g = \frac{4\pi\hbar^2 a}{m}$ is the interaction coupling constant, fixed by the s-wave scattering length a, and $V(\vec{r},t)$ is the external potential. In our experiment, the transverse degree of freedom can be considered as frozen due to the high confinement of the dipole trap (longitudinal and transverse radial frequencies of the dipole trap are: $\omega_z \sim 2\pi \times 100$ Hz and $\omega_\perp \sim 2\pi \times 1300$ Hz respectively), thus the problem can be approximately considered as unidimensional (see [98, 124] for the transverse effects). In the frame of mean-field theory, the hamiltonian becomes:

$$H = \int \mathrm{d}z \Big\{ \psi^*(z) \Big(-\frac{\hbar^2}{2m}\frac{d^2}{dz^2} + V(z,t)\Big)\psi(z) + \frac{g}{2}|\psi(z)|^4 \Big\} \tag{2.63}$$

In the first place we search for the stationary solutions of the hamiltonian, meaning a solution which verifies the Gross-Pitaevskii equation:

$$-\frac{\hbar^2}{2m}\frac{d^2\psi}{dz^2} + V(z,t)\psi + gn_0|\psi|^2\psi = \mu\psi \tag{2.64}$$

with the mean density n_0 and the chemical potential μ. In our case, the external potential is represented by only the periodic potential of the lattice (longitudinal confinement is neglected). It is created by superposing two laser beams on the atoms (see Chapter 3, section 3.2.2). In the frame of reference of the lattice, the atoms are subjected to the time independent periodic potential [40]:

$$V(z,t) = V(z) = \frac{V_0}{2}(1 - \cos(2k_{lat}z)) \tag{2.65}$$

where $k_{lat} = \frac{2\pi}{\lambda}\sin(\theta/2)$, λ is the wavelength of laser beams which make a lattice, and θ is the angle between these laser beams. The potential depth is given by:

$$V_0 = -\frac{\hbar\Gamma^2 I_0}{2I_{sat}\Delta} \tag{2.66}$$

with Γ natural width, I_0 is the amplitude of the intensity resulting from the superposition of two laser beams, I_{sat} the saturation intensity, Δ is given by $\frac{1}{\Delta} = \frac{1}{\omega-\omega_0} + \frac{1}{\omega+\omega_0}$ with ω_0 resonance frequency of atomic transition, and ω is the frequency of the laser.

In order to find the solution of the equation (2.64), we treat the interaction perturbatively, in other words, we find first the solutions without the interaction term, these are given as (in the band theory):

$$\psi_q(z) = \exp(\imath q z)u_q(z) \tag{2.67}$$

where a function $u_q(z)$ has the same periodicity as the potential and can be decomposed in terms of plane waves:

$$u_q(z) = \sum_{m=-\infty}^{\infty} a_m(q) \exp(-2\imath m k_{lat} z) \tag{2.68}$$

Then we reinject the found solution for the interaction term, and we search again for the new solutions of the Gross-Pitaevskii equation but this time including the interaction term. We repeat this procedure until we get a self-consistent solution.

Next, we study the dynamical stability of the system governed by the time dependent Gross-Pitaevskii equation:

$$\imath\hbar\frac{\partial}{\partial t}\psi(z,t) = -\frac{\hbar^2}{2m}\frac{\partial^2\psi(z,t)}{\partial z^2} + \frac{V_0}{2}(1-\cos(2k_{lat}z))\psi(z,t) + gn_0|\psi(z,t)|^2\psi(z,t). \tag{2.69}$$

To study the stability of this equation, we add a perturbation to the fundamental state of the self-consistent solution found earlier $\psi(z,t) = \psi_{q_0}(z) + \delta\psi_{q_0}(q,z,t)$. The form of the perturbation is chosen as to represent excitations with quasi-momentum $q_0 + q$ and $q_0 - q$:

$$\delta\psi_{q_0}(q,z,t) = v_{q_0}(z,q,t)\exp(\imath qz) + w^*_{q_0}(z,q,t)\exp(-\imath qz) \tag{2.70}$$

with $q \in [-k_{lat}, k_{lat}]$ and $v_{q_0}(z,q,t), w_{q_0}(z,q,t)$ functions of the same periodicity as the lattice. We are going to see that when starting with BEC at quasi momentum q_0, atoms at $q_0 \pm q$ will appear due to the non-linearity [67].

From the equation (2.69), developing up to the first order, we obtain

$$\imath\frac{\partial}{\partial t}\begin{pmatrix} v_{q_0}(z,q,t) \\ w_{q_0}(z,q,t)\end{pmatrix} = \mathcal{M}_{q_0}(q)\begin{pmatrix} v_{q_0}(z,q,t) \\ w_{q_0}(z,q,t)\end{pmatrix} \tag{2.71}$$

where

$$\mathcal{M}_{q_0}(q) = \begin{pmatrix} \mathcal{L}(q_0+q) & gn_0\psi^2_{q_0}(z) \\ -gn_0\psi^{*2}_{q_0}(z) & -\mathcal{L}(-q_0+q)\end{pmatrix} \tag{2.72}$$

and

$$\mathcal{L}(q_0) = -(\frac{\partial}{\partial z} + \imath q_0)^2 + \frac{V_0}{2}(1-\cos(2k_{lat}z)) - \mu + 2gn_0|\psi_{q_0}(z)|^2 \tag{2.73}$$

If the eigenvalues of the matrix $\mathcal{M}_{q_0}(q)$ accept an imaginary positive part for the given q_0 and q, the system becomes unstable leading to the exponential growth of the mode in time. We diagonalize the matrix for each q_0 and q and we look at the imaginary part of the eigenvalue associated to the fundamental band. Then, we can trace the imaginary part of the energy related to the mode q and the initial momentum $q_0 = k_0$ of the condensate. The curve 2.6 shows the result obtained from the numerical simulations with the typical value of the lattice depth $V_0 = 1E_r$ (in units of recoil energy $E_r = \frac{\hbar^2 k^2_{lat}}{2m}$)

in our experiment. According to the curve, for a given value of k_0 above a threshold value,

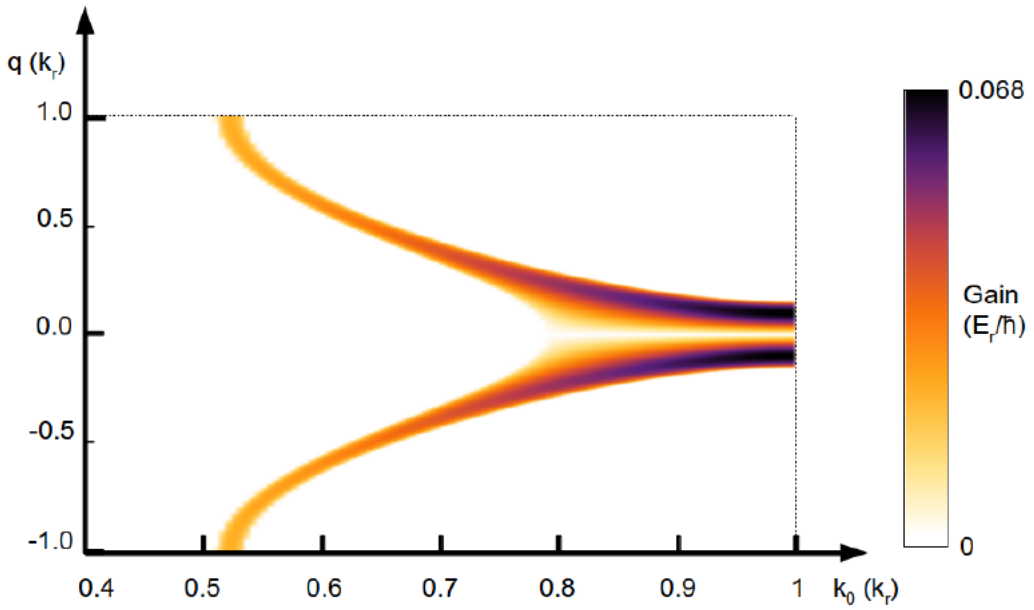

FIGURE 2.6: Gain(imaginary part of the energy) associated with the quasi momentum q (in units of k_{lat}) of the perturbation and the initial momentum of the condensate k_0 (in units of k_{lat}). The lattice depth is $V_0 = 1E_r$. We see that starting from threshold value of k_0, continuum of conjugate modes with finite width emerges. Figure adopted from [124]

we see that the imaginary part of the energy is nonzero centered on two modes q and $-q$. Therefore, the modes centered at $k_1 = k_0 - q$ and $k_2 = k_0 + q$ will grow exponentially in time and it can happen spontaneously without seeding due to the vacuum fluctuations. There are continuum of conjugate modes with finite width as a function of k_0.

This process namely dynamical instability has been studied experimentally by different groups [28, 50, 96]. The loss resulting from the instability as a function of the momentum of the condensate has been studied in [49]. The authors showed the strong increase in atomic loss rate starting from a threshold value of the quasi-momentum of the condensate $q_0 = k_0$, as shown in figure 2.7.

2.2.3.2 The dynamical instability as a four wave mixing process

The fact that the two perturbation modes grow up simultaneously suggests that the loss is pairwise. Indeed, the dynamical instability can be considered as a four wave mixing process in the presence of a periodic potential which enables the energy and momentum conservation in one dimension by modifying the dispersion relation with respect to the free space [67]. To explore it in more detail, reconsider the hamiltonian in (2.62):

$$\hat{H} = \hat{H}_0 + \hat{H}_{int} = \int \mathrm{d}\vec{r} \quad \hat{\Psi}^\dagger \Big[-\frac{\hbar^2 \nabla^2}{2m} + V(\vec{r}) \Big] \hat{\Psi} + \frac{g}{2} \int \mathrm{d}\vec{r} \quad \hat{\Psi}^\dagger \hat{\Psi}^\dagger \hat{\Psi} \hat{\Psi} \tag{2.74}$$

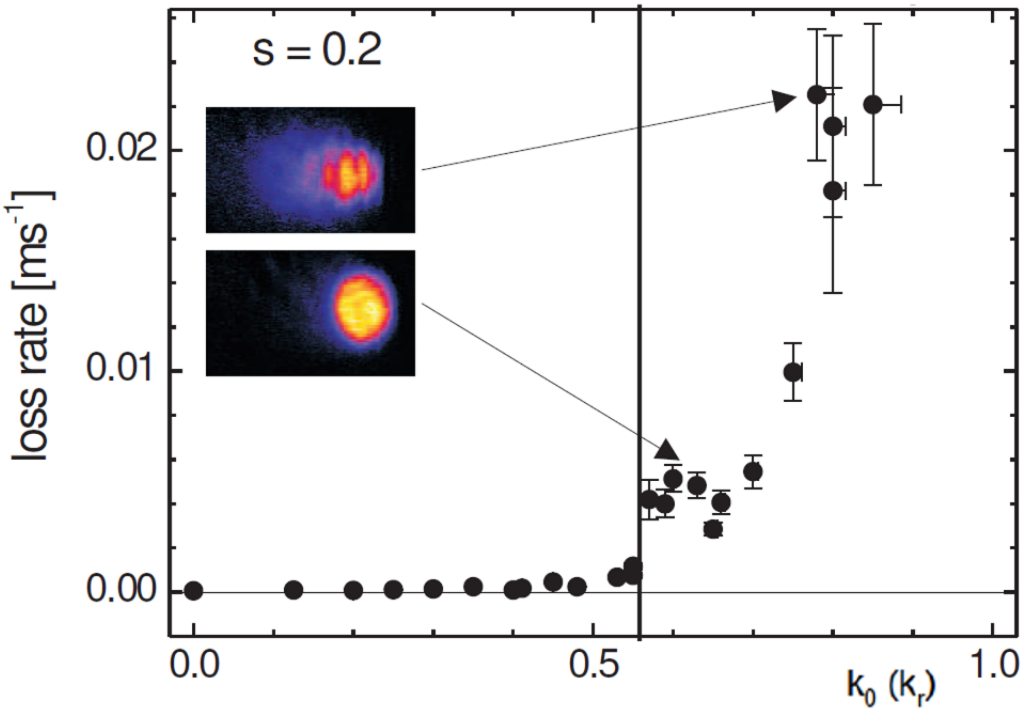

FIGURE 2.7: Loss rate of a condensate in an optical lattice as a function of its quasi-momentum k_0. Increase in the loss rate corresponds with the expected threshold value(vertical line). When the loss rate is important, the density of the condensate exhibit a complex structure, indicating the loss of the coherence. Figure extracted from [49]

Within the framework of the four-wave mixing, the field operator can be decomposed in pump (Φ_{p_1} and Φ_{p_2}), signal (Φ_{k_1}) and idle (Φ_{k_2}) (multi) modes :

$$\hat{\Psi}(\vec{r},t) = \Phi_{p_1}(\vec{r},t)\hat{a}_{p_1} + \Phi_{p_2}(\vec{r},t)\hat{a}_{p_2} + \Phi_{k_1}(\vec{r},t)\hat{a}_{k_1} + \Phi_{k_2}(\vec{r},t)\hat{a}_{k_2} \tag{2.75}$$

with $\hat{a}_i$ the annihilation operator of a particle in mode i. Inserting this decomposition for the expression of the interaction hamiltonian $\hat{H}_{int}$ in (2.74) we get numerous terms, and in particular:

$$\hat{H}_{4WM} = \frac{g}{2}\int \mathrm{d}\vec{r}\Phi^*_{p_1}(\vec{r},t)\Phi^*_{p_2}(\vec{r},t)\Phi_{k_1}(\vec{r},t)\Phi_{k_2}(\vec{r},t)\hat{a}^\dagger_{p_1}\hat{a}^\dagger_{p_2}\hat{a}_{k_1}\hat{a}_{k_2} + h.c. \tag{2.76}$$

describing the four wave mixing or in other words, the diffusion of two atoms in pump modes Φ_{p_1} and Φ_{p_2} into a pair of modes Φ_{k_1} and Φ_{k_2} (and the inverse process). The other terms, in our condition, never satisfy the energy conservation and influence hardly the evolution of the system.

In order to describe the phase matching condition of the four wave mixing process of the condensate in the presence of the optical lattice, we consider a condensate with the quasi-momentum k_0, which is loaded into the fundamental band of the shallow

optical lattice, we wait until the two diffused modes with the quasi-momenta k_1 and k_2 are populated, and then we remove the lattice. Loading and unloading atoms are considered to be adiabatic meaning that the atoms stay in the fundamental band and the quasi-momenta, defined in the first Brillouin zone, are mapped to the real momenta in the frame of lattice. Then the momentum and the energy conservation of the four wave mixing process can be written as (discarding mean field):

$$k_1 + k_2 = 2k_0 \tag{2.77}$$

$$E(k_1) + E(k_2) = 2E(k_0) \tag{2.78}$$

since the pump modes are degenerate, $k_{p_1} = k_{p_1} = k_0$ representing atoms in the condensate. These relations are represented graphically in 2.8, where the phase matching condition is satisfied for the segment $[M_1 = (k_1, E(k_1)), M_2 = (k_2, E(k_2))]$ on the dispersion relation provided that the point $M_0 = (k_0, E(k_0))$ is placed on the middle of this segment. We understand that we need a concavity for the dispersion relation to be

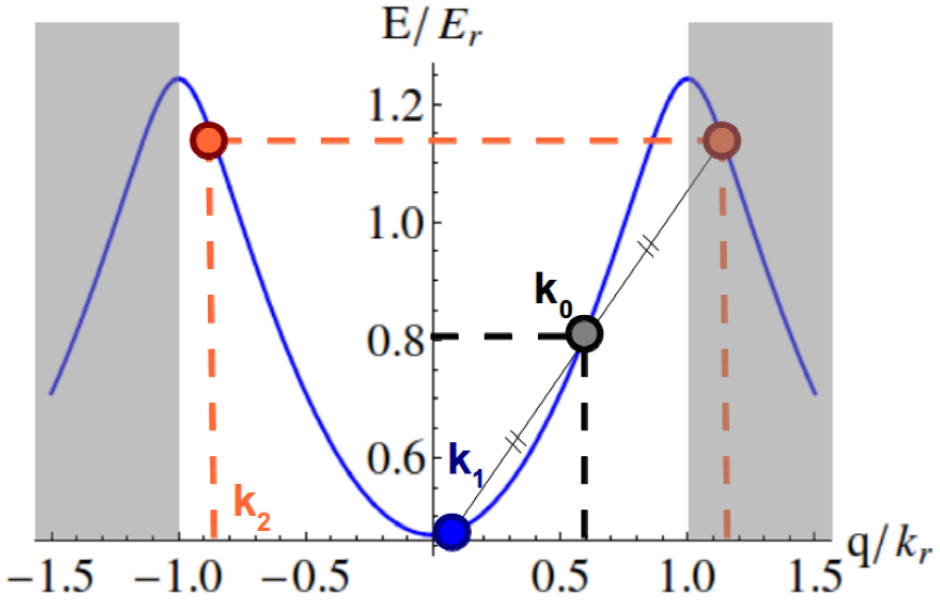

FIGURE 2.8: Examples of phase matching points of the four wave mixing process in an optical lattice. The quasi-momentums are defined modulo $2k_{lat}$, the point which is out of the first Brillouin zone, is folded. Figure extracted from [124]

able to draw such a segment. The concavity is provided by the periodic potential in our system. Also the existence of such a segment is only possible above a threshold value of the initial momentum of the condensate $k_0 \approx 0.5k_{lat}$, the exact value of which depends on the lattice depth and the interaction.

The experimental demonstration of the phase matching condition has been shown

by the group of Ketterle [29] and studied in more detail including the effects of mean-field in our group [18]. In both cases, the momentums k_1 and k_2 are tuned as a function of the initial momentum of the condensate k_0 (see figures 2.9 and 2.10).

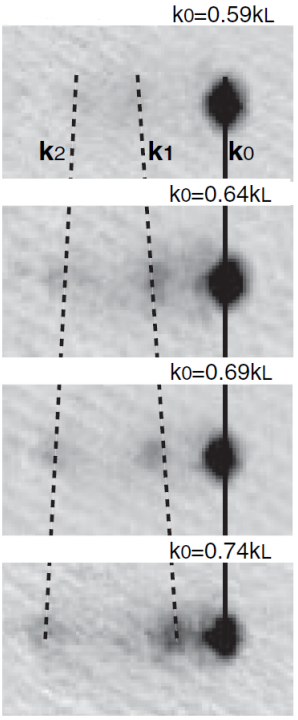

FIGURE 2.9: Absorption images for the different values of the condensate quasimomentum k_0. As k_0 varied, the k_1 and k_2 has been changed as expected. Figure extracted from [29]

2.2.3.3 The four wave mixing in the non-depleted classical pump regime

The four wave mixing hamiltonian given in (2.76) can be written as (only two modes are considered):

$$\hat{H}_{4WM} = \frac{g}{2}\left[C(\hat{a}_{k_0})^2 \hat{a}^\dagger_{k_1}\hat{a}^\dagger_{k_2} + h.c.\right] \tag{2.79}$$

where C is proportional to the overlap of the pump, signal and idle wavefunctions. If the population N_{k_0} of the pump is considered as macroscopic and non-depleted, then the operator $\hat{a}_{k_0}$ can be treated classically in terms of their mean value $\hat{a}_{k_0}(t) = \sqrt{N_{k_0}(t)} = \sqrt{N_{k_0}(0)}\exp(\frac{-\imath E_{k_0} t}{\hbar})$. This approximation is fulfilled in our experiment since the population of the pair is about 2 atoms on average and the pump consists of a condensate with $N_{k_0} \sim 10^5$ atoms, and it is far from being depleted so that we can easily neglect fluctuations of the number of the atoms in the condensate. Then, we can write the

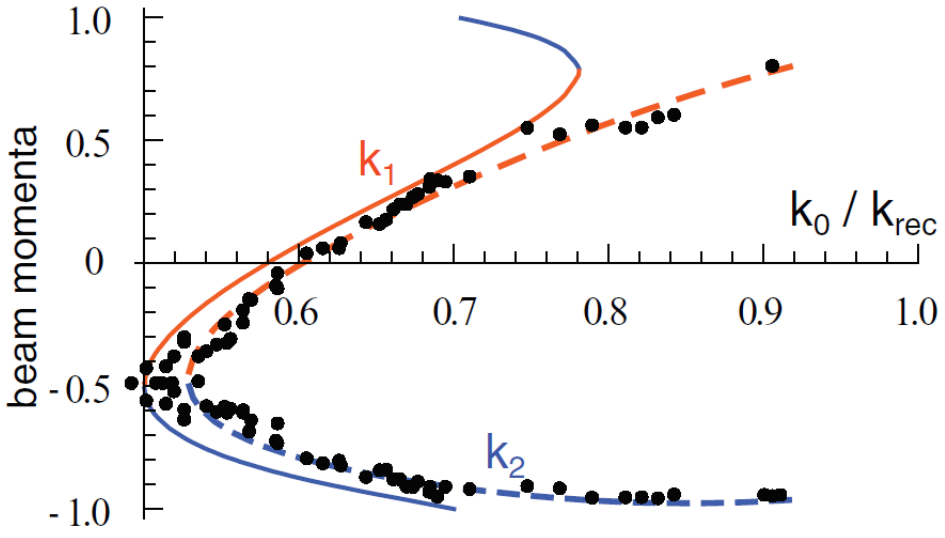

FIGURE 2.10: Measured mean momenta k_1 and k_2 (black dots, in units of k_{lat}) as a function of k_0(initial BEC momentum in the lattice frame). The solid line shows the phase-matching curve expected without interactions, while the dashed line includes the mean field effect (see [18] for the detail). Figure extracted from [18]

approximative full hamiltonian in a form:

$$\begin{aligned}\hat{H} &= \left[E_{k_0}N_{k_0} + \sum_{i=k_1,k_2} E_i \hat{a}_i^\dagger \hat{a}_i\right] + \frac{g}{2}\left[CN_{k_0}\hat{a}_{k_1}^\dagger \hat{a}_{k_2}^\dagger \exp(\frac{-2\imath E_{k_0}t}{\hbar}) + h.c.\right] \\ &= \hat{H}_0 + \hat{H}_I \end{aligned} \tag{2.80}$$

with $\hat{H}_0$ the free energy of the condensate and atoms in the signal and idle mode in the periodic potential. This expression is the analogue of the parametric amplifier hamiltonian in quantum optics where the pump is usually treated classically and assumed to be non-depleted.

2.2.3.4 The resulting state and its properties

It can be shown for the hamiltonian $\hat{H}$ in (2.80) that the difference of the number operator between signal and idle modes is a constant of the motion:

$$\left[\hat{N}_{k_1} - \hat{N}_{k_2}, \hat{H}\right] = 0 \tag{2.81}$$

implying that $\hat{N}_{k_1}(t) - \hat{N}_{k_2}(t) = \hat{N}_{k_1}(0) - \hat{N}_{k_2}(0) = 0$ when starting from vacuum. This relation expresses the fact that the signal and idle atoms are created in pair. In our

group, the normalized variance of the atom number difference:

$$V = \frac{\langle(\hat{N}_{k_1} - \hat{N}_{k_2})^2\rangle - \langle\hat{N}_{k_1} - \hat{N}_{k_2}\rangle^2}{\langle\hat{N}_{k_1} + \hat{N}_{k_2}\rangle} \tag{2.82}$$

was measured [18] to demonstrate the simultaneous creation of atoms in scattered modes. Ideally, the variance defined above tends to 0 in contrast to the classical process where the noise of the number difference is limited by the shot noise, or $V = 1$. For an atomic pair resulting from the four wave mixing process in a lattice, a variance below unity was measured indicating sub-Poissonian fluctuations on the number difference. The signal did not descend to 0 due to the limited detection efficiency. In fact, for the detection efficiency η, the normalised variance becomes:

$$V_{det} = (1 - \eta) + \eta V. \tag{2.83}$$

Two mode case: solutions of the equations of motion and statistics. The Heisenberg equation of motion for annihilation operator $\hat{a}_{k_1}(t)$ can be written as:

$$\dot{\hat{a}}_{k_1}(t) = \frac{1}{\imath\hbar}[\hat{a}_{k_1}(t), \hat{H}] \tag{2.84}$$

$$= -\imath E_{k_1}\hat{a}_{k_1}(t) - \imath\frac{g}{2}CN_{k_0}\hat{a}^\dagger_{k_2}(t)\exp(-\imath 2\frac{E_{k_0}}{\hbar}t) \tag{2.85}$$

We can simplify this equation by introducing complex amplitudes in a form:

$$\hat{\mathcal{A}}_{k_1}(t) = \hat{a}_{k_1}(t)\exp(\imath\frac{E_{k_1}}{\hbar}t) \tag{2.86}$$

$$\hat{\mathcal{A}}_{k_2}(t) = \hat{a}_{k_2}(t)\exp(\imath\frac{E_{k_2}}{\hbar}t) \tag{2.87}$$

Then, we have a simpler equation for $\hat{\mathcal{A}}_{k_1}(t)$:

$$\frac{\mathrm{d}\hat{\mathcal{A}}_{k_1}(t)}{\mathrm{d}t} = -\imath\frac{g}{2}CN_{k_0}\hat{\mathcal{A}}^\dagger_{k_2}(t)\exp(\imath\frac{E_{k_1} + E_{k_2} - 2E_{k_0}}{\hbar}t). \tag{2.88}$$

If $E_{k_1} + E_{k_2} = 2E_{k_0}$, we have

$$\frac{\mathrm{d}\hat{\mathcal{A}}_{k_1}(t)}{\mathrm{d}t} = -\imath\frac{g}{2}CN_{k_0}\hat{\mathcal{A}}^\dagger_{k_2}(t) \tag{2.89}$$

$$\frac{\mathrm{d}\hat{\mathcal{A}}_{k_2}(t)}{\mathrm{d}t} = -\imath\frac{g}{2}CN_{k_0}\hat{\mathcal{A}}^\dagger_{k_1}(t) \tag{2.90}$$

The general solutions of these equations can be obtained as

$$\hat{\mathcal{A}}_{k_1}(t) = \hat{\mathcal{A}}_{k_1}(0)\cosh(\frac{g}{2}|C|N_{k_0}t) - \imath\exp(\imath\theta)\hat{\mathcal{A}}^\dagger_{k_2}(0)\sinh(\frac{g}{2}|C|N_{k_0}t) \tag{2.91}$$

$$\hat{\mathcal{A}}_{k_2}(t) = \hat{\mathcal{A}}_{k_2}(0)\cosh(\frac{g}{2}|C|N_{k_0}t) - \imath\exp(\imath\theta)\hat{\mathcal{A}}^\dagger_{k_1}(0)\sinh(\frac{g}{2}|C|N_{k_0}t) \tag{2.92}$$

where we have written $C = |C|\exp(\imath\theta)$.

In order to calculate the expectation values of the scattered modes, we shall take the initial state of both signal and idle modes to be the vacuum state $|vac\rangle_{k_1,k_2}$. Using the solutions in (2.91) and (2.92) and taking into account the fact $\hat{\mathcal{A}}_{k_1,k_2}(0)|vac\rangle_{k_1,k_2} = 0$, we can easily show the following relations:

$$\begin{aligned}
\langle \hat{N}_{k_1} \rangle &= \langle \hat{\mathcal{A}}^\dagger_{k_1}(t)\hat{\mathcal{A}}_{k_1}(t)\rangle = \sinh^2(\frac{g}{2}|C|N_{k_0}t) = \langle \hat{N}_{k_2}\rangle \\
\langle : \hat{N}^2_{k_1} : \rangle &= \langle \hat{\mathcal{A}}^\dagger_{k_1}(t)\hat{\mathcal{A}}^\dagger_{k_1}(t)\hat{\mathcal{A}}_{k_1}(t)\hat{\mathcal{A}}_{k_1}(t)\rangle = 2\sinh^4(\frac{g}{2}|C|N_{k_0}t) = \langle : \hat{N}^2_{k_2} : \rangle \\
\langle : \hat{N}_{k_1}\hat{N}_{k_2} : \rangle &= \langle \hat{\mathcal{A}}^\dagger_{k_1}(t)\hat{\mathcal{A}}^\dagger_{k_2}(t)\hat{\mathcal{A}}_{k_2}(t)\hat{\mathcal{A}}_{k_1}(t)\rangle = \sinh^2(\frac{g}{2}|C|N_{k_0}t)[1+2\sinh^2(\frac{g}{2}|C|N_{k_0}t)]
\end{aligned}$$

The normalized local correlation $g^{(2)}_{loc}$ becomes

$$g^{(2)}_{loc}(k_1,k_1) = \frac{\langle : \hat{N}^2_{k_1} : \rangle}{\langle \hat{N}_{k_1}\rangle^2} = 2 = g^{(2)}_{loc}(k_2,k_2). \tag{2.93}$$

Similarly, the cross-correlation $g^{(2)}_{cross}$ is:

$$g^{(2)}_{cross}(k_1,k_2) = \frac{\langle : \hat{N}_{k_1}\hat{N}_{k_2} : \rangle}{\langle \hat{N}_{k_1}\rangle\langle \hat{N}_{k_2}\rangle} = 2 + \frac{1}{\sinh^2(\frac{g}{2}|C|N_{k_0}t)}. \tag{2.94}$$

We have found that

$$\langle : \hat{N}_{k_1}\hat{N}_{k_2} : \rangle = \langle : \hat{N}^2_j : \rangle + \langle \hat{N}_j\rangle \qquad (j = k_1, k_2). \tag{2.95}$$

Finally, the state of the produced pair considering only two modes is given in the interaction picture as:

$$|\psi(t)\rangle = \exp(-\imath\frac{\hat{H}_I}{\hbar})|vac\rangle \tag{2.96}$$

A detailed calculation produces [142]:

$$|\psi(t)\rangle = \frac{1}{\cosh(\frac{g}{2}|C|N_{k_0}t)}\sum_n \left[\tanh(\frac{g}{2}|C|N_{k_0}t)\right]^n |n,n\rangle_{k_1,k_2}. \tag{2.97}$$

Mutimode case: perturbative treatment of the state of pair. So far we have considered only two scattered modes: signal and idle modes. But in general, the pair can be produced in a multimode state since the phase matching condition can be satisfied for several modes (width of the gain in the figure 2.6). We can allow the possibility of having the multimode state by making a plane-wave mode expansion of each field and

expressing the interaction Hamiltonian $\hat{H}_I$ in the form [93]:

$$\hat{H}_I = \frac{1}{L_z}\sum_{k_1',k_2'} A_{k_0}\chi(k_0,k_1',k_2')\int_{L_z} e^{\imath(2k_0-k_1'-k_2')z}e^{\frac{\imath}{\hbar}(E_{k_1'}+E_{k_2'}-2E_{k_0})t}\hat{a}^\dagger_{k_1'}\hat{a}^\dagger_{k_2'}\,\mathrm{d}z + h.c.$$

where condensate is treated again classically as plane wave with amplitude A_{k_0}, L_z is the active length of the condensate in which the pair production takes place, $\chi(k_0,k_1',k_2')$ is the coupling constant in producing a pair in modes k_1' and k_2'. The state produced at time T is given by:

$$|\Psi(T)\rangle = \exp\left[\frac{\int_0^T \hat{H}_I(t')\,\mathrm{d}t'}{\imath\hbar}\right]|vac\rangle. \tag{2.98}$$

We can expand the exponential and write the state as

$$\begin{aligned}|\Psi(T)\rangle \;=\; & \sum_{k_1',k_2'}|vac_{k_1'},vac_{k_2'}\rangle + L_z^{-1}\frac{1}{\imath\hbar}\sum_{k_1',k_2'}A_{k_0}\chi(k_0,k_1',k_2')\left[\frac{\sin\left(\frac{1}{2}(2k_0-k_1'-k_2')L_z\right)}{\frac{1}{2}(2k_0-k_1'-k_2')}\right]\\ & \times e^{\frac{\imath}{\hbar}(E_{k_1'}+E_{k_2'}-2E_{k_0})T/2}\frac{\sin\left(\frac{1}{2\hbar}(E_{k_1'}+E_{k_2'}-2E_{k_0})T\right)}{\frac{1}{2\hbar}(E_{k_1'}+E_{k_2'}-2E_{k_0})}|1_{k_1'},1_{k_2'}\rangle\\ & +\ldots\end{aligned}$$

It can be written in more compact form:

$$|\Psi_{FWM}\rangle = \sum_{k_1',k_2'}|vac_{k_1'},vac_{k_2'}\rangle + \sum_{k_1',k_2'}f(k_1',k_2')|1_{k_1'},1_{k_2'}\rangle + \ldots \tag{2.99}$$

where higher order terms include a greater number of particles. If we assume a time T which is short compared with the average time interval between successive pair productions, we can omit higher order contributions to the state. At the end of the pair production, we can write the perturbative multimode state of the pair in the laboratory frame of reference as:

$$|\Psi_{FWM}\rangle \approx |\Psi_{EPR}\rangle = \sum_{k_a'}\sum_{k_b'}f_{ab}(k_a',k_b')|1_{k_a'},1_{k_b'}\rangle \tag{2.100}$$

where f_{ab} is chosen by the normalization of the state keeping in mind the phase matching condition $k_a'+k_b'=2k_{lat}$:

$$\langle\Psi_{EPR}|\Psi_{EPR}\rangle = \sum_{k_a'}\sum_{k_b'}|f_{ab}(k_a',k_b')|^2 = 1. \tag{2.101}$$

The validity of the approximation $|\Psi_{FWM}\rangle \approx |\Psi_{EPR}\rangle$ can be checked in the experiment through correlation measurements. The local and cross correlator (correlations at

specific momenta $k'_a = k_a$ and $k'_b = k_b$) of the state $|\Psi_{EPR}\rangle$ are given by:

$$\begin{aligned} G^{(2)}_{aa}(k_a, k_a) &= \langle\Psi_{EPR}|\hat{N}_{k_a}(\hat{N}_{k_a} - 1)|\Psi_{EPR}\rangle = 0 \\ G^{(2)}_{bb}(k_b, k_b) &= \langle\Psi_{EPR}|\hat{N}_{k_b}(\hat{N}_{k_b} - 1)|\Psi_{EPR}\rangle = 0 \\ G^{(2)}_{ab}(k_a, k_b) &= \langle\Psi_{EPR}|\hat{N}_{k_a}\hat{N}_{k_b}|\Psi_{EPR}\rangle = |f_{ab}(k'_a, k'_b)|^2 \end{aligned}$$

while for the state $|\Psi_{FWM}\rangle$, from equations (2.93), (2.94) we have:

$$G^{(2)}_{aa}(k_a, k_a) = \langle\Psi_{FWM}|\hat{N}_{k_a}(\hat{N}_{k_a} - 1)|\Psi_{FWM}\rangle = 2\langle\hat{N}_{k_a}\rangle^2 \quad (2.102)$$

$$G^{(2)}_{bb}(k_b, k_b) = \langle\Psi_{FWM}|\hat{N}_{k_b}(\hat{N}_{k_b} - 1)|\Psi_{FWM}\rangle = 2\langle\hat{N}_{k_b}\rangle^2 \quad (2.103)$$

$$G^{(2)}_{ab}(k_a, k_b) = \langle\Psi_{FWM}|\hat{N}_{k_a}\hat{N}_{k_b}|\Psi_{FWM}\rangle = \hat{N}_{k_a} + 2\langle\hat{N}_{k_a}\rangle\langle\hat{N}_{k_b}\rangle. \quad (2.104)$$

The correlators of $|\Psi_{FWM}\rangle$ can be approximated to produce the same result of $|\Psi_{EPR}\rangle$ only when $\langle\hat{N}_{k_a}\rangle \to 0$ and $\langle\hat{N}_{k_b}\rangle \to 0$. In other words, we should verify the condition

$$G^{(2)}_{aa}(k_a, k_a) \ll G^{(2)}_{ab}(k_a, k_b) \text{ and } G^{(2)}_{bb}(k_b, k_b) \ll G^{(2)}_{ab}(k_a, k_b) \quad (2.105)$$

In quantum optics community, photonic sources, produced via parametric down conversion process, verify easily condition above and thus the state of their source is approximated well with the state $|\Psi_{EPR}\rangle$. But in our situation, we need to still check it experimentally in the low gain regime which is waiting in the to-do list. We have a direct access to the correlation of the atomic pair source in our experimental configuration as shown in figure 2.11.a. At time $t = 0$ an atomic pair is produced (see Chapter 3) by applying an optical lattice on the Bose-Einstein condensate of meta-stable helium hold in the crossed optical dipole trap as discussed so far (more details on BEC see Chapter 3). We consider only the relevant z-axis which is the axis of the gravity. The produced pair fall on the detector situated below the center of the dipole trap at $z = -H = -46$ cm following the paths in $z - t$ diagram shown in figure 2.11.b with the corresponding diagram 2.11.c in the frame of reference of the center of mass of the pair. The correlation measurements can be easily carried out by counting atoms on each beam taking advantage of single atom resolution. The only inconvenience is the long data acquisition time for such correlation measurement due to the long experimental cycle duration ~ 30 s and low detection efficiency of the detector 25% (see Appendix D).

2.2.4 The bragg pulse

Now we have a pair of atoms, we should be able to manipulate them. In other words, we need the four compulsory elements to be able to realize an atomic interferometer.

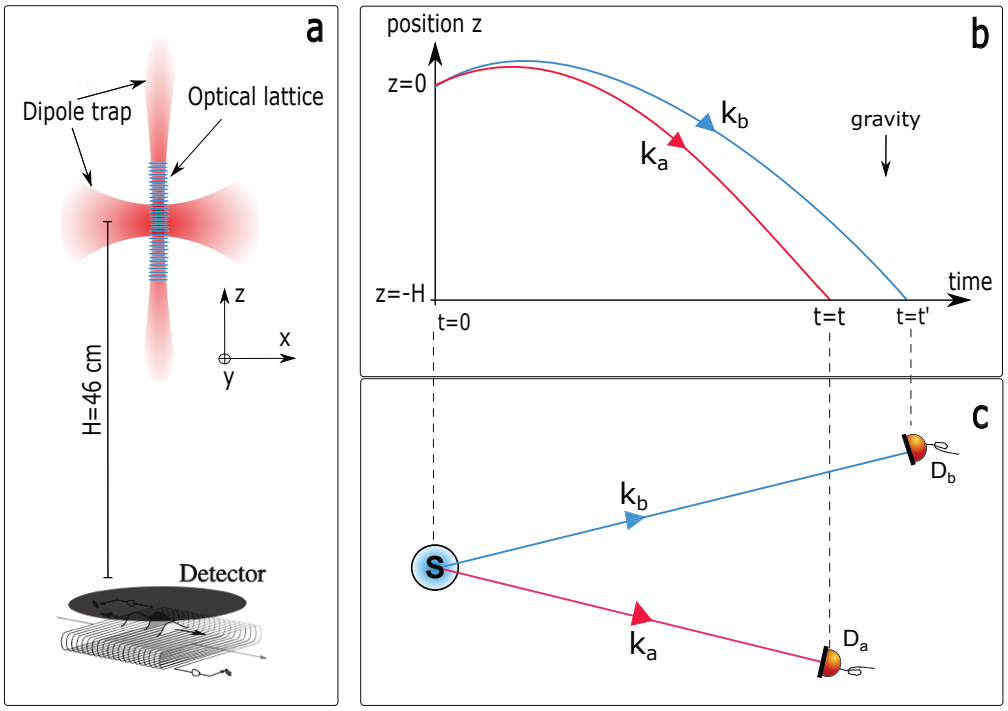

FIGURE 2.11: Experimental production of an atomic pair by applying a moving vertical ($z-$axis) optical lattice on a BEC hold in a crossed dipole trap which is $H = 45$ cm above the detector(a). The produced pair falls on the detector under the effect of the gravity following the trajectory shown in blue and in red in $z-t$ diagram (b) with the corresponding trajectories in the frame of the center of mass (c). Correlation measurements are carried out by counting atoms in each beam.

They are:

1. aperture
2. mirror
3. phase plate
4. beamsplitter

for the atoms. We will see that the Bragg pulse can replace the role of all these elements at least in our experiment. But first we will work out the principle of coherent control of the external degrees of the helium atoms using Bragg pulses.

2.2.4.1 Statement of problem

Consider a helium atom with the level scheme shown in figure 2.12 with the resonant frequency ω_{eg} of the excited level $|e\rangle = 2^3S_1(m = 0)$ to the ground level $|g\rangle = 2^3P_0(m = 0)$ of the atomic internal state transition (see Appendix A). The atom is illuminated by counter-propagating laser beams with frequencies ω_{1L} and ω_{2L}. The states are described

by both internal states and momenta parallel to the laser beams. Hence, the state $|g, p - \hbar k_{1L}\rangle$ designates that the atom has a momentum $p - \hbar k_{1L}$ parallel to the laser beams and its internal state is the metastable state $2^3S_1(m = 0)$ which is noted as $|g\rangle$. The atom is transferred from the initial state $|g, p - \hbar k_{1L}\rangle$ to the final state $|g, p + \hbar k_{2L}\rangle$ via the intermediate state $|e, p\rangle$. We are going to consider the time evolution of the wave function

$$|\Psi_p(t)\rangle = C_1(t)|g, p - \hbar k_{1L}\rangle + C_2(t)|g, p + \hbar k_{2L}\rangle + C_3(t)|e, p\rangle. \tag{2.106}$$

In the limit where the spontaneous emission can be ignored and other nonresonant or multiple diffraction effects can be neglected, the states $|g, p - \hbar k_{1L}\rangle$, $|g, p + \hbar k_{2L}\rangle$ and $|e, p\rangle$ form a closed family for an atom at specific momentum p and the wave function is normalized $\langle\Psi_p(t)|\Psi_p(t)\rangle = 1$.

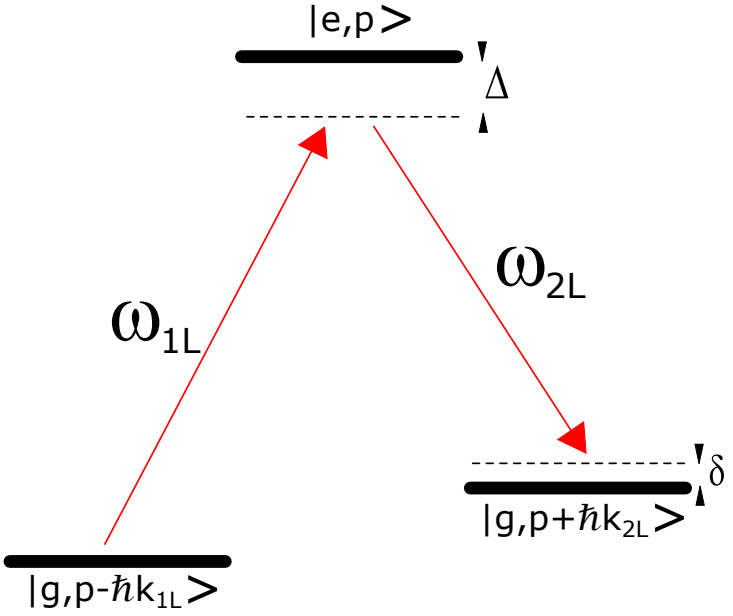

FIGURE 2.12: A scheme of the transition of helium atoms from the state $|g, p - \hbar k_{1L}\rangle$ to the state $|g, p + \hbar k_{2L}\rangle$ using a bragg pulse which consists of two laser beams with frequencies ω_{1L} and ω_{2L}.

2.2.4.2 The equations of motion

The hamiltonian is given by $H = H_A + H_{int}$ where the atomic hamiltonian is

$$H_A = \frac{P^2}{2M} + \hbar\omega_{eg}|e\rangle\langle e| \tag{2.107}$$

and the interaction hamiltonian is

$$H_{int} = -\mathbf{d} \cdot \mathbf{E}(z,t) \tag{2.108}$$

with $\mathbf{d}$ the electric dipole moment operator. The electric field is two travelling waves $\mathbf{E}_1$ and $\mathbf{E}_2$ counterpropogating along z. The total field becomes:

$$\mathbf{E}(z,t) = \frac{1}{2}\mathbf{E}_1 e^{\imath(k_{1L}z - \omega_{1L}t + \Phi_1)} + \frac{1}{2}\mathbf{E}_2 e^{\imath(-k_{2L}z - \omega_{2L}t + \Phi_2)} + c.c \tag{2.109}$$

One can define the Rabi frequencies Ω_1 and Ω_2 as

$$\Omega_n = -\frac{\langle g|\mathbf{d} \cdot \mathbf{E}_n e^{-\imath\Phi_n}|e\rangle}{2\hbar}, \qquad n = 1,2 \tag{2.110}$$

so that the interaction hamiltonian reduces to

$$H_{int} = \hbar\Omega_1^* e^{\imath(k_{1L}z - \omega_{1L}t)}|e\rangle\langle g| + \hbar\Omega_2^* e^{\imath(-k_{2L}z - \omega_{2L}t)}|e\rangle\langle g| + \text{h.c.} \tag{2.111}$$

We can substitute the relation

$$e^{\pm\imath k_j z} = \int |p\rangle\langle p \pm \hbar k_j| \, \mathrm{d}p \qquad j = 1L, 2L \tag{2.112}$$

in equation (2.111) to show the fact that an absoprtion or emission of a photon of wave number k_j shifts the atoms momentum by $\hbar k_j$ and thus for given p we have a closed momentum family as discussed above.

The time-dependent Schrodinger's equation can be written as

$$\imath\hbar\frac{\partial|\Psi_p(t)\rangle}{\partial t} = H|\Psi_p(t)\rangle. \tag{2.113}$$

From this equation it is easy to obtain the time evolution of the coefficients $C_i(t)$, $i = 1,2,3$:

$$\imath\hbar\frac{\partial}{\partial t}\begin{pmatrix} C_1(t) \\ C_2(t) \\ C_3(t) \end{pmatrix} = \begin{pmatrix} \frac{(p-\hbar k_{1L})^2}{2M} & 0 & \hbar\Omega_1 e^{\imath\omega_{1L}t} \\ 0 & \frac{(p+\hbar k_{2L})^2}{2M} & \hbar\Omega_2 e^{\imath\omega_{2L}t} \\ \hbar\Omega_1^* e^{-\imath\omega_{1L}t} & \hbar\Omega_2^* e^{-\imath\omega_{2L}t} & \frac{(p)^2}{2M} + \hbar\omega_{eg} \end{pmatrix}\begin{pmatrix} C_1(t) \\ C_2(t) \\ C_3(t) \end{pmatrix} \tag{2.114}$$

If we define B_i, $i = 1, 2, 3$, as

$$B_1(t) = C_1(t) \exp\left(\imath \frac{(p - \hbar k_{1L})^2}{2M\hbar} t\right), \tag{2.115}$$

$$B_2(t) = C_2(t) \exp\left(\imath \frac{(p + \hbar k_{2L})^2}{2M\hbar} t\right), \tag{2.116}$$

$$B_3(t) = C_3(t) \exp\left(\imath \left(\frac{p^2}{2M\hbar} + \omega_{eg}\right) t\right), \tag{2.117}$$

it is straightforward to obtain their time evolution relations in a form:

$$\frac{\mathrm{d}B_1}{\mathrm{d}t} = -\imath \Omega_1 e^{-\imath \Delta t} B_3 \tag{2.118}$$

$$\frac{\mathrm{d}B_2}{\mathrm{d}t} = -\imath \Omega_2 e^{-\imath (\Delta + \delta) t} B_3 \tag{2.119}$$

$$\frac{\mathrm{d}B_3}{\mathrm{d}t} = -\imath \Omega_1^* e^{\imath \Delta t} B_1 - \imath \Omega_2^* e^{\imath (\Delta + \delta) t} B_2 \tag{2.120}$$

with

$$\delta \equiv \left(\frac{(p - \hbar k_{1L})^2}{2M\hbar} - \frac{(p + \hbar k_{2L})^2}{2M\hbar}\right) - (\omega_{2L} - \omega_{1L}) \tag{2.121}$$

and

$$\Delta \equiv \left(\frac{(p)^2}{2M\hbar} + \omega_{eg} - \frac{(p - \hbar k_{1L})^2}{2M\hbar}\right) - \omega_{1L}. \tag{2.122}$$

2.2.4.3 Solution of the equations

The bragg resonance condition corresponds to $\delta = 0$ for the momentum $p = p_0$ given by

$$\omega_{2L} - \omega_{1L} = \frac{(p_0 - \hbar k_{1L})^2}{2M\hbar} - \frac{(p_0 + \hbar k_{2L})^2}{2M\hbar} \tag{2.123}$$

then the detuning for an arbitrary momentum p is $\delta = -(p - p_0)(k_{1L} + k_{2L})/M$. In order to suppress the spontaneous emission, the detuning Δ is usually chosen large, i.e, $\Delta \gg |\Omega_1|, |\Omega_2|, \delta$. With this condition, the equation (2.120) can be integrated directly by ignoring time dependence of $B_{1,2}$ (it can be justified by the solutions we obtain at the end). Then, we reinject the expression of B_3 in (2.118) and (2.119). Terms that oscillate at frequency Δ are neglected, since they contribute less to $B_{1,2}$ by quickly getting averaged out. The resulting effective two-level equations are

$$\frac{\mathrm{d}B_1}{\mathrm{d}t} = \imath \frac{|\Omega_1|^2}{\Delta} B_1 + \imath \frac{\Omega_1 \Omega_2^*}{\Delta} B_2 e^{\imath \delta t} \tag{2.124}$$

$$\frac{\mathrm{d}B_2}{\mathrm{d}t} = \imath \frac{\Omega_1^* \Omega_2}{\Delta} B_1 e^{-\imath \delta t} + \imath \frac{|\Omega_2|^2}{\Delta} B_2 \tag{2.125}$$

The solutions are given by [99, 116]:

$$
\begin{aligned}
B_1(p,t_0+t) &= \exp\left[\imath\left[\delta+\frac{|\Omega_1|^2}{\Delta}+\frac{|\Omega_2|^2}{\Delta}\right]\frac{t}{2}\right] \\
&\quad\times\left\{\left[\cos\frac{\omega t}{2}+\frac{\imath}{\omega}\left[\frac{|\Omega_1|^2}{\Delta}-\frac{|\Omega_2|^2}{\Delta}-\delta\right]\sin\frac{\omega t}{2}\right]B_1(t_0)+\frac{\imath}{\omega}\frac{2\Omega_1\Omega_2^*}{\Delta}\sin\frac{\omega t}{2}e^{\imath\delta t_0}B_2(t_0)\right\}, \\
B_2(p,t_0+t) &= \exp\left[\imath\left[-\delta+\frac{|\Omega_1|^2}{\Delta}+\frac{|\Omega_2|^2}{\Delta}\right]\frac{t}{2}\right]\left\{\frac{\imath}{\omega}\frac{2\Omega_1^*\Omega_2}{\Delta}\sin\frac{\omega t}{2}e^{-\imath\delta t_0}B_1(t_0)\right. \\
&\quad\left.+\left[\cos\frac{\omega t}{2}-\frac{\imath}{\omega}\left[\frac{|\Omega_1|^2}{\Delta}-\frac{|\Omega_2|^2}{\Delta}-\delta\right]\sin\frac{\omega t}{2}\right]B_2(t_0)\right\}
\end{aligned}
$$

where

$$
\omega^2=\left[\frac{|\Omega_1|^2}{\Delta}-\frac{|\Omega_2|^2}{\Delta}-\delta\right]^2+4\frac{|\Omega_1|^2|\Omega_2|^2}{\Delta^2} \tag{2.126}
$$

We can simplify the solutions of $B_{1,2}(t)$ further by

- taking $|\Omega_1|=|\Omega_2|$,
- taking $t_0=0$,
- omitting the global phase term $\exp\left[\imath\left[\frac{|\Omega_1|^2}{\Delta}+\frac{|\Omega_2|^2}{\Delta}\right]\frac{t}{2}\right]$,
- defining effective Rabi frequency $\Omega_{eff}=\frac{2\Omega_1\Omega_2^*}{\Delta}$,
- taking $\omega=\sqrt{|\Omega_{eff}|^2+\delta^2}$
- defining the phase difference between two electric fields $\Delta\Phi=\Phi_2-\Phi_1$,

So we have the solution in the compact form:

$$
\begin{pmatrix}B_2(t)\\B_1(t)\end{pmatrix}=\begin{pmatrix}\left[\cos\left(\frac{\omega t}{2}\right)+\frac{\imath\delta}{\omega}\sin\left(\frac{\omega t}{2}\right)\right]e^{-\imath\delta t/2} & \frac{\imath|\Omega_{eff}|}{\omega}\sin\left(\frac{\omega t}{2}\right)e^{-\imath(\delta t/2+\Delta\Phi)}\\ \frac{\imath|\Omega_{eff}|}{\omega}\sin\left(\frac{\omega t}{2}\right)e^{\imath(\delta t/2+\Delta\Phi)} & \left[\cos\left(\frac{\omega t}{2}\right)-\frac{\imath\delta}{\omega}\sin\left(\frac{\omega t}{2}\right)\right]e^{\imath\delta t/2}\end{pmatrix}\begin{pmatrix}B_2(0)\\B_1(0)\end{pmatrix}
$$

Now imagine that we apply the Bragg pulse on the atoms with the state $|\Psi_p(0)\rangle_{eff}=B_1(0)|g,\hbar k\rangle+B_2(0)|g,\hbar k+\Delta k_B\rangle$ with $\Delta k_B=k_{1L}+k_{2L}$. The evolution of the effective two level state $|\Psi_p(t)\rangle_{eff}$ is given by

$$
|\Psi_p(t)\rangle_{eff}=B_1(t)e^{-\imath\frac{(\hbar k)^2}{2M\hbar}t}|\hbar k\rangle+B_2(t)e^{-\imath\frac{(\hbar k+\hbar\Delta k_B)^2}{2M\hbar}t}|\hbar k+\hbar\Delta k_B\rangle. \tag{2.127}
$$

where $|g\rangle$ is skipped. So, the relation between the initial state and the final state is expressed through B coefficients in (2.127).

2.2.4.4 Beamsplitter and mirror matrix

Probabilities of ending up in each state $|B_1(t)|^2$ and $|B_2(t)|^2$ oscillate with a characteristic frequency ω as a function of time t. An example of such oscillation at resonance $\delta = 0$ is given in the figure 2.13 where the initial conditions are chosen as $|B_1(0)|^2 = 1$ and $|B_2(0)|^2 = 0$. For $t = \frac{\pi}{|\Omega_{eff}|}$, we see that the values of the probabilities are inversed, i.e. we started with $|B_1(0)|^2 = 1$ and $|B_2(0)|^2 = 0$ and we ended up with $|B_1(t = \frac{\pi}{|\Omega_{eff}|})|^2 = 0$ and $|B_2(t = \frac{\pi}{|\Omega_{eff}|})|^2 = 1$ meaning that if initially the state $|\hbar k\rangle$ is populated, a complete population inversion can be achieved via the Bragg pulse with duration $t = \frac{\pi}{|\Omega_{eff}|}$ which is called a $\pi-$pulse. So the $\pi-$pulse can be employed as an atomic mirror with a reflection coefficient $r_m = |B_2(t = \frac{\pi}{|\Omega_{eff}|})|^2$ and a transmission coefficient $t_m = |B_1(t = \frac{\pi}{|\Omega_{eff}|})|^2$. For the resonant atoms ($\delta = 0$), we recover well known mirror matrix with:

$$\begin{pmatrix} \sqrt{t_m} & \imath\sqrt{r_m}e^{-\imath\phi_m} \\ \imath\sqrt{r_m}e^{\imath\phi_m} & \sqrt{t_m} \end{pmatrix} \tag{2.128}$$

Similarly, we can have an atomic beamsplitter by fixing $t = \frac{\pi}{2|\Omega_{eff}|}$ (called $\frac{\pi}{2}-$pulse) with a reflection coefficient $r_s = |B_2(t = \frac{\pi}{2|\Omega_{eff}|})|^2$ and a transmission coefficient $t_s = |B_1(t = \frac{\pi}{2|\Omega_{eff}|})|^2$. The beamsplitter matrix is:

$$\begin{pmatrix} \sqrt{t_s} & \imath\sqrt{r_s}e^{-\imath\phi_s} \\ \imath\sqrt{r_s}e^{\imath\phi_s} & \sqrt{t_s} \end{pmatrix}. \tag{2.129}$$

We notice that the matrices contain phase terms coming from the phase difference of the Bragg beams. These phases are directly imprinted on the atoms and serve us to control θ_+ and θ_- of the interferometers in the scheme 2.5.

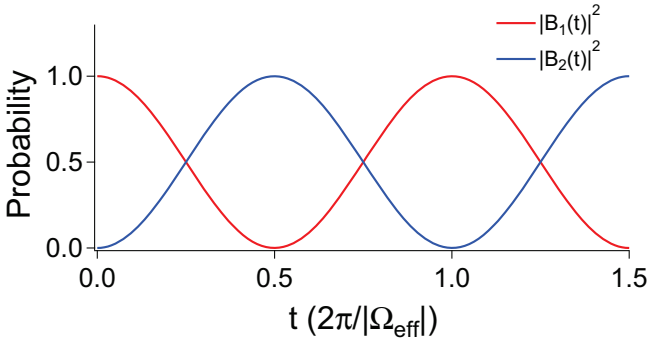

FIGURE 2.13: Oscillation of probabilities $|B_1(t)|^2$ and $|B_2(t)|^2$ of ending up in states $|\hbar k\rangle$ and $|\hbar k + \hbar\Delta k_B\rangle$ respectively as a function of the Bragg pulse duration t for resonant atoms with initial conditions $|B_1(0)|^2 = 1$ and $|B_2(0)|^2 = 0$. The oscillation frequency is equal to the effective Rabi frequency.

2.2.4.5 Aperture

Consider a Bragg pulse used as an atomic beamsplitter. In general, the coefficients r_s and t_s of this beamsplitter are functions of momentum since they depend on detuning $\delta = -(p - p_0)\Delta k_B/M$ which depends itself on momentum $p = \hbar k$. In the figure 2.14, the reflection coefficient r_s of an atomic beamsplitter is plotted as a function of δ for two different values of $|\Omega_{eff}|$. Units are given in $\frac{E_{rec}}{\hbar} = \frac{\hbar k_{rec}^2}{2M}$ where $k_{rec} = \frac{2\pi}{\lambda}$ with λ an optical wavelength of Bragg beams. Firstly, we see that it is a $sinc-$function with some bandpass in detuning and thus in momentum. This selectivity property can be used as an aperture in conducting the Bell's experiment with the scheme in the figure 2.5. Secondly, this bandpass changes with $|\Omega_{eff}|$ which allows us to adjust the widths of the two beamsplitters.

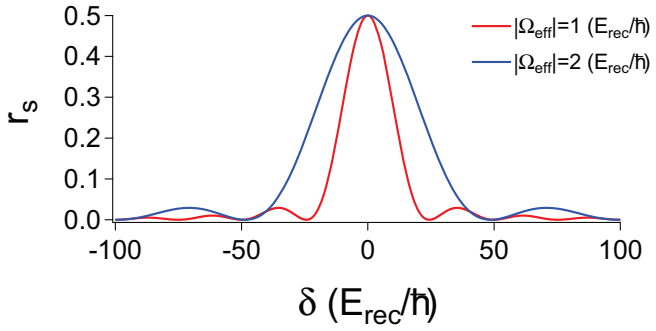

FIGURE 2.14: Atomic beamsplitter reflection coefficient $r_s = |B_2(t = \frac{\pi}{2|\Omega_{eff}|})|^2$ as a function of detuning δ for two different values of the effective Rabi frequency.

According to the scheme in the figure 2.5, we realize a mirror with the help of single bragg pulse which is not selective in momenta so that the two " + " modes and two " − " modes are reflected equivalently by the mirror. There are also two atomic beamsplitters applied at the same time but addressing different modes of the atomic pair. We will call the first beamsplitter as $S^+_{\pi/2}$ which combines modes $\{k_{b+}; k_{a+}\}$ and the second beamsplitter as $S^-_{\pi/2}$ which combines modes $\{k_{b-}; k_{a-}\}$. We ensure that they are selective enough to isolate modes. In order to illustrate the idea, refer to the figure 2.15 where we plot probability functions of two beamsplitters superposed on the vertical momentum distribution of the atomic pair. The resonant modes are chosen to be symmetrical with respect to the centers of the density distribution.

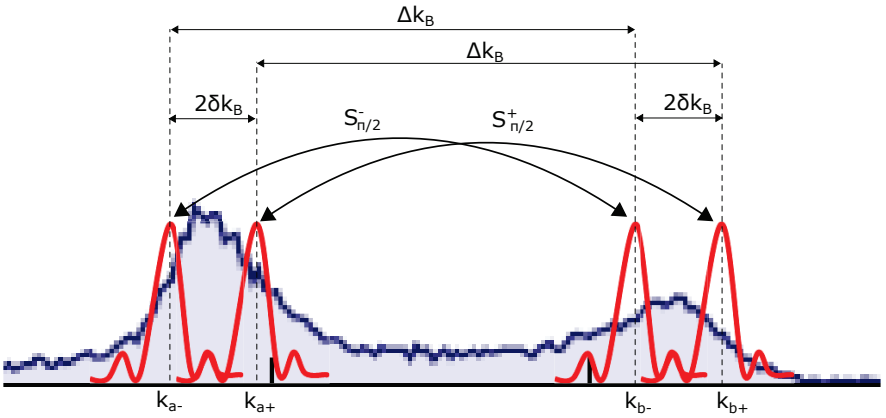

FIGURE 2.15: Schematic representation of the probability functions of the atomic beamsplitters $S^{+}_{\pi/2}$ and $S^{-}_{\pi/2}$ addressing different vertical modes of the atomic pair.

In the weak gain regime of the pair production, the state given in (2.100) is modified by the aperture and can be written as:

$$|\Psi_{EPR}\rangle = \sum_{k_a}\sum_{k_b} f_{ab}(k_a,k_b)|1_{k_a},1_{k_b}\rangle \tag{2.130}$$

$$\xrightarrow{aperture}$$

$$|\Psi'_{EPR}\rangle = \frac{1}{\sqrt{2}}\Big[\sum_{k_{a+}}\sum_{k_{b-}} f^{I}_{ab}(k_{a+},k_{b-})|1_{k_{a+}},1_{k_{b-}}\rangle + \sum_{k_{a-}}\sum_{k_{b+}} f^{II}_{ab}(k_{a-},k_{b+})|1_{k_{a-}},1_{k_{b+}}\rangle\Big] \tag{2.131}$$

The functions f_{ab}, f^{I}_{ab} and f^{II}_{ab} are determined by the normalization of the states $|\Psi_{EPR}\rangle$, $|\Psi'_{EPR}\rangle$ and the phase matching conditions $k_a + k_b = 2k_{lat}$, $k_{a+} + k_{b-} = 2k_{lat}$ and $k_{a-} + k_{b+} = 2k_{lat}$ of the pair production process:

$$\langle\Psi_{EPR}|\Psi_{EPR}\rangle = \sum_{k_a}\sum_{k_b}|f_{ab}(k_a,k_b)|^2 = 1$$

$$\langle\Psi'_{EPR}|\Psi'_{EPR}\rangle = \frac{1}{2}\Big(\sum_{k_{a+}}\sum_{k_{b-}}|f^{I}_{ab}(k_{a+},k_{b-})|^2 + \sum_{k_{a-}}\sum_{k_{b+}}|f^{II}_{ab}(k_{a-},k_{b+})|^2\Big) = 1.$$

We decided to model these functions in terms of gaussian functions as follows:

$$
\begin{aligned}
f_{ab}(k_a, k_b) &= \sqrt{\frac{2}{\pi\sigma_\perp\sigma_{\shortparallel}}}\exp\Big\{-\frac{(k_a+k_b-2k_{Lat})^2}{2\sigma_\perp^2}\Big\}\exp\Big\{-\frac{(k_b-k_a-\Delta k_B)^2}{2\sigma_{\shortparallel}^2}\Big\}\\
f^I_{ab}(k_{a+}, k_{b-}) &= \sqrt{\frac{2}{\pi\tilde{\sigma}_\perp\tilde{\sigma}_{\shortparallel}}}\exp\Big\{-\frac{(k_{a+}+k_{b-}-2k_{Lat})^2}{2\tilde{\sigma}_\perp^2}\Big\}\exp\Big\{-\frac{(k_{b-}-k_{a+}-\Delta k_B+\delta k_B)^2}{2\tilde{\sigma}_{\shortparallel}^2}\Big\}\\
f^{II}_{ab}(k_{a-}, k_{b+}) &= \sqrt{\frac{2}{\pi\tilde{\sigma}_\perp\tilde{\sigma}_{\shortparallel}}}\exp\Big\{-\frac{(k_{a-}+k_{b+}-2k_{Lat})^2}{2\tilde{\sigma}_\perp^2}\Big\}\exp\Big\{-\frac{(k_{b+}-k_{a-}-\Delta k_B-\delta k_B)^2}{2\tilde{\sigma}_{\shortparallel}^2}\Big\}
\end{aligned}
$$

which are normalized $\int\int \mathrm{d}k_a\,\mathrm{d}k_b|f_{ab}(k_a,k_b)|^2 = 1$, $\int\int \mathrm{d}k_{a+}\,\mathrm{d}k_{b-}|f^I_{ab}(k_{a+},k_{b-})|^2 = 1$ and $\int\int \mathrm{d}k_{a-}\,\mathrm{d}k_{b+}|f^{II}_{ab}(k_{a-},k_{b+})|^2 = 1$ if the limits of the integration are taken very large with respect to the widths of the gaussian functions. In this modeling, the only unknown parameters are the widths $\sigma_\perp$, $\sigma_{\shortparallel}$, $\tilde{\sigma_\perp}$ and $\tilde{\sigma}_{\shortparallel}$. For the HOM experiment (see Chapter 4), the width $\sigma_{\shortparallel}$ is important and can be deduced from the cross correlation measurement. For the Bell's inequality test (see Chapter 3 and last section of Chapter 2), the width $\tilde{\sigma}_{\shortparallel}$ is important and it can be related to the bandpass of the atomic beamsplitter which is on the same order of magnitude with the mode size measured by the local correlation function of pair.

2.2.4.6 Parameters of a Bragg pulse

As we have seen, the Bragg pulse can play a role of an aperture, a phase plate, a mirror or a beamsplitter in realizing the Bell's inequality test with atoms, i.e,

- duration $t-t_0$ allows to have right coefficients for atomic mirror and atomic 50 : 50 beamsplitter
- phase $\Delta\Phi$ allows to print a phase on atoms
- Rabi frequency Ω_{eff} allows to choose the size of an aperture
- detuning δ allows to address different modes.

All these parameters can be controlled experimentally by controlling the duration, the phase difference, intensities, and the frequency difference of the laser beams that make up a Bragg pulse (see for the experimental tests Chapter 3).

2.2.5 Calculating quantum correlation coefficients

Now we are in a state to evaluate the correlation coefficients for the Bell's inequality test experiment with helium atoms using the suggested scheme in the figure 2.5 which is shown again here. We understand that the aperture is applied by the beamsplitters

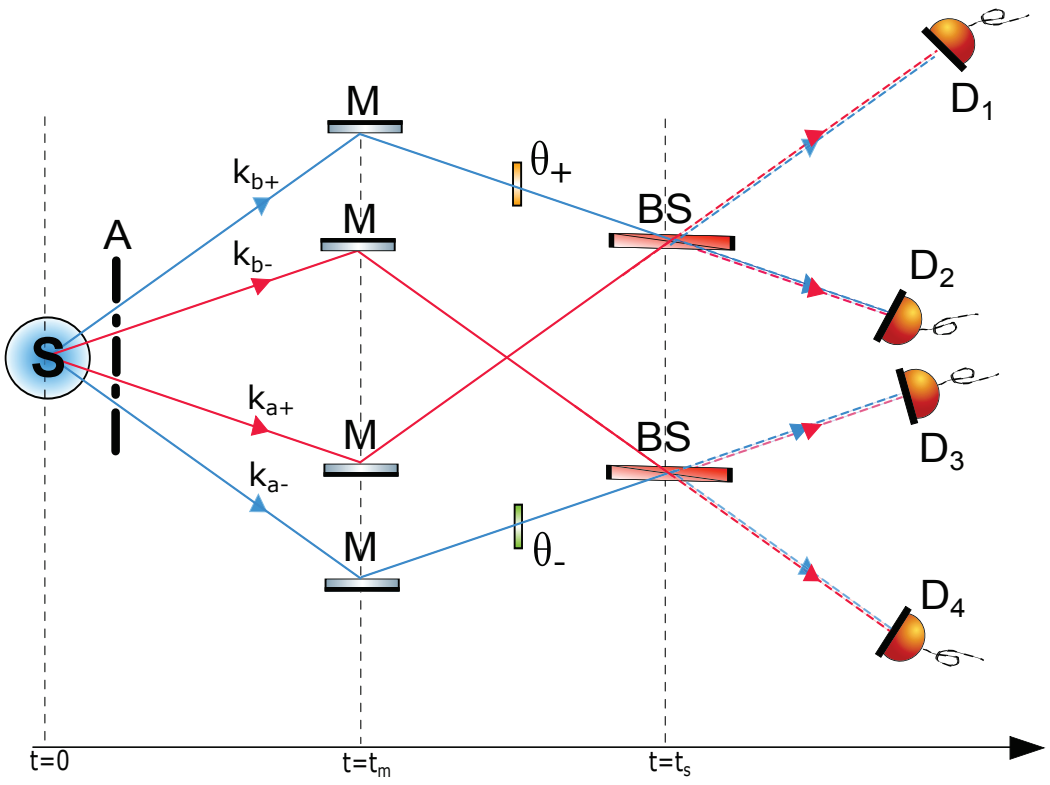

(repeating figure 2.5) **Schematics of the Bell's inequality test experiment using a pair of helium atoms correlated in momentum space** A pair of helium atoms, a and b, are emitted in a conjugate multimode momentum state by the source (S) at time $t = 0$. Two pair of conjugate modes, $\{k_{b+}; k_{a-}\}$ (shown in blue) and $\{k_{b-}; k_{a+}\}$ (shown in red) are selected by the aperture (A). The non-conjugate modes $\{k_{b+}; k_{a+}\}$ and $\{k_{b-}; k_{a-}\}$ are then made interfere on two different beamsplitters (BS) at time $t = t_s$ with the help of mirrors (M) applied at $t = t_m$. Two distinct phases θ_+ and θ_- are introduced for each interferometer, $+$ and $-$ respectively. Finally, the atoms are detected after a time of flight and the coincidence counting is made between outputs of separate interferometers.

and the phases θ_+ and θ_- are imprinted via the phase of the beamsplitter $S^+_{\pi/2}$ and the phase of the beamsplitter $S^-_{\pi/2}$ respectively.

Ultimately, we wish to calculate the CHSH parameter for four different angles:

$$S(\theta_+, \theta'_+, \theta_-, \theta'_-) = E(\theta_+, \theta_-) - E(\theta_+, \theta'_-) + E(\theta'_+, \theta_-) + E(\theta'_+, \theta'_-) \tag{2.132}$$

where the correlation coefficient is given by

$$E(\theta_+, \theta_-) = P_{+,+}(\theta_+, \theta_-) + P_{-,-}(\theta_+, \theta_-) - P_{+,-}(\theta_+, \theta_-) - P_{-,+}(\theta_+, \theta_-) \tag{2.133}$$

with the probability of joint detection

$$P_{+,+}(\theta_+,\theta_-) = \frac{G^{(2)}_{D1,D3}}{G^{(2)}_{D1,D3}+G^{(2)}_{D2,D4}+G^{(2)}_{D1,D4}+G^{(2)}_{D2,D3}}$$

$$P_{+,-}(\theta_+,\theta_-) = \frac{G^{(2)}_{D1,D4}}{G^{(2)}_{D1,D3}+G^{(2)}_{D2,D4}+G^{(2)}_{D1,D4}+G^{(2)}_{D2,D3}}$$

and so on. The cross correlation $G^{(2)}_{Di,Dj}$, $i=1,2$ and $j=3,4$ can be accessed in the experiment directly and it is defined by:

$$\begin{aligned} G^{(2)}_{Di,Dj} &= \eta^2 \int\int \mathrm{d}k_{Di}\,\mathrm{d}k_{Dj}\langle \hat{a}^\dagger_{k_{Di}}\hat{a}_{k_{Di}}\hat{a}^\dagger_{k_{Dj}}\hat{a}_{k_{Dj}}|\Psi\rangle \qquad i=1,2 \text{ and } j=3,4 \\ &= \eta^2 \int\int \mathrm{d}k_{Di}\,\mathrm{d}k_{Dj}\|\hat{a}_{k_{Di}}\hat{a}_{k_{Dj}}|\Psi\rangle\|^2 \end{aligned}$$

with η the efficiency of the momentum resolved micro channel plate detector (see Appendix D) which replaces all the detectors Di, Dj in the experiment. Here, we consider $1-$dimensional model (vertical axis) and we neglect the gravity which is not important in the following calculation. The operators are written in the Heisenberg picture and they annihilate or create a particle with corresponding plane wave momentum. The input-output relation of annihilation operators through the atomic beamsplitter or mirror is given by the Bragg matrix:

$$\begin{pmatrix}\hat{d}\\ \hat{c}\end{pmatrix} = \begin{pmatrix}\sqrt{t} & \imath\sqrt{r}e^{-\imath\phi}\\ \imath\sqrt{r}e^{\imath\phi} & \sqrt{t}\end{pmatrix}\begin{pmatrix}\hat{b}\\ \hat{a}\end{pmatrix} \tag{2.134}$$

where for the atomic mirror: $r=r_m$, $t=t_m$ and $\phi=\phi_m$ whereas for the atomic beamsplitter $S^+_{\pi/2}$: $r=r_s$, $t=t_m$, $\phi=\theta_+$ and for the atomic beamsplitter $S^-_{\pi/2}$: $r=r_s$, $t=t_m$, $\phi=\theta_-$. The input and output channels of the beamsplitter is represented graphically in the figure 2.16.

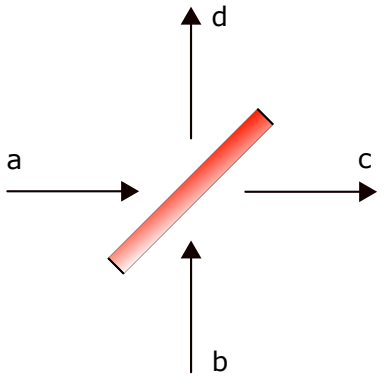

FIGURE 2.16: **The beamsplitter input-ouptut channel representation.**

We will express the operators $\hat{a}_{k_{Di}}$ and $\hat{a}_{k_{Dj}}$ in terms of operators at time $t = 0$. In other words, take as an example the operator $\hat{a}_{k_{D1}}$, it is given in terms of an operator $\hat{a}_{k_{b+}}(t > t_s)$ which is itself is written in terms of $\hat{a}_{k_{b+}}(t_m < t < t_s)$ and $\hat{a}_{k_{b+}-\Delta k_B}(t_m < t < t_s)$. Finally, $\hat{a}_{k_{b+}}(t_m < t < t_s)$ is given by $\hat{a}_{k_{b+}-\Delta k_B}(t = 0) = \hat{a}_{k_{b+}-\Delta k_B}$ and $\hat{a}_{k_{b+}-\Delta k_B}(t_m < t < t_s)$ is given by $\hat{a}_{k_{b+}}(t = 0) = \hat{a}_{k_{b+}}$. More precisely we have:

$$\begin{aligned}
\hat{a}_{k_{D2}} &= \hat{a}_{k_{a+}}(t > t_s) = e^{-\imath/\hbar E_{k_{a+}}(t-t_s)}\Big(A_{k_{a+}+\Delta k_B}\hat{a}_{k_{a+}+\Delta k_B} + A_{k_{a+}}\hat{a}_{k_{a+}}\Big) \\
\hat{a}_{k_{D1}} &= \hat{a}_{k_{b+}}(t > t_s) = e^{-\imath/\hbar E_{k_{b+}}(t-t_s)}\Big(A_{k_{b+}-\Delta k_B}\hat{a}_{k_{b+}-\Delta k_B} + A_{k_{b+}}\hat{a}_{k_{b+}}\Big)
\end{aligned}$$

with

$$\begin{aligned}
A_{k_{a+}+\Delta k_B} &= \imath\sqrt{r_m t_s}e^{\imath\phi_m}e^{-\imath/\hbar(E_{k_{a+}+\Delta k_B}t_m + E_{k_{a+}}(t_s-t_m))} \\
A_{k_{a+}} &= -\sqrt{r_m r_s}e^{\imath(\theta_+-\phi_m)}e^{-\imath/\hbar(E_{k_{a+}}t_m + E_{k_{a+}+\Delta k_B}(t_s-t_m))} \\
A_{k_{b+}} &= -\sqrt{r_m r_s}e^{\imath(\phi_m-\theta_+)}e^{-\imath/\hbar(E_{k_{b+}}t_m + E_{k_{b+}-\Delta k_B}(t_s-t_m))} \\
A_{k_{b+}-\Delta k_B} &= \imath\sqrt{r_m t_s}e^{-\imath\phi_m}e^{-\imath/\hbar(E_{k_{b+}-\Delta k_B}t_m + E_{k_{b+}}(t_s-t_m))}
\end{aligned}$$

where $E_i = \frac{\hbar^2 k_i^2}{2m}$. For the operators $\hat{a}_{k_{D3}}$ and $\hat{a}_{k_{D4}}$ we have the same relations with $+$ indices replaced by $-$ indices. So the cross-correlations on the detector in terms of operators at time $t = 0$ are given by:

$$\begin{aligned}
G^{(2)}_{D1,D3} &= \eta^2 \int\int \mathrm{d}k_{b+}\,\mathrm{d}k_{b-} \\
&\quad \times \| A_{k_{b+}-\Delta k_B}A_{k_{b-}-\Delta k_B}\hat{a}_{k_{b+}-\Delta k_B}\hat{a}_{k_{b-}-\Delta k_B}|\Psi\rangle + A_{k_{b+}}A_{k_{b-}}\hat{a}_{k_{b+}}\hat{a}_{k_{b-}}|\Psi\rangle \\
&\quad + A_{k_{b+}}A_{k_{b-}-\Delta k_B}\hat{a}_{k_{b+}}\hat{a}_{k_{b-}-\Delta k_B}|\Psi\rangle + A_{k_{b+}-\Delta k_B}A_{k_{b-}}\hat{a}_{k_{b+}-\Delta k_B}\hat{a}_{k_{b-}}|\Psi\rangle\|^2
\end{aligned} \tag{2.135}$$

and

$$\begin{aligned}
G^{(2)}_{D1,D4} &= \eta^2 \int\int \mathrm{d}k_{b+}\,\mathrm{d}k_{a-} \\
&\quad \times \| A_{k_{a-}+\Delta k_B}A_{k_{b+}}\hat{a}_{k_{a-}+\Delta k_B}\hat{a}_{k_{b+}}|\Psi\rangle + A_{k_{a-}}A_{k_{b+}-\Delta k_B}\hat{a}_{k_{a-}}\hat{a}_{k_{b+}-\Delta k_B}|\Psi\rangle \\
&\quad + A_{k_{a-}}A_{k_{b+}}\hat{a}_{k_{a-}}\hat{a}_{k_{b+}}|\Psi\rangle + A_{k_{a-}+\Delta k_B}A_{k_{b+}-\Delta k_B}\hat{a}_{k_{a-}+\Delta k_B}\hat{a}_{k_{b+}-\Delta k_B}|\Psi\rangle\|^2
\end{aligned} \tag{2.136}$$

and so on.

EPR state. First we consider the (multimode) EPR state:

$$|\Psi'_{EPR}\rangle = \frac{1}{\sqrt{2}}\Big[\int\int \mathrm{d}k_{a+}\,\mathrm{d}k_{b-}f^I_{ab}(k_{a+},k_{b-})|1_{k_{a+}},1_{k_{b-}}\rangle + \int\int \mathrm{d}k_{a-}\,\mathrm{d}k_{b+}f^{II}_{ab}(k_{a-},k_{b+})|1_{k_{a-}},1_{k_{b+}}\rangle\Big]$$

with

$$f^{I}_{ab}(k_{a+},k_{b-}) = \sqrt{\frac{2}{\pi\tilde{\sigma}_{\perp}\tilde{\sigma}_{\shortparallel}}}\exp\Big\{-\frac{(k_{a+}+k_{b-}-2k_{Lat})^2}{2\tilde{\sigma}^2_{\perp}}\Big\}\exp\Big\{-\frac{(k_{b-}-k_{a+}-\Delta k_B+\delta k_B)^2}{2\tilde{\sigma}^2_{\shortparallel}}\Big\}$$

$$f^{II}_{ab}(k_{a-},k_{b+}) = \sqrt{\frac{2}{\pi\tilde{\sigma}_{\perp}\tilde{\sigma}_{\shortparallel}}}\exp\Big\{-\frac{(k_{a-}+k_{b+}-2k_{Lat})^2}{2\tilde{\sigma}^2_{\perp}}\Big\}\exp\Big\{-\frac{(k_{b+}-k_{a-}-\Delta k_B-\delta k_B)^2}{2\tilde{\sigma}^2_{\shortparallel}}\Big\}.$$

It is an ideal state in a sense that it is the approximated state of the four wave mixing process in the low gain regime where cross correlation of a pair is much larger than the local correlation (see the discussion on the page 60, Chapter 2).

The cross correlations $G^{(2)}_{Di,Dj}$ can now be evaluated by averaging with the ideal state:

$$\begin{aligned}G^{(2)}_{D1,D3} &= \frac{\eta^2}{2}\int\int \mathrm{d}k_{b+}\,\mathrm{d}k_{b-}\\ &\quad\times\|A_{k_{b+}-\Delta k_B}A_{k_{b-}}f^{I}_{ab}(k_{b+}-\Delta k_B,k_{b-})+A_{k_{b+}}A_{k_{b-}-\Delta k_B}f^{II}_{ab}(k_{b-}-\Delta k_B,k_{b+})\|^2\\ &= \eta^2 r_m^2(r_s t_s)\int\int \mathrm{d}k_{b+}\,\mathrm{d}k_{b-}|f^{I}_{ab}(k_{b+}-\Delta k_B,k_{b-})|^2\\ &\quad\times\Big\{1+\cos\big(\Delta\theta-\frac{\hbar}{m}(t_s-2t_m)\Delta k_B(k_{b+}-k_{b-})\big)\Big\}\end{aligned}$$

where $\Delta\theta=\theta_+-\theta_-$ and $f^{II}_{ab}(k_{b-}-\Delta k_B,k_{b+})=f^{I}_{ab}(k_{b+}-\Delta k_B,k_{b-})$. Similarly, we have

$$\begin{aligned}G^{(2)}_{D1,D4} &= \frac{\eta^2}{2}\int\int \mathrm{d}k_{b+}\,\mathrm{d}k_{a-}\\ &\quad\times\|A_{k_{b+}-\Delta k_B}A_{k_{a-}+\Delta k_B}f^{I}_{ab}(k_{b+}-\Delta k_B,k_{a-}+\Delta k_B)+A_{k_{b+}}A_{k_{a-}}f^{II}_{ab}(k_{a-},k_{b+})\|^2\\ &= \frac{\eta^2 r_m^2(r_s^2+t_s^2)}{2}\int\int \mathrm{d}k_{b+}\,\mathrm{d}k_{a-}|f^{II}_{ab}(k_{a-},k_{b+})|^2\\ &\quad\times\Big\{1-\frac{2r_s t_s}{r_s^2+t_s^2}\cos\big(\Delta\theta-\frac{\hbar}{m}(t_s-2t_m)\Delta k_B(k_{b+}-k_{a-}-\Delta k_B)\big)\Big\}\end{aligned}$$

If the integration limits are large compared to the width of f^{I}_{ab} and f^{II}_{ab} which can be assured by taking larger analyse volumes, we can obtain analytical result of the cross correlations:

$$G^{(2)}_{D1,D3} = G^{(2)}_{D2,D4} = \frac{\eta^2 r_m^2(r_s^2+t_s^2)}{2}\Big[V+V\cos\big(\Delta\theta-\frac{\hbar}{m}(t_s-2t_m)\Delta k_B\delta k_B\big)e^{-\frac{(t_s-2t_m)^2}{2\sigma^2_{Bell}}}\Big]$$

$$G^{(2)}_{D1,D4} = G^{(2)}_{D2,D4} = \frac{\eta^2 r_m^2(r_s^2+t_s^2)}{2}\Big[1-V\cos\big(\Delta\theta-\frac{\hbar}{m}(t_s-2t_m)\Delta k_B\delta k_B\big)e^{-\frac{(t_s-2t_m)^2}{2\sigma^2_{Bell}}}\Big]$$

with visibility

$$V=\frac{2r_s t_s}{r_s^2+t_s^2}$$

and width

$$\sigma_{Bell} = \frac{\sqrt{2}m}{\hbar \Delta k_B} \frac{1}{\tilde{\sigma}_{\shortparallel}}.$$

The cross correlations show cosinusoidal oscillation within a Gaussian envelope as a function of time difference $t_s - 2t_m$. We have seen already similar expression with the photons in the equation (2.62).

We plot $G^{(2)}_{D1,D4}$ as a function of $t_s - 2t_m$ in figure 2.17 where we set $\Delta\theta = \theta_+ - \theta_- = 0$, $\eta = 1$, $r_m = 1$, $t_s = r_s = \frac{1}{2}$ and $\beta = \frac{\delta k_B}{\tilde{\sigma}_{\shortparallel}} = 2, 4$. We set also $\Delta k_B = 0.559 k_{rec}$ and $\tilde{\sigma}_{\shortparallel} = 0.02 k_{rec}$ which are reasonable experimental values (see Chapter 3). $\beta = \frac{\delta k_B}{\tilde{\sigma}_{\shortparallel}} = 2$ can be easily accessed in the experiment. By measuring the cross correlation as a function

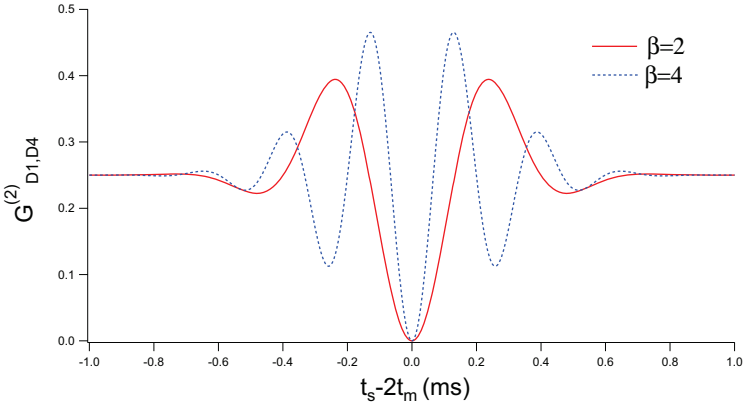

FIGURE 2.17: Joint detection coefficient $G^{(2)}_{D1,D4}$ between detectors $D1$ and $D4$ as a function of phase related to time difference $t_s - 2t_m$ for $\beta = \frac{\delta k_B}{\tilde{\sigma}_{\shortparallel}} = 2$ and $\beta = \frac{\delta k_B}{\tilde{\sigma}_{\shortparallel}} = 4$

of $t_s - 2t_m$ we will be able to calibrate the value of the phase $\theta_+ - \theta_-$ and to precisely set $t_s - 2t_m = 0$. Then the cross correlation reduces to the *cos*−function resulting in the quantum correlation coefficient given by $\cos(\theta_+ - \theta_-)$ which is specific to the EPR state. In addition, the visibility V of the cross correlation function can inform us if the Bell's inequality is violated or not. The CHSH parameter is expressed in terms of visibility for four optimized angles $\{\theta_+ - \theta_- = \frac{\pi}{4}, \theta_+ - \theta'_- = \frac{3\pi}{4}, \theta'_+ - \theta_- = -\frac{\pi}{4}, \theta'_+ - \theta'_- = \frac{\pi}{4}\}$ as:

$$S = 4\frac{V - 1 + 4V\cos(\pi/4)}{2 + 2V} \tag{2.137}$$

and it is bigger than $S > 2$ for $V > \frac{1}{2\cos(\pi/4)} = 0.70$. Experimentally, the visibility in the worst case is equal to $V \sim 0.95$ (see Chapter 3) resulting in $S = 2.7$ for which the Bell's inequality is violated. On the other hand if one considers the classical source with relative randomly varying phase, the classical correlation can be stated as [117]:

$$\begin{aligned} G^{classical}_{Di,Dj} &= \langle I_{Di} I_{Dj} \rangle \\ &= I_{Di} I_{Dj} \left[1 + \frac{(-1)^{i+j}}{2} \cos(\theta_+ - \theta_-) \right] \end{aligned}$$

which has the maximum visibility of 50% implying $S \leq 2$.

Obviously, if the actual state of an atomic pair can be approximated by the EPR state, we can expect a violation of Bell's inequality. The condition is that the cross correlation of pair should be much larger than the local correaltion of pair. To fulfill this condition we need to work with very small average population of atomic pair which can be very time demanding especially with experiments of long cycle duration. One can search the limit of the low gain regime for which the Bell's inequality would still be possible. It can be done using two mode state of the parametric down conversion process [86].

Two mode parametric down conversion state. We will consider two independent parametric state which can be written as (in analogy with equation (2.97)):

$$|\Psi_{FWM}\rangle = \sum_n \frac{\tanh^n(\lambda_1)}{\cosh(\lambda_1)} \sum_m \frac{\tanh^m(\lambda_2)}{\cosh(\lambda_2)} |n_{k_{a+}}, n_{k_{b-}}\rangle |m_{k_{a-}}, m_{k_{b+}}\rangle \tag{2.138}$$

with $\sinh^2(\lambda_1) = \langle n \rangle$ and $\sinh^2(\lambda_2) = \langle m \rangle$. From the general definition of the cross correlation in (2.135), we have

$$\begin{aligned} G^{(2)}_{D1,D3} &= |A_{k_{b+}-\Delta k_B} A_{k_{b-}-\Delta k_B}|^2 G^{(2)}_{k_{a+},k_{a-}} + |A_{k_{b+}} A_{k_{b-}}|^2 G^{(2)}_{k_{b+},k_{b-}} \\ &\quad + |A_{k_{b+}} A_{k_{b-}-\Delta k_B}|^2 G^{(2)}_{k_{b+},k_{a-}} + |A_{k_{b+}-\Delta k_B} A_{k_{b-}}|^2 G^{(2)}_{k_{a+},k_{b-}} \\ &\quad + 2\mathrm{Re}\Big[\eta^2 A_{k_{b+}} A_{k_{b-}-\Delta k_B} A^*_{k_{b+}-\Delta k_B} A^*_{k_{b-}} \langle \hat{a}^\dagger_{k_{a+}} \hat{a}^\dagger_{k_{b-}} \hat{a}_{k_{b+}} \hat{a}_{k_{a-}} \rangle \Big] \end{aligned}$$

where $G^{(2)}_{k_i,k_j} = \eta^2 \langle \Psi_{FWM} | \hat{a}^\dagger_{k_i} \hat{a}_{k_i} \hat{a}^\dagger_{k_j} \hat{a}_{k_j} | \Psi_{FWM} \rangle$ with $i = a+, b+$ and $j = a-, b-$. By fixing $r_s = t_s = \frac{1}{2}$ and $t_m = 0$, $r_m = 1$, one can show that

$$\begin{aligned} G^{(2)}_{D1,D3} &= G^{(2)}_{D2,D4} = \frac{1}{4}\Big[G^{(2)}_{k_{b+},k_{b-}} + G^{(2)}_{k_{a+},k_{a-}} + G^{(2)}_{k_{b+},k_{a-}} + G^{(2)}_{k_{a+},k_{b-}} \\ &\quad + 2\mathrm{Re}\Big\{\eta^2 e^{\imath(\Delta\theta - \frac{\hbar}{m}(t_s - 2t_m)\Delta k_B \delta k_B)} \langle \hat{a}^\dagger_{k_{a+}} \hat{a}^\dagger_{k_{b-}} \hat{a}_{k_{b+}} \hat{a}_{k_{a-}} \rangle \Big\}\Big] \\ G^{(2)}_{D1,D4} &= G^{(2)}_{D2,D3} = \frac{1}{4}\Big[G^{(2)}_{k_{b+},k_{b-}} + G^{(2)}_{k_{a+},k_{a-}} + G^{(2)}_{k_{b+},k_{a-}} + G^{(2)}_{k_{a+},k_{b-}} \\ &\quad - 2\mathrm{Re}\Big\{\eta^2 e^{\imath(\Delta\theta - \frac{\hbar}{m}(t_s - 2t_m)\Delta k_B \delta k_B)} \langle \hat{a}^\dagger_{k_{a+}} \hat{a}^\dagger_{k_{b-}} \hat{a}_{k_{b+}} \hat{a}_{k_{a-}} \rangle \Big\}\Big] \end{aligned}$$

The autocorrelations $G^{(2)}_{k_{b+},k_{b-}}, G^{(2)}_{k_{a+},k_{a-}}$ and cross correlations $G^{(2)}_{k_{b+},k_{a-}}, G^{(2)}_{k_{a+},k_{b-}}$ are easily evaluated (from (2.102)):

$$G^{(2)}_{k_{b+},k_{b-}} + G^{(2)}_{k_{a+},k_{a-}} = 2\eta^2 \langle n \rangle \langle m \rangle \tag{2.139}$$

$$G^{(2)}_{k_{b+},k_{a-}} + G^{(2)}_{k_{a+},k_{b-}} = \eta^2 \langle n \rangle (1 + 2\langle n \rangle) + \eta^2 \langle m \rangle (1 + 2\langle m \rangle). \tag{2.140}$$

For the symmetric average population $\langle n\rangle = \langle m\rangle$, it is shown [86] that

$$\langle \hat{a}^{\dagger}_{k_{a+}} \hat{a}^{\dagger}_{k_{b-}} \hat{a}_{k_{b+}} \hat{a}_{k_{a-}} \rangle = \langle n\rangle(1+\langle n\rangle). \tag{2.141}$$

Finally, the quantum correlation coefficient takes form:

$$E(\theta_+, \theta_-) = \frac{(1+\langle n\rangle)\cos(\theta_+ - \theta_- - \frac{\hbar}{m}(t_s - 2t_m)\Delta k_B \delta k_B)}{\langle n\rangle(1+3\langle n\rangle)} \tag{2.142}$$

leading to the CHSH parameter (for the optimized set of phases θ_+, θ_- and $t_s - 2t_m = 0$):

$$S = 2\sqrt{2}\frac{1+\langle n\rangle}{1+3\langle n\rangle}. \tag{2.143}$$

The threshold value of $\langle n\rangle$ to have S bigger than 2 is as small as 0.26. We can reduce the average population in practice at the cost of the longer integration times. We will estimate next the reasonable number of repetitions to achieve acceptable signal to noise ratio.

Error of the CHSH parameter. We can estimate naively the standard error of the CHSH parameter δS. From the definition of the S parameter:

$$S(\theta_+, \theta'_+, \theta_-, \theta'_-) = E(\theta_+, \theta_-) - E(\theta_+, \theta'_-) + E(\theta'_+, \theta_-) + E(\theta'_+, \theta'_-)$$

we can write

$$\delta S = \sqrt{(\delta E)^2 + (\delta E)^2 + (\delta E)^2 + (\delta E)^2} = 2\delta E \tag{2.144}$$

and from the definition of the correlation coefficient:

$$E(\theta_+, \theta_-) = \frac{G^{(2)}_{D1,D3} + G^{(2)}_{D2,D4} - G^{(2)}_{D1,D4} - G^{(2)}_{D2,D3}}{G^{(2)}_{D1,D3} + G^{(2)}_{D2,D4} + G^{(2)}_{D1,D4} + G^{(2)}_{D2,D3}}$$

we can write

$$\Big(\frac{\delta E}{E}\Big)^2 = \Big(\frac{2\delta G^{(2)}_{Di,Dj}}{G^{(2)}_{D1,D3} + G^{(2)}_{D2,D4} - G^{(2)}_{D1,D4} - G^{(2)}_{D2,D3}}\Big)^2 + \Big(\frac{2\delta G^{(2)}_{Di,Dj}}{G^{(2)}_{D1,D3} + G^{(2)}_{D2,D4} + G^{(2)}_{D1,D4} + G^{(2)}_{D2,D3}}\Big)^2$$

with (for $\langle n\rangle \ll 1$)

$$E = \frac{1+\langle n\rangle}{1+3\langle n\rangle}\cos(\Delta\theta) \sim 1$$

$$G^{(2)}_{D1,D3} + G^{(2)}_{D2,D4} - G^{(2)}_{D1,D4} - G^{(2)}_{D2,D3} = 2\langle n\rangle(1+\langle n\rangle)\cos(\Delta\theta) \sim 2\langle n\rangle$$

and

$$G^{(2)}_{D1,D3} + G^{(2)}_{D2,D4} + G^{(2)}_{D1,D4} + G^{(2)}_{D2,D3} = 2\langle n\rangle + 6\langle n\rangle^2 \sim 2\langle n\rangle.$$

So, the error of the E is

$$\delta E = \sqrt{2}\frac{\delta G^{(2)}_{Di,Dj}}{\langle n\rangle}. \tag{2.145}$$

The expression of $G^{(2)}_{Di,Dj}$ is

$$G^{(2)}_{Di,Dj} = \frac{1}{4}\Big\{2\langle n\rangle^2 + 2\langle n\rangle(1+2\langle n\rangle) + (-1)^{i+j}2\langle n\rangle(1+\langle n\rangle)\cos(\Delta\theta)\Big\} \sim \langle n\rangle$$

suggesting that

$$\delta G^{(2)}_{Di,Dj} = \delta\langle n\rangle. \tag{2.146}$$

The standard error of the average population can be written for $\mathcal{N}$ experimental realizations as

$$\delta\langle n\rangle = \frac{1}{\mathcal{N}}(\langle n^2\rangle - \langle n\rangle^2)$$

while the standard error of the detected average population is

$$\delta\langle n_{det}\rangle = \sqrt{\eta^2(\delta\langle n\rangle)^2 + \frac{\eta(1-\eta)}{\mathcal{N}}\langle n\rangle} \sim \sqrt{\frac{\eta(1-\eta)}{\mathcal{N}}\langle n\rangle}. \tag{2.147}$$

Finally, the standard error of S can be reduced to:

$$\delta S = 2\sqrt{2}\sqrt{\frac{\eta(1-\eta)}{\mathcal{N}\langle n\rangle}}. \tag{2.148}$$

If we want to have $S \pm \delta S = 2.2 \pm 0.1$, the number of experimental realizations should be

$$S = 2\sqrt{2}\frac{(1+\langle n\rangle)}{(1+3\langle n\rangle)} = 2.2 \longrightarrow \langle n\rangle = 0.16$$

$$\delta S = 2\sqrt{2}\sqrt{\frac{\eta(1-\eta)}{\mathcal{N}\langle n\rangle}} = 0.1 \longrightarrow \mathcal{N} \sim 940.$$

The total number of realizations is $\mathcal{N}_{tot} = 4 \times \mathcal{N} \sim 4000$ where factor 4 is for four set of phases. It is indeed a reasonable number for us to carry out an experiment amounting to about one week of data acquisition.

2.2.6 Conclusion

In this chapter we have presented the Bell's inequalities starting with the experiment of spin entangled photons. Then we have looked at the scheme of the Bell's inequality test experiment based on the correlation of the external degrees of freedom which can be mapped one to one with the experiment using spin entangled photons. We have presented also the analogical scheme for the experiment with helium atoms correlated in momentum. The atom pair production and the manipulation of this source by using Bragg pulse is presented theoretically in detail. Finally, we have evaluated the quantum

correlation coefficient using an approximated state $|\Psi'_{EPR}\rangle$ which is valid in low gain regime of the pair production. Low gain regime means long data acquisition to acquire enough data, so it will not be possible to decrease the gain arbitrarily. In order to estimate the upper threshold of the low gain regime, the correlation function is evaluated assuming the state of two independent modes of the parametric down-conversion process which allows having more than two atoms at a time. We think that it is possible to carry out the experiment with reasonable data acquisition period to achieve the satisfactory signal to noise ratio.

Chapter 3

Bell's inequality test with massive particles: experimental preparation

This chapter will be devoted to the experimental preparation of the atomic Bell's inequality test using momentum correlated pair in which I was fully engaged in the last year of my thesis work in the quantum atom optics team. We have realized plenty of experimental tests and improved several aspects of the basic elements of the proposed scheme in the figure 2.5 to check if it is experimentally plausible at all and if we control all the parameters. After all, in real life, the situation could be more complex than what is given in the theoretical description of the Chapter 2.

This chapter is organized as follows: in the first section, the overview of the experimental sequence is presented, in the next section the tests on the atomic pair source is described. The third section is devoted to the tests on the Bragg beam, which plays the role of aperture, phase shifter, mirror and beamsplitter, and the last section will describe the perspective.

3.1 Experimental preparation of the protocol of the atomic Bell's test experiment

The scheme in figure 3.1 (replica of the figure 2.5 in Chapter 2) for the realisation of the Bell's inequality test with helium atoms is not chosen by chance. On the contrary, it was found to be an optimised scheme specifically in terms of the phase control among the other possible schemes we have investigated. In addition, this particular scheme requires minimum modification on top of the existing experimental set-up of the atomic Hong-Ou-Mandel (HOM) experiment (discussed in Chapter 4). So, what are the basic

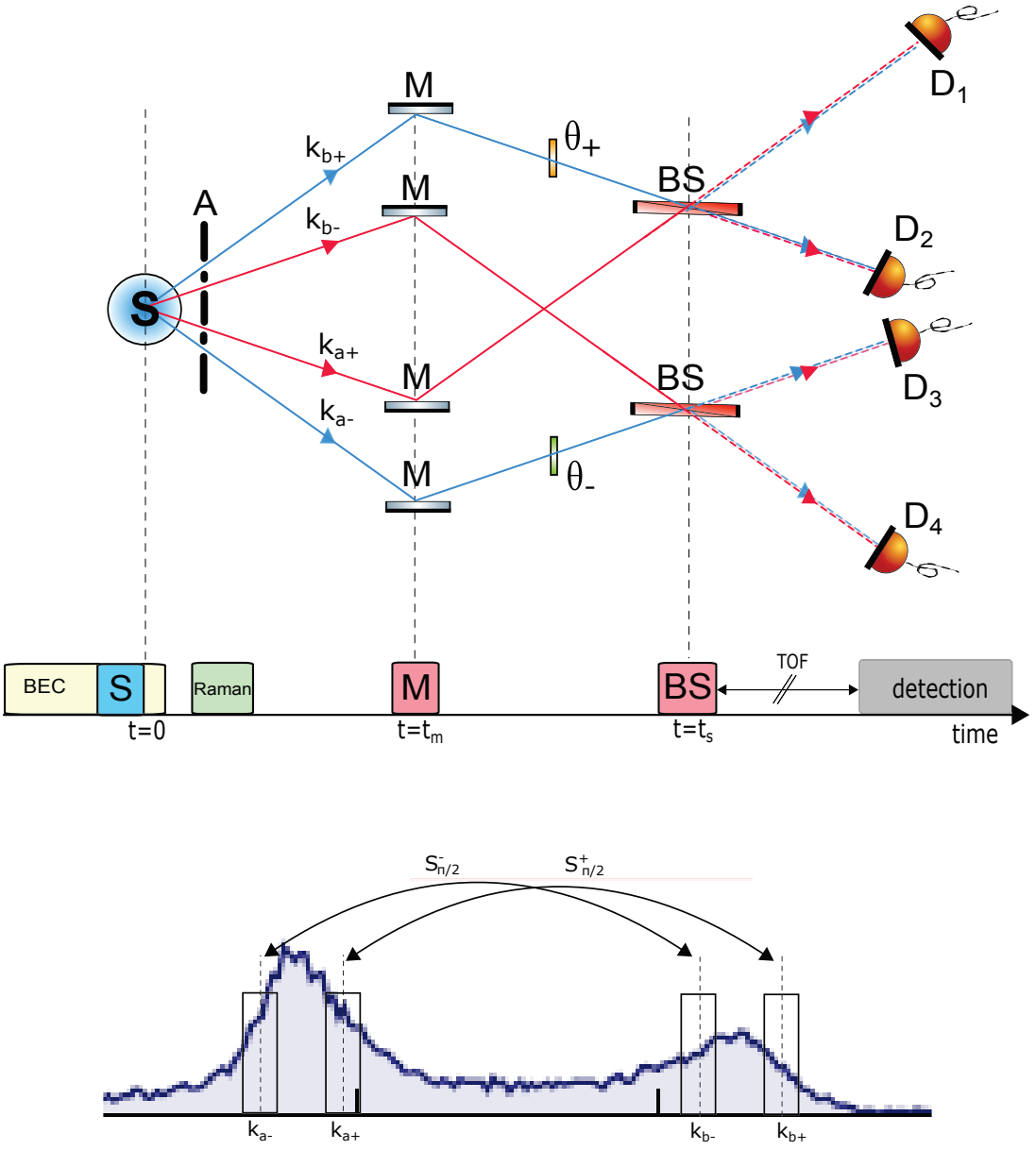

FIGURE 3.1: **Top: Schematics of the Bell's inequality test experiment using a pair of helium atoms correlated in momentum space and the corresponding experimental sequence.** Initially we prepare a condensate of metastable helium in the crossed dipole trap which serves as a nonlinear medium to create pairs (BEC). Then the multimode atomic pair is created through the dynamical instability process by applying a moving optical lattice on the condensate (S). Later we switch off the trap and transfer the atomic pair in the magnetic insensitive substate $m = 0$ by a Raman process to avoid the deviations of trajectories of atoms due to the stray magnetic field in the science chamber (Raman). We apply then a single Bragg pulse at $t = t_m$ which is not selective in mode. It will play the role of the atomic mirror (M). At t_s, we apply two simultaneous Bragg pulses which act as a beamsplitter for the two separate interferometers of the non-conjugate modes (BS). In the end, the particles are detected and the correlation analysis is made (detection).**Bottom: The vertical modes of the atomic pair addressed by the two beamsplitters.**

ingredients of the proposed experimental protocol for the atomic Bell's inequality test in the figure 3.1? They are:

- multi-mode atomic pair,
- aperture,
- mirror,
- phase shifter,
- beamsplitter,
- detector.

Recall that the aperture, phase shifter, beamsplitter and mirror are all taken care by the Bragg pulse (see 2.2.4). So, we see that the Bragg pulse plays a huge role in realising the atomic Bell's test experiments and we should have a good command of it.

The global picture of the experimental sequence as shown in the figure 3.1 is as follows:

1. **Preparation of the BEC in the dipole trap:** it is our non-linear medium for the atomic pair creation
2. **Creation of an atomic pair in the crossed dipole trap:** we create an atomic pair through the process of the dynamical instability by applying the moving optical lattice on the BEC as discussed in the Chapter 2.
3. **Releasing pair from the trap and transferring them to the magnetic field insensitive substate $m = 0$:** we release the pair and the condensate from the trap simply by switching off the laser beams of the dipole trap and later we transfer the atomic pair in the magnetic field insensitive substate $m = 0$ using Raman beams (discussed in appendix C).
4. **Atomic mirror:** An atomic mirror is realised with the single Bragg pulse which is not selective in momentum. Thus, it will shift the momentum of all modes by the same amount.
5. **Atomic beamsplitter:** An atomic beamsplitter is realised with the two simultaneous Bragg pulses which address different modes. Thus, it serves as an aperture and allows us to control the phase between the two atomic interferometers.
6. **Detection and analysis:** At the end of the sequence after long time of flight, the pair is detected (discussed in appendix D) and the correlation analysis is made.

In the following, I am going to describe the experimental realisation of the stages listed above including their experimental characterisation and the tests that validate the possibility of realising Bell's experimental protocol in figure 3.1. To do so, in the next section, the characterization of the condensate of the metastable helium atom in the crossed dipole trap and the correlation properties of the multimode atomic pair is discussed. Then following the next section, the Bragg pulse, its selectivity and phase control will be covered in detail. Refer to the table 3.1 for the list of tests.

Test	Section
BEC	3.2.1
Setup of dipole trap beams	3.2.1.1
Dipole trap potential	3.2.1.2
BEC of metastable helium	3.2.1.3
Atomic pair	3.2.2
Setup and calibration of moving lattice	3.2.2.1
Correlation measurement of atomic pair	3.2.2.2
Bragg pulse	3.3
Setup and calibration of Bragg beams	3.3.1
Selectivity test	3.3.2
Phase test	3.3.3

TABLE 3.1: Reference of experimental tests

3.2 Atomic pair source preparation

3.2.1 BEC in the crossed dipole trap and its characterization

3.2.1.1 The optical beams

The crossed dipole trap consists of two focused beams: vertical and horizontal beams which are superposed at the center of the science chamber 46 cm above the MCP detector shown in figure 3.2. Due to the intensity gradient, the atoms feel a potential via the interaction of the induced dipole and the electromagnetic field [58]. When the light is red detuned with respect to the atomic transition, the atoms are attracted to the maximum intensity thus creating a trapping potential. For this purpose, we use an IPG laser with the output power 5 W at 1550 nm (the atomic transition is at 1083 nm) to create the dipole trap in which we obtain eventually the BEC of the metastable helium atoms. The output laser beam is divided in horizontal and vertical arms as shown in figure 3.3. We introduce 80 MHz of the frequency difference between two arms by using different orders diffracted by the acousto-optic modulators (AOMs). In this way, we avoid the intensity modulation at lower frequencies which may lead to the parametric excitation resonances. In addition, by controlling the strength of the RF signal in AOMs we dictate the optical power in two arms to adiabatically load, cool atoms by evaporation, to switch off the

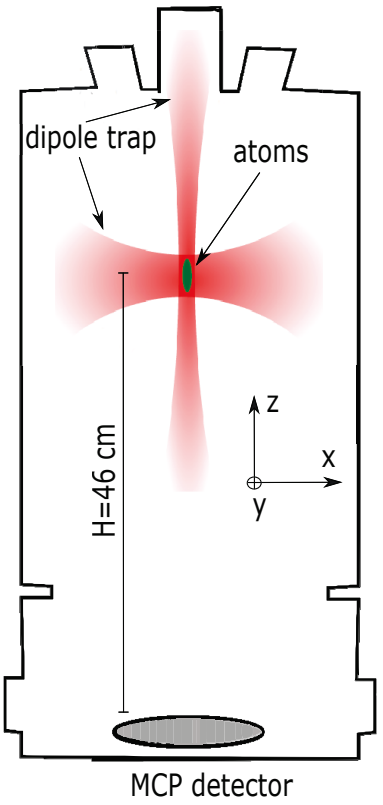

FIGURE 3.2: Crossed dipole trap inside science chamber(drawing not to scale)

trap rapidly. The photodiodes after the AOMs serve as the feedback for the power control [74]. The available power on the atoms is 2 W, and the typical power at the end of the evaporation in the vertical beam is 600 mW and in the horizontal beam is 30 mW. At the entry of the science chamber the two beams are focused with the lenses. The measurement of the beam waists resulted in $\omega_0^{hor} = 58(1)\ \mu m$ and $\omega_0^{vert} = 35(1)\ \mu m$. To retrieve these values the waist of the beam around the focal point was measured and fit by

$$\omega(r) = \omega_0\sqrt{1 + \left(\frac{r}{r_R}\right)^2}, \qquad r = x, z \tag{3.1}$$

with Rayleigh length $r_R = \frac{\pi\omega_0^2}{\lambda}$. However, these values are not exactly the same ones with what atoms really feel. The more precise values for beam waists are obtained by measuring the trapping frequencies using atoms for different powers of the beam and deducing the waist which is contained in the relations between these two (for details on the technique [74, 87]). So the real values are $\omega_0^{hor} = 82(4)\ \mu m$ and $\omega_0^{vert} = 43.0(5)\ \mu m$. The deviation of these latter values from the results of the direct measurement is possibly due to the aberrations introduced by the science chamber windows.

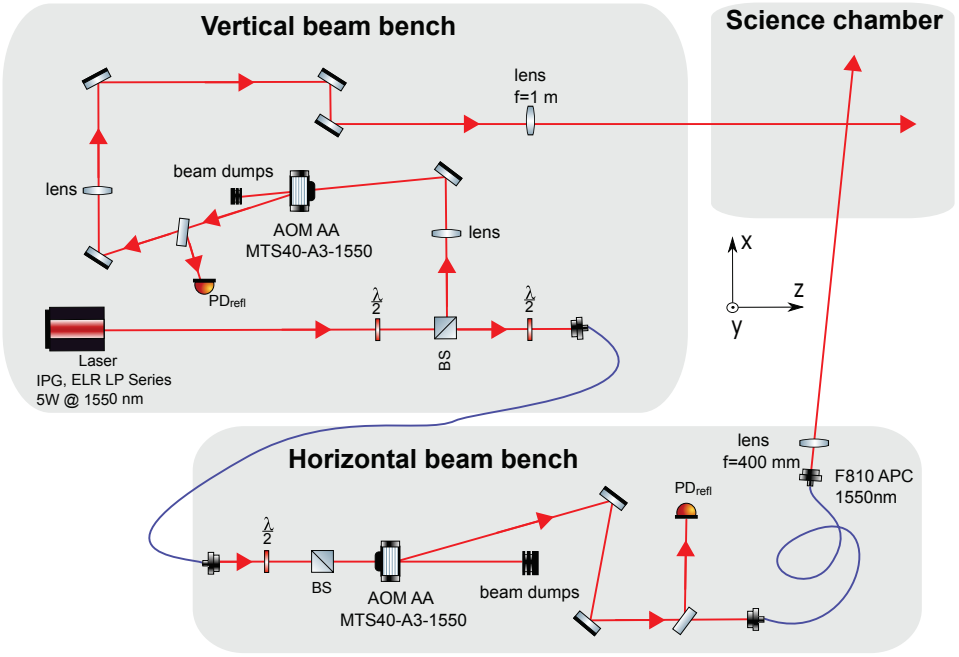

FIGURE 3.3: **Optical bench of a vertical and horizontal dipole trap beams.** The laser beam is split into two by a polarization cube and one arm is injected into a fiber to send it on the horizontal beam optical bench. Both arms are diffracted with an efficiency of 90% by the acousto-optic modulators (AOM) which are used to control the power of the two beams. The photodiodes on each path collect 1% of the power to lock the power of the trapping beams. The two lenses before and after the vertical beam AOM are used as telescope to optimize the diffraction efficiency. The last lenses on each path before the science chamber focuses beams on the center of the science chamber. The horizontal beam makes 8.6° with respect to x-axis defined by the magnetic trap.

3.2.1.2 The trapping potential

To load atoms from the magnetic trap to the optical trap, we ramp up the intensity of the vertical beam up to a full power ≈ 1 W and the intensity of the horizontal beam to its final power value 30 mW as shown in figure 3.4. At this stage we mainly load atoms in the vertical beam trap whose potential depth is ~ 7 μK along the vertical direction. Typically we transfer $1 - 3 \times 10^5$ atoms whose thermalisation temperature is 3 μK. The magnetic trap is then turned off quickly in 100 μs. We keep however a bias magnetic field of 3 G in the horizontal direction to maintain the polarisation of the $m_j = +1$ atoms [105]. The measured lifetime of polarised atoms in the dipole trap is 22 s. The condensation is achieved by adiabatically ramping down the intensity of the vertical beam according to the formula

$$I(t) = (I_0 - I_F)e^{-t/\tau_{ev}} + I_F \tag{3.2}$$

with the time constant $\tau_{ev} = 1$ s. The potential created by two superposed beams can

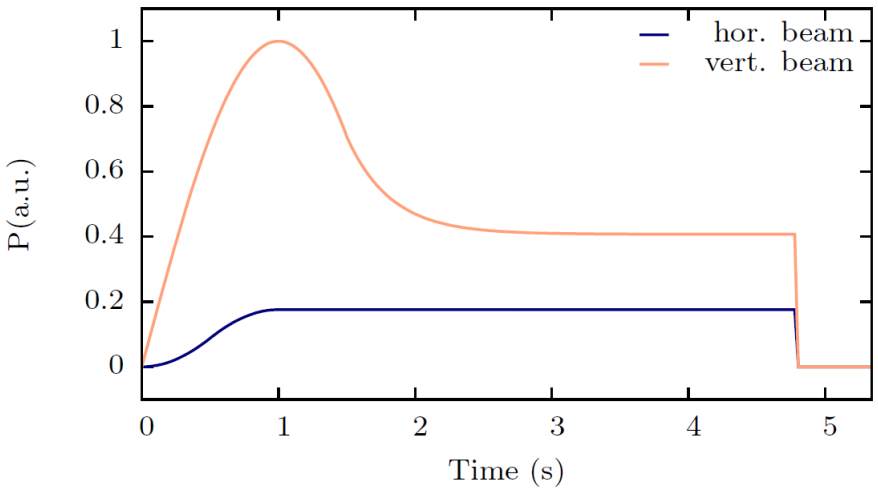

FIGURE 3.4: The power ramp of the dipole trap beams in a typical experimental sequence. Between $0-1$ s the atoms are loaded adiabatically in the dipole trap (mainly with vertical beam) from the magnetic trap, between $1-5$ s the intensity of the vertical beam is decreased adiabatically to evaporate the thermal cloud. The condensation occurs in the crossed dipole trap at the end of the sequence. (figure credit to [87])

be written as:

$$U(x,y,z) = U_{vert}\frac{\exp\left\{-\frac{2(x^2+y^2)}{w_{vert}^2\left((\frac{z-z_0}{z_{vert}})^2+1\right)}\right\}}{\left(\frac{z-z_0}{z_{vert}}\right)^2+1} + U_{hor}\frac{\exp\left\{-\frac{2(y^2+z^2)}{w_{hor}^2\left((\frac{x}{x_{hor}})^2+1\right)}\right\}}{\left(\frac{x}{x_{hor}}\right)^2+1} - mgz \tag{3.3}$$

with

$$U_{vert} = -\frac{3\pi c^2}{2\omega_0^3}\frac{2P_{vert}}{\pi w_{vert}^2}\left(\frac{\Gamma}{\omega_0-\omega_{dip}}+\frac{\Gamma}{\omega_0+\omega_{dip}}\right) \tag{3.4}$$

and

$$U_{hor} = -\frac{3\pi c^2}{2\omega_0^3}\frac{2P_{hor}}{\pi w_{hor}^2}\left(\frac{\Gamma}{\omega_0-\omega_{dip}}+\frac{\Gamma}{\omega_0+\omega_{dip}}\right) \tag{3.5}$$

where $\Gamma = 2\pi \times 1.6$ MHz natural width of the transition $2^3S_1 \longrightarrow 2^3P_2$, ω_0 the frequency of this transition, ω_{dip} the frequency of light, $w_{vert}(w_{hor})$ the waist of the vertical(horizontal) beam, $z_{vert} = \frac{\pi w_{vert}^2}{\lambda_{dip}}$ ($x_{hor} = \frac{\pi w_{hor}^2}{\lambda_{dip}}$) the vertical (horizontal) beam's Rayleigh length, $z_0 = 2.3$ mm the central position of the vertical waist. The potential profile $U(0,0,z)$ in $z-$direction is depicted in the figure 3.5 for the final laser beam powers. We see two different scales, the big one and the smaller one. The big one is due to the vertical beam and the gravity. We see that the flat potential appears around $z = 0$ meaning that the gravity is compensated by the potential of the vertical beam (this is actually how z_0 is chosen). The smaller potential which is zoomed in the inset is the real trap potential along $z-$ direction which solely comes from the horizontal beam with the shallow potential depth of 400 nK. Along the transverse directions x and y,

the trap potential is dictated by the potential created by the vertical beam as shown in figure 3.6 with relatively bigger potential depth 19.5 μK.

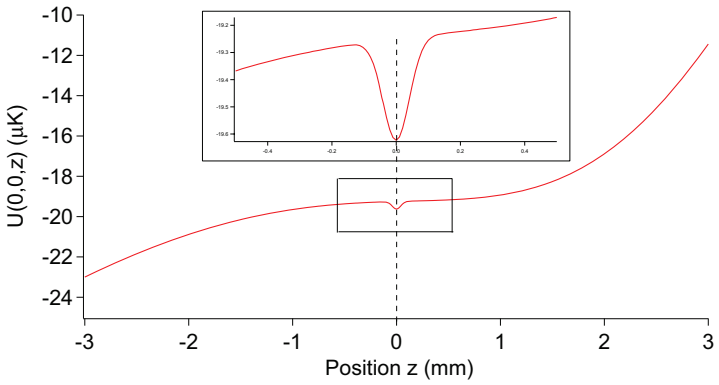

FIGURE 3.5: Dipole potential $U(0,0,z)$ of a crossed beam as a function of position z. We see two different scales, the first one which is larger is the potential of the vertical beam which compensates the gravity thus creating flat potential around position 0, and the smaller one which is the potential trap created by the horizontal beam. It is the latter one which traps atoms in z-direction with potential depth 400 nK which is zoomed in inset graph.

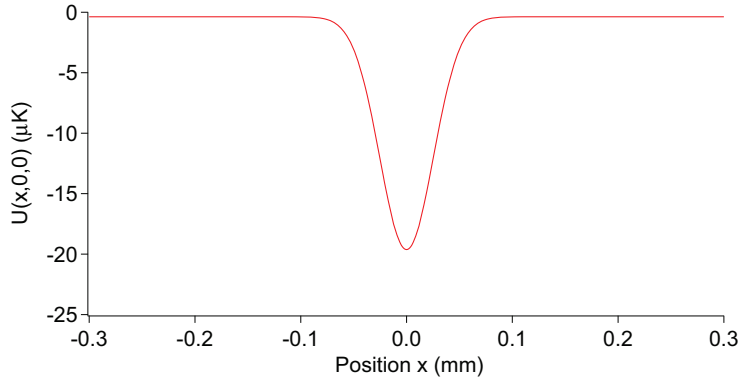

FIGURE 3.6: Dipole potential $U(x,0,0)$ of a crossed beam as a function of position x. The trap created here is solely due to the vertical beam with the potential depth of 19.5 μK.

We have experimentally measured the longitudinal (along z) and transverse (plane perpendicular to z) frequencies of the dipole trap which can also be deduced from the Taylor expansion of the expression of the potential in (3.3).

To determine the transverse frequency which is given mainly by the vertical beam, the intensity of the vertical beam is modulated at variable frequency ω_{mod}. When the modulation frequency approaches the double of the frequency of the trap, we can excite atoms by injecting the energy of the modulation and expel them from the trap. By looking at the distribution of the atoms which stays in the trap one can retrieve the resonant frequency. The effect is seen both on the momentum distribution of the atoms

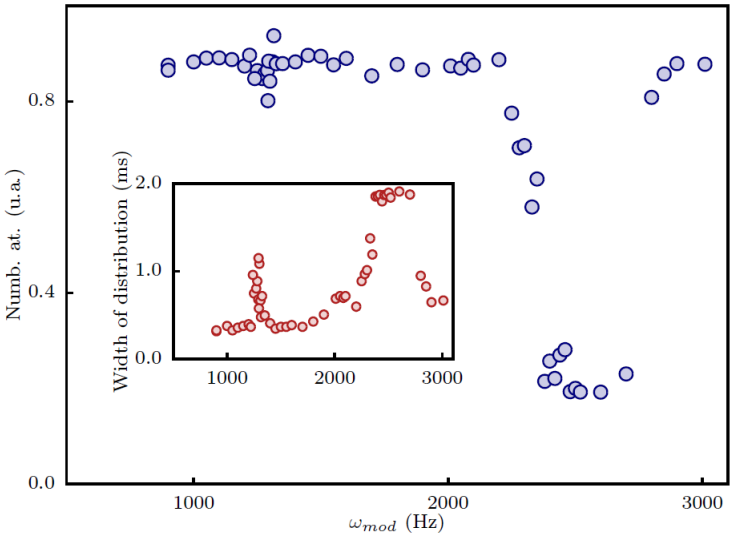

FIGURE 3.7: **Determining the transverse frequency of the dipole trap experimentally.** The number of atoms, which stay in the trap when the intensity of the vertical beam is modulated, is plotted as a function of the modulation frequency(blue points). The momentum distribution is plotted as a function of the modulation frequency in inset (red points). In both cases, we see the expected resonance frequency at the multiple integer of the transverse frequency of the trap. (figure credit to [87])

and on the atom number. These two parameters are plotted as a function of ω_{mod} in figure 3.7 where we clearly see the drastic drop on the number of atoms (blue points) and expansion of the width of the momentum distribution of the atoms (red points in the inset) at the expected resonance frequency, $\omega_{mod} = 2\omega_{\perp} = 2542(15)$ Hz and also at $\omega_{mod} = \omega_{\perp} = 1275(8)$ Hz with smaller effect. We see also the latter one since, the effect being maximal for $\omega_{mod} = 2\omega_{\perp}$, the parametric resonance can occur at all frequencies $\omega_{mod} = \frac{2\omega_{\perp}}{n}$ with n integral [82]. The measured value of the transverse frequency is compatible with the theoretically expected value $\omega_{\perp} = 2\pi \times 1277$ Hz.

On the other hand, to determine the longitudinal frequency, we employ another method although the first method works fine as well. We give an initial speed to the atoms in the trap, after which they start oscillating in the trap. We hold the atoms in the trap for some duration and release them from the trap. We can reconstruct the speed of the atoms at the time when they are released from the arrival time of the atoms on the detector. By plotting this speed of the atoms as a function of the holding duration of the trap, one can easily estimate the longitudinal trap frequency as shown in figure 3.8 where the vertical potential depth is increased by setting $P_{hor} = 110$ mW. In this configuration the measured frequency is $\omega_z = 2\pi \times 210(1)$ Hz suggesting $\omega_z = 2\pi \times 93(4)$ Hz for the typical value of the power of the horizontal beam $P_{hor} = 30$ mW. Note that the initial speed is given via Bragg diffraction (Chapter 2).

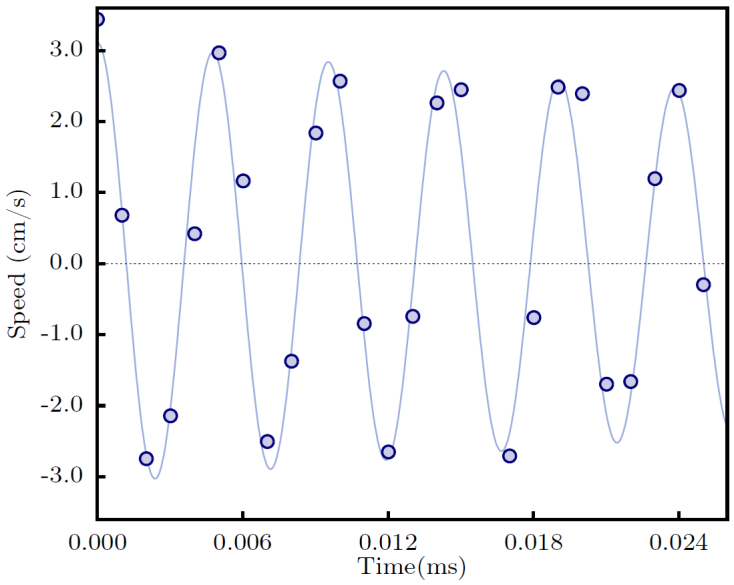

FIGURE 3.8: **Determining the longitudinal frequency of the dipole trap experimentally.** The center of mass of the atoms in the dipole trap is put in motion by giving initial speed. The speed at the moment of release from the trap as a function of holding duration of trap is plotted. The frequency of the oscillation is the frequency of the trap along $z-$direction. (figure credit to [87])

To sum up this subsection, we give the key parameters of the dipole trap beams in table 3.2.

Parameter	Notation	Value	Unit
Beam wavelength	λ_{dip}	1550	nm
Horizontal beam power	P_{hor}	30	mW
Vertical beam power	P_{ver}	585	mW
Horizontal beam waist	w_{hor}	82	μm
Vertical beam waist	w_{vert}	43	μm
Longitudinal trap frequency	ω_z	$2\pi \times 93$	Hz
Transverse trap frequency	$\omega_\perp$	$2\pi \times 1275$	Hz

TABLE 3.2: Parameters associated with the dipole trap beams

3.2.1.3 Bose-Einstein condensate of the metastable helium atom in the crossed dipole trap

In his famous paper [46] dating back to 1924, Einstein predicted that, below a certain temperature, a macroscopic occupation of the lowest-energy quantum state take place for the bosonic particles. The quantum states of the particles at thermal equilibrium saturate, and any excess particles 'condense' into the quantum ground state since the indistinguishable bosons have greater probability to end up in the same state which is already occupied by other bosons than in initially empty states. The condition for which

this remarkable phase transition known today as the Bose-Einstein condensation (BEC) occurs is given by the value

$$n\lambda_{dB}^3 \cong 2.61 \tag{3.6}$$

where n is the central atomic density in three dimensional position space, and λ_{dB} is the thermal de Broglie wavelength, which is defined by

$$\lambda_{dB} = \sqrt{\frac{2\pi\hbar^2}{mk_BT}} \tag{3.7}$$

at temperature T. The condition in (3.6) states that the quantum statistical effects appear when λ_{dB} is on the order of average separation $n^{-1/3}$, i.e. when the atomic wave functions overlap. Note that, for an ideal homogeneous gas at room temperature and under standard pressure, the quantity $n\lambda_{dB}^3$ is much less than unity.

One can reach the condensation either by increasing the density n or by decreasing the temperature T in λ_{dB} according to the condition (3.6). However, by increasing the density one can not avoid forming solids or liquids ($n \sim 10^{28}$ m^{-3})where electromagnetic interactions such as chemical bonds, van der Waals forces... are responsable for the ordinary phase transitions masking the quantum statistical effect. The solution is to work with a density below 10^{18} m^{-3} and reduce the temperature under the critical temperature which is in microkelvin range, beyond the accessible range via standard cryogenic techniques. The Bose-Einstein condensation was achieved experimentally in 1995 under dilute conditions [3] by combining laser cooling and trapping with the evaporative cooling as shown in figure 3.9. This experimental success is rewarded by the Nobel Prize in 2001.

One can identify a Bose-Einstein condensate in an experiment from the thermal gas by looking at the velocity distribution. Consider a condensate without interactions in a harmonic trap with cylindrical symmetry in the $z-$direction. The mean squared deviation of the velocity is given by [111]

$$\Delta V_\perp = \frac{1}{2}\sqrt{\frac{\hbar\omega_\perp}{m}} \qquad \Delta V_z = \frac{1}{2}\sqrt{\frac{\hbar\omega_z}{m}} \tag{3.8}$$

while for a cloud at thermal equilibrium the velocity distribution is isotropic and standard width does not depend on the trap stiffness ω_i

$$\Delta V_i = \sqrt{\frac{k_BT}{m}}. \tag{3.9}$$

Then in the experiment, if one takes an image of the velocity distribution by releasing the cloud from the trap and letting it to expand for long time of flight, one will observe a double structure with an anisotropic central profile and with gaussian wing profile.

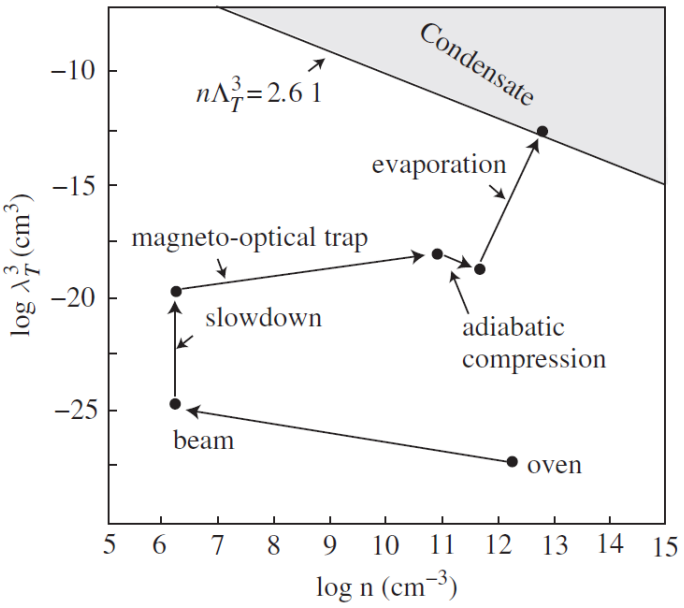

FIGURE 3.9: The path which leads to the condensation in $n\lambda_{dB}^3$ space with the bold line corresponding to the threshold value 2.61. The final density is similar but the gain in temperature is crucial. (figure credit to [62])

From the wings, one can determine the temperature of the thermal fraction of the atomic cloud. In case of interacting gas the scales are different but the behaviour is same.

When the average number of particles in the condensate $\langle N \rangle$ is very large, the fluctuations in particle number can be neglected. In this situation one can approximate the wave function of the condensate by the $N-$particle classical wave function:

$$\Psi = \sqrt{N} e^{-\imath\varphi} u_0(\mathbf{r}) e^{-\imath \frac{\mu}{\hbar} t} \tag{3.10}$$

where a phase φ is the condensate phase, the energy μ is the chemical potential. In the mean field approximation, each atom feels a time-independent average interaction potential and $u_0(\mathbf{r})$ obeys the nonlinear Schrödinger equation, known as the Gross-Pitaevski equation:

$$-\frac{\hbar^2}{2m}\Delta u_0(\mathbf{r}) + V(\mathbf{r}) u_0(\mathbf{r}) + Ng|u_0(\mathbf{r})|^2 u_0(\mathbf{r}) = \mu u_0(\mathbf{r}) \tag{3.11}$$

with

$$g = \frac{4\pi\hbar^2}{m} a \tag{3.12}$$

which characterizes the interaction between ultracold atoms by a single parameter, the scattering length a (for Helium in $m = 1$ it is 7.5×10^{-9} m [97]).

A good approximative solution of the condensate wave function for a large number of atoms can be obtained by solving the Gross-Pitaevskii equation, neglecting totally the

kinetic energy term which is small compared with other energies. This has the solution

$$Ng|u_0(\mathbf{r})|^2 = \mu - V(\mathbf{r}) \tag{3.13}$$

when the right hand side is positive and zero otherwise. In a harmonic potential, the density profile is an inverted paraboloid vanishing on an ellipsoidal surface with semi-axes(Thomas-Fermi radii):

$$R_\perp = \frac{1}{\omega_\perp}\Big(\frac{2\mu}{m}\Big)^{1/2} \text{ and } R_z = \frac{1}{\omega_z}\Big(\frac{2\mu}{m}\Big)^{1/2} \tag{3.14}$$

with anisotropy $\frac{\omega_\perp}{\omega_z}$. The chemical potential can be found from the normalization of the wave function $u_0(\mathbf{r})$ and it is equal to

$$\mu = \frac{\hbar\bar{\omega}}{2}\Big[15Na\sqrt{\frac{m\bar{\omega}}{\hbar}}\Big]^{2/5} \tag{3.15}$$

where $\bar{\omega} = (\omega_z\omega_\perp^2)^{1/3}$.

Once the trap is switched off, for $\omega_z \ll \omega_\perp$, the evolution of the Thomas-Fermi radii is given by [31]:

$$R_\perp(t) = R_\perp\sqrt{1+(\omega_\perp t)^2} \tag{3.16}$$

$$R_z(t) = R_z\big(1+(\frac{\omega_z}{\omega_\perp})^2\big[\omega_z t\arctan(\omega_z t) - \log(\sqrt{1+(\omega_z t)^2})\big]\big) \tag{3.17}$$

If we measure experimentally the Thomas-Fermi radii after time of flight, we can estimate the chemical potential and therefore the number of atoms in the condensate according to [31]. But in our experiment the description can not be directly applied due to two main reasons: first one is that when the trap is switched off, we transfer atoms in the $m = 0$ sub-level state in which atoms are immune against stray magnetic fields and their expansion is not affected by these fields. However, the scattering length is changed from 7.5 $\rightarrow$ 5 nm, and it can modify the evolution in a non-trivial way. The second reason is that our electronic detection saturates when the BEC falls on it. To avoid saturation, we could transfer only a few percent of the total atoms in $m = 0$ state and the rest is swept away by the magnetic field gradient. For the sake of comparison we measure the Thomas-Fermi radii of the non-saturated distributions after time of flight along x and z directions as shown in figure 3.10. We extract the Thomas-Fermii radii of the BEC and the temperature of the thermal cloud by fitting the time of flight density distribution with the gaussian plus inverted parabola function. The extracted values are $R_z(t) = 1.3$ mm and $R_\perp(t) = 9.7$ mm. Also we find the temperature of the residual thermal cloud to be $T \approx 200$ nK.

It is possible to determine independently the number of atoms of BEC on the detector by simply counting them if the saturation could be avoided. For this purpose,

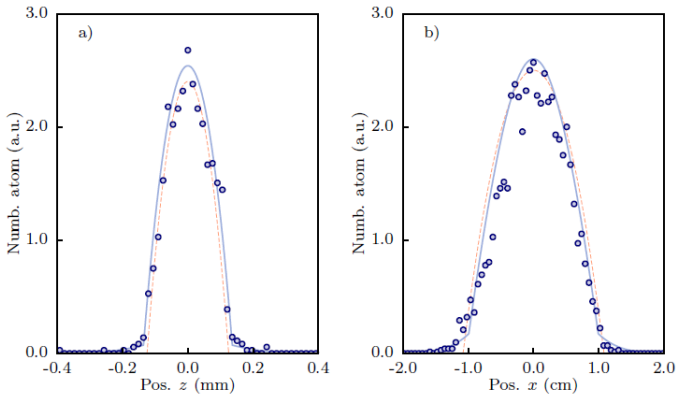

FIGURE 3.10: **Time of flight density profiles (circles) of the condensate along $z-$axis in a and along $x-$axis in b.** The result of the fit by the gaussian plus inverted parabola in two directions is represented by the solid lines.

the BEC's arrival time distribution is broadened by applying a deep moving lattice on the condensate. The typical profile we obtain is shown in figure 3.11 where we plot the distribution before broadening and after broadening. Thus the number of atoms in the BEC is around $N = 5 \times 10^4$ atoms for the detection efficiency estimation $\eta = 0.25(5)$.

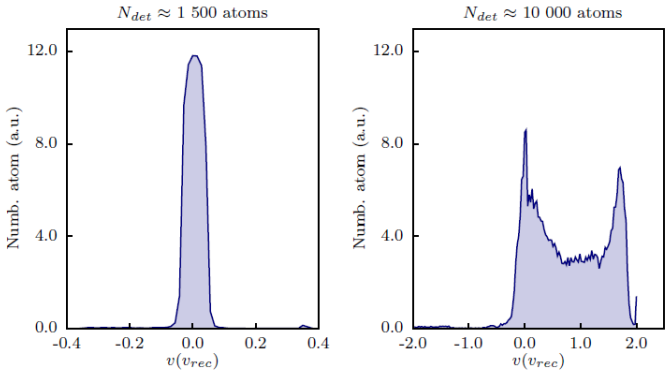

FIGURE 3.11: **Longitudinal density profile of the BEC before and after momentum broadening to estimate the population of the BEC.** The picture on the left is before broadening and on the right it is after broadening. By broadening the momentum of the condensate the saturation of the detector is avoided thus allowing to determine the number of atoms in the BEC.

For $N = 5 \times 10^4$ we estimate the Thomas Fermi radii $R_z(t) = 1.25$ mm and $R_\perp(t) = 10.8$ mm which are not far from the extracted values. The estimated critical temperature is $T_c \approx N^{1/3}\hbar\bar{\omega}/k_B = 600$ nK where $\bar{\omega} = (\omega_z\omega_\perp^2)^{1/3}$ for the trap frequencies $\omega_\perp = 2\pi \times 1275$ Hz and $\omega_z = 2\pi \times 93$ Hz and $N = 5 \times 10^4$ atoms.

To check the purity of the condensate, we measure the second-order auto-correlation of the BEC. We expect a flat correlation function for the pure coherent source suggesting the suppression of the density fluctuations in contrast to the thermal source which is

characterized by the bell shaped function describing the bunching effect. As before the saturation is avoided by transferring a small fraction of the atoms in the condensate in the $m = 0$ state for the correlation measurements. The second-order autocorrelation function is obtained experimentally by evaluating the quantity defined in (3.24). The correlation measurement in y and z directions are depicted in figure 3.12. We see almost a flat correlation confirming our expectations.

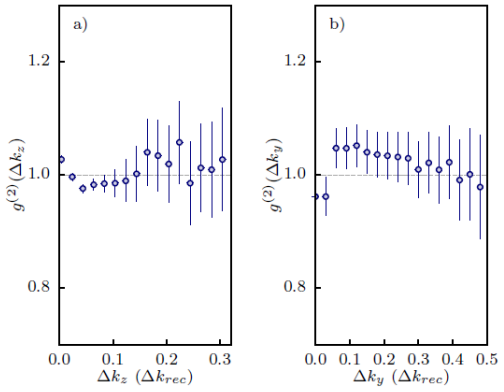

FIGURE 3.12: **The second order normalized auto-correlation function $g^{(2)}$ of the BEC projected in z and y directions.** The fact that it is a flat function with value 1 shows the purity of the BEC source.

Another important test we make on the condensate is the arrival time fluctuations of the BEC. When the condensate is hold merely in the vertical dipole trap, it was observed that the arrival time fluctuated (RMS width of 0.1 ms of the center of the condensate [17]). It results from the initial speed fluctuation of the condensate and can reproduce artificial two-body correlations. Also, for our pair production process, the initial speed of the condensate should be stable to guarantee the stability of the atomic pair velocities. The crossed-dipole trap was the solution to suppress the arrival time fluctuations. In such situation, we measure the fluctuation of the RMS width of 0.04(1) ms (4×10^{-3} v_{rec}) vertically and transversally we have 700(300) μm (2×10^{-2} v_{rec}) which are very close to the resolution of the detector.

In summary, we give the typical parameters of the helium BEC in table 3.3.

Parameters	Value for $\omega_\perp = 2\pi \times 1275$ Hz $\omega_z = 2\pi \times 93$ Hz, $N = 5 \times 10^4$ atoms
Critical temperature T_c (nK)	600
Temperature of residual gas T (nK)	200
Chemical potential μ (kHz)	$2\pi \times 6.4$
Transverse Thomas-Fermi radii $R_\perp$ (μm)	4.4
Vertical Thomas-Fermi radii R_z (μm)	60

TABLE 3.3: BEC parameters

3.2.2 Experimental pair creation and its characterization

3.2.2.1 The set-up and the calibration of 1D-moving optical lattice for the atomic pair creation

Set-up. As it is mentioned in the Chapter 2, we need a moving 1D-optical lattice with a velocity above the threshold value to trigger the atomic pair creation via the dynamical instability. So, the 1D-moving optical lattice is created along the $z-$axis by superposing two laser beams at distinct frequencies ω_t (top beam) and ω_b (bottom beam) with an angle $\theta = 166°$ between the two beams along the $z-$axis as shown in figure 3.13.a. We apply the moving optical lattice at speed $-\frac{\omega_t - \omega_b}{2k_{lat}}$ with k_{lat} the wavenumber of the lattice beams, on the condensate which is hold in the crossed dipole trap. The beam waists are 200 μm which is much larger than the condensate's transverse size $R_\perp = 4.4$ μm to impose transversally uniform intensity profile on the condensate.

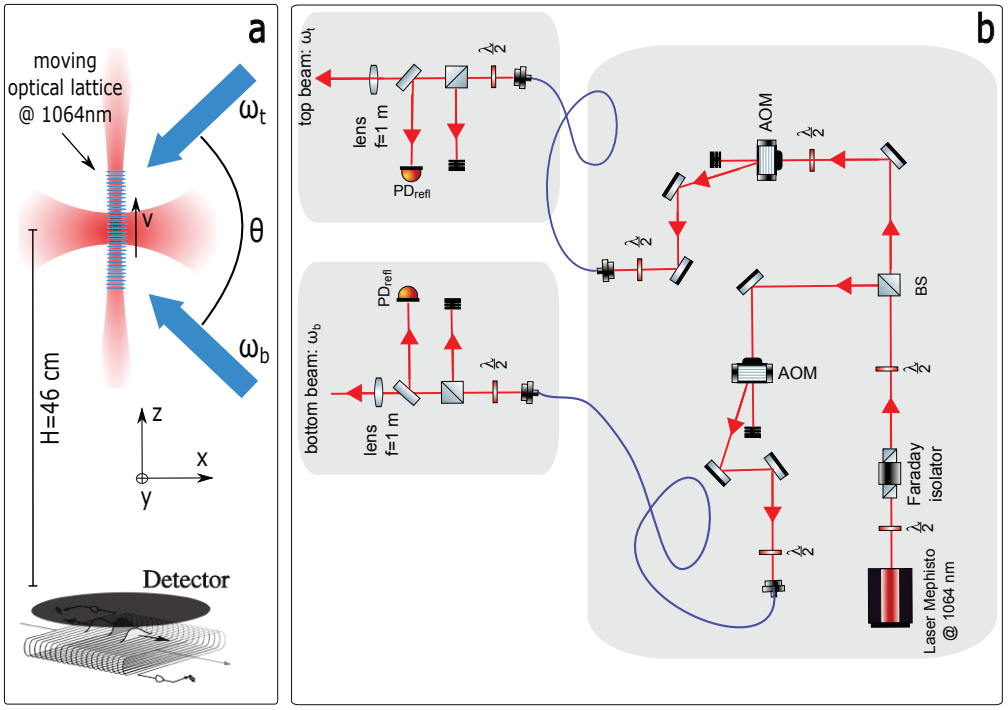

FIGURE 3.13: (a) The 1D-moving optical lattice at 1064 nm for an atomic pair creation is obtained by superposing two laser beams at distinct frequencies ω_t (top beam) and ω_b (bottom beam) with angle $\theta = 166°$ between two beams along the $z-$axis. (b) The optical bench of the top beam and the bottom beam. The two beams originate from the same source and the frequency difference between these two beams is introduced via acousto-optic modulators (AOMs).

Geometrical alignment of the lattice beams on the atoms. To align geometrically the moving lattice beams on the atoms we proceed as following: we release the condensate from the trap and we apply one of the lattice beams with power ~ 50

mW and duration ~ 1 ms on the condensate. Since the beams are blue detuned, the atoms feel a repulsive dipole force that pushes atoms away from the maximum of the light. Consequently, one can observe the effect of light easily by looking at the transverse density distribution of atoms after long time of flight. When the lattice beams are well centered on the condensate, the repulsive potential creates a hole at the center of the transverse density distribution in $xy-$ plane as shown in figure 3.14.

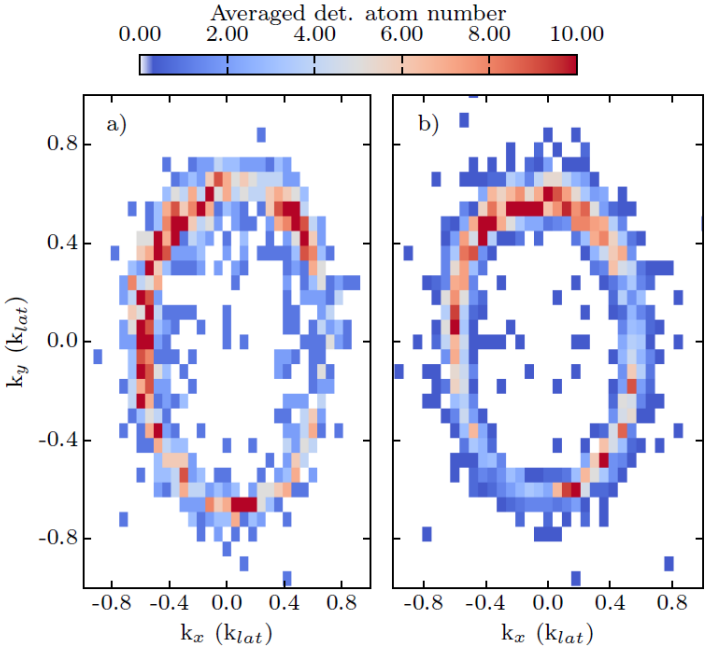

FIGURE 3.14: **Geometrical alignment of the optical lattice beams on the condensate.** By applying each lattice beams independently on the free-falling condensate, the repulsive potential is imposed on the atoms due to the blue detuned dipole force of the light. When a good geometrical alignment is achieved, the repulsive potential creates a hole on the transversal 2D-density distribution of the atoms. The alignment of the the top beam in (a) and the bottom beam in (b).

Alignment of the 1D-optical lattice with the vertical axis. In the experiment, all the physics happen along the $z-$ axis: we create an atomic pair which propagate along the $z-$axis, the Bragg pulses interfere along the $z-$axis, etc. Thus we should make the 1D-moving optical lattice lie perfectly along the $z-$axis. Although, the geometrical alignment method mentioned above is a good indication, it does not guarantee that the 1D-lattice is along the vertical axis. So, for this purpose we diffract the free-falling condensate (after transferring in $m = 0$ by using the Raman transfer) in the Kapitza-Dirac regime using our 1D-lattice. By looking at the momentum of each diffracted order we retrieve the angle of the optical lattice with respect to the $z - axis$ (more details on this method is in the Bragg pulse section

3.3 where we use the same method to determine the angle of the Bragg lattice with respect to the vertical axis). We found that the optical lattice makes 0.16° degrees along $y-axis$ with respect to $z-$axis and 0.34° degrees along $x-axis$ with respect to $z-$axis according to the coordinate system shown in figure 3.13. Although it is difficult to know the necessary precision, we can hope that the atomic pair we create using 1D-moving optical lattice will lie along the $z-$axis up to sufficient degree.

Calibrating the depth of the optical lattice. It has been discussed in the Chapter 2 that the lattice depth modifies the dispersion relation and hence the phase matching condition of the dynamical instability process. Therefore the lattice depth (V_0) should be calibrated and fixed. One can deduce the potential depth from the intensity of the lattice beams according to the relation:

$$V_0 = -\frac{\hbar\Gamma^2 I_0}{2I_{sat}\Delta_{lat}} \tag{3.18}$$

where $\Delta_{lat} = 2\pi c\big(1/\lambda_0 - 1/\lambda_{lat}\big)$. But the more precise calibration is carried out by the measurement of the effective Rabi oscillation (Ω_{eff}) of the Bragg diffraction by the optical lattice which is directly related to the potential depth of the lattice:

$$V_0 = 2\hbar\Omega_{eff} \tag{3.19}$$

In our case, we work with a shallow potential depth which is set to $V_0 = 0.8$ E_{lat} corresponding to the 13.5 mW of power for each beam of the lattice. The calibration of the potential depth measuring the Rabi oscillation works fine as long as we are in the Bragg regime, i.e. $V_0 < 4$ E_{lat}

Adiabatic loading. As it is discussed in Chapter 2, while loading and unloading the condensate in the moving lattice, the free space momenta of the BEC and the atomic pair should be mapped with quasi momenta in the fundamental band of the shallow lattice. It is achieved by switching adiabatically on and off the optical lattice. In other words, we make sure that the switching time of the optical lattice is slower then the period related with the inter-band energies. Experimentally, one can determine easily the time for being adiabatic. It consists of ramping up linearly the lattice depth to its maximum value with duration τ on the condensate and ramping down the lattice symmetrically. If the loading and unloading are non-adiabatic, then diffraction peaks (atoms projected to higher energy bands) will be observed around the arrival time distribution of the condensate as shown in figure 3.15. We see that for durations 25 μs and 50 μs the diffraction peaks do not appear meaning that the adiabatic condition is respected.

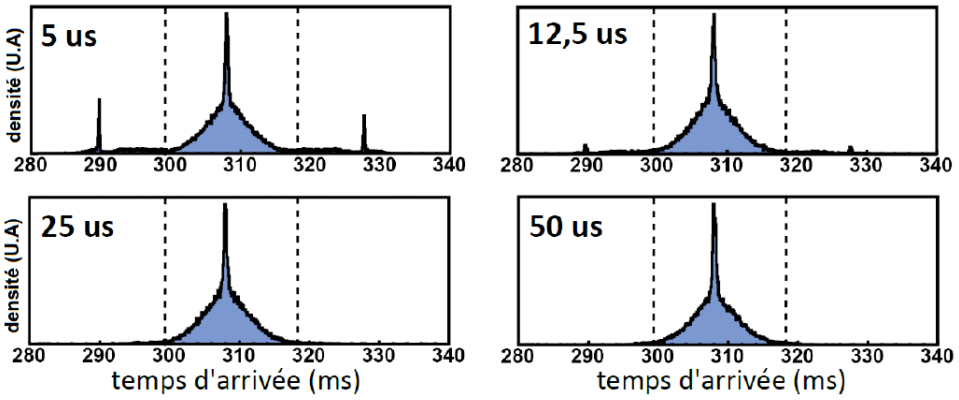

FIGURE 3.15: Test of the adiabatic switching on and off the optical lattice. For duration of 25 μs or longer we do not observe the diffraction peaks indicating the satisfaction of the adiabatic condition. (figure credit to [17]).

Heating by the optical lattice. The potential heating of the atoms results in loss. Heating may come from different sources: spontaneous emission, modulation of the lattice potential due to the vibration of the structure holding the lattice beams, etc. The contribution from the spontaneous emission for a power of 13 mW is [17]:

$$\frac{\mathrm{d}E}{\mathrm{d}t} = 2 \times \Gamma_{sp} \times E_{rec} = 72 \text{ nK} \cdot \text{ s}^{-1} \tag{3.20}$$

where factor 2 is for two beams,

$$\Gamma_{sp} = \frac{\Gamma^3 P_0}{\pi I_{sat} w_{lat}^2 \Delta_{lat}^2} \tag{3.21}$$

and $w_{lat} = 200$ μm. Obviously for a typical duration of the lattice 1 ms, the spontaneous emission has little effect.

The heating due to the modulation of the lattice potential has been found to be non-dominant in [17] for a deep potential depth $V_0 = 18E_{lat}$.

3.2.2.2 Correlation property of the produced atomic pair

Momentum distribution of the atomic pair. We create atomic pair by introducing the frequency difference between the top beam ω_t and the bottom beam ω_b which is controlled using AOMs as shown in figure 3.13.b. It is set to $\delta_{lat} = \omega_t - \omega_b = 2\pi \times 100.5$ kHz ($q_0 = -\frac{m\delta_{lat}}{2\hbar k_{lat}} = -0.57k_{lat}$) and the potential depth is set to $V_0 = 0.8E_{lat}$. These parameters are chosen in such a way that the produced pair can be addressed with the Bragg beams (the angle between the Bragg beams is constraint due to the limited optical access). As it is mentioned before, the population of the atomic pair is controlled by τ_{latt}, the duration of the optical lattice.

For $\tau_{latt} = 350\ \mu$s, the momentum distribution of the experimentally produced atomic pair is plotted in figure 3.16. Referring to the momentum profile of the

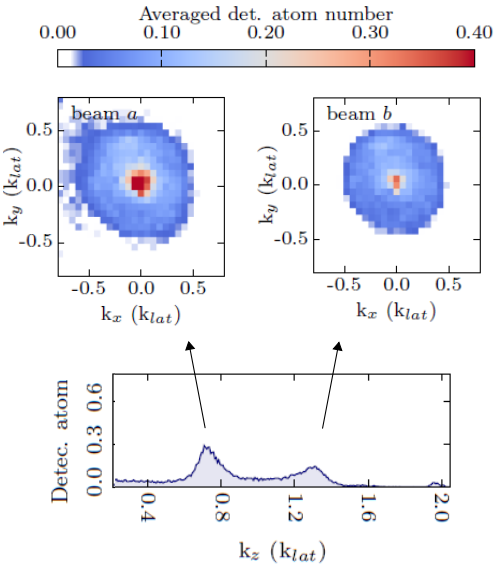

FIGURE 3.16: **Momentum distribution of the atomic pair.** The $z-$axis density profile of the atomic pair. We identify pairs centered at $k_a = 0.73k_{lat}$ and $k_b = 1.27k_{lat}$ (bottom row). Corresponding transverse distribution of the pairs at k_a and k_b where the high gain of the pair production can be seen at the center (top row).

atomic pair along $z-$axis in figure 3.16, we can make few remarks.

- **Width of the momentum distribution**. The momentum width along $z-$axis of the atomic pair a and b can be attributed to the finite width σ_{q_0} of the condensate momentum that has been verified through simulation studies in [87].
- **Anisotropy of the pair population**. There is an anisotropy between the population of the cloud a and b. We suspect that the cloud b might undergo secondary four-wave mixing process with the condensate since it possesses a quasi-momenta greater than the threshold value to trigger the process. We believe that it is a physical process rather than an experimental defect because the same anisotropy has been reported in another group [29].
- **Background noise**. The atomic population between the pair clouds is more stronger than what is expected from the theoretical model including transverse modes [17]. Although we do not have a quantitative answer for this background noise, we suspect that it might result from the collision of the atoms in a and b with the condensate.

Variance of the population difference We have measured $V(N_{k_a}, N_{k_b})$, the normalized variance of the population difference of a and b in the equation (2.82):

$$V(N_{k_a}, N_{k_b}) = \frac{\langle(\hat{N}_{k_a} - \hat{N}_{k_b})^2\rangle - \langle\hat{N}_{k_a} - \hat{N}_{k_b}\rangle^2}{\langle\hat{N}_{k_a} + \hat{N}_{k_b}\rangle} \tag{3.22}$$

to demonstrate the sub-Poissonian fluctuation of the population difference. To do so, we evaluate $V(N_{k_a}, N_{k_b})$ as a function of k by counting number of atoms in the two identical integration volumes $\Omega_V = \left[\Delta k_\perp^2 \times \Delta k_z\right] = \left[0.26^2 \times 0.19\right] k_{rec}^3$ where the first one is centered at k_a and the second one is at k which is scanned around k_b. The result is plotted in figure 3.17. We measure a variance below unity when the second integration volume is centered approximately at k_b indicating sub-Poissonian fluctuations on the number difference. The signal did not descend to 0 due to the limited detection efficiency. In fact, for the detection efficiency η, the normalised variance becomes:

$$V_{det} = (1 - \eta) + \eta V. \tag{3.23}$$

So, in best case scenario, we can attain $V_{det} = 1 - \eta$, which is the case with the experimental data for the estimated detection efficiency $\eta = 25\%$.

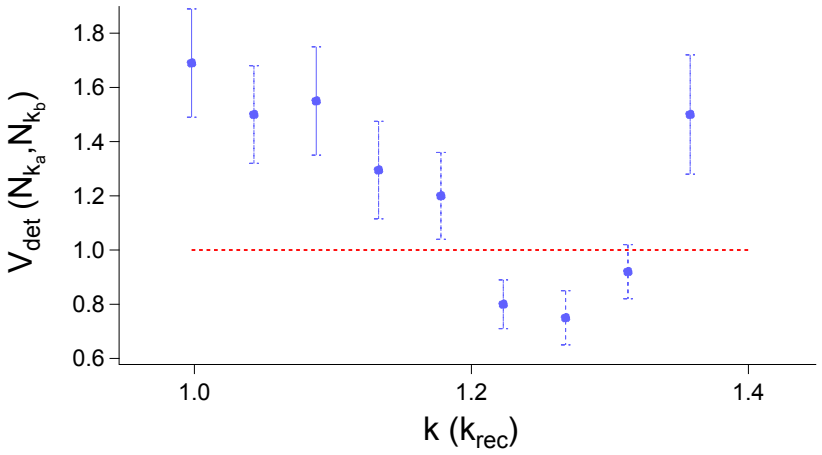

FIGURE 3.17: Measured normalized variance of an atom number difference $V_{det}(N_{k_a}, N_{k_b})$ as a function of k where N_{k_a} is the atomic population inside a volume $\Omega_V = \left[\Delta k_\perp^2 \times \Delta k_z\right] = \left[0.26^2 \times 0.19\right] k_{rec}^3$ centered at k_a while N_{k_b} is the atomic population inside the second identical integration volume which is centered at k. A variance of below unity is observed around $k = k_b$ indicating the sub-Poissonian fluctuation in atom number difference between two diffused modes.

Second order auto-correlation function. We measured $g_{loc}^{(2)}$, the auto-correlation function of the atomic beam a or b independently whose two-mode version is evaluated in the equation (2.93) where it was found that $g_{loc}^{(2)}(k_a, k_a) = g_{loc}^{(2)}(k_b, k_b) = 2$.

For the multi-mode case, we expect that the $g^{(2)}_{loc}$ is a bell-shaped function. Assuming that all modes are equivalent, we can define an integrated version of the 3D auto-correlation function:

$$g^{(2)}_{loc}(\Delta k_x, \Delta k_y, \Delta k_z) = \int_{\Omega_V} \mathrm{d}^3\mathbf{k} \frac{\langle : \hat{n}(\mathbf{k})\hat{n}(\mathbf{k}+\Delta\mathbf{k}) : \rangle}{\langle \hat{n}(\mathbf{k})\rangle\langle \hat{n}(\mathbf{k}+\Delta\mathbf{k})\rangle}. \tag{3.24}$$

where the integration volume Ω_V is taken to be comparable to the momentum distribution width of the atomic beams and $\langle :: \rangle$ indicates normal ordering as before. The integration over $\mathbf{k}$ maximises the signal to noise ratio of the autocorrelation function. We project the 3D autocorrelation function along one axis by integrating over small area in the other two axes. For example, along axes y and z we have (x and y are same since our system is symmetrical transversally)

$$g^{(2)}_{loc}(\Delta k_z) = \int_{\Omega_z} \mathrm{d}\Delta k_x \, \mathrm{d}\Delta k_y \int_{\Omega_V} \mathrm{d}^3\mathbf{k} \frac{\langle : \hat{n}(\mathbf{k})\hat{n}(\mathbf{k}+\Delta\mathbf{k}) : \rangle}{\langle \hat{n}(\mathbf{k})\rangle\langle \hat{n}(\mathbf{k}+\Delta\mathbf{k})\rangle}, \tag{3.25}$$

$$g^{(2)}_{loc}(\Delta k_y) = \int_{\Omega_y} \mathrm{d}\Delta k_x \, \mathrm{d}\Delta k_y \int_{\Omega_V} \mathrm{d}^3\mathbf{k} \frac{\langle : \hat{n}(\mathbf{k})\hat{n}(\mathbf{k}+\Delta\mathbf{k}) : \rangle}{\langle \hat{n}(\mathbf{k})\rangle\langle \hat{n}(\mathbf{k}+\Delta\mathbf{k})\rangle}. \tag{3.26}$$

These two functions are plotted in figure 3.18 where we see that the amplitudes rise for the atoms with small momentum difference. Thus they can be attributed

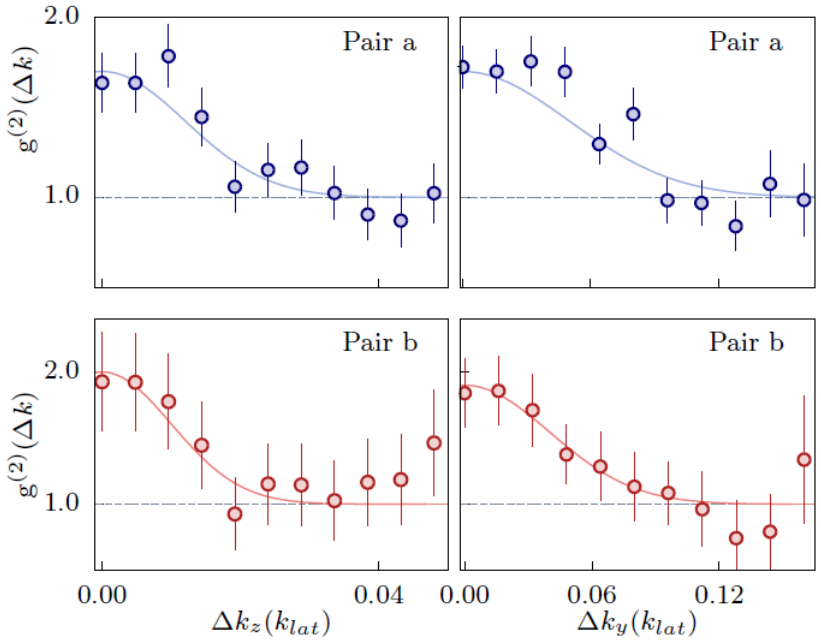

FIGURE 3.18: **Second order auto-correlation function of atomic beams a and b.** Left panel: Auto-correlation functions for a and b along $z-$axis with the area of integration $\Omega_z = [\mathcal{L}_x \times \mathcal{L}_y] = [2 \times 10^{-2}]^2 k^2_{lat}$. Right panel: Auto-correlation functions for a and b along $y-$axis with the area of integration $\Omega_y = [\mathcal{L}_x \times \mathcal{L}_z] = [2 \times 10^{-2} \times 1 \times 10^{-2}] k^2_{lat}$. The solid lines represent the result of the fit by a Gaussian function to extract the mode sizes.(figure credit to [87])

to the same mode for which the value 2 for the amplitude is expected. As can be seen in the figure 3.18, for beam a the amplitude does not reach to 2, which is not well understood at the moment. When the momentum difference gets larger the amplitude of the auto-correlation function drops indicating that the modes are different. This behaviour indicates the fact that the probability of detecting two atoms in the same mode is enhanced as opposed to the multimode case where modes are in competition and thus the probability of detecting two atoms in two different modes at the same time is not expected to get enhanced. So, by measuring the width of the auto-correlation function we can estimate the mode size in a given axis. To measure the mode sizes, we fit the auto-correlation functions in figure 3.18 with a Gaussian function with an offset:

$$g^{(2)}_{loc}(\Delta k_i) = A_i \exp\Big\{-\frac{\Delta k_i^2}{2\sigma_i^2}\Big\} + 1 \qquad i = x, y, z \tag{3.27}$$

where A_i the amplitude and σ_i the half-width at $1/\sqrt{e}$ are the free parameters of the fit. The solid lines in figure 3.18 correspond to the fit result with the fitted values given in table 3.4.

Local	Cloud a	Cloud b
σ_z (k_{lat})	0.012(2)	0.010(2)
σ_y (k_{lat})	0.05(1)	0.04(2)
A_z	0.7(5)	1.00(5)
A_y	0.7(5)	0.90(5)

TABLE 3.4: Fitted parameters of the auto-correlation function of atomic beams a and b (see text)

Estimation of the number of modes. To realise the atomic Bell's inequality test experiment we need to have a multi-mode source at our disposal according to the protocol in figure 3.1. For this purpose we would like to estimate the number of modes in each atomic beam. We know the single mode size from the auto-correlation function width and we can measure the width of the momentum distribution of each atomic beam in figure 3.16. So, the ratio of these two gives an estimation for the number of modes along different axes. We measure the half-width (at $1/\sqrt{e}$) of the density by fitting with a Gaussian function and we get the following values:

$$\begin{aligned} \sigma_{n(k_z)} &= 0.06(1)k_{lat} \\ \sigma_{n(k_\perp)} &= 0.08(1)k_{lat}. \end{aligned}$$

So the ratio of the half-widths of the density and the auto-correlation gives number of modes per atomic beam:

$$\begin{aligned} N_{mode,z} &= 4-8 \\ N_{mode,\perp} &= 1-2 \end{aligned}$$

We find a small number of modes transversally as expected since the phase-matching condition of the four-wave mixing process is principally along $z-$axis. Also we find longitudinally few modes. This is exactly what we would like to have: a multi-mode source along $z-$axis and a single-mode source transversally. Next point we should check is how the longitudinal modes in the beams a and b are correlated with each other. In other words, we should verify that the modes at k_{b+} is correlated with k_{a-} and k_{b-} is correlated with k_{a+} in 3.16.

Inter-mode second-order cross-correlation function. The protocol in the figure 3.1 relies on the fact that the source contains conjugate modes $\{k_{b+}, k_{a-}\}$ and $\{k_{b-}, k_{a+}\}$. In order to show that such conjugate modes exist we looked at the 2D second-order correlation function of a recent data set along $z-$axis defined as:

$$g^{(2)}_{cross}(k_{z,a}, k_{z,b}) = \frac{\langle : \hat{n}(k_{z,a})\hat{n}(k_{z,b}) : \rangle}{\langle \hat{n}(k_{z,a}) \rangle \langle \hat{n}(k_{z,b}) \rangle} \tag{3.28}$$

where $\hat{n}(k_{z,i}) = \int_{\Omega_V} \mathrm{d}^3\mathbf{k}_i \hat{n}(k_{x,i}, k_{y,i}, k_{z,i})$, $i = a, b$ with the integration volume $\Omega_V = [\mathcal{L}_\perp \times \mathcal{L}_z] = [0.4 \times 0.025]k_{lat}^2$. The 2D plot of the $g^{(2)}_{cross}(k_{z,a}, k_{z,b})$ function is plotted in the figure 3.19. The fact that the $g^{(2)}_{cross}(k_{z,a}, k_{z,b})$ function has an elliptic shape with slope of -1 shows that the source contains conjugate modes $\{k_{b+}, k_{a-}\}$ and $\{k_{b-}, k_{a+}\}$ and it is a promising signature of the realisation of the Bell's experiment protocol. The amplitude of the $g^{(2)}_{cross}(k_{z,a}, k_{z,b})$ function does not rise above 2 as predicted by equation (2.94). It is partially due to the size of the integration volume which is taken relatively large to maximise the signal to noise ratio. But even taking small integration volume the cross-correlation function never raised to 2 for the earlier data sets of the atomic pair [87]. It might be due to the secondary losses on beam b as discussed before.

In order to estimate the characteristic widths of the $g^{(2)}_{cross}(k_{z,a}, k_{z,b})$ function, we plot $1D$ projections of the correlation function along the major axis of ellipse: $k_{z,a} + k_{z,b} = 2\ k_{rec}$ and the minor axis of ellipse: $k_{z,b} - k_{z,a} = 0.55\ k_{rec}$ in the figure 3.20. The projections are taken as:

$$g^{(2)}_{\shortparallel}(k_{z,b} - k_{z,a}) = \frac{1}{\mathcal{L}_{\shortparallel}} \int_{-\mathcal{L}_{\shortparallel}}^{\mathcal{L}_{\shortparallel}} g^{(2)}_{cross}(k_{z,a}, k_{z,b})\, \mathrm{d}(k_{z,b} + k_{z,a} - 2k_{rec}) \tag{3.29}$$

and

$$g_{\perp}^{(2)}(k_{z,b}+k_{z,a}) = \frac{1}{\mathcal{L}_{\perp}} \int_{-\mathcal{L}_{\perp}}^{\mathcal{L}_{\perp}} g_{cross}^{(2)}(k_{z,a}, k_{z,b})\, \mathrm{d}(k_{z,b} - k_{z,a} - 0.55 k_{rec}) \tag{3.30}$$

where $\mathcal{L}_{\perp} = \mathcal{L}_{\shortparallel} = 0.007 k_{rec}$. Then we fit $g_{\perp}^{(2)}(k_{z,b}+k_{z,a})$ and $g_{\shortparallel}^{(2)}(k_{z,b}-k_{z,a})$ with the gaussian function of the form $A_{0,i} + A_i e^{-\frac{(k-\mu_i)^2}{2\sigma_i^2}}$ (solid lines in the figure 3.20) where $A_{0,i}, A_i, \mu_i, \sigma_i$ with $i = \shortparallel, \perp$ are free parameters of fit. We find $\mu_{\perp} = 2.003(1)\ k_{rec}$ which corresponds to the phase matching condition $k_{z,b}+k_{z,a} = 2k_{lat}$ and $\mu_{\shortparallel} = 0.573(2)\ k_{rec}$ which is given by the velocity of the moving lattice and compatible with the expected value $\sim 0.56\ k_{rec}$. The widths are $\sigma_{\perp} = 0.0238(1)\ k_{rec}$ and $\sigma_{\shortparallel} = 0.072(2)\ k_{rec}$. The first one is dictated by the width of the gain of the pair production process and the second one gives the idea of the length of the cross correlation between atomic beam a and b. Note that it is on the order of the width of density of a or b.

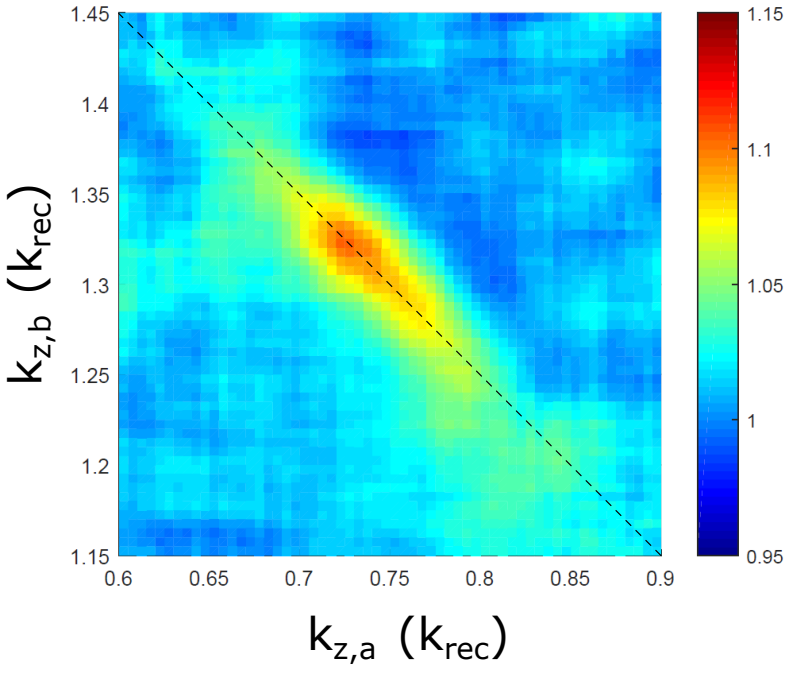

FIGURE 3.19: Plot of the second order inter-mode 2D cross-correlation function $g_{cross}^{(2)}(k_{z,a}, k_{z,b})$. The fact that the $g_{cross}^{(2)}(k_{z,a}, k_{z,b})$ function has an elliptic shape with slope of -1 (dashed line) shows that the source contains conjugate modes $\{k_{b+}, k_{a-}\}$ and $\{k_{b-}, k_{a+}\}$.

Perspective Up to know we have studied an atomic pair source with average number of atoms $\langle n \rangle \sim 0.8$ in the integration volume $\Omega_V = [0.048^2 \times 0.028] k_{lat}^3$ per beam. In order to violate the Bell's inequality, we should work in the low gain regime

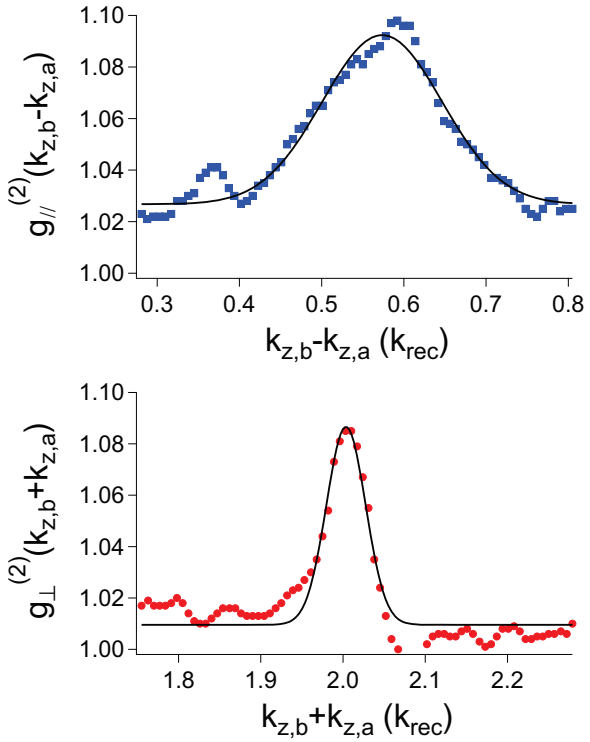

FIGURE 3.20: (top) Plot of $g^{(2)}_{//}(k_{z,b}-k_{z,a})$ (1D projection of $g^{(2)}_{cross}(k_{z,a},k_{z,b})$ along the axis $k_{z,b}-k_{z,a}$) as a function of $k_{z,b}-k_{z,a}$ and (bottom) $g^{(2)}_{\perp}(k_{z,b}+k_{z,a})$ (1D projection of $g^{(2)}_{cross}(k_{z,a},k_{z,b})$ along the axis $k_{z,b}+k_{z,a}$) as a function of $k_{z,b}+k_{z,a}$. The solid lines are the result of gaussian fit function (see text).

$\langle n\rangle \ll 1$ to reduce the probability of having more than two particles in an atomic source per realisation. This regime is still to be investigated experimentally. In this regime, we expect the amplitude of the cross-correlation to increase according to the equation (2.94).

3.3 Bragg pulse preparation

3.3.1 Realisation of the Bragg pulse

Set-up The Bragg pulse is obtained by superposing two laser beams, whose wavelength $\lambda_0 = 1083$ nm, with a 0.8 mm radius flat intensity profile and a relative angle $\theta_B = 32.5°$ (determined by the Kapitza-Dirac method discussed in the following) along the $z-$axis. The two laser beams of the Bragg pulse form a 1D optical lattice and coherently diffract atoms along the $z-$axis. The momentum transferred to the diffracted atoms is

$$\Delta k_B = 2k_{rec}\sin(\frac{\theta_B}{2}) = 0.559k_{rec} \tag{3.31}$$

where $k_{rec} = \frac{2\pi}{\lambda_0}$. Both Bragg beams are linearly polarized ($\pi-$polarized) and are red-detuned by $2\pi \times 600$ MHz from the atomic transition $2^3S_1 - 2^3P_0$ as shown in figure 3.21.

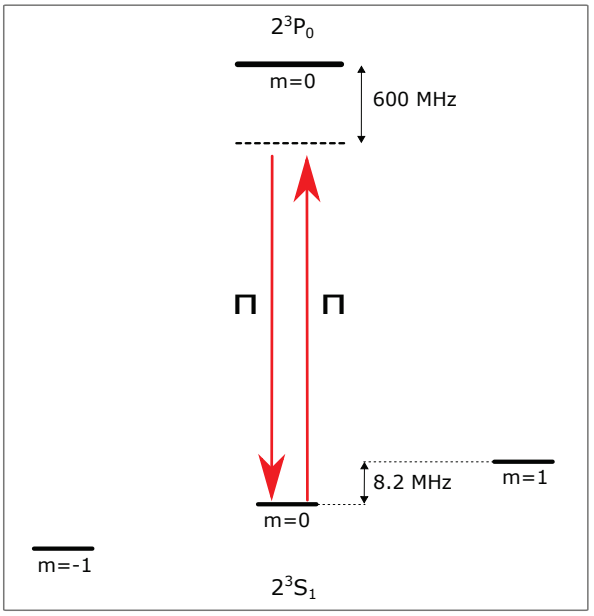

FIGURE 3.21: Bragg diffraction using off-resonant two $\pi-$polarized laser pulses which are red detuned by 600 MHz from the $2^3S_1(m=0) \rightarrow 2^3P_0(m=0)$ transition. The zeeman sublevels of the 2^3S_1 have the energy splitting 8.2 MHz corresponding to a magnetic bias field ~ 3 G.

Alignment of the Bragg lattice with the $z-$axis We need to guarantee that the lattice created by the Bragg pulse lies along the vertical $z-$axis as we have done for the moving optical lattice since we have decided to perform the experiment along this axis. The alignment is carried out by diffracting condensate into many diffraction orders in the Kapitza-Dirac regime [78] using a very strong and very short pulse of the Bragg beams. An example of such a diffraction is illustrated in figure 3.22. In the top panel we see the momentum distribution on the k_zk_x-plane and k_zk_y- plane of the diffracted orders which are spaced by Δk_B along $z-$axis as expected. The spacing of the diffracted orders allows us to measure precisely the Δk_B for which we find $0.559(8)k_{rec}$. To determine the angle of the lattice created by the Bragg beams with respect to the vertical axis, we retrieve the average momentum of each diffracted order along the 3 axes and we make a plot of $k_x(k_y)$ vs k_z from the retrieved numbers as shown in the bottom panel of the figure 3.22. The slope of each plot gives the angle of the lattice with respect to the vertical along the corresponding axis, i.e. the slope of the k_x vs k_z plot gives the angle $(\theta_{B,x})$ of the lattice along $x-$axis and the slope of the k_y vs k_z plot gives the angle $(\theta_{B,y})$ of the lattice along $y-$axis with respect to the vertical. We measure

$\theta_{B,x} = 0.79(1)°$ and $\theta_{B,y} = 1.35(1)°$ from the data in figure 3.22. Experimentally, we could correct these angles by iteratively aligning and measuring the angles with the mentioned method to obtain a Bragg lattice aligned with vertical.

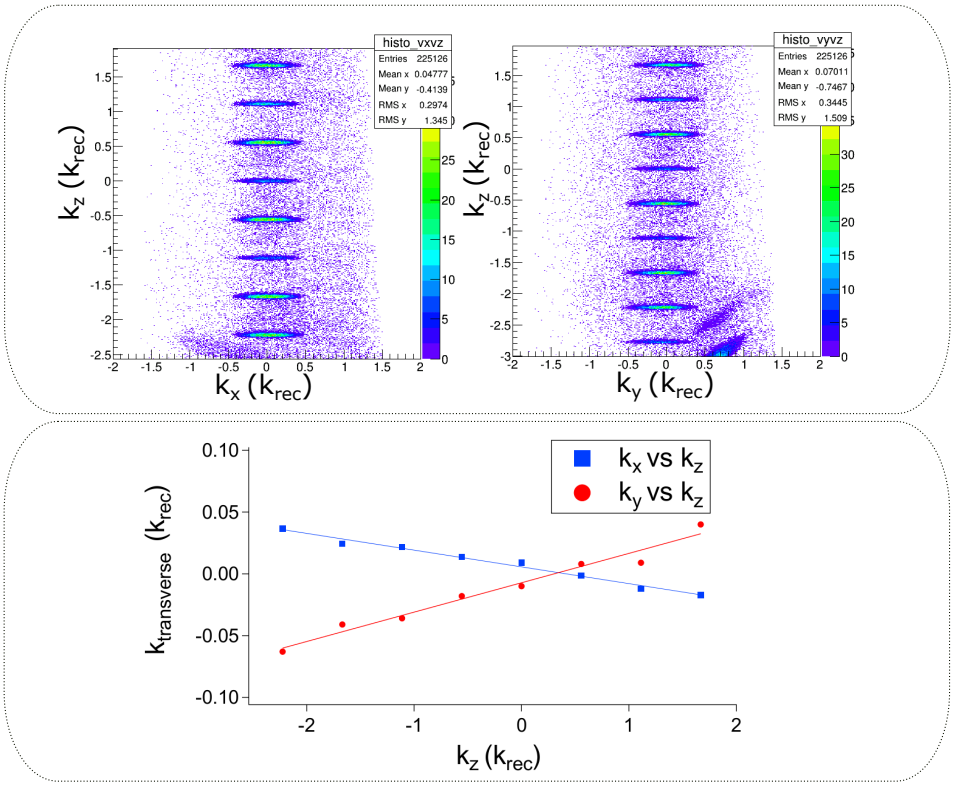

FIGURE 3.22: Measuring the angle of the lattice, created by the Bragg beams, with respect to the vertical axis using Kapitza-Dirac diffraction. Momentum distribution of the diffracted orders of the condensate on the $k_z k_x-$plane and $k_z k_y-$plane (top panel). Corresponding plots of the average momentum of the diffracted orders (bottom panel). Slope of these plots give the angle of the Bragg lattice with respect to the $z-$axis.

Bragg diffraction For the purpose of calibration, we apply the Bragg pulse on the condensate (N_0 atoms) to diffract it from the state $|\phi_{k_0}\rangle$ to the state $|\phi_{k_0+\Delta k_B}\rangle$. As we have seen in Chapter 2, the populations of these states evolves with the duration of the Bragg pulse, in other words, they will oscillate with the effective Rabi frequency:

$$N_{k_0+\Delta k_B}(t) = N_0 \frac{|\Omega_{eff}|^2}{|\Omega_{eff}|^2 + \delta^2} \sin^2\left(\sqrt{|\Omega_{eff}|^2 + \delta^2}\frac{t}{2}\right) \tag{3.32}$$

$$N_{k_0}(t) = N_0 - N_{k_0+\Delta k_B}(t). \tag{3.33}$$

with initial condition $N_{k_0+\Delta k_B}(t=0) = 0$ and $N_{k_0}(t=0) = N_0$. Note that only at the resonance condition $\delta = 0$ we can have a 100% population exchange. So,

we should find the resonance which is defined as (from (2.121)):

$$\delta = \left(\frac{\hbar(k_0)^2}{2m} - \frac{\hbar(k_0 + \Delta k_B)^2}{2m}\right) - (\omega_1 - \omega_3) \tag{3.34}$$

where ω_1 and ω_3 are the frequencies of the top and bottom Bragg laser beams respectively. So, the resonance condition ($\delta = 0$) for the atoms with momentum k_0 is given by:

$$\omega_1 - \omega_3 = -\frac{\hbar}{2m}\Delta k_B(2k_0 + \Delta k_B) \tag{3.35}$$

suggesting that the resonance condition depends on the frequency difference between the two beams of the Bragg pulse which is very well controlled in the experiment. The transfer efficiency of the Bragg pulse η_B is defined as

$$\eta_B(t) = \frac{N_{k_0+\Delta k_B}(t)}{N_{k_0+\Delta k_B}(t) + N_{k_0}(t)}. \tag{3.36}$$

In order to find the resonance condition experimentally we look at this quantity $\eta_B(t = \frac{3\pi}{2|\Omega_{eff}|})$ by fixing the Bragg pulse duration to $t = \frac{3\pi}{2|\Omega_{eff}|}$ and by scanning the frequency difference $\omega_1 - \omega_3$ of the Bragg laser beam which is applied just after the Raman transfer. We expect that at resonance this quantity attains its maximal value. We predict to find the resonance for $k_0 = k_{Raman} = 0.2k_{rec}$ (the momentum acquired during Raman transfer, see Appendix C) at:

$$\omega_1 - \omega_3 = -\frac{\hbar}{2m}\big(\Delta k_B(2k_0 + \Delta k_B)\big) = -2\pi \times 22.8 \text{ kHz}$$

This value is relatively in good agreement with what is found experimentally as shown in figure 3.23 where we plot $\eta_B(t = \frac{3\pi}{2|\Omega_{eff}|})$ as a function of the $\omega_1 - \omega_3$. We find the peak centered at $-2\pi \times 23.27(6)$ kHz.

Another important issue regarding the resonance is the gravity. The free-falling condensate acquires velocity due to the gravitational acceleration. To stay at the resonance during the Bragg pulse application time we sweep the frequency difference with the rate $g\Delta k_B = 5.0$ kHz/ms. We verified this value experimentally by using the same Bragg pulse above with duration $t = \frac{3\pi}{2|\Omega_{eff}|}$ but we apply it 2 ms later than before (2 ms after Raman transfer). We look at the diffraction efficiency $\eta_B(t = \frac{3\pi}{2|\Omega_{eff}|})$ as a function of the rate of the linear chirp which is plotted in figure 3.24. By fitting the experimental data (red points) by a Gaussian fit (solid line) we find a rate of the linear chirp 4.96(5) kHz/ms which is in a good agreement with the predicted rate.

Having established the resonance condition, we look next to the two photon Rabi oscillation $|\Omega_{eff}|$. For this purpose, we measure $\eta_B(t)$ defined in equation 3.36 as a function of t at resonance and compensating the effect of gravity. We apply the

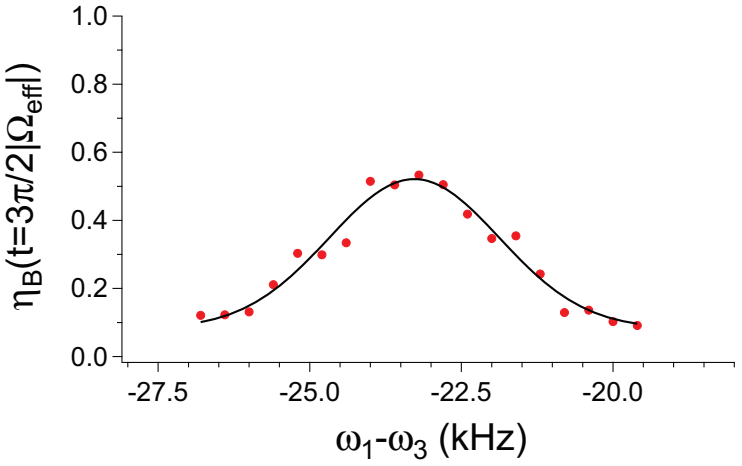

FIGURE 3.23: **BEC Bragg diffraction resonance**. We measure $\eta_B(t = \frac{3\pi}{2|\Omega_e ff|})$ as a function of the laser beams' frequency difference $\omega_1 - \omega_3$. At the resonance frequency the quantity $\eta_B(t = \frac{3\pi}{2|\Omega_e ff|})$ achieves to its maximum. We see a resonance frequency at $-2\pi \times 23.27(6)$ kHz with the expected FWHM value of 3.3(2) kHz. Here we are only interested in the center frequency, the amplitude and width will be studied more in detail later. (Dots are the experimental data and solid line is the gaussian fit to retrieve the resonance frequency.)

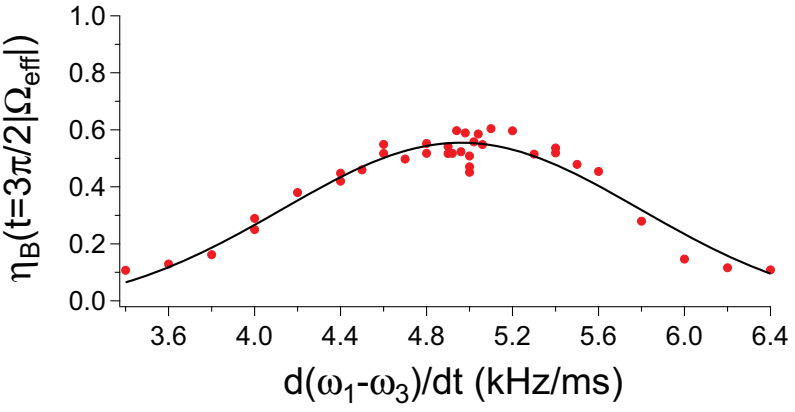

FIGURE 3.24: **Compensating Bragg resonance shift due to the gravity.** Plot of the experimental diffraction efficiency $\eta_B(t = \frac{3\pi}{2|\Omega_e ff|})$ versus the rate of the linear chirp of the frequency difference of the Bragg beams. The Bragg pulse is applied 2 ms after the Raman transfer. The solid line corresponds to the gaussian fit whose center is at 4.96(5) kHz/ms.

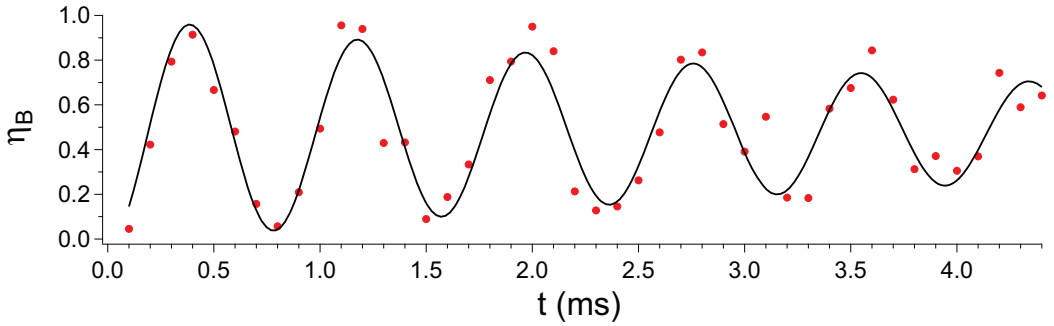

FIGURE 3.25: **Two photon Rabi oscillation with each Bragg laser beam power at 12 μW.** The solid line is the result of the fit function $f(t)$ (see text).

Bragg beams for time t on the condensate by setting their power to 12 μW. The Bragg beams are applied as square pulse by switching on and off rapidly the beams using AOMs (measured turn off time $\sim$ 500 ns). The result is plotted in figure 3.25. Each point is obtained from the single experimental realisation and we have considered only atoms longitudinally inside (not to be limited by the selectivity of the Bragg pulse) $|k_0 + \Delta k_B| < 0.0025 k_{rec}$ and $|k_0| < 0.0025 k_{rec}$ and transversally we consider all the atoms. To retrieve the Rabi oscillation, we fit the experimental points by the following function:

$$f(t) = f_0 + A\sin(\omega t + \phi_0)e^{-\Gamma_{dec}t} \tag{3.37}$$

by leaving parameters f_0, A, ω, ϕ_0 and Γ_{dec} as free parameters of the fit. We find the experimental value of the Rabi frequency $\omega = 2\pi \times 1.25$ kHz which is in good agreement with the theoretical prediction for the given power 12 μW of the Bragg beams:

$$|\Omega_{eff}| = \frac{\Gamma^2 I_0 d_{0,0}^2}{4 I_{sat}\Delta} = 2\pi \times 1.26 \text{ kHz} \tag{3.38}$$

where the dipole matrix element associated to the transition in the figure 3.21 is $d_{0,0} = \frac{1}{\sqrt{(3)}}$. The fact that these two values are compatible shows that the Bragg beams are well aligned on the atoms. We measure experimental decoherence rate $\Gamma = 0.19$ ms^{-1} which is greater than the rate of the spontaneous emission of two Bragg beams:

$$\Gamma_{sp} = \Gamma \frac{s}{s + 1 + (\frac{2\Delta}{\Gamma})^2} = 0.06 \text{ ms}^{-1}. \tag{3.39}$$

The reason of the experimental decoherence is not well established, we know that it does not depend on the intensity of the beams. But in any case it is encouraging to see the coherence time going beyond the 4 ms because in the experiment we are interested in the first oscillation to realise atomic mirror $t = \frac{\pi}{|\Omega_{eff}|}$ and the beamsplitter $t = \frac{\pi}{2|\Omega_{eff}|}$. Another interesting point is that experimentally the

reflection coefficient of the atomic mirror can go up to $\eta_B(t = \frac{\pi}{|\Omega_{eff}|}) = 0.95(6)$ (from the fit, we have $f_0 + A = 0.99(6)$).

Controlling the phase. When realizing the atomic Bell's inequality test experimental sequence in figure 3.1, we have chosen to apply a single atomic mirror pulse which is not selective in mode and two simultaneous atomic beamsplitters which are selective in modes. The reason is that such scheme provides a very easy control of the phase of the Bragg beams. Specifically, since the atomic mirror is the same for all modes it does not introduce any phase difference between the two interferometers in figure 3.1. Therefore, the result of the correlation coefficient calculation in (2.133) does not depend on the atomic mirror phase meaning that we do not need to control the phase of the atomic mirror. Experimentally, for the atomic mirror we inject the frequency ω_1 to the Bragg top beam and the frequency ω_3 to the Bragg bottom beam which creates a single optical lattice beam (figure 3.26.(left panel)). On the other hand, we have seen that the correlation coefficient does depend on the phase difference $\theta_+ - \theta_-$ between two atomic interferometers in the scheme 3.1 and this phase difference is given by $\theta_+ - \theta_- = \Delta\Phi = \Delta\Phi^+_{\pi/2} - \Delta\Phi^-_{\pi/2}$ which is the phase difference between the two atomic beamsplitters represented by $S^+_{\pi/2}$ and $S^-_{\pi/2}$ in the figure 2.15. Thus we should control the phase difference $\Delta\Phi$. In the experiment, for the atomic beamsplitter we inject two frequencies ω_1 (phase φ_1) and ω_2 (phase φ_2) to the Bragg top beam and the single frequency ω_3 (phase φ_3) to the Bragg bottom beam which creates a double optical lattice (figure 3.26.(right panel)). From now on we represent the lattice created by $\{\omega_1, \omega_3\}$ with $S^+_{\pi/2}$ and by $\{\omega_2, \omega_3\}$ with $S^-_{\pi/2}$. So, the phase difference is

$$\begin{aligned} \Delta\Phi^+_{\pi/2} &= \varphi_1 - \varphi_3, \\ \Delta\Phi^-_{\pi/2} &= \varphi_2 - \varphi_3, \\ \Delta\Phi &= \Delta\Phi^+_{\pi/2} - \Delta\Phi^-_{\pi/2} = \varphi_1 - \varphi_2. \end{aligned}$$

The result says that we have to control just the frequency difference between the two frequencies in the top beam of the Bragg pulse. Controlling the phase of an optical beam is not an easy task since changes in temperature, mechanical vibrations of the optical elements can easily make fluctuate the phase and locking the phase of the laser beam in some cases gets complicated when the feedback signal is not easily achievable. But, if the two frequencies coexist in the same laser beam and they are applied at the same time, all the phase fluctuations are common during the laser propagation, and it turns out that the phase difference $\varphi_1 - \varphi_2$ is very well controlled.

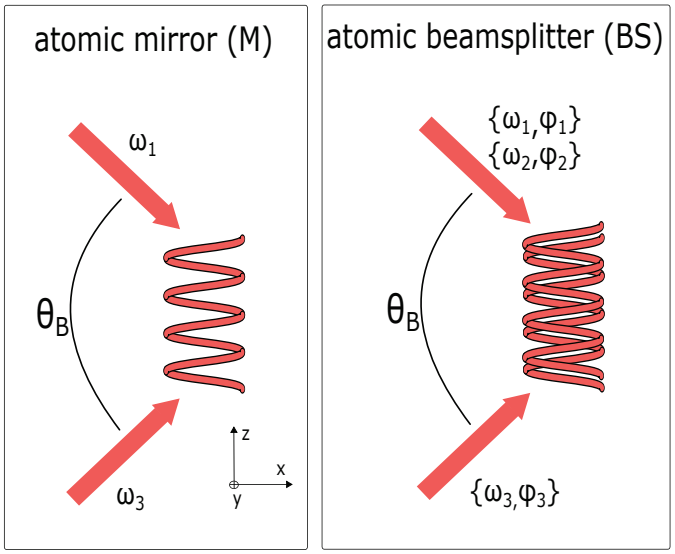

FIGURE 3.26: **Atomic mirror and beamsplitter Bragg pulse.** The Bragg pulse consists of two laser beams with relative angle θ_B between them which diffracts atoms along $z-$axis. The atomic mirror consists of single lattice made of ω_1, ω_3 while the atomic beamsplitter is made of two lattices ω_1, ω_3 and ω_2, ω_3. For the Bell's inequality test, we need to control only the phase difference between the two beamsplitter lattices, i.e. $\varphi_1 - \varphi_2$.

Selectivity of the atomic beamsplitter. Using two Bragg lattices is indeed a good idea to control the phase but we should make sure that we can address the different modes of the atomic pair when applying two lattices simultaneously. To clarify this point, referring to the scheme 3.1, we see that the beamsplitter $S^{+}_{\pi/2}$ is interfering modes k_{b+} and k_{a+} and the beamsplitter $S^{-}_{\pi/2}$ is interfering modes k_{b-} and k_{a-}. The transfer functions of $S^{+}_{\pi/2}$ and $S^{-}_{\pi/2}$ are defined as

$$\eta_{S^{+}_{\pi/2}}(\delta_+) = \eta_B(t = \frac{\pi}{2|\Omega_{eff}|}) = \frac{|\Omega_{eff}|^2}{|\Omega_{eff}|^2 + \delta_+^2} \sin^2\left(\sqrt{|\Omega_{eff}|^2 + \delta_+^2}\frac{\pi}{4|\Omega_{eff}|}\right)$$

$$\eta_{S^{-}_{\pi/2}}(\delta_-) = \eta_B(t = \frac{\pi}{2|\Omega_{eff}|}) = \frac{|\Omega_{eff}|^2}{|\Omega_{eff}|^2 + \delta_-^2} \sin^2\left(\sqrt{|\Omega_{eff}|^2 + \delta_-^2}\frac{\pi}{4|\Omega_{eff}|}\right)$$

where the resonance condition $\delta_+ = 0$ is centered at k_{a+} implying $\omega_1 - \omega_3 = -\frac{\hbar}{2m}\big(\Delta k_B(2k_{a+} + k_B)\big)$ and the resonance condition $\delta_- = 0$ is centered at k_{a-} implying $\omega_2 - \omega_3 = -\frac{\hbar}{2m}\big(\Delta k_B(2k_{a-} + k_B)\big)$. The $\eta_{S^{+}_{\pi/2}}$ and $\eta_{S^{-}_{\pi/2}}$ have a finite width in momentum and the widths are proportional to the Rabi frequency Ω_{eff}. The lower the Rabi frequency is, the smaller the widths become. Experimentally, firstly, we need to avoid the overlap of the transfer functions and secondly, we need to isolate modes $k_{a+}, k_{a-}, k_{b+}, k_{b-}$ since the Bell's protocol is based only on these modes and having additional modes will ruin the signal. The idea is to check experimentally if we can arrange the width of the transfer function comparable

to the width of the mode given in the table 3.4. In figure 3.27, we represent schematically the transfer functions of $S^{+}_{\pi/2}$ and $S^{-}_{\pi/2}$ superposed on the vertical momentum distribution of the atomic pair presented before in the figure 3.16. The

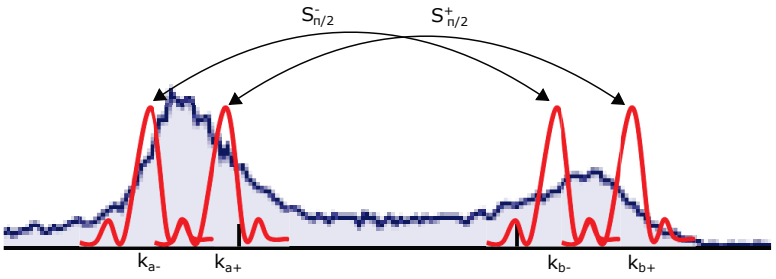

FIGURE 3.27: Schematic representation of the transfer functions of the atomic beamsplitters $S^{+}_{\pi/2}$ and $S^{-}_{\pi/2}$ addressing different vertical modes of the atomic pair.

rest of this Chapter is devoted to the experimental validation of the phase control and the selectivity of the atomic beamsplitters.

3.3.2 Atomic beamsplitter: selectivity test

For the purpose of the test of the selectivity we work only with a single beamsplitter made of ω_1 and ω_3. The power of each Bragg beam is set to 5 μW corresponding to the Rabi frequency $|\Omega_{eff}| = 2\pi \times 0.52$ kHz for which we expect a satisfactory selectivity of the beamsplitter transfer function. To obtain the experimental transfer function of the beamsplitter, we do the following procedure: we heat the condensate by modulating the horizontal dipole trap close to the parametric resonance which provides atoms having sufficiently large momentum distribution but not as large as the momentum distribution of thermal cloud which would cause a problem in identifying diffracted and non-diffracted clouds of atoms. Next, we apply the atomic beamsplitter ($t = \frac{\pi}{2|\Omega_{eff}|} \sim 500$ μs) and we measure the transfer function from the population ratio as in equation (3.36) but this time resolving in momentum, that is counting the number of atoms inside a box of size 0.005 k_{rec}. We average ~ 200 realisations to obtain the experimental transfer function. We plot it together with its theoretical estimation as a function of the atomic momentum where 0 corresponds to the resonance momentum in the figure 3.28. The theoretical function is obtained from the equations (3.33) and (3.32) by fixing $|\Omega_{eff}| = 2\pi \times 0.52$ kHz and $t = 500$ μs. The half-width 0.0210(5) k_{rec} at half maximum of the measured beamsplitter transfer function is small enough to ensure that two beamspiltters will not overlap when applied on the atomic pair with the density half-width $0.06k_{rec}$ with $k_{a+} - k_{a-} = k_{b+} - k_{b-} = 0.12k_{rec}$. Also, we can expect the amplitude of the transfer function on average stay between 0.45 and 0.5 for the momentum interval $-0.01k_{rec}$

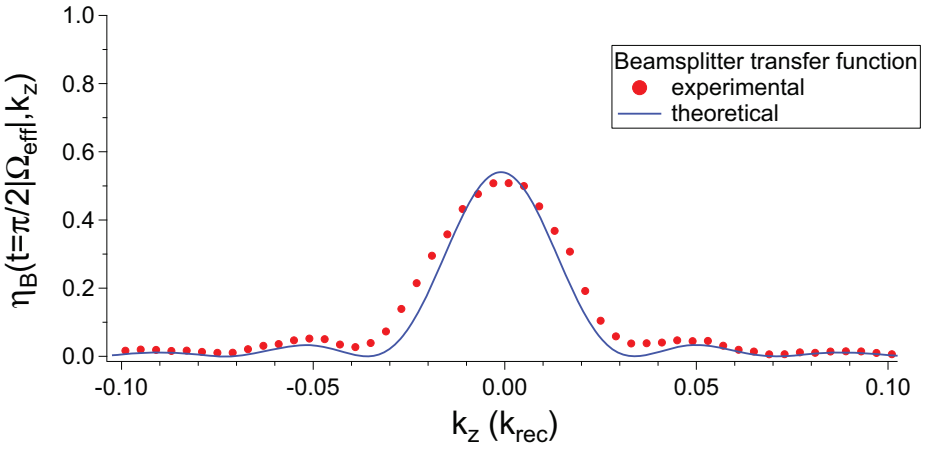

FIGURE 3.28: Schematic of the transfer function of the atomic beamsplitter: experimental (in red)(obtained by averaging 200 realisations) and theoretical (in black) as a function of the vertical momentum k_z with 0 corresponding to the resonance momentum.

and $0.01k_{rec}$ which corresponds to the single mode size. So, we have a rather satisfactory result in terms of selectivity. However, we see that the measured transfer function is enlarged with respect to the theoretically predicted one. We suspected two reasons of this difference: first it could the intensity of the Bragg beams fluctuate and secondly the phase of the Bragg beams $\varphi_1 - \varphi_3$ could fluctuate and hence change the resonance position. These effects are also translated to the fluctuation of the amplitude of the beamsplitter transfer function. The statistical distribution of the amplitude of the beamsplitter transfer function at the resonance position $|k_z| < 0.0025$ over several experimental realisations is shown in the figure 3.29. The standard deviation of the fluctuation equals to 0.085(5). This means that the beamsplitter resonance amplitude will fluctuate between 0.58 and 0.42.

So we have decided to quantify the intensity and the phase fluctuations of the Bragg beams. First the optical intensity fluctuation originating mainly from the laser amplifier will be discussed and later the phase fluctuation due to vibrations of the turbo pumps will be explained.

3.3.2.1 Intensity fluctuation of the Bragg beams

We measured the intensity fluctuation of the Bragg beams closer to the laser source since we had a doubt about the laser amplifier. The optical bench of the Bragg beams is illustrated in the figure 3.30 where we start from a diode laser at 1083 nm. Its frequency is locked using a helium cell to 200 MHz red detuned from the transition $2^3S_1 - 2^3P_0$. The laser is then amplified and splitted into three: 1 Raman beam and 2 Bragg beams. 2 Bragg beams double pass the AOMs and are sent to the science chamber. It is via

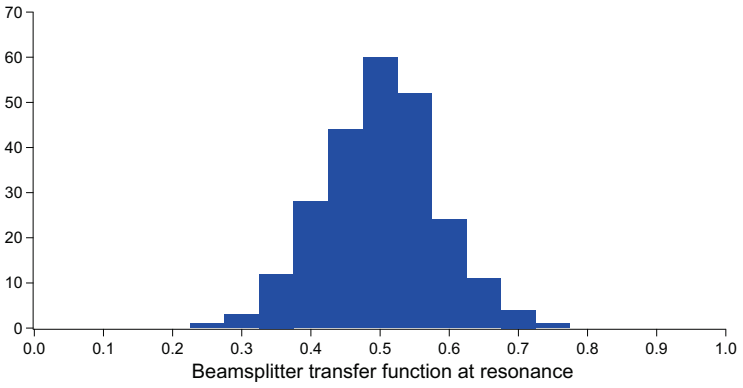

FIGURE 3.29: The distribution of the amplitude of the transfer function of an atomic beamsplitter at resonance momentum. The standard deviation of the distribution equals to 0.085(5) and its mean value is 0.500(3).

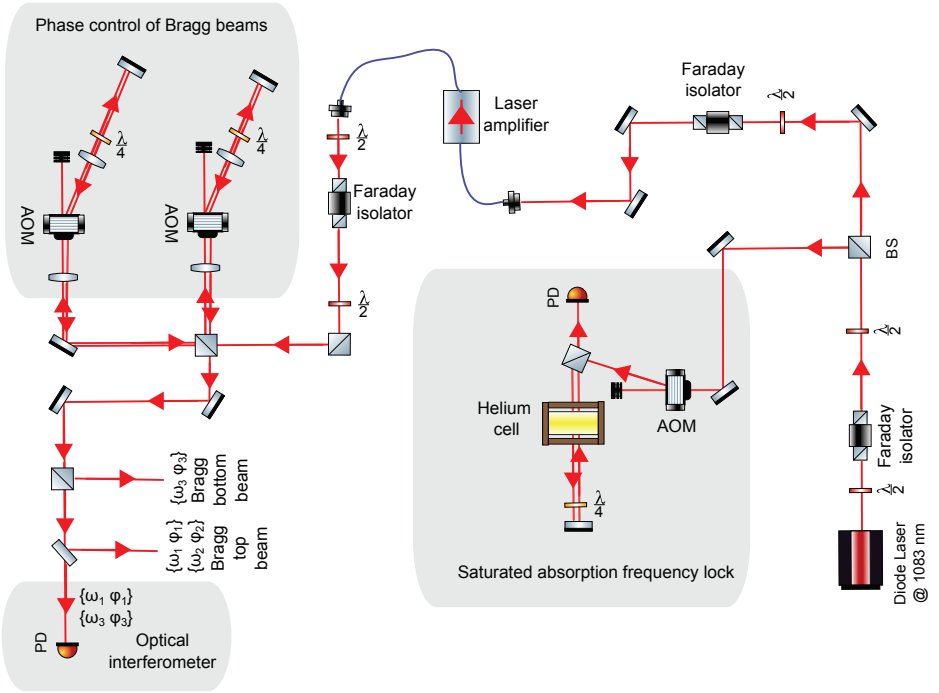

FIGURE 3.30: Optical bench of the Bragg laser beams before the implementation of the intensity lock (see text).

the AOMs that we control the frequency of the Bragg beams. As it is clear from the optical bench of the Bragg beams, we did not have initially any intensity lock. So, we surveyed the laser intensity before and after the laser amplifier at the same time. We plot the intensity as a function of time in figure 3.31. The intensity of the diode laser is rather stable and no correlation of the noise between the amplifier and the laser is apparent. But, we had clearly a big problem with the laser amplifier. It exhibited very brutal jumps of 20% in relative amplitude and the time constant of intensity jumps were on the order of $\sim$ 1 ms. To correct the intensity fluctuation first we maximized the

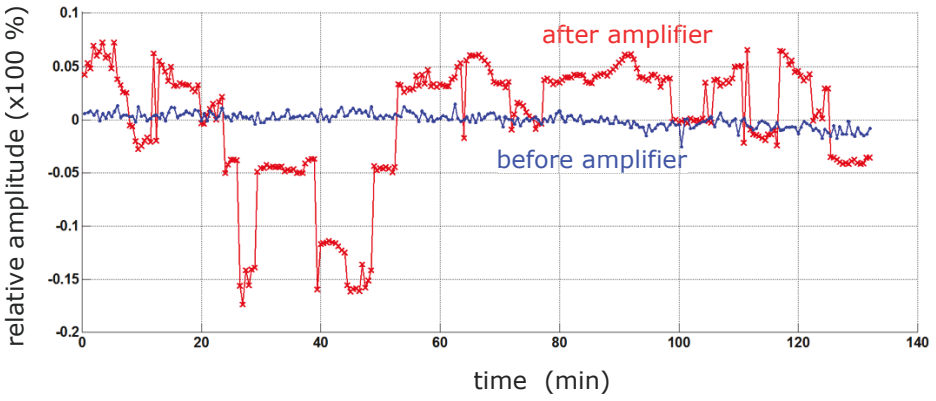

FIGURE 3.31: **Intensity survey of the Bragg beams before and after the laser amplifier**. The relative fluctuations in percentage is shown. The intensity of the laser after amplifier exhibits very brutal jumps of 20% in relative amplitude.

intensity at the input of the laser amplifier. The effect was that the brutal jumps of the intensity after the amplifier are more smoothed but the slow drift in intensity persists. So, we decided to lock the output optical intensity of the laser amplifier. For this purpose the AOM of the frequency lock is removed and placed after the laser amplifier in order to act on the optical intensity. The new optical bench now looks like as in the figure 3.32. We use the home made proportional-integral controller (PI) [74] to modulate the intensity of the RF signal of the AOM as a function of the feedback photodiode signal. The achieved bandwidth of the system is about 1 kHz. The optical intensity is surveyed independently via the photodiode of the optical interferometer.

We compare the intensity with and without the lock in the figure 3.33 where in the former case we see that a very impressive stability is established.

Having dealt with the intensity, next we look at the phase fluctuation of the Bragg laser beams.

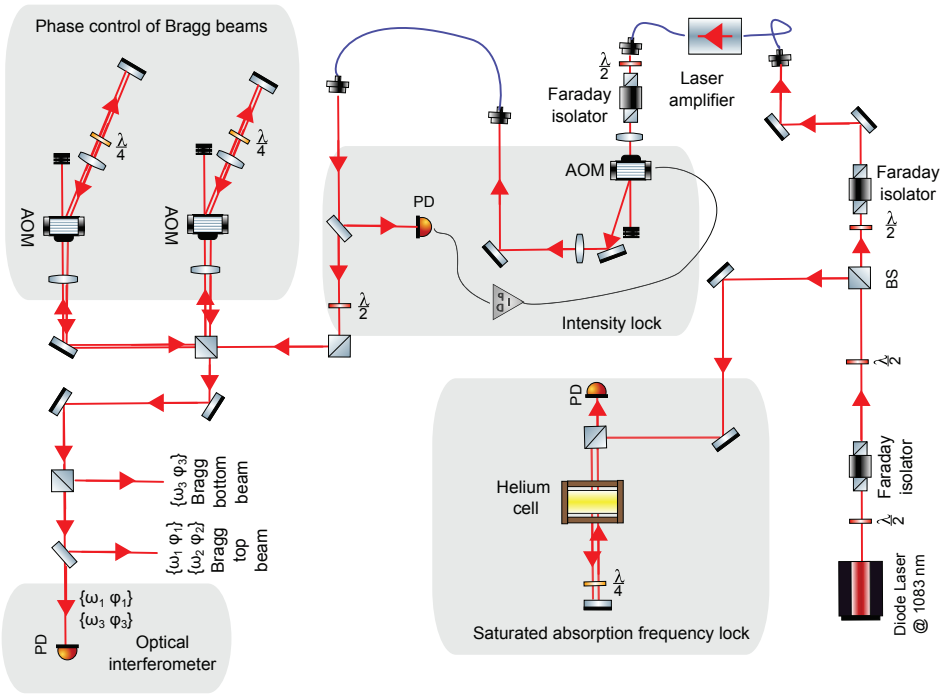

FIGURE 3.32: Optical bench of the Bragg laser beams after the implementation of the intensity lock (see text).

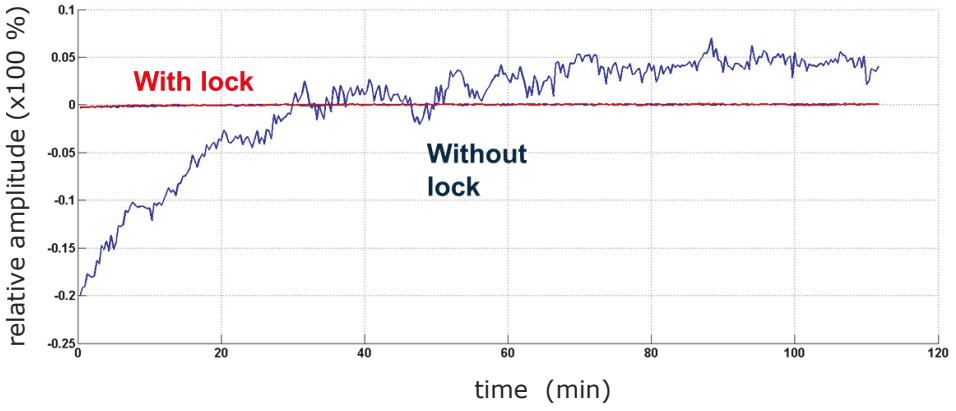

FIGURE 3.33: Comparison between the intensity surveys with and without the intensity lock. The optical intensity is surveyed independently by the optical interferometer photodiode.

3.3.2.2 Fluctuation of the phase $\varphi_1 - \varphi_3$

We measure the fluctuation of $\varphi_1 - \varphi_3$ using two methods. The first method consists in using the optical beating signal collected on the optical bench shown in figure 3.32. Remember that for these measurements we are not interested in the frequency ω_2 and we inject only ω_1 to the top laser beam. The second method consists in using an atomic interferometer. The phase fluctuations of the laser beam mainly result from the mechanical vibrations of the optical elements and thus they depend on the position where the measurement is made. It is the second method which gives the resulting phase fluctuation imprinted on the atoms.

Both tests can be implemented simultaneously using the experimental sequence shown in the figure 3.34. We apply two atomic beamsplitters ($\frac{\pi}{2}-$pulses) with time interval $\tau_2 - \tau_1$ on the condensate. We chirp the frequency difference $\omega_1 - \omega_3$ to compensate the gravity.

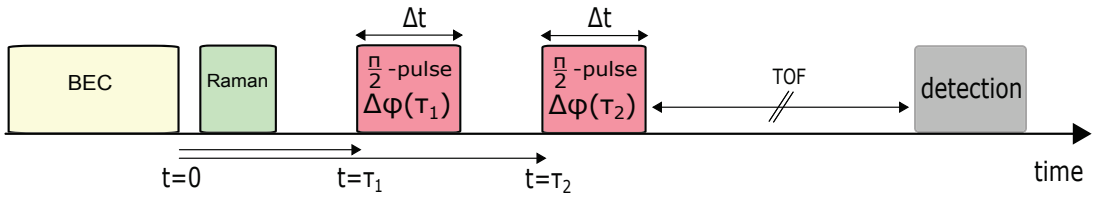

FIGURE 3.34: Experimental sequence for the phase $\varphi_1 - \varphi_3$ test.

Beating of the laser beams We register the optical beating signals of the two $\frac{\pi}{2}-$pulses. The first beating signal has a phase $\Delta\varphi(\tau_1) = \varphi_1(\tau_1) - \varphi_3(\tau_1)$ and the second one has $\Delta\varphi(\tau_2) = \varphi_1(\tau_2) - \varphi_3(\tau_2)$. If we do not consider the fluctuations, $\Delta\varphi(\tau_2)$ can be deduced from $\Delta\varphi(\tau_1)$ because the phase relation between the first Bragg pulse and the second Bragg pulse is maintained experimentally, i.e,

$$\Delta\varphi(\tau_2) = \Delta\varphi(\tau_1) + \int_{\tau_1-\tau_2} \mathrm{d}t \Delta\omega(t). \tag{3.40}$$

where $\Delta\omega(t) = \omega_1 - \omega_3$ depends on time since we chirp the frequency difference to compensate the gravity effect on the Bragg resonance condition. $\Delta\varphi(\tau_1)$ is not controlled in the experiment, it fluctuates between 0 and 2π from one realisation to another. However, the phase difference $\Delta\varphi(\tau_1) - \Delta\varphi(\tau_2)$ is well controlled unless there are phase fluctuations between τ_1 and τ_2. So by measuring the standard deviation of the phase difference $std[\Delta\varphi(\tau_1) - \Delta\varphi(\tau_2)]$ as a function of $\tau_1 - \tau_2$ we get the amplitude of the phase fluctuation due to the external effects. We obtain $\Delta\varphi(\tau_1)$ and $\Delta\varphi(\tau_2)$ by fitting the registered beating signals with sinusoidal function with chirped frequency. An example of the single realisation picture of such beating signal with its fit is shown in the figure 3.35. By repeating this procedure over

many realisations we get the standard deviation of the phase difference $\sigma_{opt} = std[\Delta\varphi(\tau_1) - \Delta\varphi(\tau_2)]$ for a given τ_1 and τ_2.

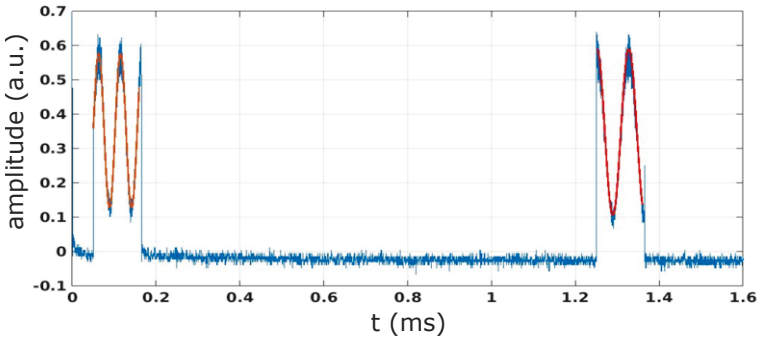

FIGURE 3.35: Optical beating signal of the Bragg pulses with chirped frequency difference $\omega_1 - \omega_3$. The signal is fitted (in red) with the chirped sin −function to estimate the phase difference between two Bragg pulses.

Atomic interference We can also estimate the standard deviation of the phase difference $std[\Delta\varphi(\tau_1) - \Delta\varphi(\tau_2)]$ via atomic (open) interferometer which is accomplished by appying consecutive $\frac{\pi}{2}-$pulses on the condensate as it is illustrated in the figure 3.36. The first Bragg pulse splits the condensate into two: the first cloud centered at momentum k_0 and the second cloud centered at momentum $k_0 + \Delta k_B$, which then propagate freely before the second Bragg pulse is applied. Then, it splits each beams in two resulting in four beams: two at k_0 and two at $k_0 + \Delta k_B$. After long time of flight two atomic clouds are detected with the density modulation along the $z-$axis. The phase of this modulation depends on the phase difference of the Bragg beams $\Delta\varphi(\tau_1) - \Delta\varphi(\tau_2)$ and its fluctuation results in the instability of the fringes from experimental shot to shot. We will estimate the phase imprinted on the atoms by the $\frac{\pi}{2} - \frac{\pi}{2}$ pulse scheme. For this we will neglect the interaction of the atoms in the condensate and express its wavefunction through the fundamental state of the harmonic trap with cylindrical symmetry along $z-$axis. So, in the momentum space, the BEC wavefunction at time $t = 0$ is given by (in analogy to (3.10)):

$$\tilde{\Psi}(\mathbf{p}, t = 0) = \sqrt{N_0} e^{-\imath\phi_0} \tilde{u}_0(\mathbf{p}) \tag{3.41}$$

where ϕ_0 is the initial condensate phase and the momentum dependence is expressed as [111]:

$$\tilde{u}_0(\mathbf{p}) = \frac{1}{\pi^{3/4}(c_\perp^2 c_z)^{1/2}} e^{-\frac{p_\perp^2}{2c_\perp^2}} e^{-\frac{p_z^2}{2c_z^2}} \tag{3.42}$$

with

$$c_\perp = \sqrt{m\hbar\omega_\perp}, \qquad c_z = \sqrt{m\hbar\omega_z}.$$

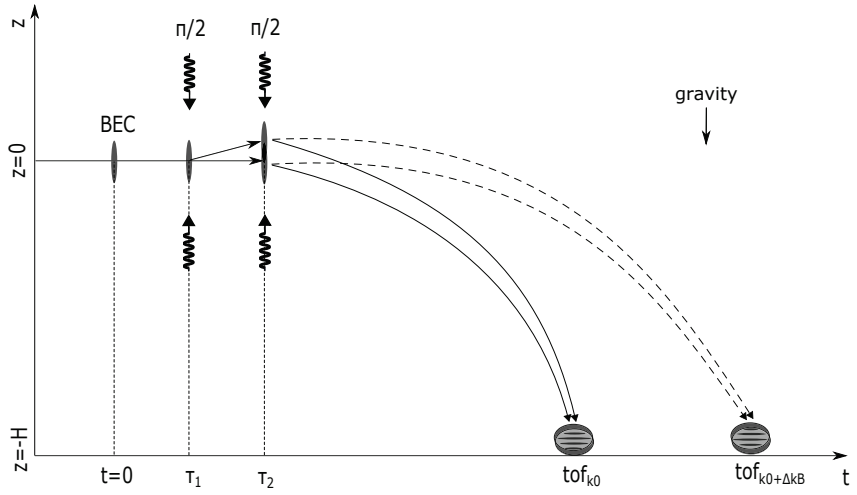

FIGURE 3.36: Schematic representation of the open atomic interferometer using two successive Bragg pulses. Due to the phase difference accumulated during $\tau_1 - \tau_2$ the density of each order is modulated

After the first beamsplitter we have:

$$\tilde{\Psi}(\mathbf{p},\tau_1) = \left[T\tilde{\Psi}(\mathbf{p},t=0) + \imath R e^{-\imath\Delta\varphi(\tau_1)}\tilde{\Psi}(\mathbf{p}+\hbar\Delta k_B, t=0)\right] e^{\imath\frac{\mathbf{p}^2}{2m\hbar}\tau_1}$$

where for an ideal beamsplitter the reflection and transmission coefficients are equal to $R = T = \frac{1}{\sqrt{2}}$. The common phase factor is not important and will be omitted in the following. In between the two $\frac{\pi}{2}-$pulses, the state evolves to:

$$\begin{aligned}\tilde{\Psi}(\mathbf{p}, t\to\tau_2) &= T\tilde{\Psi}(\mathbf{p},t=0)e^{\imath\frac{(\tau_2-\tau_1)}{2m\hbar}(p_\perp^2+p_z^2)} \\ &\quad +\imath R e^{-\imath\Delta\varphi(\tau_1)}\tilde{\Psi}(p_\perp, p_z+\hbar\Delta k_B, t=0)e^{\imath\frac{(\tau_2-\tau_1)}{2m\hbar}(p_\perp^2+(p_z+\hbar\Delta k_B)^2)}.\end{aligned}$$

After the second beamsplitter we have:

$$\tilde{\Psi}(\mathbf{p},\tau_2) = \tilde{\Psi}_{k_0}(\mathbf{p},\tau_2) + \tilde{\Psi}_{k_0+\Delta k_B}(\mathbf{p},\tau_2) \tag{3.43}$$

with

$$\begin{aligned}\tilde{\Psi}_{k_0+\Delta k_B}(\mathbf{p},\tau_2) &= \imath T R e^{-\imath\Delta\varphi(\tau_2)}\tilde{\Psi}(p_\perp, p_z+\hbar\Delta k_B, t=0)e^{\imath\frac{(\tau_2-\tau_1)}{2m\hbar}(p_\perp^2+p_z^2)} \\ &\quad +\imath T R e^{-\imath\Delta\varphi(\tau_1)}\tilde{\Psi}(p_\perp, p_z+\hbar\Delta k_B, t=0)e^{\imath\frac{(\tau_2-\tau_1)}{2m\hbar}(p_\perp^2+(p_z+\hbar\Delta k_B)^2)}.\end{aligned}$$

and so on for $\tilde{\Psi}_{k_0}(\mathbf{p},\tau_2)$. The density of the cloud centered at momentum $k_0+\hbar\Delta k_B$ is then:

$$\begin{aligned} n_{k_0+\hbar\Delta k_B}(\mathbf{p},tof) &= \|\tilde{\Psi}_{k_0+\Delta k_B}(\mathbf{p},\tau_2)e^{\imath\frac{(tof-\tau_2)}{2m\hbar}(p_\perp^2+(p_z+\hbar\Delta k_B)^2)}\|^2 \\ &= \frac{N_0}{2}\left[\tilde{u}_0(p_\perp,p_z+\hbar\Delta k_B)\right]^2 \times \\ &\quad \times\Big(1+\cos\big\{\Delta\varphi(\tau_2)-\Delta\varphi(\tau_1)+\frac{(\tau_2-\tau_1)\Delta k_B}{m}p_z+\frac{\hbar(\tau_2-\tau_1)\Delta k_B^2}{2m}\big\}\Big). \end{aligned} \tag{3.44}$$

The density is modulated by the cos −function which depends on the vertical velocity $v_z=\frac{p_z}{m}$. The fringe separation is

$$\Delta v_z^{theor}=\frac{2\pi}{(\tau_2-\tau_1)\Delta k_B}. \tag{3.45}$$

We compare the theoretically predicted fringe size with the measured one for four different values of $\tau_2-\tau_1$ in the figure 3.37. A good agreement between these two

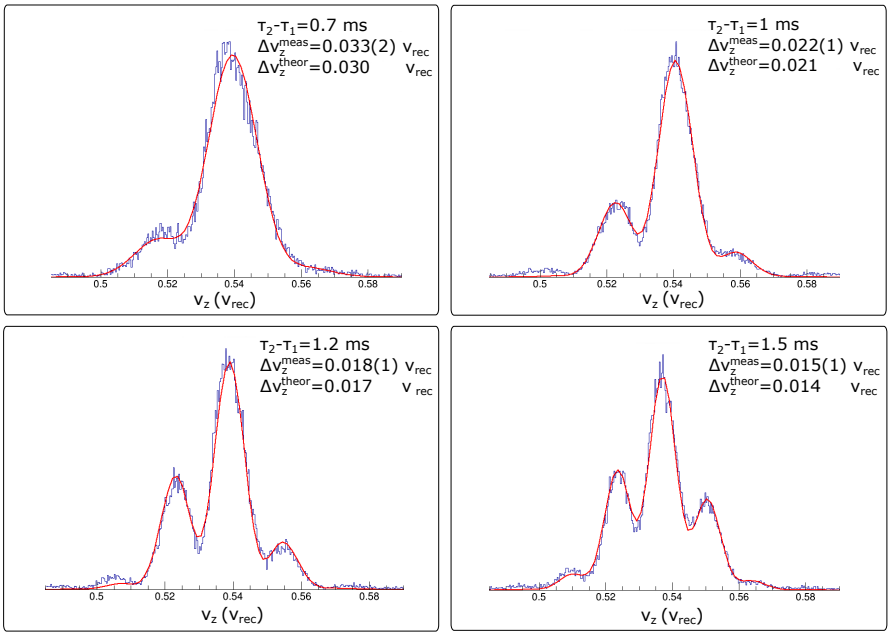

FIGURE 3.37: Density profile along v_z of the diffracted atoms of the open atomic interferometer for four values of $\tau_2-\tau_1$. To obtain the profiles, transversally we integrate all the atoms and also we average over several realisations ~ 50. The $\frac{\pi}{2}-$ pulses have the duration of 0.1 ms. The red solid curves are the result of the fit function $f(v_z)$, from which we obtain the fringe separations Δv_z^{meas} that are in good agreement with the predicted values Δv_z^{theor}.

has been recorded. The measured values of the fringe size Δv_z^{meas} are obtained by averaging several interference patterns ~ 50 and fitting them by a function

$$f(v_z)=Ae^{-\frac{v_z^2}{2\sigma_{v_z}^2}}\left(1+C\cos(\frac{2\pi v_z}{\Delta v_z^{meas}}+\phi)\right) \tag{3.46}$$

where $A, \sigma_{v_z}, C, \Delta v_z^{meas}, \phi$ are free parameters of the fit. Of course this fit function works up to certain time interval $\tau_2 - \tau_1$ since the atomic interferometer is the open one meaning that the interfering clouds are spatially moving away as a function of $\tau_2 - \tau_1$. They will not be superposed during the second $\pi/2-$pulse for greater values of $\tau_2 - \tau_1$ while we need a spatial overlap between two atomic clouds in order to observe an interference. It can be easily seen by switching to the real space $\tilde{\Psi}_{k_0+\Delta k_B}(\mathbf{p}, \tau_2) \rightarrow \tilde{\Psi}_{k_0+\Delta k_B}(\mathbf{r}, \tau_2)$. The separation distance is given by

$$z - z' = \frac{\hbar \Delta k_B (\tau_2 - \tau_1)}{m} \tag{3.47}$$

which equals to 0.1 mm for $\tau_2 - \tau_1 = 2$ ms. The fringes are visible as long as the separation is smaller with respect to the BEC size after expansion $R_z(tof) = 1.3$ mm.

The absolute value of the phase ϕ is discussed towards the end of this chapter and here we will be interested only on the fluctuation of the phase ϕ. The standard deviation of the phase $\sigma_{atom} = std[\phi]$ which is found from the fit function in (3.46) is directly related with that of the laser beam $\sigma_{opt} = std[\Delta\varphi(\tau_1) - \Delta\varphi(\tau_2)]$. We are in a position to compare the measured phase fluctuations σ_{atom} and σ_{opt} using two methods. The two quantities are plotted in the figure 3.38 as a function of $\tau_2 - \tau_1$. There is a very close correlation between the results of the two methods

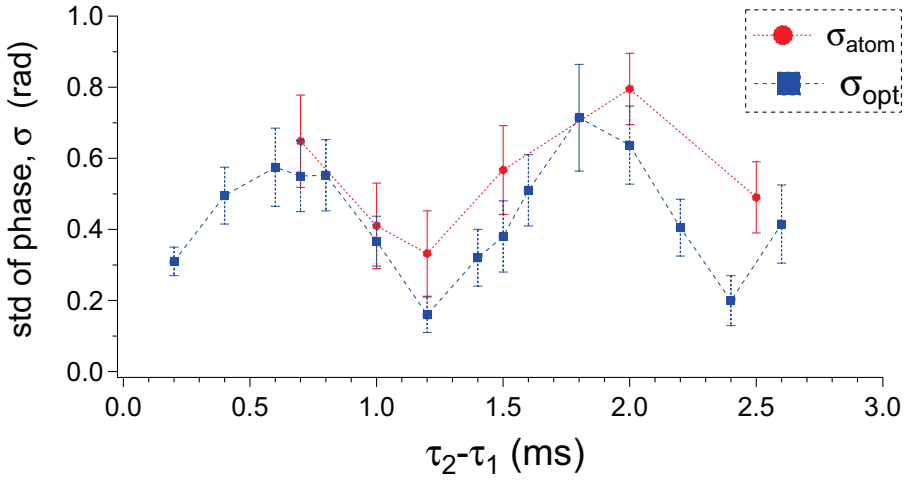

FIGURE 3.38: Comparison between σ_{opt} and σ_{atom} as a function of $\tau_2 - \tau_1$

which suggests that optical trajectories between the optical interferometer and the atomic interferometer do not contribute much to the phase fluctuation $\varphi_1 - \varphi_3$. We see that the two quantities are oscillating at frequency ~ 830 Hz. We realise that the source of this fluctuation is due to the turbo pumps but mainly from the frequency of the turbo pump located in the upper part of the science chamber

turning at 820 Hz. We model the phase induced by the turbo pump modulates the phase with a term $\Phi\cos(\omega_p t+\phi_p)$ where ϕ_p is a random phase:

$$\begin{aligned}\Delta\varphi'(\tau_1) &= \Delta\varphi(\tau_1)+\Phi\cos(\omega_p\tau_1+\phi_p)\\ \Delta\varphi'(\tau_2) &= \Delta\varphi(\tau_1)+\int_{\tau_1}^{\tau_2}\mathrm{d}t(\omega_1-\omega_3)+\Phi\cos(\omega_p\tau_2+\phi_p)\end{aligned}$$

which can be used to estimate the $std[\Delta\varphi'(\tau_2)-\Delta\varphi'(\tau_1)]$:

$$\begin{aligned}std[\Delta\varphi'(\tau_2)-\Delta\varphi'(\tau_1)] &= std\Big[\int_{\tau_1}^{\tau_2}\mathrm{d}t(\omega_1-\omega_3)+\Phi\cos(\omega_p\tau_2+\phi_p)-\Phi\cos(\omega_p\tau_1+\phi_p)\Big]\\ &= std\Big[-2\Phi\sin(\frac{\omega_p(\tau_2-\tau_1)}{2})\sin(\frac{\omega_p(\tau_2+\tau_1)+2\phi_p)}{2}\Big]\\ &= \sqrt{2}\Phi\Big|\sin(\frac{\omega_p(\tau_2-\tau_1)}{2})\Big|\end{aligned}$$

The signal corresponds to the experimental observation in the figure 3.38 from which we estimate $\Phi=20°$. In addition, there is an offset of the quantity $std[\Delta\varphi'(\tau_2)-\Delta\varphi'(\tau_1)]$ indicating that there are other sources of the phase fluctuation. Independently, using an accelerometer device (Analog Devices $ADXL335$) we have seen also the vibration of another turbo pump located in the bottom part of the science chamber which certainly contributes to the offset signal we have seen.

The values obtained for the average contrast of the single shot fringes is shown in the figure 3.39. We see that the maximum value can go up to 68% and it corresponds to the minimum of the phase fluctuation. The contrast never goes above 68% and we do not understand it well at the moment, neither the drop of the contrast at long $\tau_2-\tau_1$ is understood.

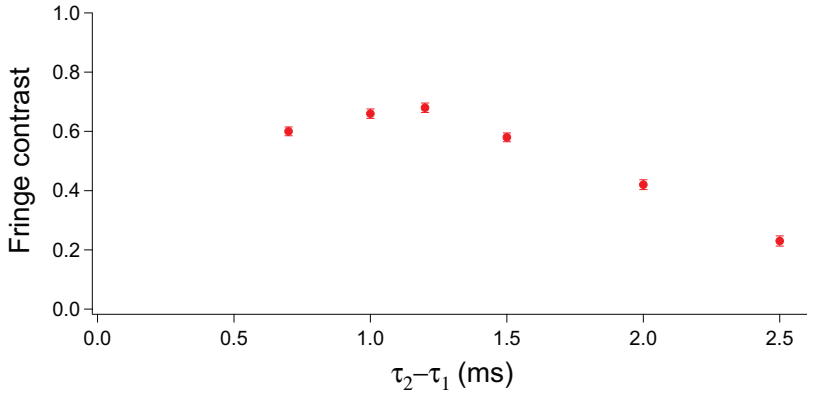

FIGURE 3.39: Average contrast of the single shot fringes as a function of $\tau_2-\tau_1$.

The effect of the phase fluctuation is that it can lead to the decoherence by shifting the resonance condition and the effect gets higher for the longer duration of the

Bragg pulse.

To study the decoherence of the Bragg pulse, we measure the Rabi oscillations as we have done before for 12 μW power of the Bragg beams. Note that for 12 μW the decoherence rate was found to be decent and we have seen oscillations going beyond 4 ms duration of the Bragg pulse. So what is different with 5 μW? Well, the two photon Rabi frequency $|\Omega_{eff}|_{5\ \mu\mathrm{W}} = 2\pi \times 520$ Hz gets closer to the frequency of the phase fluctuation frequency $2\pi \times 820$ Hz and thus the effect of the phase fluctuation on the decoherence gets amplified as we see from the figure 3.40 where we plot the Rabi oscillations for three different powers of the Bragg pulse: 12 μW, 7 μW and 5 μW. Each experimental point (red points) is obtained by counting number of atoms inside 0.005 k_{rec} longitudinally (no transverse momentum limit) and averaging over several experimental realisations. We can see the decoherence effect can be violent closer to the resonance. By introducing phase fluctuation in the form $\Phi\cos(\omega_p\tau_1 + \phi_p)$ for the Bragg beams with the earlier estimated value of Φ and in addition, including the decoherence rate $\Gamma = 0.19$ ms^{-1} which is the governing decoherence rate away from the resonance and which is independent of power of the Bragg beams, we simulated the resulting Rabi oscillations by solving numerically the time-dependent Schrodinger's equation. The result of the numerical study are given by solid lines and as we can see it can explain efficiently what is observed.

The effect of the upper turbo pump could be easily corrected by adding the sinusoidal phase to the phase of the RF signal which is sent to the AOM. We have not implemented it immediately. Instead, we decided to investigate the coherence properties of the single point in the last graph of 3.40 corresponding to the 500 μs duration of the 5 μW of Bragg laser beam power which corresponds to our atomic beamsplitter to be employed for the Bell's test. So, we need to check the effect of the phase fluctuation on the beamsplitter transfer and reflection coefficient and more importantly its effect on the imprinted phase on the atoms. The effect of the phase fluctuation on the transmission and reflection coefficient of the beamsplitter is through shifting the resonance condition by $\frac{\Phi}{2\pi}\omega_p = 50$ Hz over the resonance half-width $\Delta\omega_{res} = \frac{\hbar}{2m}\Delta k_B(2 \times 0.02k_{rec})/2\pi = 950$ Hz. We estimate that it has a small effect changing the coefficients by 4%. The important issue for us was to make sure that the imprinted phase on the atoms by the atomic beamsplitter is well controlled. This is what we are going to discuss next.

3.3.3 Atomic beamsplitter: phase test

Remember that we apply simultaneously two atomic beamsplitters made of $\{\omega_1, \omega_3\}$ and $\{\omega_2, \omega_3\}$ which imprint phases $\varphi_1 - \varphi_3$ and $\varphi_2 - \varphi_3$ respectively on the atoms. Our aim

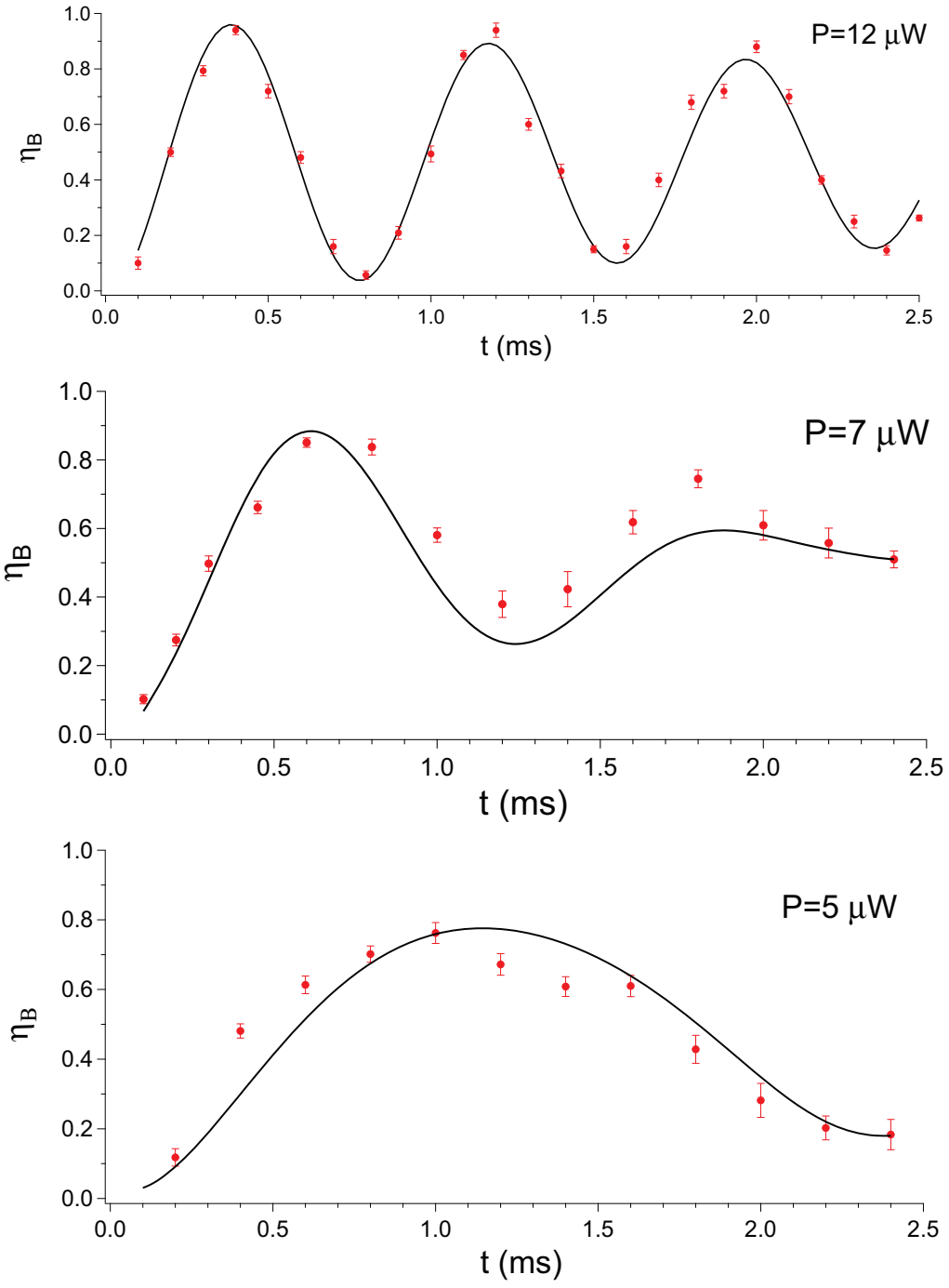

FIGURE 3.40: Two photon Rabi oscillations, averaged over several realisations, for three different optical powers of the Bragg beams in order from top graph to bottom graph: 12 μW, 7 μW and 5 μW . Solid lines represent numerical study including the phase fluctuation introduced by the vibration of the turbo pump.

is to check if we control the phase difference $\Delta\Phi = (\varphi_1 - \varphi_3) - (\varphi_2 - \varphi_3) = \varphi_1 - \varphi_2$. Up to know we have studied the phase difference $\varphi_1 - \varphi_3$ which is found to be not stable. However, we can hope that the phase difference $\varphi_1 - \varphi_2$ stays stable since the phase fluctuations of both atomic beamsplitters are common. We are going to verify if this is indeed the case, but in the first place we explain the electronic control of the phase difference $\varphi_1 - \varphi_2$.

3.3.3.1 RF source for the phase control

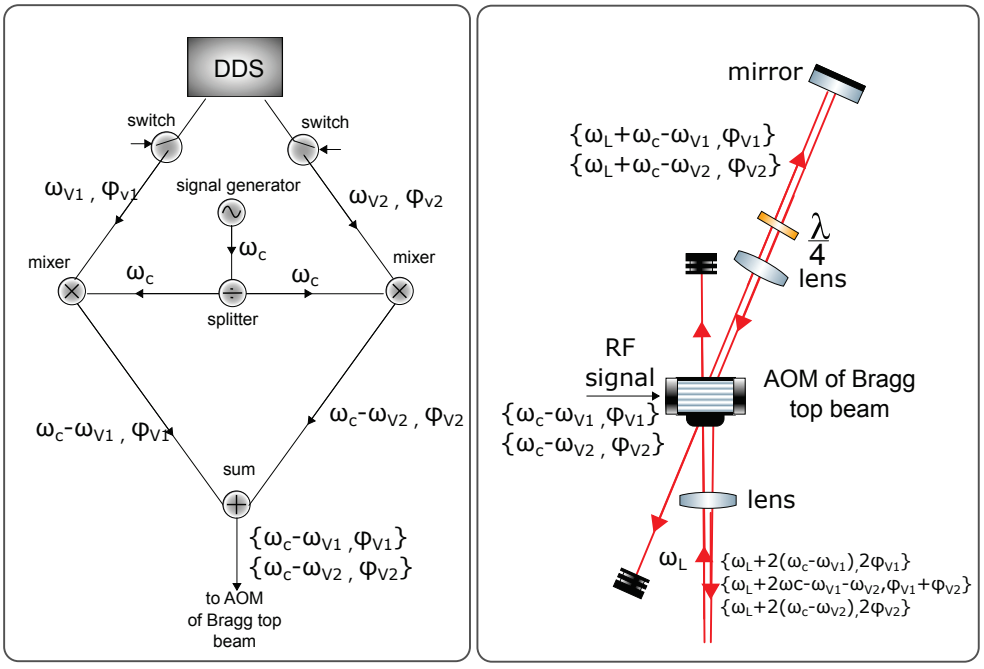

FIGURE 3.41: Left panel: Generation of two RF frequencies for the Bragg top beam using the DDS device whose phase difference $\varphi_{V1} - \varphi_{V2}$ between two outputs is commanded. Right panel: The AOM double pass configuration of the top Bragg beam.

The phase difference $\Delta\Phi = \varphi_1 - \varphi_2$ is imprinted on the Bragg laser beams via AOMs, so we need to control the phase difference of the two RF frequencies injected to the AOM of the top Bragg laser beam. We generate electronically the mentioned two RF frequencies according to the scheme in the figure 3.41.(left panel). The starting point is the double digital synthesizer (DDS) device on the base of which lies the two RF digital generators that are locked in phase. The DDS has been assembled by the electrician F. Moron in our laboratory and it genererates two frequencies ω_{V1} and ω_{V2} with their phase difference $\varphi_{V1} - \varphi_{V2}$ controlled by a trigger signal. We have measured the phase difference $\varphi_{V1} - \varphi_{V2}$ generated by the DDS as a function of the input phase difference, the result is plotted in the figure 3.42. We see that there is an inherent offset of 33.8° which might come from the propagation time difference of the digital

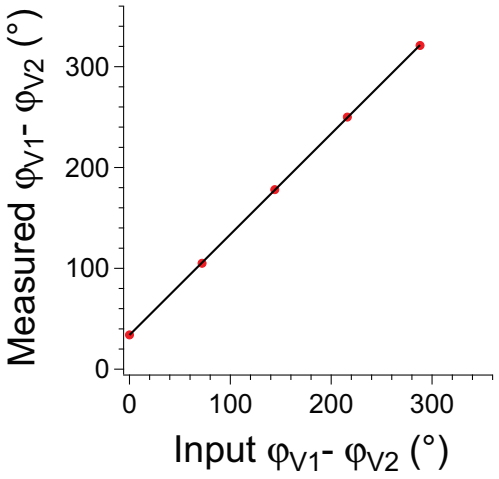

FIGURE 3.42: **Calibrating the phase difference between two outputs of the DDS device.** The measured phase difference $\varphi_{V1} - \varphi_{V2}$ versus the input phase difference $\varphi_{V1} - \varphi_{V2}$ is plotted. The linear fit (black solid line) gives a slope of 0.998(2) and an offset of 33.8(4)°.

synthesizers to the phase locking unit. We find the slope of 1 indicating that the output phase difference is indeed controlled. However, unluckily the control happens only 83% of times and the other 17% of times the phase is shifted by $-108°$ from the input value of $\varphi_{V1} - \varphi_{V2}$. It was measured by looking at the statistics of the $\varphi_{V1} - \varphi_{V2}$ whose distribution is shown in the figure 3.43. The reason of such behaviour of the device is not well established. However the situation is not so dramatic, we can always use the missed shots as independent set of data since we keep independently track of the phase $\varphi_{V1} - \varphi_{V2}$. A new version of the DDS device is currently developed with the two twin generators (not with independent generators like with actual one) and we expect that the imperfections will be corrected with the new device. The half-width at $1/\sqrt{e}$ of the distribution of $\varphi_{V1} - \varphi_{V2}$ is equal to 0.6°.

Unfortunately, the DDS can not generate more than 80 MHz whereas we use an AOM centered at 200 MHz. To obtain the required frequency we mix the two output frequencies of the DDS with the common RF source at frequency ω_c, which does not alter the phase difference $\varphi_{V1} - \varphi_{V2}$. After the mixer, we have the sum $\omega_c - \omega_i$ and the difference $\omega_c + \omega_i$ frequencies where $i = V1, V2$. We use the AOM as the bandpass filter since it has a non-zero diffraction efficiency only between 100 MHz and 250 MHz in double pass. So, we choose $\omega_c = 270$ MHz and $\omega_i \sim 70$ MHz to center the $\omega_c - \omega_i$ around 200 MHz. We recombine the two useful frequencies $\omega_c - \omega_{V1}$ and $\omega_c - \omega_{V2}$ by using combiner (power splitter in inverse configuration) before sending it to the RF amplifier of the AOM of the top Bragg laser beam. The spectrum of the two coexisting frequencies centered around 200 MHz with 100 Hz difference after the combiner is shown in the figure 3.44. Two signals at the designated frequencies appear clearly with the FWHM

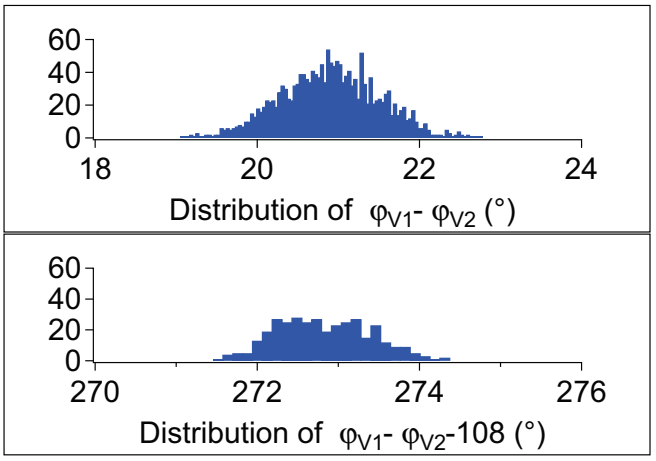

FIGURE 3.43: Top panel: The distribution of the measured phase difference $\varphi_{V1} - \varphi_{V2} = 20.86(1)°$ which happens 83% of times. Bottom panel: The distribution of the missed phase difference by 108°, $\varphi_{V1} - \varphi_{V2} - 108 = 272.72(4)°$, which happens 17% of times.

of < 5 Hz. The generated two RF frequencies $\omega_c - \omega_{V1}$ and $\omega_c - \omega_{V2}$ arrive on the AOM

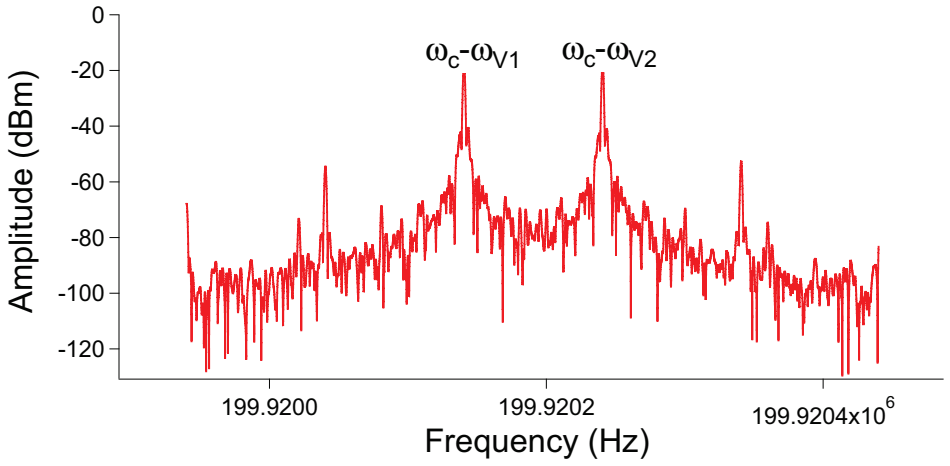

FIGURE 3.44: Spectrum of the coexisting two RF frequencies $\omega_c - \omega_{V1}$ and $\omega_c - \omega_{V2}$ which are injected on the AOM of the top Bragg beam. The two frequencies are 100 Hz apart and have FWHM < 5 Hz.

of the top Bragg beam as shown in the figure 3.41.(right panel) and the phases φ_{V1} and φ_{V2} are printed on the laser beams. The top Bragg laser beam is arranged in the double pass configuration which in turn creates (mainly) three frequencies: $\omega_L + 2(\omega_c - \omega_{V1})$, $\omega_L + 2\omega_c - \omega_{V1} - \omega_{V2}$ and $\omega_L + 2(\omega_c - \omega_{V2})$ with ω_L the optical frequency (right panel of the figure 3.41). The double-pass configuration allows us firstly to introduce the detuning of $\sim$ 400 MHz from the atomic transition (Bragg beams are diffracted to +1 order in both ways) to avoid the spontaneous emission. Conversely, having three frequencies is not a problem in our case, since we choose such that the frequency $\omega_L + 2(\omega_c - \omega_{V1})$ at

resonance with k_{a-} and k_{b-} and the frequency $\omega_L + 2\omega_c - \omega_{V1} - \omega_{V2}$ at resonance with k_{a+} and k_{b+} and the third frequency $\omega_L + 2(\omega_c - \omega_{V2})$ is going to address atoms which we do not consider. Hence, the third frequency will not intervene. Another way to eliminate the third frequency is by decreasing the power of RF frequency at $\omega_c - \omega_{V2}$ which leaves us only with two frequencies $\omega_1 = \omega_L + 2(\omega_c - \omega_{V1})$ and $\omega_2 = \omega_L + 2\omega_c - \omega_{V1} - \omega_{V2}$ after the double-pass.

3.3.3.2 Testing $\varphi_1 - \varphi_2$ with the atoms

As mentioned before we would like to check if the phase $\Delta\Phi = \varphi_1 - \varphi_2$ is imprinted on the atoms. For this test, we employ the open atom interferometer sequence employed before. We fix the time interval between two $\frac{\pi}{2}-$pulses to $\tau_1 - \tau_2 = 1.2$ ms. The first $\frac{\pi}{2}-$pulse is made of $\{\omega_1 = \omega_L + 2(\omega_c - \omega_{V1}), \omega_3\}$ during which ω_{V2} is cut by the electronic switch and the second one is made of $\{\omega_2 = \omega_L + 2(\omega_c - \omega_{V2}), \omega_3\}$ during which similarly ω_{V1} is cut off. Note that the latter one is the third frequency which we are not going to employ in the actual test. Nevertheless we have verified the phase stability using the beating signal between $\{\omega_1 = \omega_L + 2(\omega_c - \omega_{V2}), \omega_3\}$ and $\omega_L + 2\omega_c - \omega_{V1} - \omega_{V2}$. The phase difference $\varphi_{V1} - \varphi_{V2}$ between ω_{V1} and ω_{V2} is locked and the two atomic beamsplitters are set on resonance with the condensate. So, the first $\frac{\pi}{2}-$pulse has a phase:

$$\Delta\varphi(\tau_1) = (\varphi_1 - \varphi_3) + \Phi\cos(\omega_p\tau_1 + \phi_p) \tag{3.48}$$

while the second one has:

$$\Delta\varphi(\tau_2) = (\varphi_2 - \varphi_3) + \Phi\cos(\omega_p\tau_2 + \phi_p) \tag{3.49}$$

The density modulation of the diffracted order is given by (see (3.44)):

$$n_{k_0+\hbar\Delta k_B}(\mathbf{p}, tof) = \times\Big(1 + \cos\big\{\Delta\varphi(\tau_2) - \Delta\varphi(\tau_1) + \frac{(\tau_2 - \tau_1)\Delta k_B}{m}p_z + \frac{\hbar(\tau_2 - \tau_1)\Delta k_B^2}{2m}\big\}\Big)$$

which depends on the aforementioned phase difference $\varphi_1 - \varphi_2$ and noise of the turbo pump. We can control its value directly via the DDS device owing to the relation $\varphi_1 - \varphi_2 = 2(\varphi_{V1} - \varphi_{V2})$ where factor 2 results from the double pass through the AOM. So, the idea is to see if the phase of the cos −term in the equation (3.44) is actually commanded by $\varphi_{V1} - \varphi_{V2}$. To determine the phase of the density modulation we proceed as following. Firstly, for a given input value of $\varphi_{V1} - \varphi_{V2}$ we estimate the average values of the parameters $\sigma_{v_z}, C, \Delta v_z^{meas}, v_{z0}$ by fitting the integrated data of entire experimental realisations adopting the regular fitting function in a form:

$$f(A, \phi) = Ae^{-\frac{(v_z - v_{z0})^2}{2\sigma_{v_z}^2}}\big(1 + C\cos(\Delta v_z^{meas}v_z + \phi)\big). \tag{3.50}$$

where all the parameters are free parameters of the fit function. Next, we estime the phase ϕ imprinted on the atoms for each experimental realisation letting only A and ϕ to be fitted in the fitting function. The result of the measured phase ϕ as a function of the commanded angle $\varphi_{V1} - \varphi_{V2}$ is plotted in the figure 3.45. The dense data points in red correspond to the 83% occurrence of the demanded angle $\varphi_{V1} - \varphi_{V2}$ and the scarce data points represent 17% occurrence of the demanded angle shifted by 108° due to the imperfection of the DDS device discussed before. By fitting the data with the linear function we find the slope of 1.978(17) meaning that the phase printing on the atoms was successful. It is a very encouraging result. We measure also the offset 266.8(3)° which is compatible with the predicted offset angle:

$$\phi_{offset} = 2(\varphi_{V1} - \varphi_{V2})_{offset} + \frac{\hbar(\tau_2 - \tau_1)\Delta k_B^2}{2m} = 2 * 33.6° + 196.6° = 269.8°. \quad (3.51)$$

Next, we looked at the standard deviation of the measured angle $std[\phi]$ in order to

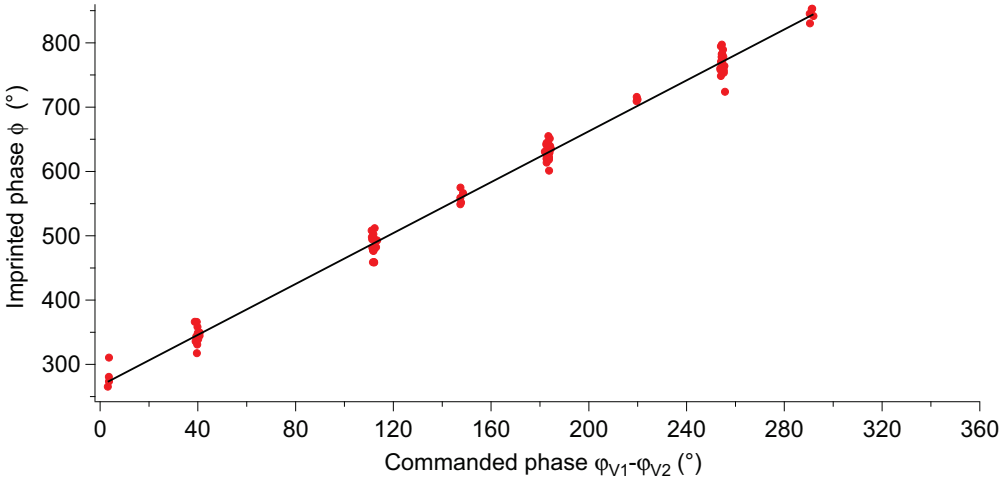

FIGURE 3.45: **Imprinted phase on the atoms ϕ versus commanded phase $\varphi_{V1} - \varphi_{V2}$.** The linear fit gives the slope of 1.978(17) and offset angle 266.8(3)°.

compare it with the preceding results for $\tau_1 - \tau_2 = 1.2$ ms given in the figure 3.38. An example of the distribution of the phase ϕ is shown in the figure 3.46 for which the standard deviation is $std[\phi] = 0.242(3)$ rad or $\sim 14°$. The found value is consistent with the estimated phase fluctuation of the Bragg laser beams (see figure 3.38). Here we applied two beamsplitters that are temporally separated. In the actual Bell's inequality test experiment the two beamsplitters are going to be applied simultaneously and in such scenario being common for both beamsplitters, the phase fluctuation will cancel out. This is the great advantage of the scheme 3.1!

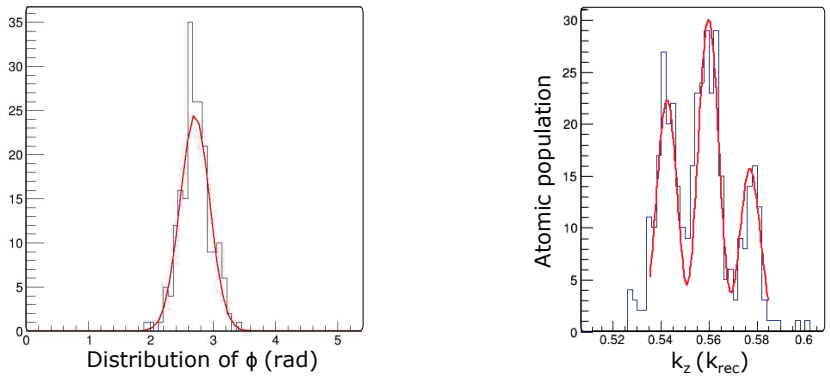

FIGURE 3.46: Left panel: Distribution of the imprinted phase ϕ on the atoms. The standard deviation of the distribution is $std[\phi] = 0.242(3)$ rad found by fitting with gaussian (in red solid line). Right panel: An example of the fit of the atomic fringes to estimate the phase ϕ imprinted on the atoms in single realisation.

3.4 Perspective

To sum up, at the moment we dispose experimentally all the necessary elements which we covered in this chapter to run the Bell's inequality test with the momentum entangled atomic pair. The last step before starting the data acquisition of the Bell's experiment will be calibrating the timing $t_s = 2t_m$ of the sequence in the scheme 3.1. It can be done by two methods, first one is with the HOM type experiment (see Chapter 4) where the t_s is set to the position for which the HOM dip is observed or the second method consists of following the Bell's scheme 3.1 and looking at the signal of the correlation coefficient in equation (2.133) which is expected to exhibit modulation as a function of $t_s - 2t_m$. The advantage of the latter one is that the contrast of the modulation gives the indication of the violation of the Bell's inequality and will be the direct realisation of the scheme 3.1. In addition, we can get also information of the initial value of the phase $\Delta\Phi$ in order to fix it later to the preferred values of the four optimized angles for which the greatest violation is expected.

Although we have shown that the present experimental tools are good enough to start the first experimental realisation there are always rooms for improvements, namely:

reducing experimental cycle duration: currently the cycle duration is about ~ 30 s and it takes a very long data acquisition time especially for Bell-type experiments where we are in the low gain regime of the atomic pair production. We have two methods in mind that can be potentially employed to reduce the data acquisition time, first one is for example recycling the condensate to generate several times an atomic pair or second one is reducing the cycle duration by utilizing hybrid

cooling technique for which the experimental proof is already shown achieving condensation in every 6 s [20].

implementing Bragg pulses with square transfer function: the transfer function currently we are working with are the *sinc*−function as we have seen. The disadvantage of such functions is that they do not provide flat transfer efficiency for all momentum class of the atoms addressed by the atomic beamsplitter. The ideal function would be the square transfer function and it can be generated using the idea of the adiabatic pulses which exist in the RMN area [13].

measuring cross correlation of pair at lower pair population: finally we have to measure and verify if the cross correlation of pair is higher than the local correlation function for the lower average population (see 2.2.5).

Chapter 4

Atomic Hong-Ou-Mandel experiment

In this chapter, the realisation of an atomic Hong-Ou-Mandel (HOM) experiment [88] in our group using the momentum correlated atomic source we discussed in 2.2.3 will be described. The successful demonstration of the two-particle quantum interference effect opens an opportunity to test the Bell's inequality with massive particles correlated in momentum. I was engaged in this experiment with my senior experimental partner Raphael (see his thesis work for further details on the experiment [87]) during the second year of my thesis work.

This chapter is organised as follows, first we will explain the HOM effect stating the criteria between quantum and classical threshold. Then the result of our experiment will be shown with the calculation of the prediction of the HOM signal.

4.1 Description of HOM effect

4.1.1 The HOM effect with two particles

The Hong-Ou-Mandel (HOM) experiment [71] is indeed a landmark experiment revealing the mysterious properties of quantum mechanics which has no classical counterpart. It is a wonderful demonstration of the interference between two-particle amplitudes that is impossible to describe by any classical model. In the HOM experiment two indistinguishable bosonic particles arriving simultaneously in the input channels of a beamsplitter always emerge together in one of the output channels. In other words, consider an input state $|1_a, 1_b\rangle$ at the input channels of a and b of the beamsplitter illustrated in the figure 4.1, the output state is given by

$$|1_a, 1_b\rangle = \hat{a}^\dagger \hat{b}^\dagger |0,0\rangle \rightarrow \left((\sqrt{t})^2 \hat{c}^\dagger \hat{d}^\dagger + (-\imath\sqrt{r})^2 \hat{d}^\dagger \hat{c}^\dagger + (-\imath\sqrt{rt})\hat{d}^\dagger \hat{d}^\dagger + (-\imath\sqrt{tr})\hat{c}^\dagger \hat{c}^\dagger\right)|0,0\rangle \tag{4.1}$$

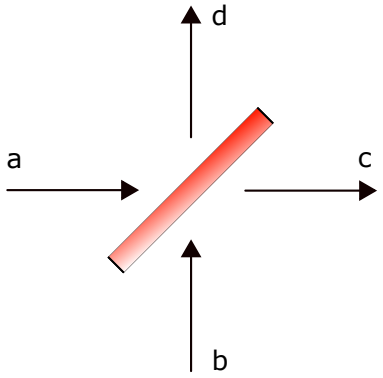

FIGURE 4.1: **The beamsplitter input-ouptut channel representation.**

where we used the lossless beamsplitter input-output relations:

$$\begin{pmatrix} \hat{d} \\ \hat{c} \end{pmatrix} = \begin{pmatrix} \sqrt{t} & \imath\sqrt{r} \\ \imath\sqrt{r} & \sqrt{t} \end{pmatrix} \begin{pmatrix} \hat{b} \\ \hat{a} \end{pmatrix}. \tag{4.2}$$

Note that the terms $\left((\sqrt{t})^2\hat{c}^\dagger\hat{d}^\dagger + (-\imath\sqrt{r})^2\hat{d}^\dagger\hat{c}^\dagger\right)|0,0\rangle$ cancel each other for a $50:50$ beamsplitter with $t = r = \frac{1}{2}$ and for bosonic particles obeying commutation relations $[a_i, a_j] = 0$ and $[a_i, a_j^\dagger] = 1\ \forall i, j$. It is this interference effect we are interested in and it corresponds to the destructive interference between the transmitted and reflected two-particle amplitudes as shown in the figure 4.2. The output state of the bosonic particles

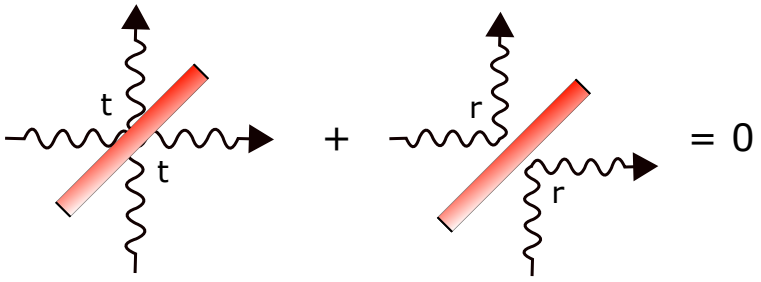

FIGURE 4.2: **The destructive interference between the transmitted and reflected two-particle amplitudes.**

$$|\psi\rangle = \frac{-\imath}{\sqrt{2}}\left(|2_c, 0\rangle + |0_c, 2_d\rangle\right) \tag{4.3}$$

is the maximally entangled two-particle state. So the consequence is that the joint detection of two particles at the output channels of the beamsplitter vanishes i.e. $G^{(2)}_{cd} = \langle\hat{c}^\dagger\hat{d}^\dagger\hat{d}\hat{c}\rangle = 0$. In contrast, for the fermionic particles with the anti-commutation relations

$\{a_i, a_j\} = 0$ and $\{a_i, a_j^\dagger\} = 1\ \forall i, j$, the resulting state is simply a pure state $|\psi\rangle = \hat{c}^\dagger \hat{d}^\dagger |0,0\rangle$ for which we expect maximum value of the joint detection.

The phase of the input state $|1_a, 1_b\rangle$ is totally random. The crucial point of the two-particle quantum interference effect is that it survives even after averaging out over random phase of the incoming particles, i.e. $G^2_{cd} = \langle \hat{c}^\dagger \hat{d}^\dagger \hat{d}\hat{c}\rangle = 0$ where the statistical average is taken over the input state with random phase.

On the other hand, consider the classical waves $\mathcal{E}_a = \mathcal{E}_0 e^{\imath\phi_a}$ and $\mathcal{E}_b = \mathcal{E}_0 e^{\imath\phi_b}$ with random phases ϕ_a and ϕ_b in the input channels a and b of the beamsplitter respectively. In case where the beams interfere (indistinguishable case), the outcoming waves are given by

$$\begin{aligned} \mathcal{E}_c &= \frac{1}{\sqrt{2}}(\mathcal{E}_a + \imath\mathcal{E}_b) \\ \mathcal{E}_d &= \frac{1}{\sqrt{2}}(\mathcal{E}_b + \imath\mathcal{E}_a). \end{aligned}$$

while when the beams do not interfere (distinguishable case), we sum the intensities instead of the amplitudes (see figure 4.3). The similar classical definition of the joint

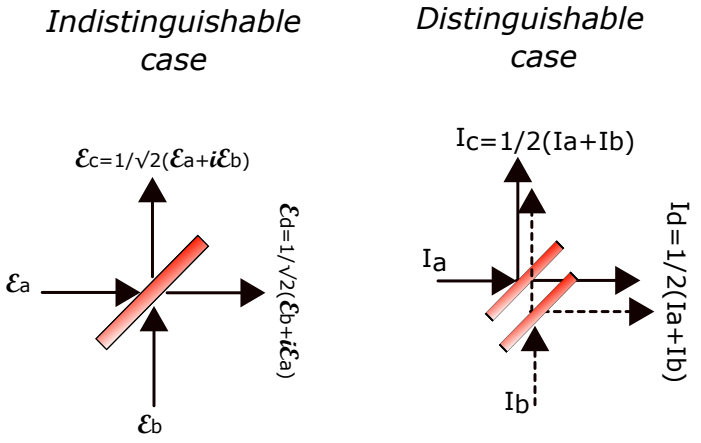

FIGURE 4.3: **Comparison between distinguishable and indistinguishable case for the classical waves.**

detection for the indistinguishable case results in

$$\langle I_c I_d\rangle = I_0^2 \langle \sin^2(\phi_a - \phi_b)\rangle = \frac{I_0^2}{2}. \tag{4.4}$$

with the ouptut average intensities $\langle I_c\rangle = \langle I_d\rangle = I_0$, while for the distinguishable case we have $\langle I_c I_d\rangle = \langle I_c\rangle\langle I_d\rangle = I_0^2$. An appropriate quantity in comparing the classical versus quantum scenario is then the visibility of the joint detection [85] when passing

from distinguishable to indistinguishable particles:

$$\bar{V} = 1 - \frac{G^{(2)}_{cd,Ind}}{G^{(2)}_{cd,Dis}}. \tag{4.5}$$

where $G^{(2)}_{cd,Ind}$ ($G^{(2)}_{cd,Dis}$) is the joint detection of indistinguishable (distinguishable) particles.

Hence, classically the visibility of the joint detection can be given as

$$\bar{V}_{class} = 1 - \frac{\langle I_c I_d \rangle}{\langle I_c \rangle \langle I_d \rangle} = 0.5. \tag{4.6}$$

In fact, 50% of the visibility is the upper bound of what classical models can produce implying that exceeding this value refers necessarily to the quantum mechanical interference.

To see the two-particle quantum interference effect, the particles should be indistinguishable from each other meaning that they should be in the same state. To illustrate this point, suppose that the particle a arriving on the beamsplitter has the horizontal polarization H and the particle b has the vertical polarization V. Then, the output state is:

$$|1_{a,H}, 1_{b,V}\rangle = \hat{a}^\dagger_H \hat{b}^\dagger_V |0,0\rangle \rightarrow \Big((\sqrt{t})^2 \hat{c}^\dagger_H \hat{d}^\dagger_V + (-\imath\sqrt{r})^2 \hat{d}^\dagger_H \hat{c}^\dagger_V + (-\imath\sqrt{rt}) \hat{d}^\dagger_H \hat{d}^\dagger_V + (-\imath\sqrt{tr}) \hat{c}^\dagger_H \hat{c}^\dagger_V \Big) |0,0\rangle$$

for which obviously the sum $(\sqrt{t})^2 \hat{c}^\dagger_H \hat{d}^\dagger_V + (-\imath\sqrt{r})^2 \hat{d}^\dagger_H \hat{c}^\dagger_V$ will not vanish provided that the detector can distinguish polarization of particles. Another example where the interference effect can be degraded is due to the existence of the phase difference between the terms $(\sqrt{t})^2 \hat{c}^\dagger \hat{d}^\dagger |0,0\rangle$ and $(-\imath\sqrt{r})^2 \hat{d}^\dagger \hat{c}^\dagger |0,0\rangle$. Such phase difference reflects the fact that the two-particle probability amplitude of the case where both particles are transmitted is distinguishable from the two-particle probability amplitude of the case where both particles are reflected that are shown in the figure 4.2. In practice, it is possible to compensate this phase difference by changing the path difference of the input particles. Indeed, in the original experiment of C. K. Hong, Z. Y. Ou and L. Mandel in 1987, they were able to cross from distinguishable case to indistinguishable case by controlling the optical path of the photons with the beamsplitter position. Their setup is shown in the figure 4.4.right panel. In the left panel of the figure 4.4 the result of the experiment is shown which is a plot of the coincidence count of the detectors on the ouptut channels of the beamsplitter as a function of the beamsplitter position. We see a dip with the visibility as high as 90% suggesting the fully quantum two-photon interference. The authors attribute the 10% of the visibility loss due to the nonperfect overlap of the photons. The dip occurred at the position of the beamsplitter ~ 302 μm where reflected photons were indistinguishable from the transmitted photons. The width of the dip gives the measure

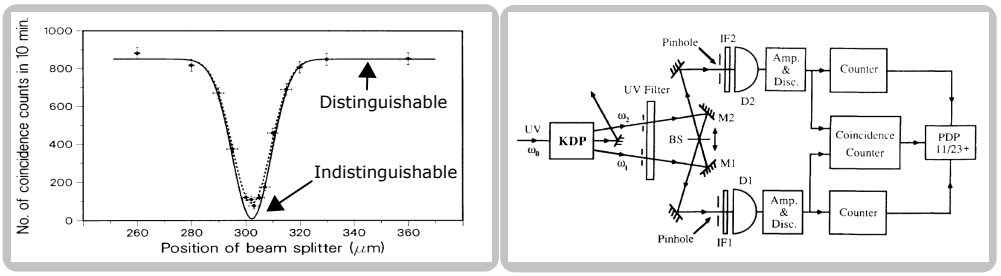

FIGURE 4.4: **The scheme and the result of the experiment by Hong, Ou and Mandel in** 1987 **with two photons.** Right panel: The setup of the experiment which consists of two photons generated as a result of parametric down-conversion, a beamsplitter, detectors and spatial and spectral filters. Left panel: The result of the experiment which is a plot of the coincidence count of the detectors on the ouptut channels of the beamsplitter as a function of the beamsplitter position. The dip of the $\sim 90\%$ of visibility has been observed indicating the quantum two-photon interference effect. Solid line is the theoretical prediction while the dashed line is the attenuated version of the solid line by factor of 0.9. (Figures are extracted from [71])

of the temporal length of the photon wave packet. It is found to be 16 μm at half height corresponding to duration of about 50 fs which is what is expected from the passband of the filters used in the experiment.

Although the HOM effect allows one to measure the duration of short wavepackets with a good resolution which was the intention of the authors originally, today it has a wide application in generating entangled states for quantum computing and phase testing interferometers, in quantifying the purity of the source or the indistinguishability by measuring the visibility of the dip [14, 126].

4.1.2 The HOM effect with N particles

Consider a (two-mode) input state

$$|\psi\rangle_{in} = \sum_{n=0}^{N} \sqrt{P(n)}|n,n\rangle \tag{4.7}$$

where $P(n)$ is some probability function which characterizes the statistics of the state. We will calculate the visibility $\bar{V}$ defined in the equation (4.5). The joint detection is

$$\begin{aligned} G_{cd}^{(2)} &= \langle \hat{c}^\dagger \hat{d}^\dagger \hat{d}\hat{c} \rangle \\ &= \|\hat{d}\hat{c}|\psi\rangle_{in}\|^2 \end{aligned}$$

where the average is taken over the input state $|\psi\rangle_{in}$ in the equation (4.7). It can be shown that the joint probabilities of the indistinguishable case and the distinguishable

particles are given by [87]:

$$G^{(2)}_{cd,Ind} = \frac{1}{4}\Big(G^{(2)}_{aa} + G^{(2)}_{bb}\Big), \tag{4.8}$$

$$G^{(2)}_{cd,Dis} = \frac{1}{4}\Big(G^{(2)}_{aa} + G^{(2)}_{bb}\Big) + \frac{1}{2}G^{(2)}_{ab}. \tag{4.9}$$

where $G^{(2)}_{aa} = {}_{in}\langle\psi|\hat{a}^\dagger\hat{a}^\dagger\hat{a}\hat{a}|\psi\rangle_{in}$, $G^{(2)}_{bb} = {}_{in}\langle\psi|\hat{b}^\dagger\hat{b}^\dagger\hat{b}\hat{b}|\psi\rangle_{in}$ and $G^{(2)}_{ab} = {}_{in}\langle\psi|\hat{a}^\dagger\hat{b}^\dagger\hat{b}\hat{a}|\psi\rangle_{in}$. Now, we can evaluate the visibility by using a concrete example of the input state $|\psi\rangle_{in}$ which is the state of a (two-mode) parametric down-conversion process introduced in the equation (2.97):

$$|\psi\rangle_{in} = \sum_{n=0}^{N} \frac{\tanh^n(\lambda)}{\cosh(\lambda)}|n,n\rangle \tag{4.10}$$

where λ is related to the average number of particles $\langle n\rangle = \sinh^2(\lambda)$. From the equations (2.93) and (2.94), we obtain

$$G^{(2)}_{cd,Ind} = 2\langle n\rangle^2,$$
$$G^{(2)}_{cd,Dis} = \langle n\rangle(1+2\langle n\rangle)$$

which produces the visibility of

$$\bar{V} = 1 - \frac{G^{(2)}_{cd,Ind}}{G^{(2)}_{cd,Dis}} = 1 - \frac{1}{2+\frac{1}{2\langle n\rangle}}. \tag{4.11}$$

The plot of the visibility $\bar{V}$ as a function of the average population $\langle n\rangle$ is shown in the figure 4.5. We see that as the average population increases $\langle n\rangle \to \infty$ the visibility tends to the classical limit value 0.5.

So far we considered two-mode input state with equal populations and we have seen that when the average population per mode increases the visibility approaches the classical limit. In this regime, we can not talk about quantum effect anymore. This behaviour is in general true when the input particle population and as well as the number of modes increase [30, 73, 137].

The visibility $\bar{V}$ can be related to the Cauchy-Schwarz inequality (CS) which can be written as [81]

$$G^{(2)}_{ab} \leq \sqrt{G^{(2)}_{aa}G^{(2)}_{bb}}. \tag{4.12}$$

The CS inequality is omnipresent in physics and mathematics and it is used in the proofs of the number of theorems. It simply states the fact that the inner product of two vectors cannot be larger than the product of their lengths or if we apply to classical fields it states that no classical fields can produce the joint probability of detection at two different points in space where the mean intensities are equal, greater than that

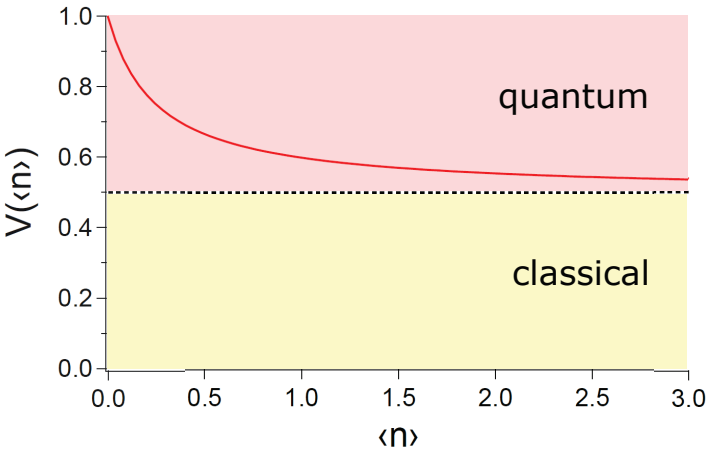

FIGURE 4.5: **The visibility of the HOM dip as a function of the average population with the source of the two-mode parametric down conversion process(solid line in red).** It converges rapidly to the classical limit 0.5 shown with black dashed lines, as a function of the average population.

for two detections at the same point. Therefore, violation of the CS inequality is only possible for nonclassical states such as $|1_a, 1_b\rangle$ for which $G^{(2)}_{ab} = 1$ and $G^{(2)}_{aa} = G^{(2)}_{bb} = 0$. The connection between the CS inequality violation and the entanglement is discussed in [143].

Using (4.8) and (4.9), the visibility can be rewritten as:

$$\bar{V} = \frac{1}{1 + \frac{\delta}{C}} \tag{4.13}$$

with

$$\delta = \frac{G^{(2)}_{aa} + G^{(2)}_{bb}}{2\sqrt{G^{(2)}_{aa} G^{(2)}_{bb}}}$$

and

$$C = \frac{G^{(2)}_{ab}}{\sqrt{G^{(2)}_{aa} G^{(2)}_{bb}}}.$$

Having the value of the CS parameter greater than one ($C > 1$), indicates the violation of the CS inequality. Also, we see that the parameter δ is lower bounded $\delta \geq 1$, since $G^{(2)}_{aa,bb} \geq 0$ and it is equal to 1 when $G^{(2)}_{aa} = G^{(2)}_{bb}$. The classical limit of 0.5 is obtained for the minimum value of δ, i.e. for $\delta = 1$. By fixing $\delta = 1$, the visibility is given in terms of the paramter C:

$$\bar{V} = \frac{1}{1 + \frac{1}{C}}. \tag{4.14}$$

For $C \geq 1$, the visibility $\bar{V}$ goes above 50% as expected. The advantage of expressing the visibility in terms of the CS parameter C is that one can predict the visibility of the

HOM dip by measuring the C parameter before carrying out the HOM experiment.

4.2 The atomic HOM signal

The ability to create nonclassical source is at the heart of the experimental advancements of quantum physics. The cold atoms community is in the developing stage of nonclassical pair creation and manipulation compared to the mature quantum optics community. Nevertheless, several promising results were already obtained in the atomic community concerning the creation of atomic pairs correlated with internal degrees of freedom [19, 59, 91] as well as with external degrees of freedom [25, 29, 110, 141]. Such atomic sources can provide more degrees of freedom (internal, external, bosonic and fermionic) and strong non-linearity for quantum information in contrast to the optical sources. To manipulate atomic pair in the low gain regime which is necessary for the realisation of HOM type experiments with atoms, the detection at single atomic level is desirable. Today, several single atom resolved imaging techniques exist such as fluorescence imaging of trapped atoms in the lattice or in an array of tweezers [9, 132, 145], or again fluorescence resonance imaging with light sheet [26], or the electronic detection of metastable helium atoms (see Appendix D). Possessing the essential experimental ingredient: the detector with single atom resolution we realised the HOM experiment using neutral atoms and by manipulating their external degrees of freedom. The other known example of an HOM-like experiment with neutral atoms in real space is in [80]. Note that for the HOM experiment the atomic pair source is not obligatory but using the pair source provides good statistics. Moreover, in our case, observing the two particle interference with our atomic source opens the way to test the Bell's inequality involving external degrees of massive particles. The experimental scheme we employ for the atomic HOM experiment is shown in the figure 4.6 which is very similar to the one we discussed for the Bell's experiment. The only difference is that here we do not control the phase of the interferometer and we are not selective in momentum modes with the beamsplitter. Thus we apply a single mirror Bragg pulse and a single beamsplitter Bragg pulse. In order to tune the distinguishability we adjust the application time of the beamsplitter Bragg pulse. The scheme of the experiment in the figure 4.6 is very similar to the original experiment (figure 4.4) carried out with photons. The main difference is that the atomic mirror and beamsplitter translate the momentum distribution while mirror and beamsplitter for photons make a mirror image of momentum distribution. The pair of atoms a and b are produced at $t \approx 0$ from the dynamical instability process as explained before. The paths of a and b is made to interfere by applying a mirror and a beamsplitter. We apply a single π-pulse at time $t = t_m$ and a single $\pi/2$ pulse at time $t = t_s$ to realize the interferometer. We measure the joint-detection or equivalently

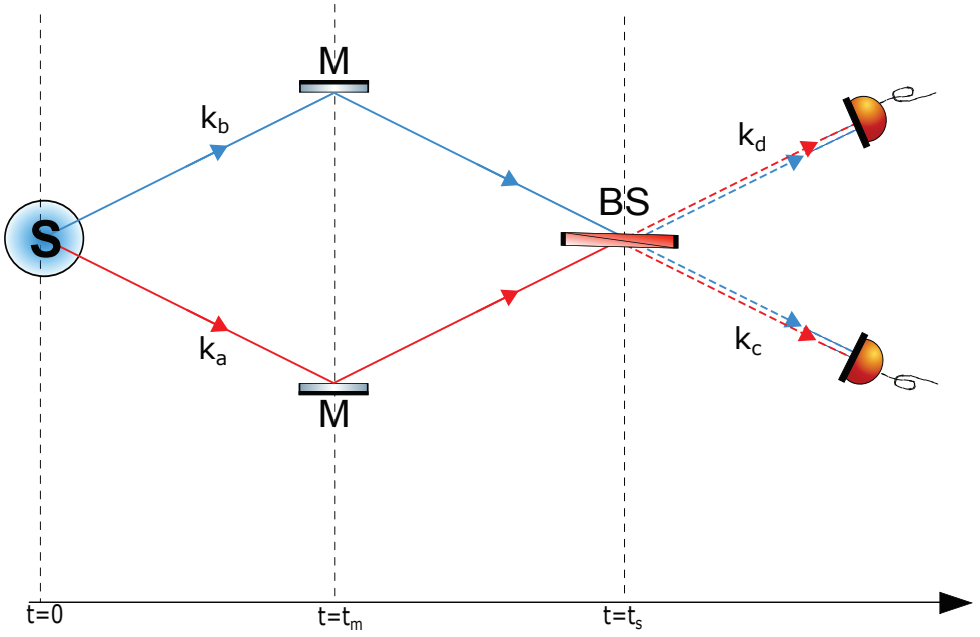

FIGURE 4.6: **The experimental scheme of an atomic Hong-Ou-Mandel experiment.** A pair of atoms a and b is produced at time $t = 0$, they propagate freely before the π-bragg pulse (atomic mirror)is applied to superpose them on to the atomic beamsplitter, $\pi/2$-bragg pulse. The joint detection between the outputs at the detector is measured and it is expected the full suppression of the joint detection when the two bosonic particles are indistinguishable.

cross-correlation between the two outputs of the beamsplitter on the detector:

$$G^{(2)}_{cd} = \frac{\eta^2}{\Omega_{V_c}\Omega_{V_d}} \int_{\Omega_{V_c}} \int_{\Omega_{V_d}} \mathrm{d}^3\mathbf{k_c}\, \mathrm{d}^3\mathbf{k_d} \langle \hat{n}_{\mathbf{k_c}} \hat{n}_{\mathbf{k_d}} \rangle. \tag{4.15}$$

where Ω_{V_c}, Ω_{V_d} are volumes of analysis centered around mean momenta $\bar{\mathbf{k}}_\mathbf{c}$ and $\bar{\mathbf{k}}_\mathbf{d}$ respectively. Note that in the real experiment, the MCP detector with efficiency η registers the atoms resolving in momentum. The quantity $G^{(2)}_{cd}$ is measured by counting the number of atoms inside the volumes of analysis. The result of the measurement of the experimental cross-correlation $G^{(2)}_{cd}$ is plotted as a function of the duration $\tau = t_s - t_m$ in the figure 4.7. The HOM-dip appears clearly from the experimental data points (filled circles) at the expected value of duration $\tau = 550(50) \simeq t_m$ μs for which the two particle amplitudes become indistinguishable. The error bars denote the standard deviation of the statistical ensemble. The integration volumes are chosen as to optimize the signal to noise ratio of the visibility of the HOM-dip and are set to $\Omega_{V_c} = \Omega_{V_d} = [\mathcal{L}^2_\perp \mathcal{L}_z] = [0.048^2 \times 0.028](k^3_{rec})$ centered longitudinally around $k_c = 0.740\ k_{rec}$ and $k_d = 1.275\ k_{rec}$. Each experimental point is averaged over 500 to 1000 repetitions of the experiment amounting to 10 hours of integration time. The product of the output mean populations

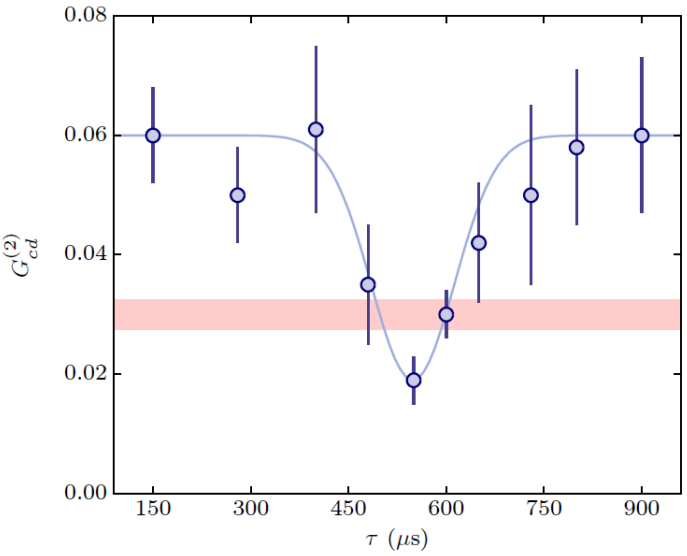

FIGURE 4.7: **The atomic HOM-dip signal: the cross-correlation function $G^{(2)}_{cd}$ between outputs of the beamsplitter as a function of the duration $\tau = t_s - t_m$.** The HOM-dip appears clearly from the experimental data points (filled circles) at the expected value of duration $\tau = 550(50)$ μs $\simeq t_m$ for which the two-particle amplitudes become indistinguishable. Each experimental point is averaged over 500 to 1000 repetitions of the experiment and error bars denote the standard deviation of the statistical ensemble. A Gaussian fit (blue line) gives the half width at $1/\sqrt{e}$ of 70(30) μs and the visibility of $\bar{V} = 0.65(7)$. The measured visibility is two standard deviations below the estimated classical-to-quantum threshold represented by the red shaded area.

$\langle n_c \rangle \cdot \langle n_d \rangle$ is kept constant during the two weeks of data acquisition time [87]. We fit the experimental data with the empirical Gaussian function (blue line) defined as

$$G^{(2)}(\tau) = G^{(2)}_0 \left(1 - \bar{V} e^{-\frac{(\tau-\tau_0)^2}{2\sigma^2_{hom}}}\right) \tag{4.16}$$

From the fit result, we obtain the half width at $1/\sqrt{e}$ of $\sigma_{hom} = 70(30)$ μs and the visibility of $\bar{V} = 0.65(7)$. The measured visibility is two standard deviations below the estimated classical-to-quantum threshold represented by the red shaded area. The threshold value is set to the half of the measured value of $G^{(2)}_{cd,Dis}$. The width of the threshold band comes from the uncertainty of the measured correlation function.

In the following, we are going to consider a 1-dimensional model ($z-$axis) and we will neglect the gravity as it does not play a role here. We will evaluate

$$\begin{aligned} G^{(2)}_{cd} &= \eta^2 \int\int \mathrm{d}k_c \, \mathrm{d}k_d \langle \hat{a}^\dagger_{k_c} \hat{a}_{k_c} \hat{a}^\dagger_{k_d} \hat{a}_{k_d} \rangle. \\ &= \eta^2 \int\int \mathrm{d}k_c \, \mathrm{d}k_d \| \hat{a}_{k_c} \hat{a}_{k_d} \rangle \|^2 \end{aligned}$$

where the operators are written in the Heisenberg picture and they annihilate or create a particle with corresponding plane wave momentum. We will write the operators $\hat{a}_{k_c}(t >$

$t_s) = \hat{a}_{k_a}(t > t_s)$ and $\hat{a}_{k_d}(t > t_s) = \hat{a}_{k_b}(t > t_s)$ in terms of operators at time $t = 0$. In doing so, we will use the atomic beamsplitter input-output relations similar to the matrix 4.2:

$$\begin{pmatrix} \hat{d} \\ \hat{c} \end{pmatrix} = \begin{pmatrix} \sqrt{t} & \imath\sqrt{r}e^{-\imath\phi} \\ \imath\sqrt{r}e^{\imath\phi} & \sqrt{t} \end{pmatrix} \begin{pmatrix} \hat{b} \\ \hat{a} \end{pmatrix} \tag{4.17}$$

where for ideal atomic mirror $r = r_m = 1$, $t = t_m = 0$ and $\phi = \phi_m$ whereas for ideal atomic beamsplitter $r = r_s = \frac{1}{2}$, $t = t_m = \frac{1}{2}$, $\phi = \phi_s$. Here the phase ϕ comes from the phase of the optical lattice created by the Bragg beams. So the annihilation operators on the detector are related to the annihilation operators at time $t = 0$ by (we did similar calculation in the Chapter 2 subsection 2.2.5):

$$\begin{aligned} \hat{a}_{k_a}(t > t_s) &= e^{-\imath/\hbar E_{k_a}(t-t_s)}\Big(A_{k_a+\Delta k_B}\hat{a}_{k_a+\Delta k_B} + A_{k_a}\hat{a}_{k_a}\Big) \\ \hat{a}_{k_b}(t > t_s) &= e^{-\imath/\hbar E_{k_b}(t-t_s)}\Big(A_{k_b-\Delta k_B}\hat{a}_{k_b-\Delta k_B} + A_{k_b}\hat{a}_{k_b}\Big) \end{aligned}$$

where

$$\begin{aligned} A_{k_a+\Delta k_B} &= \imath\sqrt{r_m t_s}e^{\imath\phi_m}e^{-\imath/\hbar(E_{k_a+\Delta k_B}t_m + E_{k_a}(t_s-t_m))} \\ A_{k_a} &= -\sqrt{r_m r_s}e^{\imath(\phi_s-\phi_m)}e^{-\imath/\hbar(E_{k_a}t_m + E_{k_a+\Delta k_B}(t_s-t_m))} \\ A_{k_b} &= -\sqrt{r_m r_s}e^{\imath(\phi_m-\phi_s)}e^{-\imath/\hbar(E_{k_b}t_m + E_{k_b-\Delta k_B}(t_s-t_m))} \\ A_{k_b-\Delta k_B} &= \imath\sqrt{r_m t_s}e^{-\imath\phi_m}e^{-\imath/\hbar(E_{k_b-\Delta k_B}t_m + E_{k_b}(t_s-t_m))} \end{aligned}$$

with $E_i = \frac{\hbar^2 k_i^2}{2m}$. So the cross-correlation on the detector in terms of operators at time $t = 0$ is given by:

$$\begin{aligned} G^{(2)}_{cd} = \eta^2 \int\int \mathrm{d}k_a\,\mathrm{d}k_b \\ \times\|A_{k_a+\Delta k_B}A_{k_b}\hat{a}_{k_a+\Delta k_B}\hat{a}_{k_b}|\Psi\rangle + A_{k_a}A_{k_b-\Delta k_B}\hat{a}_{k_a}\hat{a}_{k_b-\Delta k_B}|\Psi\rangle \\ + A_{k_a}A_{k_b}\hat{a}_{k_a}\hat{a}_{k_b}|\Psi\rangle + A_{k_a+\Delta k_B}A_{k_b-\Delta k_B}\hat{a}_{k_a+\Delta k_B}\hat{a}_{k_b-\Delta k_B}|\Psi\rangle\|^2. \end{aligned} \tag{4.18}$$

Ideal state. First we consider the ideal state (in analogy with 2.130):

$$|\Psi\rangle = \int\int \mathrm{d}k_a\,\mathrm{d}k_b f_{ab}(k_a, k_b)|1_{k_a}, 1_{k_b}\rangle \tag{4.19}$$

in which only two correlated atoms at a time is produced and where

$$f_{ab} = \sqrt{\frac{2}{\pi\sigma_\perp\sigma_{\shortparallel}}}\exp\Big\{-\frac{(k_a+k_b-2k_{Lat})^2}{2\sigma_\perp^2}\Big\}\exp\Big\{-\frac{(k_b-k_a-\Delta k_B)^2}{2\sigma_{\shortparallel}^2}\Big\}$$

Inserting this state, the $G^{(2)}_{cd}$ becomes:

$$\begin{aligned} G^{(2)}_{cd} &= \eta^2 \int\int \mathrm{d}k_a\, \mathrm{d}k_b \| A_{k_a} A_{k_b} f_{ab} + A_{k_a+\Delta k_B} A_{k_b-\Delta k_B} f_{ab} \|^2 \\ = \; & r_m^2 (r_s^2 + t_s^2)\eta^2 \int\int \mathrm{d}k_a\, \mathrm{d}k_b |f_{ab}|^2 \Big\{ 1 - \frac{2 r_s t_s}{r_s^2 + t_s^2} \cos\big(\frac{\hbar}{m} \Delta k_B (t_s - 2t_m)(k_b - k_a - \Delta k_B)\big) \Big\} \end{aligned} \tag{4.20}$$

We see that the interference is between two particle amplitudes that are reflected $A_{k_a} A_{k_b}$ and transmitted $A_{k_a+\Delta k_B} A_{k_b-\Delta k_B}$ as it was discussed in the figure 4.2. If the integration limits $\mathcal{L}_{k_a}$ and $\mathcal{L}_{k_b}$ are large compared to the width of f_{ab}, we can obtain analytical result of the cross correlation:

$$G^{(2)}_{cd}(\tau) = \eta^2 r_m^2 (r_s^2 + t_s^2) \Big(1 - \bar{V} e^{-\frac{(\tau - t_m)^2}{2\sigma^2_{hom}}} \Big) \tag{4.21}$$

where $\tau = t_s - t_m$ and the half-width of HOM signal at $1/\sqrt{e}$ is given by

$$\sigma_{hom} = \frac{\sqrt{2} m}{\hbar \Delta k_B} \frac{1}{\sigma_{\shortparallel}} \tag{4.22}$$

and the visibility is given by

$$\bar{V} = \frac{2 r_s t_s}{r_s^2 + t_s^2}. \tag{4.23}$$

It is exactly the same result of the original HOM experiment with photons.

We assumed that limits of the integrations are large compared to the size of integrand. However, experimentally we have one of the size of f_{ab} ($\sigma_{\shortparallel} = 0.072$ k_{rec}, $\sigma_{\perp} = 0.024$ k_{rec}) greater than the size of volumes of analyse ($\mathcal{L}_z = 0.028$ k_{rec}) and it should be taken into account. With photons, by varying the delay between two incident photons, they measured a temporal width which was proportional to the inverse of passband of temporal filter while with atoms by varying the spatial overlap of atoms we measure a spatial width which is proportional to the inverse of momentum width $\sigma_{\shortparallel}$. This width can be in general modified by the size of the volumes of analysis and the selectivity of a Bragg pulse that act as a spatial filter. The spatial filtering effect of volumes of analysis is taken care by setting the limits of the integration in the equation 4.20 and the spatial filtering effect of the Bragg pulse can be taken care by expressing the coefficients r_m, r_s and t_s in the equation 4.20 as a probability function of the Bragg pulse (see Bragg selectivity in the Chapter 3). We simplify the Bragg selectivity by considering it only for π pulse which is more selective than the $\pi/2$ pulse and we model the reflectivity of a π pulse with a gaussian. In other words, we write

$$r_m^2 = \exp\Big\{ - \frac{(k_a - \bar{k}_a)^2 + (k_b - \bar{k}_b)^2}{2\sigma_m^2} \Big\}.$$

So, the equation 4.20 becomes

$$G^{(2)}_{cd} = (r_s^2 + t_s^2)\eta^2 \int_{-\mathcal{L}_z/2}^{+\mathcal{L}_z/2} \int_{-\mathcal{L}_z/2}^{+\mathcal{L}_z/2} \mathrm{d}k_a\, \mathrm{d}k_b |f_{ab}|^2 e^{\left(-\frac{(k_a-\bar{k}_a)^2+(k_b-\bar{k}_b)^2}{2\sigma_m^2}\right)} \times \left\{1 - \frac{2r_s t_s}{r_s^2 + t_s^2} \cos\left(\frac{\hbar}{m}\Delta k_B (t_s - 2t_m)(k_b - k_a - \Delta k_B)\right)\right\}.$$

We integrate above expression numerically for two different values of the integration limit $\mathcal{L}_z = 0.048\ \mathrm{k}_{rec}$ and $\mathcal{L}_z = 0.028\ \mathrm{k}_{rec}$ and we plot the result in the figure 4.8 as a function of τ, the time of application of the $\pi/2$ pulse where we fix the following parameters to their experimental values (see Chapter 3 and thesis [87]): $\eta = 0.25$, $r_s = t_s = \frac{1}{2}$, $\sigma_{\shortparallel} = 0.072\ \mathrm{k}_{rec}$, $\sigma_{\perp} = 0.024\ \mathrm{k}_{rec}$, $\sigma_m = 0.07\ \mathrm{k}_{rec}$, $\Delta k_B = 0.56\ \mathrm{k}_{rec}$, $\bar{k}_a = 0.74\ \mathrm{k}_{rec}$ and $\bar{k}_b = 1.3\ \mathrm{k}_{rec}$. Firstly, we see that the amplitude of $G^{(2)}_{cd}$ scales proportional to

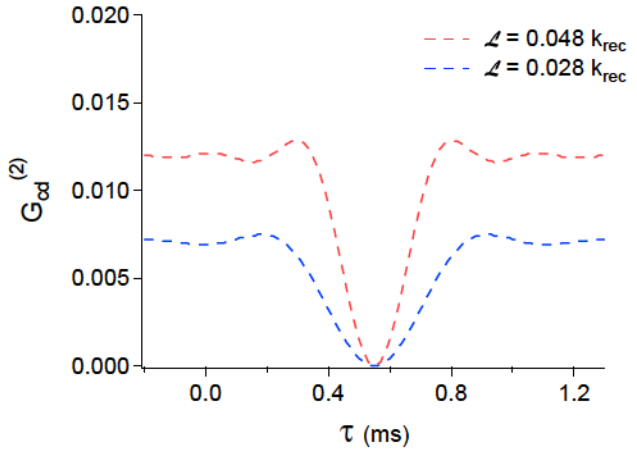

FIGURE 4.8: Plot of theoretical $G^{(2)}_{cd}$ as a function of τ for two different integration lengths $\mathcal{L}_z = 0.048(k_{rec})$ and $\mathcal{L}_z = 0.028(k_{rec})$.

the integration limit size which is expected since we integrate smaller signal for smaller integration length. Secondly, $G^{(2)}_{cd}$ scales inversely with the size of length of analyse $\mathcal{L}_z$ showing that the width of the HOM signal is modified essentially by the size of the volume of analysis. It is acceptable since the size of the analysis is the smallest length scale in the experiment. The estimated half-widths at $1/\sqrt{e}$ (figure 4.8) are 140 μs and 95 μs for $\mathcal{L}_z = 0.028\ \mathrm{k}_{rec}$ and $\mathcal{L}_z = 0.048\ \mathrm{k}_{rec}$ respectively. We compare these values with the measured values [87] $\sigma_{HOM,\mathcal{L}_z=0.028} = 70(30)$ μs and $\sigma_{HOM,\mathcal{L}_z=0.048} = 45(10)$ μs from the experimental data which is shown in the figure 4.9. Although the scaling behaviour is correct (larger $\mathcal{L}_z \rightarrow$ smaller σ_{HOM}), the experimental values of widths of HOM signal is not totally described by the $1D$ theoretical model. We suspect that transverse dimensions play a role in determining the width of the HOM signal. For example, any tilt of the Bragg lattice from the vertical axis translates into imperfect overlap of the atomic beams resulting in a thinner dip.

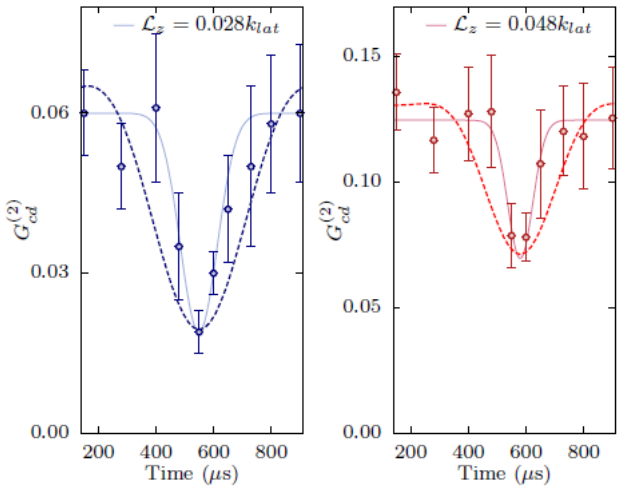

FIGURE 4.9: Experimental HOM dip for two different integration volumes for $\Omega_V = [0.048^2 \times 0.028](k^3_{rec})$ and $\Omega_V = [0.048^2 \times 0.048](k^3_{rec})$. We see that the width of the cross correlation scales inversely with length of analyse box.

The theoretical visibility of the HOM dip $\bar{V}$ is given only in terms of beamsplitter coefficients r_s and t_s and it is 100% for the ideal case $r_s = t_s = \frac{1}{2}$ while it is greater than 90% for non-perfect experimental values of transmission and reflection coefficients $r_s = 0.4$ and $t_s = 0.6$. Also, the visibility does not depend on the detector efficiency η. So the observed visibility 0.65(7) does not fit with the description using the ideal state $|\Psi\rangle$ and we knew it already from the experimental measurements of auto and cross correlation functions where latter one was not higher than the former one to allow the approximation of pair state with $|\Psi\rangle$ (see Chapter 2 subsection 2.2.3.4). For photons, the approximation of the state of their source by the similar expression as (4.19) is easily justified because they can reduce the average population of pair to a very small values, i.e. $\langle n \rangle \ll 1$ so that the probability of having more than two particles in a pair is negligible. They can do so thanks to the short experimental repetition duration. On the other hand, for atoms with our current experimental cycle duration, attaining the same regime can amount to a quite long data acquisition. In fact, we estimate [87] average populations $\langle n_a \rangle = 0.8(3)$ and $\langle n_b \rangle = 0.5(3)$ for our atomic pair.

To understand the visibility and the width of the observed HOM signal, we take an experimental approach which is described below.

Experimental approach. The real state of our atomic pair contains higher order terms in population. So, here we will not specify the exact state, instead we will make use of the relation between the cross-correlation function $G^{(2)}_{cd}$ and the CS parameter C which we can measure experimentally. The expression 4.18 is general and it contains 16 terms but terms such as $\langle \hat{a}^\dagger_{k_a+\Delta k_B} \hat{a}^\dagger_{k_b} \hat{a}_{k_a} \hat{a}_{k_b-\Delta k_B} \rangle$, $\langle \hat{a}^\dagger_{k_a} \hat{a}^\dagger_{k_b-\Delta k_B} \hat{a}_{k_a} \hat{a}_{k_b} \rangle$, etc. are simplified for

the pair states (containing terms $|n,n\rangle$). The surviving terms are

$$\begin{aligned} G^{(2)}_{cd} &= \eta^2 \int\int \mathrm{d}k_a\,\mathrm{d}k_b \\ &\times \|A_{k_a+\Delta k_B} A_{k_b} \hat{a}_{k_a+\Delta k_B}\hat{a}_{k_b}|\Psi\rangle + A_{k_a} A_{k_b-\Delta k_B}\hat{a}_{k_a}\hat{a}_{k_b-\Delta k_B}|\Psi\rangle\|^2 \\ &+ \|A_{k_a} A_{k_b}\hat{a}_{k_a}\hat{a}_{k_b}|\Psi\rangle + A_{k_a+\Delta k_B} A_{k_b-\Delta k_B}\hat{a}_{k_a+\Delta k_B}\hat{a}_{k_b-\Delta k_B}|\Psi\rangle\|^2. \quad (4.24) \end{aligned}$$

The interfering term of the second line is proportional to the phase of the Bragg lattice $\phi_s - 2\phi_m$ which we do not control in the experiment and it will average to zero. So, the cross-correlation further reduces to:

$$\begin{aligned} G^{(2)}_{cd} &= \eta^2 \int\int \mathrm{d}k_a\,\mathrm{d}k_b \\ &\times \Bigg(\frac{1}{4}\langle \hat{a}^\dagger_{k_a}\hat{a}^\dagger_{k_b-\Delta k_B}\hat{a}_{k_a}\hat{a}_{k_b-\Delta k_B}\rangle + \frac{1}{4}\langle \hat{a}^\dagger_{k_a+\Delta k_B}\hat{a}^\dagger_{k_b}\hat{a}_{k_a+\Delta k_B}\hat{a}_{k_b}\rangle \\ &+ \frac{1}{4}\langle \hat{a}^\dagger_{k_a}\hat{a}^\dagger_{k_b}\hat{a}_{k_a}\hat{a}_{k_b}\rangle + \frac{1}{4}\langle \hat{a}^\dagger_{k_a+\Delta k_B}\hat{a}^\dagger_{k_b-\Delta k_B}\hat{a}_{k_a+\Delta k_B}\hat{a}_{k_b-\Delta k_B}\rangle \\ &- \frac{1}{2}\cos\Big(\frac{\hbar}{m}\Delta k_B(t_s-2t_m)(k_b-k_a-\Delta k_B)\Big)\langle \hat{a}^\dagger_{k_a+\Delta k_B}\hat{a}^\dagger_{k_b-\Delta k_B}\hat{a}_{k_a}\hat{a}_{k_b}\rangle \Bigg) \end{aligned}$$

where the last term is equal to the cross correlation for $k_b - \Delta k_B = k_a$. Assuming that the contributions of this term for $k_b - \Delta k_B \neq k_a$ can be neglected (phase matching condition of the pair production corresponds to $k_b - \Delta k_B = k_a$), we can cast $G^{(2)}_{cd}$ in the known form:

$$\begin{aligned} G^{(2)}_{cd,Ind} &\approx \frac{1}{4}\Big(G^{(2)}_{aa} + G^{(2)}_{bb}\Big), \\ G^{(2)}_{cd,Dis} &\approx \frac{1}{4}\Big(G^{(2)}_{aa} + G^{(2)}_{bb}\Big) + \frac{1}{2}G^{(2)}_{ab}. \end{aligned}$$

and as we have seen before in the equation 4.13 the visibility is given by

$$\bar{V} = \frac{1}{1+\frac{\delta}{C}} \quad (4.25)$$

with $\delta = \frac{G^{(2)}_{aa}+G^{(2)}_{bb}}{2\sqrt{G^{(2)}_{aa}G^{(2)}_{bb}}}$ and $C = \frac{G^{(2)}_{ab}}{\sqrt{G^{(2)}_{aa}G^{(2)}_{bb}}}$. We measure C as a function of the integration volume which is plotted in the figure 4.10. For the integration volume of the atomic HOM-signal, $\mathcal{L}_z = 0.028\ k_{rec}$ and $\mathcal{L}_\perp = 0.048\ k_{rec}$, we find $C = 1.75(2)$ and $\delta = 1.15(5)$. The expected visibility is then equal to

$$\bar{V} = 0.60(1) \quad (4.26)$$

which agrees with the measured visibility 0.65(7). Therefore, we conclude that the visibility is constrained by the population of the two incoming beams.

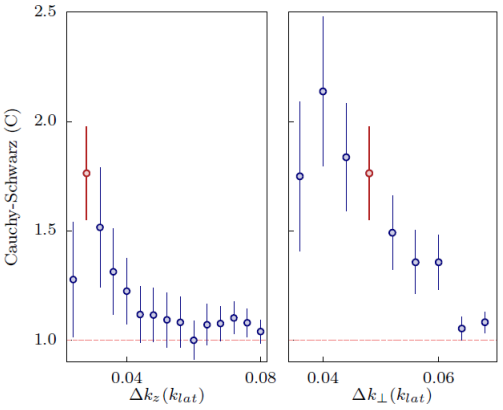

FIGURE 4.10: The CS parameter C as a function of the integration volume along a) longitudinal axis fixing $\Delta k_\perp = 0.05\ k_{rec}$ and b) transverse axis fixing $\Delta k_z = 0.028\ k_{rec}$.The threshold limit between classical and quantum correlations $C = 1$ is represented by the red dashed line and the experimental data in red corresponds to the integration volume of the HOM-dip signal.

In contrast to photons, atoms interact with each other and it is interesting to know the role of the interactions. The effect of the interactions between atoms in evaluating the HOM-dip visibility is studied in detail in [4] and their result is shown in the figure 4.11. The relevant parameter is the ratio between the two photon Rabi frequency of the Bragg pulse and the chemical potential of the pairs which is equal to $\frac{\mu}{2\hbar\Omega_R} = 0.033$ for our experimental parameters [87]. It is obvious that this value is too small to shift the visibility considerably.

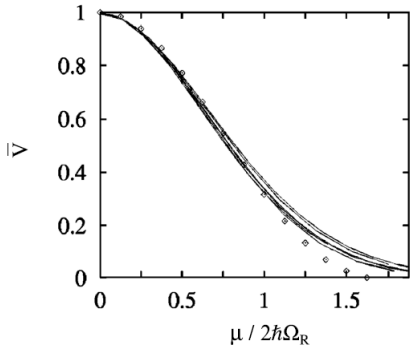

FIGURE 4.11: Evolution of the HOM visibility as a function of the ratio between the chemical potential and 2−photon Rabi frequency(figure copied from [4]).

4.3 Conclusion

We can conclude that our atomic pair source is indeed non-classical source and we were able to characterize and manipulate with it coherently via the HOM experiment. It

opens an opportunity to test the Bell's inequality with massive particles correlated in external degrees of freedom.

LETTER

doi:10.1038/nature14331

Atomic Hong–Ou–Mandel experiment

R. Lopes[1], A. Imanaliev[1], A. Aspect[1], M. Cheneau[1], D. Boiron[1] & C. I. Westbrook[1]

Two-particle interference is a fundamental feature of quantum mechanics, and is even less intuitive than wave–particle duality for a single particle. In this duality, classical concepts—wave or particle—are still referred to, and interference happens in ordinary space-time. On the other hand, two-particle interference takes place in a mathematical space that has no classical counterpart. Entanglement lies at the heart of this interference, as it does in the fundamental tests of quantum mechanics involving the violation of Bell's inequalities[1–4]. The Hong, Ou and Mandel experiment[5] is a conceptually simpler situation, in which the interference between two-photon amplitudes also leads to behaviour impossible to describe using a simple classical model. Here we report the realization of the Hong, Ou and Mandel experiment using atoms instead of photons. We create a source that emits pairs of atoms, and cause one atom of each pair to enter one of the two input channels of a beam-splitter, and the other atom to enter the other input channel. When the atoms are spatially overlapped so that the two inputs are indistinguishable, the atoms always emerge together in one of the output channels. This result opens the way to testing Bell's inequalities involving mechanical observables of massive particles, such as momentum, using methods inspired by quantum optics[6,7], and to testing theories of the quantum-to-classical transition[8–11]. Our work also demonstrates a new way to benchmark non-classical atom sources[12,13] that may be of interest for quantum information processing[14] and quantum simulation[15].

A pair of entangled particles is described by a state vector that cannot be factored as a product of two state vectors associated with each particle. Although entanglement does not require that the two particles be identical[2], it arises naturally in systems of indistinguishable particles owing to the symmetrization of the state, which leads to non-trivial, multiparticle interference. A remarkable illustration is the Hong, Ou and Mandel (HOM) experiment, in which two photons enter the two input channels of a 50:50 beam-splitter (one photon in each channel) and the correlation is measured between detectors at the two outputs.

A joint detection at these detectors arises from two possible processes: either both photons are transmitted by the beam-splitter or both are reflected (Fig. 1c). For two indistinguishable photons, both processes lead to the same final quantum state and the probability of joint detection results from the addition of their amplitudes. Because the beam-splitter corresponds to a unitary operation, these amplitudes have same modulus but opposite signs, thus their sum vanishes and so also the probability of joint detection[16,17] (see also Methods). To be truly indistinguishable, not only must the photons have the same energy distribution and polarization, but their final spatio-temporal modes must be identical. Thus, the two photons must enter the beam-splitter in modes that are the exact images of each other. As a result, when measured as a function of the delay between the arrival times of the photons on the beam-splitter, the correlation exhibits the 'HOM dip', ideally going to zero at zero delay.

Our experiment is equivalent in all important respects to the HOM experiment, but is performed with bosonic atoms instead of photons. We produce freely propagating twin beams of metastable ^{4}He atoms[18], which we then reflect and overlap on a beam-splitter using Bragg scattering on an optical lattice (ref. 19 and Fig. 1). The photon counters after the beam-splitter are replaced by a time-resolved, multi-pixel atom-counting detector[20], which enables the measurement of intensity correlations between the atom beams in well defined spatial and spectral regions. The temporal overlap between the atoms can be continuously tuned by changing the moment when the atomic beam-splitter is applied. We observe the HOM dip when the atoms simultaneously pass through the beam-splitter. The key technical advance that has enabled

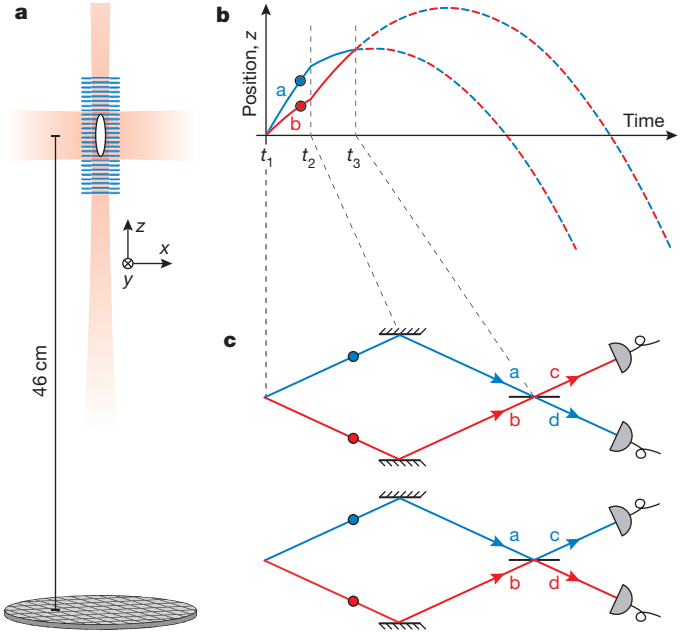

Figure 1 | Schematic of the experiment. a, A Bose–Einstein condensate (BEC, white oval) of metastable ^{4}He atoms is trapped in an elongated optical trap (red shaded area). A moving optical lattice, here depicted in blue, is superimposed on the BEC and triggers the scattering of atom pairs along the z axis. When this lattice and the trap are switched off, the atoms fall towards a microchannel plate detector located 46 cm below the initial position of the BEC (drawing not to scale). **b**, The time diagram shows the evolution of the twin atoms' vertical coordinates (blue line for beam a and red line for beam b). Between t_1 and t_2, t_2 and t_3, and after t_3, the atoms move under the sole influence of gravity (drawing not to scale). At t_2, the twin atom velocities are swapped using Bragg diffraction on an optical lattice. At time t_3, when the atomic trajectories cross again, the same lattice is applied for half the amount of time in order to realize a beam-splitter. The lines alternately dashed in red and blue symbolize the indiscernibility of the atoms' trajectories after the beam-splitter. The filled red and blue circles indicate the position of the atoms at a given time before the beam-splitter is applied. **c**, In the centre-of-mass frame of reference, the trajectories of the atoms resemble those of the photons in the Hong–Ou–Mandel experiment. A joint detection arises either when both atoms are transmitted through the beam-splitter (upper panel) or when both are reflected (lower panel). If the two particles are indistinguishable, these processes end in the same final quantum state and the probability of joint detection results from the addition of their amplitudes. For bosons these amplitudes have same modulus but opposite signs, thus their sum vanishes and so also does the probability of joint detection.

[1]Laboratoire Charles Fabry, Institut d'Optique Graduate School – CNRS – Université Paris Sud, 2 avenue Augustin Fresnel, 91127 Palaiseau, France.

this work was the improvement of the atom pair production so as to permit optimal adjustment of the mode populations[18].

We begin by producing a Bose–Einstein condensate (BEC) of metastable ^{4}He atoms in the $1s2s\ ^3S_1$ internal state (here we represent this by $2\ ^3S_1$), with the projection of the total electronic angular momentum $m = 1$. The BEC contains $(5–6) \times 10^4$ atoms and is confined in an elliptical optical trap with its long axis along the vertical (z) direction (Fig. 1a). The atomic cloud has radii of 58 and 5 μm along the longitudinal (z) and transverse ($\perp$) directions, respectively. A moving optical lattice, superimposed on the BEC for 300 μs, induces the scattering of atom pairs (hereafter referred to as twin atoms) in the longitudinal direction through a process analogous to spontaneous four-wave mixing[18,21,22] (see also Methods). This mixing process resembles that used in refs 23–25 to generate entangled states in the spin sector, but it involves the motional degrees of freedom. One beam, labelled a, has a free-space velocity $v_z \approx 12.1\ \mathrm{cm\ s^{-1}}$ in the laboratory frame of reference and the other beam, labelled b, has a velocity $v_z \approx 7.0\ \mathrm{cm\ s^{-1}}$ (Fig. 1b, c). The twin atom beams clearly appear in the velocity distribution of the atoms, which is displayed in Fig. 2. The visible difference in population between the beams is attributed to secondary scattering processes in the optical lattice, leading to the decay over time of the quasi-momentum states[18]. After the optical lattice has been switched off (at time t_1), the twin atoms propagate in the optical trap for 200 μs. At this moment, the trap itself is switched off and the atoms are transferred to the magnetically insensitive $m = 0$ internal state by a two-photon Raman transition (Methods).

From here on, the atoms evolve under the influence of gravity and continue to move apart (Fig. 1b). At time $t_2 = t_1 + 500$ μs, we deflect the beams using Bragg diffraction on a second optical lattice, so as to make them converge. In the centre-of-mass frame of reference, this deflection reduces to a simple specular reflection (Fig. 1c and Methods). At time $t_3 \approx 2t_2 - t_1$, we apply the same diffraction lattice for half the amount of time in order to realize a beam-splitting operation on the crossing atom beams. Changing the time t_3 allows us to tune the degree of temporal overlap between the twin atoms. Figure 1c shows the atomic trajectories in the centre-of-mass frame of reference and reveals the close analogy with a photonic HOM experiment.

The atoms end their fall on a microchannel plate detector located 46 cm below the position of the initial BEC, and we record the time and transverse position of each atomic impact with a detection efficiency $\eta \approx 25\%$ (Methods). The time of flight to the detector is approximately 300 ms, long enough for the recorded signal to yield the three components of the atomic velocity. By collecting data from several hundred repetitions of the experiment under the same conditions, we are able to reconstruct all desired atom number correlations within variable integration volumes of extent $\Delta v_z \times \Delta v_\perp^2$. These volumes play a similar role to that of the spatial and spectral filters in the HOM experiment and can be adjusted to erase the information that could allow tracing back the origin of a detected particle to one of the input channels.

The HOM dip should appear in the cross-correlation between the detection signals in the output channels of the beam-splitter[16] (see also Methods), $G^{(2)}_{\mathrm{cd}}$:

$$G^{(2)}_{\mathrm{cd}} = \left(\frac{\eta}{\Delta v_z \Delta v_\perp^2}\right)^2 \int\int_{\mathcal{V}_\mathrm{c}\times\mathcal{V}_\mathrm{d}} \left\langle \hat{a}^\dagger_{v_\mathrm{c}} \hat{a}^\dagger_{v_\mathrm{d}} \hat{a}_{v_\mathrm{d}} \hat{a}_{v_\mathrm{c}} \right\rangle \mathrm{d}^3 v_\mathrm{c}\, \mathrm{d}^3 v_\mathrm{d} \qquad (1)$$

Here, $\hat{a}_v$ and $\hat{a}^\dagger_v$ denote the annihilation and creation operators of an atom with three-dimensional velocity $\boldsymbol{v}$, respectively, $\langle\cdot\rangle$ stands for the quantum and statistical average and $\mathcal{V}_{\mathrm{c,d}}$ designates the integration volumes centred on the output atom beams c and d (Fig. 1c). We have measured this correlation as a function of the duration of propagation $\tau = t_3 - t_2$ between the mirror and the beam-splitter (Fig. 3) and for various integration volumes (see Methods and Extended Data Fig. 1). We observe a marked reduction of the correlation when τ is equal to the duration of propagation from the source to the mirror ($t_3 - t_2 \approx t_2 - t_1$) and for small enough integration volumes, corresponding to a

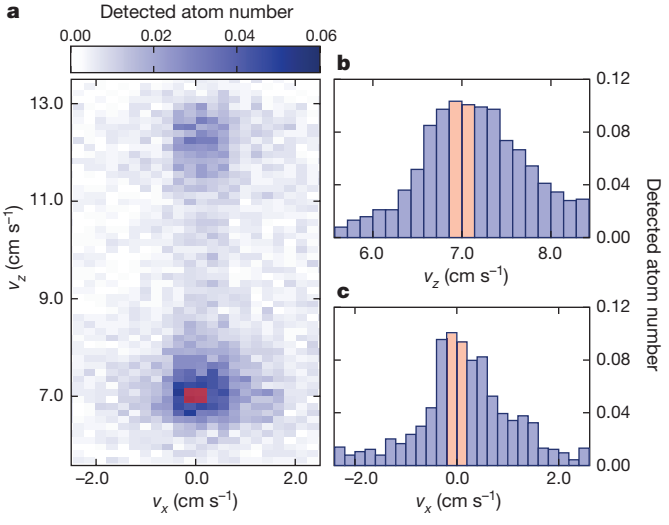

Figure 2 | Velocity distribution of the twin atoms. **a**, Two-dimensional velocity distribution of the twin atom beams emitted by the source. The red shaded area, drawn here only for the lower beam, labelled b in Fig. 1b and c, shows the integration volume $\mathcal{V}_\mathrm{b}$ used for computing the correlation function displayed in Fig. 3. The distribution corresponds to an average over about 1,100 measurements and is not corrected for the limited detection efficiency. The velocities are given relative to the laboratory frame of reference. The size of each pixel is $0.24\ \mathrm{cm\ s^{-1}}$ in the transverse directions (x and y) and $0.14\ \mathrm{cm\ s^{-1}}$ in the longitudinal (z) direction and an integration over 2 pixels is performed along the y direction. **b**, **c**, Cuts of the two-dimensional velocity distribution through the centre of the lower beam along the longitudinal (**b**) and transverse (**c**) directions. The data points result from the average over 2 pixels along the direction perpendicular to the cut. The red shaded area again shows the integration volume.

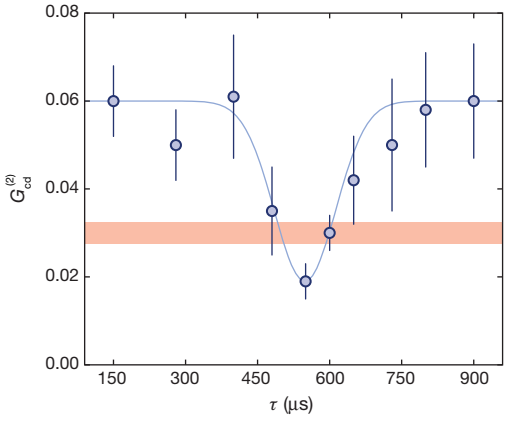

Figure 3 | HOM dip in the cross-correlation function. The correlation $G^{(2)}_{\mathrm{cd}}$ between the output channels of the beam-splitter, defined in equation (1), was measured as a function of the duration of propagation $\tau = t_3 - t_2$ between the mirror and the beam splitter. The HOM dip is directly visible as a marked reduction of the correlation when τ approximately equals the duration of propagation between the source and the mirror, $t_2 - t_1 \approx 500$ μs. This situation corresponds to symmetric paths between the source and the beam-splitter, that is, when one cannot distinguish between the two diagrams of Fig. 1c. A Gaussian fit (blue line) precisely locates the dip at $\tau = 550(50)$ μs, with a full-width at half-maximum of 150(40) μs, where the uncertainty corresponds to the 68% confidence interval. The fitted value of the background correlation is 0.060(5) and the measured visibility is $V = 0.65(7)$. It is two standard deviations beyond the classical-to-quantum threshold represented by the red shaded area, at half the background correlation value. Each data point was obtained from an average over about 500 to 1,400 repetitions of the experiment. Error bars denote the standard deviation of the statistical ensemble. The mean detected atom number was constant over the range of values of τ displayed here (see Methods and Extended Data Fig. 2).

full overlap of the atomic wave-packets on the beam-splitter. Fitting the data with an empirical Gaussian profile yields a visibility:

$$V = \frac{\max_\tau G^{(2)}_{cd}(\tau) - \min_\tau G^{(2)}_{cd}(\tau)}{\max_\tau G^{(2)}_{cd}(\tau)} = 0.65(7) \quad (2)$$

where the number in parenthesis stands for the 68% confidence interval. As we shrink the integration volumes, we observe that the dip visibility first increases and then reaches a saturation value, as is expected when the integration volumes become smaller than the elementary atomic modes. The data displayed in Fig. 3 were obtained for $\Delta v_z = 0.28\ \mathrm{cm\ s^{-1}}$ and $\Delta v_\perp = 0.48\ \mathrm{cm\ s^{-1}}$, which maximizes the reduction of the correlation while preserving a statistically significant number of detection events (see Methods and Extended Data Fig. 1).

The dip in the cross-correlation function cannot be explained in terms of classical particles, for which we would have no correlation at all between the detections in the output channels (Methods). But when the atoms are viewed as waves, demonstrating the quantum origin of the dip necessitates a deeper analysis. The reason is that two waves can interfere at a beam-splitter and give rise to an intensity imbalance between the output channels. If, in addition, the coherence time of the waves is finite, the cross-correlation can display a dip similar to the one observed in our experiment. But once averaged over the phase difference between the beams, the classical visibility is bounded from above and cannot exceed 0.5 (ref. 26 and Methods). In our experiment, this phase difference is randomized by the shot-to-shot fluctuations of the relative phase between the laser beams used for Bragg diffraction (Methods). Since our measured visibility exceeds the limit for waves by two standard deviations, we can safely rule out any interpretation of our observation in terms of interference between two 'classical' matter waves or, in other words, between two ordinary wave functions describing each of the two particles separately.

Two contributions may be responsible for the non-zero value of the correlation function at the centre of the dip: the detected particles may not be fully indistinguishable and the number of particles contained in the integration volume may exceed unity for each beam (see Methods). The effect of the atom number distribution can be quantified by measuring the intensity correlations of the twin atom beams upstream of the beam-splitter (Fig. 1c), which bound the visibility of the dip through the relation:

$$V_{max} = 1 - \frac{G^{(2)}_{aa} + G^{(2)}_{bb}}{G^{(2)}_{aa} + G^{(2)}_{bb} + 2G^{(2)}_{ab}} \quad (3)$$

where $G^{(2)}_{aa}$, $G^{(2)}_{bb}$ and $G^{(2)}_{ab}$ are defined by analogy to equation (1) (ref. 26 and Methods) and the integration volumes $\mathcal{V}_{a,b}$ have the same extent as $\mathcal{V}_{c,d}$. Here, one immediately sees that the finite probability of having more than one atom per input channel, which translates to finite values of the auto-correlations $G^{(2)}_{aa}$, $G^{(2)}_{bb}$, leads to a reduced visibility. We have performed the measurement of these correlations following the same experimental procedure as before, except that we did not apply the mirror and beam-splitter. We find non-zero values $G^{(2)}_{aa} = 0.016(5)$, $G^{(2)}_{bb} = 0.047(9)$, and $G^{(2)}_{ab} = 0.048(7)$, yielding $V_{max} = 0.60(10)$, where the uncertainty is the standard deviation of the statistical ensemble. Because of the good agreement with the measured value of the visibility, we conclude that the atom number distribution in the input channels entirely accounts for the visibility of the HOM dip. For the present experiment, we estimate the average number of incident atoms to be 0.5(1) in $\mathcal{V}_a$ and 0.8(2) in $\mathcal{V}_b$, corresponding to a ratio of the probability for having two atoms to that for having one atom of 0.25(5) and 0.40(10), respectively (Methods). Achieving much smaller values is possible, for instance by reducing the pair production rate, but at the cost of lower counting statistics.

Although multiparticle interference can be observed with independently prepared photons[27,28], atoms[13] and electrons[29,30], twin particle sources are at the heart of many protocols for quantum information processing[14] and quantum simulation[15]. The good visibility of the HOM dip in our experiment demonstrates that our twin atom source produces beams that have highly correlated populations and are well mode matched. This is an important achievement in itself, which may have the same impact on quantum atom optics as the development of twin photon sources using nonlinear crystals had for quantum optics.

Online Content Methods, along with any additional Extended Data display items and Source Data, are available in the online version of the paper; references unique to these sections appear only in the online paper.

Received 9 November 2014; accepted 6 February 2015.

1. Bell, J. S. On the Einstein-Podolsky-Rosen paradox. *Physics* **1,** 195–200 (1964).
2. Aspect, A. Bell's inequality test: more ideal than ever. *Nature* **398,** 189–190 (1999).
3. Giustina, M. *et al.* Bell violation using entangled photons without the fair-sampling assumption. *Nature* **497,** 227–230 (2013).
4. Christensen, B. G. *et al.* Detection-loophole-free test of quantum nonlocality, and applications. *Phys. Rev. Lett.* **111,** 130406 (2013).
5. Hong, C. K., Ou, Z. Y. & Mandel, L. Measurement of subpicosecond time intervals between two photons by interference. *Phys. Rev. Lett.* **59,** 2044–2046 (1987).
6. Rarity, J. G. & Tapster, P. R. Experimental violation of Bell's inequality based on phase and momentum. *Phys. Rev. Lett.* **64,** 2495–2498 (1990).
7. Lewis-Swan, R. J. & Kheruntsyan, K. V. Motional-state Bell inequality test with ultracold atoms. Preprint at http://arXiv.org/abs/1411.0191 (2014).
8. Penrose, R. Quantum computation, entanglement and state reduction. *Phil. Trans. R. Soc. Lond. A* **356,** 1927–1939 (1998).
9. Zurek, W. H. Decoherence, einselection, and the quantum origins of the classical. *Rev. Mod. Phys.* **75,** 715–775 (2003).
10. Schlosshauer, M. Decoherence, the measurement problem, and interpretations of quantum mechanics. *Rev. Mod. Phys.* **76,** 1267–1305 (2005).
11. Leggett, A. J. How far do EPR-Bell experiments constrain physical collapse theories? *J. Phys. A* **40,** 3141–3149 (2007).
12. Bücker, R. *et al.* Twin-atom beams. *Nature Phys.* **7,** 608–611 (2011).
13. Kaufman, A. M. *et al.* Two-particle quantum interference in tunnel-coupled optical tweezers. *Science* **345,** 306–309 (2014).
14. Nielsen, M. A. & Chuang, I. L. *Quantum Computation and Quantum Information* (Cambridge Univ. Press, 2000).
15. Kitagawa, T., Aspect, A., Greiner, M. & Demler, E. Phase-sensitive measurements of order parameters for ultracold atoms through two-particle interferometry. *Phys. Rev. Lett.* **106,** 115302 (2011).
16. Ou, Z. Y. *Multi-Photon Quantum Interference* (Springer, 2007).
17. Grynberg, G., Aspect, A. & Fabre, C. *Introduction to Quantum Optics: From the Semiclassical Approach to Quantized Light* (Cambridge Univ. Press, 2010).
18. Bonneau, M. *et al.* Tunable source of correlated atom beams. *Phys. Rev. A* **87,** 061603 (2013).
19. Cronin, A. D., Schmiedmayer, J. & Pritchard, D. E. Optics and interferometry with atoms and molecules. *Rev. Mod. Phys.* **81,** 1051–1129 (2009).
20. Schellekens, M. *et al.* Hanbury Brown Twiss effect for ultracold quantum gases. *Science* **310,** 648–651 (2005).
21. Hilligsøe, K. M. & Mølmer, K. Phase-matched four-wave mixing and quantum beam splitting of matter waves in a periodic potential. *Phys. Rev. A* **71,** 041602 (2005).
22. Campbell, G. K. *et al.* Parametric amplification of scattered atom pairs. *Phys. Rev. Lett.* **96,** 020406 (2006).
23. Gross, C. *et al.* Atomic homodyne detection of continuous-variable entangled twin-atom states. *Nature* **480,** 219–223 (2011).
24. Lücke, B. *et al.* Twin matter waves for interferometry beyond the classical limit. *Science* **334,** 773–776 (2011).
25. Bookjans, E., Hamley, C. & Chapman, M. Strong quantum spin correlations observed in atomic spin mixing. *Phys. Rev. Lett.* **107,** 210406 (2011).
26. Lewis-Swan, R. J. & Kheruntsyan, K. V. Proposal for demonstrating the Hong–Ou–Mandel effect with matter waves. *Nature Commun.* **5,** 3752 (2014).
27. Beugnon, J. *et al.* Quantum interference between two single photons emitted by independently trapped atoms. *Nature* **440,** 779–782 (2006).
28. Lang, C. *et al.* Correlations, indistinguishability and entanglement in Hong–Ou–Mandel experiments at microwave frequencies. *Nature Phys.* **9,** 345–348 (2013).
29. Bocquillon, E. *et al.* Coherence and indistinguishability of single electrons emitted by independent sources. *Science* **339,** 1054–1057 (2013).
30. Dubois, J. *et al.* Minimal-excitation states for electron quantum optics using levitons. *Nature* **502,** 659–663 (2013).

Acknowledgements We thank J. Ruaudel and M. Bonneau for contributions to the early steps of the experiment. We also thank K. Kheruntsyan, J. Chwedenczuk and P. Deuar for discussions. We acknowledge funding by IFRAF, Triangle de la Physique, Labex PALM, ANR (PROQUP, QEAGE), FCT (scholarship SFRH/BD/74352/2010 co-financed by ESF, POPH/QREN and EU to R.L.) and EU (ERC grant 267775, QUANTATOP, and Marie Curie CIG 618760, CORENT).

Author Contributions All authors contributed extensively to this work.

Author Information Reprints and permissions information is available at www.nature.com/reprints. The authors declare no competing financial interests. Readers are welcome to comment on the online version of the paper. Correspondence and requests for materials should be addressed to R.L. (raphael.lopes@institutoptique.fr) or M.C. (marc.cheneau@institutoptique.fr).

METHODS

Twin atom source. The twin atom beams result from a scattering process between pairs of atoms from the BEC occurring when the gas is placed in a moving one-dimensional optical lattice. The use of a BEC is dictated primarily by the need to maximize the atomic density to assure a sufficiently high scattering rate. The experimental set-up has been described in ref. 18. The lattice is formed by two laser beams derived from the same source emitting at the wavelength $\lambda = 1{,}064$ nm. In contrast to our previous work, the axis of the optical lattice was now precisely aligned with the long axis of the optical trap confining the atoms. The laser beams intersect with an angle of $\theta = 166^\circ$, their frequency difference is set to 100.5 kHz and the lattice depth to 0.8 E_{rec} (see below). This constrains the longitudinal wave vector of the twin atoms to the values $k_{z,\mathrm{a}} = 0.75\,k_{\mathrm{rec}}$ and $k_{z,\mathrm{b}} = 1.30\,k_{\mathrm{rec}}$ in order to fulfil the conservation of quasi-momentum and energy in the frame co-propagating with the lattice. Here, $k_{\mathrm{rec}} = 2\pi\sin(\theta/2)/\lambda$ is the recoil wave vector along the longitudinal axis gained upon absorption of a photon from a lattice laser and $E_{\mathrm{rec}} = \hbar^2 k_{\mathrm{rec}}^2/2m$ is the associated kinetic energy, with $\hbar$ the reduced Planck constant and $m = 6.64 \times 10^{-27}$ kg the mass of a ^{4}He atom. The observed velocities of the twin atom beams coincide with the expected values above, using the relation $v = \hbar k/m$. The optical lattice is turned on and off adiabatically so as to avoid diffraction of the atoms during this phase of the experiment. The relative velocities of the pair is such that during the interferometer sequence, the maximum separation of the beams is only 25 μm, smaller than the size of the clouds. This separation, however, plays no role in the experiment; we need only ensure that the atoms in a pair are distinguishable by some observable, in our case the momentum. Thus a second reason to use a BEC in the experiment is to benefit from its narrow momentum distribution, which results in well separated pairs in momentum space.

Transfer to the magnetically insensitive internal state. Transfer to the $m = 0$ state after the optical trap has been switched off is made necessary by the presence of stray magnetic fields in the vacuum chamber that otherwise would lead to a severe deformation of the atomic distribution during the long free fall. The transfer is achieved by introducing a two-photon coupling between the $m = 1$ state, in which the atoms are initially, and the $m = 0$ state using two laser beams derived from a single source emitting at 1,083 nm and detuned by 600 MHz from the $2\,^3S_1$ to $2\,^3P_0$ transition. The frequency difference of the laser beams is chirped across the two-photon resonance so as to realize an adiabatic fast passage transition (the frequency change is 300 kHz in 300 μs). We have measured the fraction of transferred atoms to be 94%. The remaining 6% stay in the $m = 1$ state and are pushed away from the integration volumes by stray magnetic field gradients.

Atomic mirror and beam-splitter. The mirror and beam-splitter are both implemented using Bragg scattering on a second optical lattice. This effect can be seen as a momentum exchange between the atoms and the laser beams forming the lattice, a photon being coherently absorbed from one beam and emitted into the other. In our experiment, the laser beams forming the lattice have a waist of 1 mm and are detuned by 600 MHz from the $2\,^3S_1$ to $2\,^3P_0$ transition (they are derived from the same source as the beams used for the Raman transfer). In order to fulfil the Bragg resonance condition for the atom beams, the laser beams are made to intersect at an angle of 32° and the frequency of one of the beams is shifted by 57 kHz. In addition to this fixed frequency difference, a frequency chirp is performed to compensate for the acceleration of the atoms during their free fall. The interaction time between the atoms and the optical lattice was 100 μs for the mirror operation (π-pulse) and 50 μs for the beam-splitter operation (π/2-pulse). The resonance condition for the momentum state transfer is satisfied by all atoms in the twin beams but only pairs of states with a well defined momentum difference are coupled with each other. We measured the reflectivity of the mirror and the transmittance of the beam-splitter to be 0.95(2) and 0.49(2), respectively. Spontaneous scattering of photons by the atoms was negligible.

Interactions between atoms can alter the effect of the beam-splitter[31]. In our experiment, however, the atomic density at the beam-splitter is so low that the frequency associated with the typical interparticle interaction energy is more than 3 orders of magnitude smaller than the inverse of the time it takes for Bragg scattering to take place. Thus particle interactions are negligible during the beam splitting process.

Detection efficiency. Our experiment relies on the ability to detect the atoms individually. The detection efficiency is an essential parameter for achieving good signal to noise ratios, although it does not directly influence the visibility of the HOM dip. Our most recent estimate of the detection efficiency relies on the measurement of the variance of the atom number difference between the twin beams. For this we use the same procedure as described in ref. 18, but with an integration volume that includes the entire velocity distribution of each beam. We find a normalized variance of 0.75(5), well below the Poissonian floor. Since for perfectly correlated twin beams the measured variance would be $1 - \eta$, we attribute the lower limit of 25(5)% to our detection efficiency. This value for η is a factor of about 2 larger than the lower bound quoted in ref. 32. The difference is due to the change of method employed for transferring the atoms from the $m = 1$ to the $m = 0$ state after the optical trap has been switched off. We previously used a radio-frequency transfer with roughly 50% efficiency whereas the current optical Raman transfer has close to 100% efficiency.

Distribution of the number of incident atoms. We have estimated the average number of incident atoms in each input channel of the beam-splitter, n_{a} and n_{b}, by analysing the distribution of detected atoms in the integration volumes $\mathcal{V}_{\mathrm{a}}$ and $\mathcal{V}_{\mathrm{b}}$. We fitted these distributions by assuming an empirical Poissonian law for the distribution of incident atoms and taking into account the independently calibrated detection efficiency. The values of n_{a} and n_{b} given in the main text are the mean values of the Poissonian distributions that best fit the data. The probabilities for having one or two atoms in each of the input channels of the beam-splitter was obtained from the same analysis. The uncertainty on these numbers mostly stems from the uncertainty on the detection efficiency.

The HOM effect. The HOM effect appears in the correlator $\left\langle \hat{a}^\dagger_{v_c}\hat{a}^\dagger_{v_d}\hat{a}_{v_d}\hat{a}_{v_c}\right\rangle$ of equation (1). The simplest way to calculate such a correlator is to transform the operators and the state vector back in the input space before the beam-splitter and to use the Heisenberg picture. The transformation matrix between the operators $\hat{a}_{v_c}(t_3)$, $\hat{a}_{v_d}(t_3)$ and $\hat{a}_{v_a}(t_3)$, $\hat{a}_{v_b}(t_3)$ can be worked out from first principles. For the Bragg beam-splitter, and using a Rabi two-state formalism, we find:

$$\begin{cases} \hat{a}_{v_c} = \dfrac{1}{\sqrt{2}}\left(i\,\mathrm{e}^{i\phi}\hat{a}_{v_a} + \hat{a}_{v_b}\right) \\ \hat{a}_{v_d} = \dfrac{1}{\sqrt{2}}\left(\hat{a}_{v_a} + i\,\mathrm{e}^{-i\phi}\hat{a}_{v_b}\right) \end{cases}$$

where ϕ is the relative phase between the laser beams forming the optical lattice. In the ideal case of an input state with exactly one atom in each channel, $|1_{v_a},1_{v_b}\rangle$, we therefore obtain:

$$\begin{aligned} \|\hat{a}_{v_d}\hat{a}_{v_c}|1_{v_a},1_{v_b}\rangle\|^2 &= \frac{1}{4}\left\|\left(i\,\mathrm{e}^{i\phi}\hat{a}^2_{v_a} + i\,\mathrm{e}^{-i\phi}\hat{a}^2_{v_b} + \hat{a}_{v_a}\hat{a}_{v_b} + i^2\hat{a}_{v_b}\hat{a}_{v_a}\right)|1_{v_a},1_{v_b}\rangle\right\|^2 \\ &= \frac{1}{4}\left\|0 + \left(1+i^2\right)|0_{v_a},0_{v_b}\rangle\right\|^2 \\ &= 0 \end{aligned}$$

meaning that the probability of joint detection is strictly zero. (Here we use $||...||$ to indicate vector norm.) The detailed calculation above makes clear that the perfect destructive interference between the two-particle state amplitudes associated with the two diagrams of Fig. 1c is at the heart of the HOM effect. By contrast, input states containing more than one atom per channel are transformed into a sum of orthogonal states and the interference can only be partial. Taking $|2_{v_a},2_{v_b}\rangle$, for instance, yields:

$$\begin{aligned} \|\hat{a}_{v_d}\hat{a}_{v_c}|2_{v_a},2_{v_b}\rangle\|^2 &= \frac{1}{4}\left\|\left(i\,\mathrm{e}^{i\phi}\hat{a}^2_{v_a} + i\,\mathrm{e}^{-i\phi}\hat{a}^2_{v_b} + \hat{a}_{v_a}\hat{a}_{v_b} + i^2\hat{a}_{v_b}\hat{a}_{v_a}\right)|2_{v_a},2_{v_b}\rangle\right\|^2 \\ &= \frac{1}{2}\left\|i\,\mathrm{e}^{i\phi}|0_{v_a},2_{v_b}\rangle + i\,\mathrm{e}^{-i\phi}|2_{v_a},0_{v_b}\rangle + \sqrt{2}\left(1+i^2\right)|1_{v_a},1_{v_b}\rangle\right\|^2 \\ &= \frac{1}{2}\left\|\mathrm{e}^{i\phi}|0_{v_a},2_{v_b}\rangle + e^{-i\phi}|2_{v_a},0_{v_b}\rangle\right\|^2 \\ &= 1 \end{aligned}$$

Finally, we note that losses in one of the incident beams, for instance beam a, can be modelled by a fictitious beam-splitter with a transmission coefficient T. In the above calculation, these losses would therefore only manifest by an additional factor $\sqrt{T}$ in front of every operator $\hat{a}_{v_a}$, leaving unaffected the destructive interference that gives rise to the HOM effect.

Stability of the atom number in the output ports. The mean detected atom number in the output ports c and d is plotted as a function of τ in Extended Data Fig. 2a and b. It remains constant within the statistical uncertainty, which confirms the interpretation of the dip as a destructive two-particle interference. To easily compare the atom number fluctuations with the variation of the cross-correlation across the HOM dip, the product of the averaged populations $\langle n_c\rangle \cdot \langle n_d\rangle$ and the cross-correlation $G^{(2)}_{cd}$ are displayed together as a function of τ in Extended Data Fig. 2c. In contrast to the cross-correlation, it is impossible to identify a marked reduction of $\langle n_c\rangle\cdot\langle n_d\rangle$ around $\tau = 550$ μs.

Influence of the integration volume on the dip visibility. The visibility of the HOM dip is plotted in Extended Data Fig. 1 as a function of the longitudinal (Extended Data Fig. 1a) and transverse (Extended Data Fig. 1b) integration volumes. The red dots identify the integration volume used in Fig. 3 of the main text and correspond to a compromise between signal-to-noise ratio and visibility amplitude. As we shrink the integration volumes, the dip visibility first increases and then reaches a saturation value, meaning that the integration volume becomes smaller than the elementary atomic modes[33–35]. Reducing further the integration volume only leads to an increase of the statistical uncertainty.

The visibility V is obtained by fitting the cross-correlation function $G^{(2)}_{cd}(\tau)$ measured in the experiment with the empirical function:

$$f(\tau) = G^{(2)}_{bg}\left(1 - V\exp\left(-(\tau-\tau_0)^2/2\sigma^2\right)\right)$$

where the background correlation $G^{(2)}_{bg}$, the centre of the dip τ_0 and the width of the dip σ are all left as free parameters.

Visibility of the HOM dip. A slightly less general form of equation (3) has been derived in ref. 26 assuming a two-mode squeezed state as an input state. The same calculation can be performed for an arbitrary input state. Leaving aside the integration over the velocity distribution, we find that the cross-correlation for indistinguishable particles can be expressed as:

$$G^{(2)}_{cd}\Big|_{indisc.} = \frac{1}{4}\left(G^{(2)}_{aa} + G^{(2)}_{bb} + \Delta\right) \quad , \quad \Delta = 2\eta^2\,\mathrm{Re}\left[e^{2i\phi}\left\langle \hat{a}^\dagger_{\nu_a}\hat{a}^\dagger_{\nu_a}\hat{a}_{\nu_b}\hat{a}_{\nu_b}\right\rangle\right]$$

whereas that of distinguishable particles reads:

$$G^{(2)}_{cd}\Big|_{disc.} = \frac{1}{4}\left(G^{(2)}_{aa} + G^{(2)}_{bb} + 2G^{(2)}_{ab}\right)$$

Here, the correlators appearing in the right-hand side are taken at time t_1, that is, immediately after the atom beams have been produced. The term Δ corresponds to an interference between single-particle matter waves. It depends on both the relative phase between the atom beams and the relative phase between the laser beams used for Bragg diffraction. The latter is counted once for the atomic mirror and once for the atomic beam-splitter. Twin beams with perfect correlations in their population would have a fully random relative phase. In our experiment however, the population imbalance between the atom beams could entail a residual phase coherence. Instead, the relative phase between the laser beams was left uncontrolled and its value was randomly distributed between two repetitions of the experiment. As a result, the term Δ must average to zero and the visibility of the HOM dip be given by equation (3), as observed in the experiment. Following ref. 26, we also note that equation (3) yields the ultimate bound for waves interfering on the beam-splitter: because waves must fulfil the Cauchy–Schwarz inequality, $G^{(2)}_{ab} < \sqrt{G^{(2)}_{aa}G^{(2)}_{bb}}$, the visibility of the classical dip cannot exceed 0.5 (ref. 36).

The above results hold true for a finite integration over the atomic velocity distribution provided that two conditions are met: (1) it must remain impossible to distinguish the atoms entering the beam-splitter through channel a from the atoms entering through channel b once they have exited the beam-splitter; (2) the transformation matrix of the beam-splitter must keep the same form after integration. In our experiment, the second condition is naturally satisfied because the Bragg diffraction only couples atomic states with a well defined momentum difference and we fulfil the first condition by reducing the integration volume as much as it is necessary.

31. Andersson, E., Fontenelle, M. & Stenholm, S. Quantum statistics of atoms in microstructures. *Phys. Rev. A* **59,** 3841–3850 (1999).
32. Jaskula, J.-C. *et al.* Sub-Poissonian number differences in four-wave mixing of matter waves. *Phys. Rev. Lett.* **105,** 190402 (2010).
33. Rarity, J. G. & Tapster, P. R. Fourth-order interference in parametric downconversion. *J. Opt. Soc. Am. B* **6,** 1221–1226 (1989).
34. Treps, N., Delaubert, V., Maître, A., Courty, J. M. & Fabre, C. Quantum noise in multipixel image processing. *Phys. Rev. A* **71,** 013820 (2005).
35. Morizur, J.-F., Armstrong, S., Treps, N., Janousek, J. & Bachor, H.-A. Spatial reshaping of a squeezed state of light. *Eur. Phys. J. D* **61,** 237–239 (2011).
36. Ou, Z. Y. Quantum theory of fourth-order interference. *Phys. Rev. A* **37,** 1607–1619 (1988).

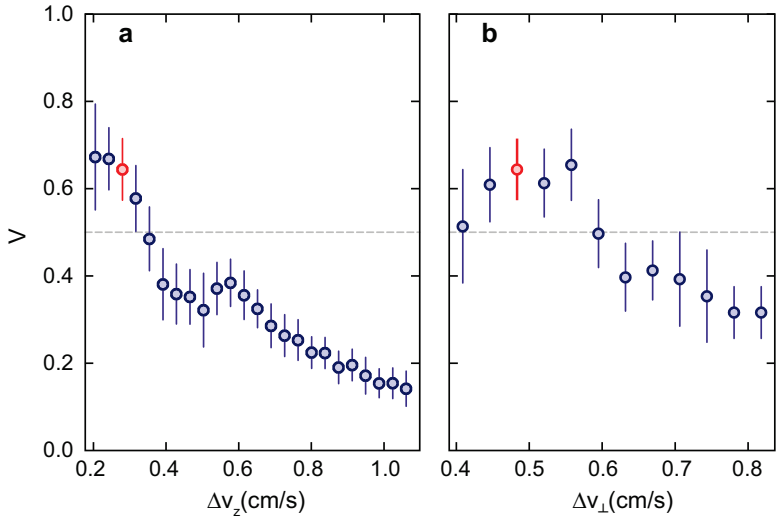

Extended Data Figure 1 | HOM dip visibility as a function of the integration volumes. **a**, Visibility V as a function of the longitudinal integration interval Δv_z. The transverse integration interval is kept constant at $\Delta v_\perp = 0.48\,\mathrm{cm\,s^{-1}}$. **b**, Visibility as a function of the transverse integration interval $\Delta v_\perp$. The longitudinal integration interval is kept constant at $\Delta v_z = 0.28\,\mathrm{cm\,s^{-1}}$. The red points mark the values discussed in the main text. Error bars denote the standard deviation of the statistical ensemble.

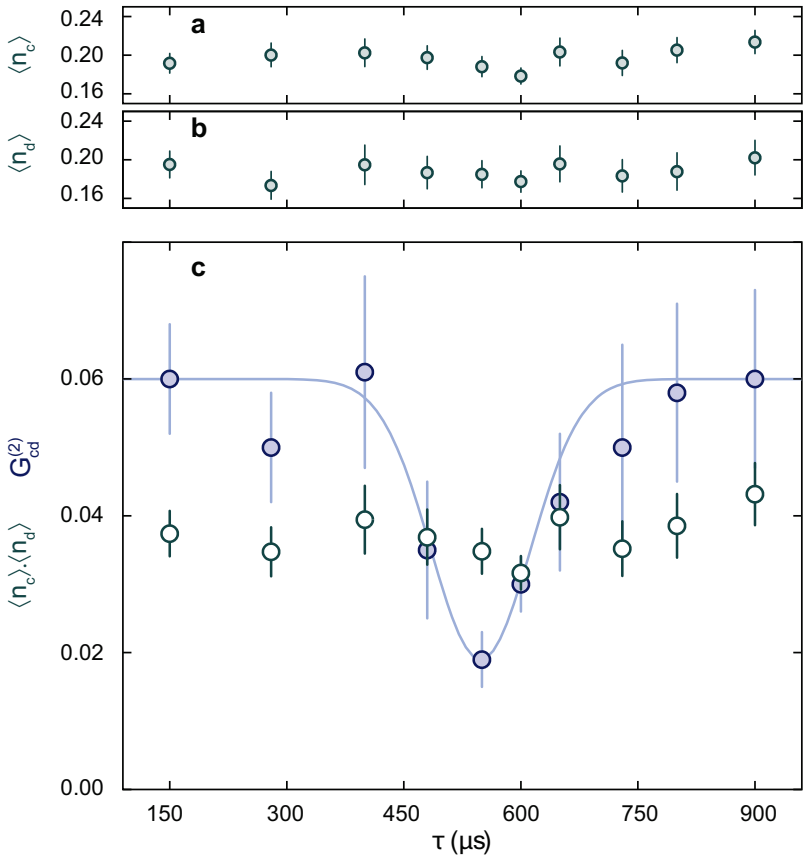

Extended Data Figure 2 | Averaged number of incident atoms over the HOM dip. **a**, Averaged atom number detected in $\mathcal{V}_c$, n_c, as a function of the propagation time τ. The mean value of $n_c(\tau)$ is 0.20 with a standard deviation of 0.01. **b**, Averaged atom number detected in $\mathcal{V}_d$, n_d, as a function of the propagation time τ. The mean value of $n_d(\tau)$ is 0.19 with a standard deviation of 0.01. **c**, The cross-correlation between the output ports c and d (solid blue circles), displaying the HOM dip, is compared to $\langle n_c \rangle \cdot \langle n_d \rangle$ (open grey circles). Error bars denote the standard deviation of the statistical ensemble.

Conclusion

The metastable helium experiment of the Charles-Fabry laboratory has been actively involved in the development in the domain generating nonclassical atomic pair source in momentum space through correlation studies. The pair creation through dynamical instabilities allows us to produce a stable and tunable source of atomic pairs in momentum space with non-classical correlations. To perform Bell's inequality test with matter waves using this source, we prepared the scheme and characterized main element, the Bragg beams for the test.

In this thesis, we have described different steps leading to our ultimate goal. In Chapter 1, the correlation function was introduced which is an essential tool in revealing quantum effects and studying nonclassical sources. In this chapter, we have presented the correlation measurement of the collective emission from the Bose-Einstein condensate. The measurement result demonstrates the thermal statistics of the emission.

In Chapter 2, the theoretical description of the Bell's inequality is established in addition to the theoretical descriptions of the pair production, Bragg diffraction. We conclude this chapter with the evaluation of the prediction of the quantum mechanics for the CHSH parameter.

Chapter 3 is entirely devoted to the experimental tests and characterization of the Bell's inequality experiment. We start with the metastable helium Bose-Einstein condensate in the crossed dipole trap, which is our coherent source to produce an atomic pair. Then we present the atomic pair production together with the correlations between atomic beams in the pair. We also present the scheme we have chosen for the Bell's inequality test in which the Bragg beams play an important role. We finalize the chapter by showing the satisfactory achievements for the Bragg pulse in terms of phase control and the selectivity.

In Chapter 4, we present the two-particle interference experiment with the same atomic source. This experiment opened a way to realise the Bell's inequality by demonstrating the nonclassical feature of the source.

Appendix A

Helium atom

Helium was first discovered by the French astronomer Pierre Janssen in 1868 when observing a solar eclipse in India. Helium can be observed at 587.49 nanometres, corresponding to the yellow spectral emission lines in the spectrum of the chromosphere of the Sun. Therefore, its name helium was proposed after the Greek name for the sun, Helios. In 1895, Sir William Ramsay was able to observe it in the lab after treating cleveite, a uranium mineral, with mineral acids [37].

Helium (chemical element symbol **He**) is a colorless, odorless, tasteless, non-toxic, monoatomic gas that takes the first place among the noble gas group in the periodic table. It is the second lightest element, consisting of two electrons, two protons along with one (^{3}**He**) or two neutrons (^{4}**He**) depending on the isotope. Mainly, helium is extracted from natural gas, containing up to 7% helium, by fractional distillation method which is based on the fact that the helium has a lower boiling point than any other element so that the other gases can be liquefied at low temperature and high pressure. The isotope ^{4}**He** is the most abundant 99.999863% in the nature. Apart from scientific uses, helium is used as a protective gas in growing silicon and germanium crystals since it is less reactive. Cooling the superconducting magnets in modern MRI scanners, leakage detection and filling balloons are only few examples of wide applications of helium.

The isotope ^{4}**He** is a bosonic isotope and the ^{3}**He** is a fermionic isotope. In our lab, the ^{4}**He** atom is used with the energy levels shown in figure A.1. The helium-4 atom is prepared in its triplet metastable state 2^3S_1, $^4He^*$, for which there exist optical transitions to the excited states to be able to manipulate helium-4 atoms with lasers . Throughout the experimental sequence which lasts about $\sim$ 30 s, the metastable state 2^3S_1 is considered to be the ground state with the lifetime of $\sim$ 8000 seconds [41]. We use the transition $2^3S_1 \rightarrow 2^3P_2$ to cool and trap the metastable helium-4 atoms whereas the transition $2^3S_1 \rightarrow 2^3P_0$ is used for the Bragg diffraction and Raman transfer.

The typical parameters associated with the helium-4 atom is given in the table A.1.

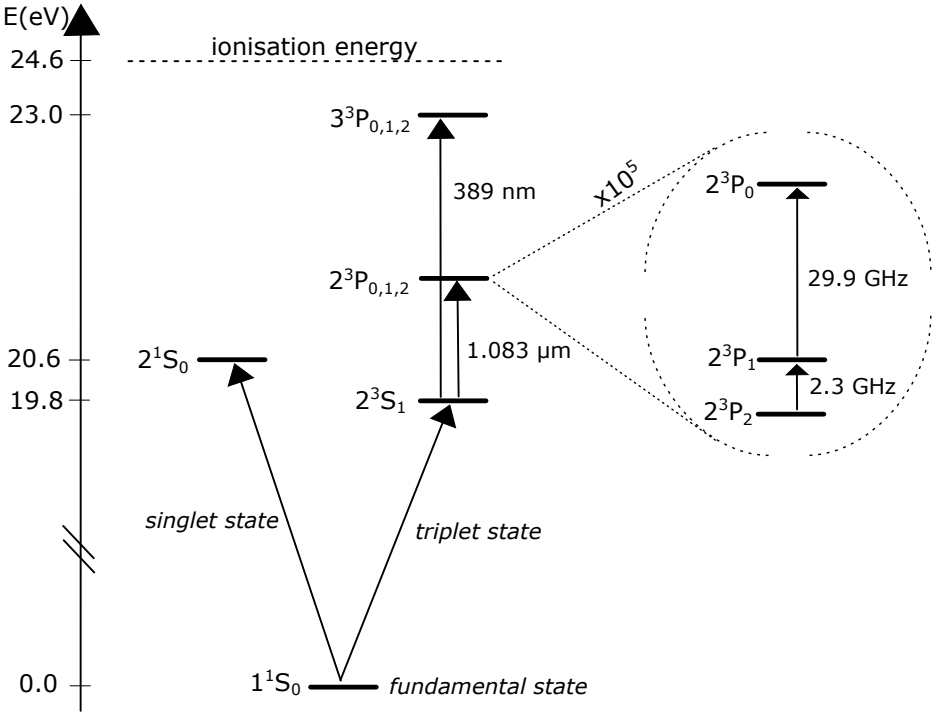

FIGURE A.1: **Energy levels of ^{4}He for the laser manipulation.** The ^{4}**He** atoms are prepared in the metastable triplet state 2^3S_1 with the lifetime of ~ 8000 seconds and with the stocked internal energy of 19.8 eV. We use the transition from "ground" state 2^3S_1 to the excited state 2^3P_2 with optical transition $\lambda = 1.083$ μm for cooling and optical detection of the helium atoms. For Bragg diffraction and Raman transfer the transition $2^3S_1 \rightarrow 2^3P_0$ is addressed.

Parameter	Notation	Value	Unit
Lifetime of state 2^3S_1		7870(510)	s
Mass of ^{4}**He**	m	6.65×10^{-27}	kg
Wavelength of $2^3S_1 \rightarrow 2^3P_{0,1,2}$	λ	1.083	μm
Natural linewidth of $2^3S_1 \rightarrow 2^3P_{0,1,2}$	Γ	$2\pi \times 1.6 \times 10^6$	rad/s
Saturation intensity	I_{sat}	0.16	mW/cm^2
Recoil velocity	v_{rec}	9.2	cm/s
Recoil energy	E_{rec}	2.8×10^{-29}	J
Recoil temperature	T_{rec}	2.06	μK

TABLE A.1: Parameters associated with helium-4 atom

Appendix B

Cooling helium atoms

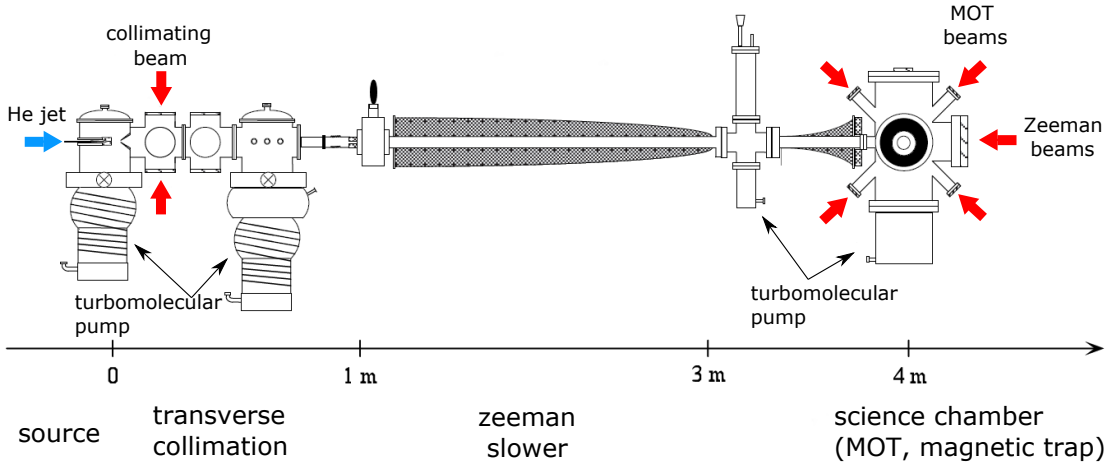

FIGURE B.1: General scheme of the helium experiment apparatus. Figure adapted from [22]

The short overview of the experimental sequence of the metastable helium BEC will be discussed in a few words, more details on this subject can be found in the theses of earlier PhD students who worked on the experiment [22, 120]. **Source**. The general overview of the apparatus is shown in figure B.1. The helium-4 atoms initially found in the fundamental state 1^1S_0 are excited to the metastable state 2^3S_1 by applying 2.3 kV of electric potential difference. The high voltage difference creates a plasma which consists of the mixture of helium atoms with various excited levels including ionised particles. A small fraction $\leq 10^{-2}\%$ of useful atoms in the state 2^3S_1 is then addressed optically at wavelength 1083 nm to select from the rest. This happens as follows: two transverse retro-reflected near resonant beams are used to collimate the atomic beam to the science chamber where it is loaded into the Magneto-optical trap (MOT). To be able to load into the MOT, the atoms should be slowed down before. The liquid

nitrogen is used to decrease the temperature of the plasma below 77 K which reduces the longitudinal average velocity to only 1200 m/s. **Zeeman slower**.So, it is compulsory

to use the Zeeman slower to slow down atoms further. The Zeeman slower reduces the longitudinal speed of the atomic jet with the help of the radiation force created by a laser beam which is red detuned by 400 MHz of the atomic transition and sent in the opposite direction of the atomic jet. Spatially varying magnetic field helps to keep the laser beam always at resonance by compensating the Doppler shift of the atomic beam along the 3 m long Zeeman slower. The necessity of such long distance, being unique for helium atoms among present cold atoms experiments, comes from the fact that the excited state 2^3P_2 has a very long lifetime 0.1 μs which converts to long distance for the atoms to undergo necessary number of cycles to bring the velocity 1500 m/s down to $\sim$ 100 m/s. **MOT**. The MOT consists of three laser beams(polarization σ^-) which

are retro-reflected (polarization σ^+) summing up to six beams on the atoms. These beams are detuned by 56 MHz to the red of the atomic transition. Together with a magnetic quadrupole field, the MOT traps and cools the neutral atom. The MOT phase saturates in 2 s with an atomic flux $10^8 - 10^9$ at/s. The short molasses phase follow the MOT phase where atoms are cooled only by optical means reducing temperature of the atoms down to 300 μK. **Magnetic trap**. About 10^8 helium atoms are loaded in a

Ioffe-Pritchard like magnetic trap where in the first place we optically pump the atoms in the $m = 1$ sublevel of 2^3S_1 state. Next, a 1D Doppler cooling stage is performed with a retroreflected low intensity near-resonant optical beam which lasts 6 s. This reduces the temperature to 150 μK with $1 - 5 \times 10^7$ atoms. The last step in the magnetic trap is the evaporation using radio-frequency RF ramp. It can in principle lead to the condensation in the magnetic trap which was the way actually how the first BEC of the metastable helium was achieved [44, 121]. Instead, we choose to evaporate till an approximate temperature of 15 μK with 5×10^6 atoms by ramping from 30 MHz to 6.2 MHz in 6. We condense in a crossed dipole trap where it is more stable in terms of the arrival time fluctuations.

Appendix C

Raman transfer

The condensate is prepared in the zeeman sublevel $m = 1$ of the 2^3S_1 state in the crossed dipole trap. Due to the stray magnetic gradients, we prefer to transfer atoms in the magnetic field insensitive sublevel $m = 0$ to avoid the deformation of the atomic cloud distribution during the time of flight. The transfer is achieved via Raman chirped adiabatic passage method (RCAP) [32, 134, 140] which has a high efficiency (theoretically $> 99\%$) in coherent transferring of atomic population between two quantum states. The method makes use of an off-resonant Raman transition with one $\pi-$polarized, monochromatic and one σ^--polarized, chirped laser pulse as shown in figure C.1. The frequency of the σ^- pulse is chirped linearly by 300 kHz in 300 μs. The two pulses have rectangular form and are applied at the same time with the same intensity 400 μW.

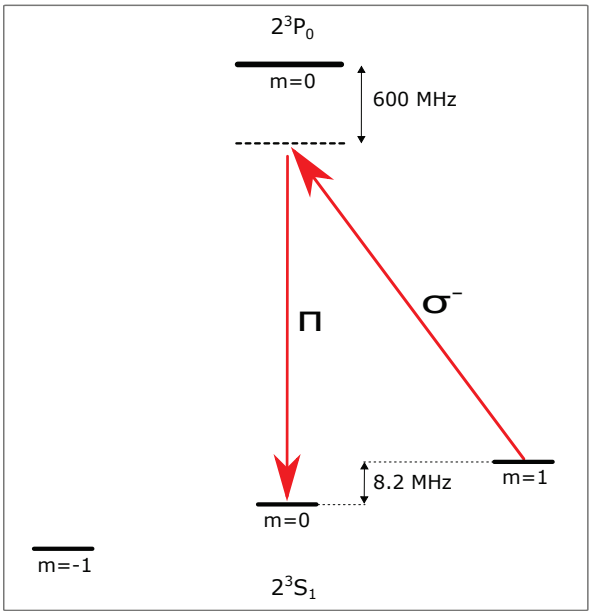

FIGURE C.1: Raman transfer using off-resonant π and σ^- polarized laser pulses between the zeeman sublevels $m = 1$ and $m = 0$ with the energy splitting 8.2 MHz corresponding to a magnetic bias field of 3 G.

When applying the RCAP between two states, it has been shown [134] that the final probabilities of state 1 and state 2 is given by

$$P_1(\infty) = e^{-\pi \frac{\Omega^2}{2r}} \qquad P_2(\infty) = 1 - P_1(\infty) \tag{C.1}$$

where r is the rate of linear chirping. Here, it is assumed that initally $P_1(0) = 1$ and $P_2(0) = 0$. To complete the population transfer, we require $\Omega^2 \gg 2r$ which turns out to be the adiabaticity condition.

In our case, if the problem can be treated in terms of two effective states $m = 0$ and $m = 1$ with the effective Rabi oscillation $\Omega_{eff} = \frac{\Omega_\pi \Omega_{\sigma^-}}{\Delta} = \frac{\Gamma^2 I_0}{4 I_{sat} \Delta}$, we respect the adiabaticity condition: $\Omega_{eff}^2 \approx 460 \times 10^9$ Hz^2 $\gg 2r = 2 \times 10^9$ Hz^2 and experimentally, the efficiency of transfer 95% is achieved.

The experimental value of the efficiency was measured by looking at the number of atoms in $m = 1$ and in $m = 0$ since they arrive at different times on the detector due to the stray magnetic gradient force acting on atoms in $m = 1$. In addition, the density of atomic cloud is lowered by expanding the momentum distribution (we heat atoms by an optical lattice in the vertical direction) in order to avoid the saturation of the detector. A single shot picture is illustrated in figure C.2. When transferring an atomic cloud to

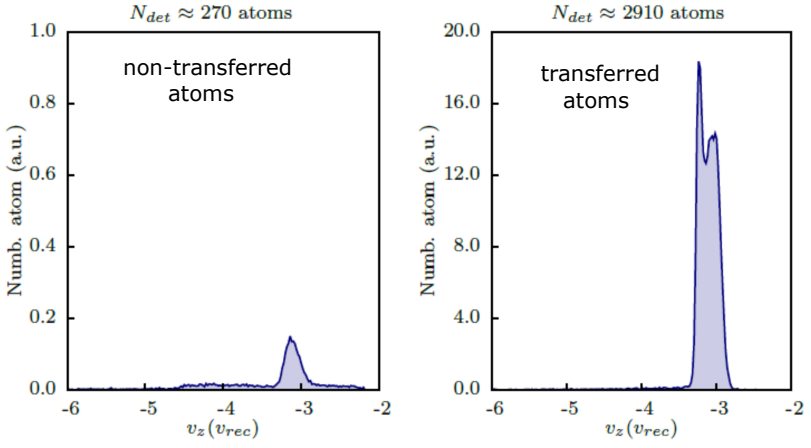

FIGURE C.2: Raman transfer efficiency

sublevel $m = 0$, we give a small offset velocity 0.2 (in units of v_{lat} to the ensemble of atoms along the vertical (axis of gravity) axis due to the small angle between the two laser beams in vertical direction.

In the experiment, σ^-−polarization is not pure and in fact this beam has two polarization components σ^- and σ^+ with the same intensity proportion. Because there is no allowed transition for σ^+, it does not affect the atomic cloud.

Appendix D

Electronic detection of the metastable helium atom

Here, we give the working principle of the MCP detector, more details can be found in the following thesis works [69, 127].

It has already been stated that a metastable helium atom possess a high internal energy of 19.8 eV. It allows to extract one or more electrons when a helium atom gets in contact with the micro-channel plate (MCP) as shown in figure D.1. Later these electrons are amplified. The principle of the amplification is quite analogous with that of avalanche photodiode where a single photon creates a small electronic signal by photoelectric effect which is later amplified by the avalanche process. Similarly, in our case, the extracted electrons are accelerated through the channel with the help of a high voltage difference applied at the ends of the plate. Each time the electrons hit the internal surface of the channel, they extract more electrons which result in an electronic burst at the end of the channel. The MCP plate is placed 46 cm below the trapping region, inside the vacuum chamber which reduces the noise due to the residual gas whose rate is estimated to be as low as 1 $\mathrm{cm}^{-2}{\cdot}\mathrm{s}^{-1}$.

The three-dimensional position (x, y, t) of a helium atom which hits the MCP can be inferred via the delay lines that are nothing but metallic wires. The electronic burst at the exit of the MCP channel will produce counter-propagating electric pulses when they bump into the delay line suited below the MCP. These pulses propagate to the two extremes of the wire and they are firstly amplified by fast electronics, then they are treated by the constant fraction discriminator (CFD) which triggers TTL signal when the amplitude of the pulse is above certain threshold tagging its arrival time. The TTL signal is then digitalized by a time-to-digital convertor (TDC) with a 275 ps coding time step and once the atomic cloud detection is completed the data transferred to the server PC. We install delay lines horizontally in two directions as shown in figure D.2.b to register four arrival times t_{x1}, t_{x2}, t_{y1} and t_{y2} for each atom on the server PC. If the

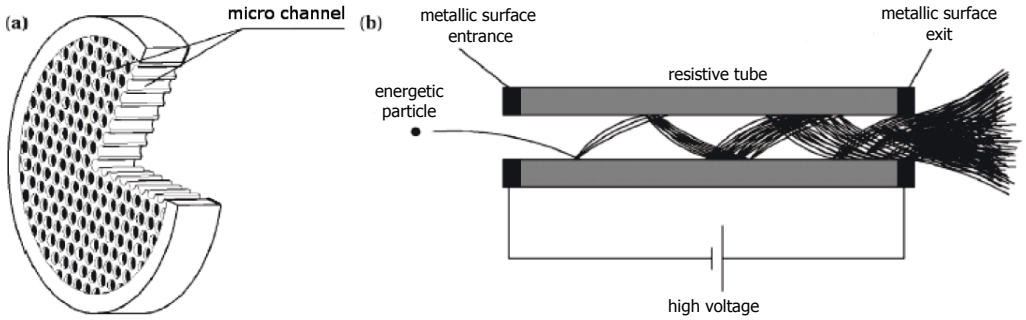

FIGURE D.1: (a) Micro-channel plate scheme. (b) The amplification principle in a micro-channel. Metastable helium atom is capable to extract an electron which then accelerates and extracts itself other electrons to create a strong pulse of electrons at the exit of the channel. This macroscopic signal can be used to count an atom, identify its position and arrival time on the MCP.

total length of the wire is L and the pulse propagation speed is v, we can theoretically infer the position x, y, t of an atom from the relation:

$$x = \frac{v}{2}(t_{x1} - t_{x2}) \tag{D.1}$$

$$y = \frac{v}{2}(t_{y1} - t_{y2}) \tag{D.2}$$

$$t = \frac{1}{2}(t_{x1} + t_{x2} - \frac{L}{v}) = \frac{1}{2}(t_{y1} + t_{y2} - \frac{L}{v}) \tag{D.3}$$

In reality, more elaborated algorithm is implemented to deduce the position of an atom [127]. The initial velocity of an atom (v_x, v_y, v_z) is calculated from its position (x, y, t)

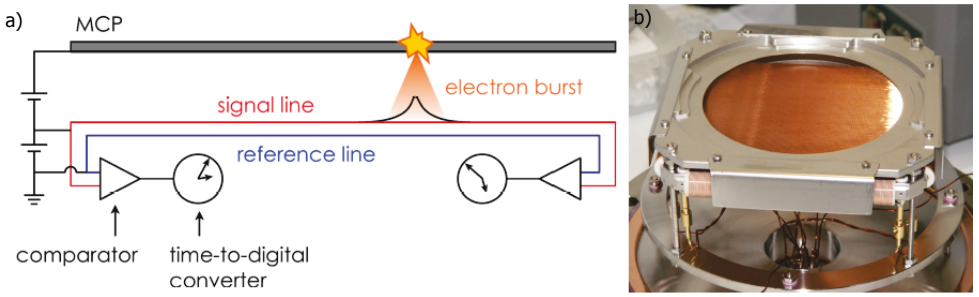

FIGURE D.2: (a) Delay lines scheme. The electron burst generated by the micro-channel plate falls on the metallic wire called delay line, then the resulting current signal propagates to the left and to the right. The signals' arrival times are identified by the comparator and digitalized by the time-to-digital converter(TDC). Knowing the speed of the propagation of the current on the delay line and the length of the delay line one can infer the position of the electron burst from the registered arrival times. (b) The experimental assembly of delay lines in two dimension which allows to register four arrival times to infer a position of a particle on a surface.

on the detector and its position (x_0, y_0, z_0) in the trap. During this conversion, we

assume the ballistic expansion and neglect the accelerations due to the mean-field effect intervening after the release of atoms from the trap. It is reasonable, since the density of atoms dilutes rapidly. Furthermore, we consider that all atoms belong to one single point. We neglect its initial size with respect to the long time of flight expansion which equals to 308 ms for an atom initially at rest to arrive on the MCP situated 46 cm below. It is justified for the condensate whose Thomas-Fermii radii after expansion are $R_z(tof) = 1.3$ mm, $R_\perp(tof) = 9.7$ mm which are large from the initial Thomas-Fermii radii $R_z(tof) = 0.06$ mm, $R_\perp(tof) = 0.004$ mm. **MCP detector saturation** When

the flux of atoms arriving on the detector is too high the MCP detector saturates whose signature can be observed on the data collected by the detector. There are three types of saturation which were observed [17]:

- Local saturation: When a great number of electrons are extracted inside neighbour channels, the successive detection of an atom becomes impossible. Starting from the local flux of atoms around 10^5 at·cm^{-2}·s^{-1}, the drop of the detection efficiency is observed that demonstrated in the asymmetric form of the temporal profile of the condensate as in figure D.3.a. It should be noted that this type of saturation is local, only the zones of the high flux has an impact from which the hole in figure D.3.b. is resulted. It is not the case for the other types of the saturation where the total flux plays an important role.

- Electronic saturation: The TDC imposes limit on the atomic flux. The plateau on the temporal profile of the condensate in figure D.3.c is the clear signification of the fact that the condensate flux is superior of the limit value 5×10^7 at·s^{-1}.

- Reconstruction saturation: To avoid the erroneous reconstruction of the position of an atom, sometimes we are forced to reject the signals which are very close to each other. When the cloud is very dense, this selection may become very severe creating a dip in the temporal profile of the condensate as in figure D.3.d.

MCP detector efficiency The detector efficiency is estimated to be $\eta = 25(5)$ % which is a reasonable value if we argue rudely that an atom has a 50 % chance to enter inside the MCP channel and the extracted electron has also 50 % chance to propagate in the preferred direction. One way to estimate this value was to look at the amplitude of the sub-shot noise variance of the population difference of a pair mentioned in Chapter 2. Assuming that the produced pair has a negligible variance of the population difference, the lower value of the detection efficiency is estimated to be $\eta = 25(5)$ %.

MCP detector resolution Transversely the resolution is limited by the width of the electric pulse which is approximatively 400 μm (1.4×10^{-2} in v_{rec}) and longitudinally the resolution is limited by the inclination of the channels ($7 - 8°$) which results in

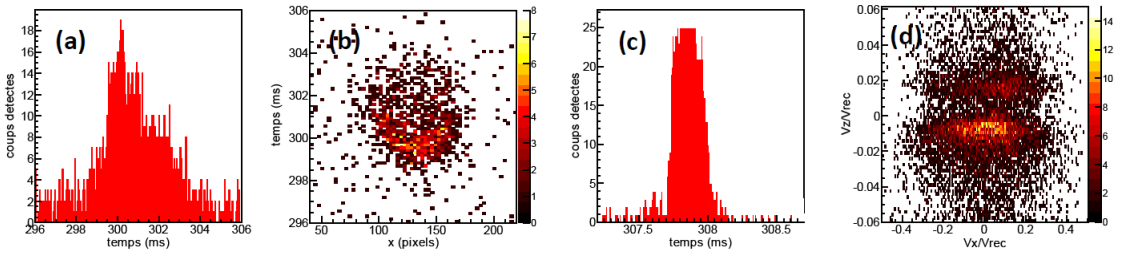

FIGURE D.3: Local saturation of the channels results from the high flux of atoms along $z-$direction which is the case for the BEC produced in the magnetic trap. We observe therefore an asymmetry in the profile of the non-reconstructed time of flight (a) and hole at the center of the reconstructed data of the condensate (b). The condensate produced in the dipole trap takes the form of horizontal pancake, and it is the flux on the whole detector which limits: the electronic data treatment leads to the maximum rate at each of the 4 ports as shown on the non-reconstructed arrival time distribution (c). Finally, for the strict selection on the events used in the reconstruction, we obtain the hole on the whole horizontal plane corresponding to the time interval where the condensate is more dense (from [17]).

resolution of 150 μm (5×10^{-3} in v_{rec}) (see for the details how these resolutions are estimated [124, 127]).

In summary, although it has relatively lower detection efficiency, the MCP detector has an advantage over the classical optical imaging where only two dimensional position of an atomic cloud is accessed while the MCP detector gives access to single atom resolution with its positions coordinates in space.

Bibliography

[1] A. Acín, N. Brunner, N. Gisin, S. Massar, S. Pironio, and V. Scarani, *Device-independent security of quantum cryptography against collective attacks*, Physical Review Letters, 98 (2007), p. 230501.

[2] M. H. Anderson, J. R. Ensher, M. R. Matthews, C. E. Wieman, and E. A. Cornell, *Observation of bose-einstein condensation in a dilute atomic vapor*, science, 269 (1995), pp. 198–201.

[3] M. H. Anderson, J. R. Ensher, M. R. Matthews, C. E. Wieman, and E. A. Cornell, *Observation of bose-einstein condensation in a dilute atomic vapor*, Science, 269 (1995), pp. 198–201.

[4] E. Andersson, M. T. Fontenelle, and S. Stenholm, *Quantum statistics of atoms in microstructures*, Physical Review A, 59 (1999), p. 3841.

[5] A. Aspect, *Closing the door on einstein and bohr's quantum debate*, Physics, 8, p. 123.

[6] A. Aspect, *Bell's inequality test: more ideal than ever*, Nature, 398 (1999), pp. 189–190.

[7] A. Aspect, J. Dalibard, and G. Roger, *Experimental test of bell's inequalities using time- varying analyzers*, Phys. Rev. Lett., 49 (1982), pp. 1804–1807.

[8] A. Aspect, P. Grangier, and G. Roger, *Experimental realization of Einstein-Podolsky-Rosen-Bohm Gedankenexperiment: A new violation of Bell's inequalities*, Physical Review Letters, 49 (1982), pp. 91–94.

[9] W. S. Bakr, J. I. Gillen, A. Peng, S. Fölling, and M. Greiner, *A quantum gas microscope for detecting single atoms in a hubbard-regime optical lattice*, Nature, 462 (2009), pp. 74–77.

[10] J. S. Bell, *On the Einstein Podolsky Rosen paradox*, Physics, 1 (1964), pp. 195–200.

[11] J. S. Bell, *Speakable and unspeakable in quantum mechanics: Collected papers on quantum philosophy*, Cambridge university press, 2004.

[12] P. R. Berman, *Atom interferometry*, Academic press, 1997.

[13] M. Bernstein, K. King, and X. Zhou, *Handbook of MRI Pulse Sequences*, Academic Press, Burlington, 2004.

[14] J. Beugnon, M. P. Jones, J. Dingjan, B. Darquié, G. Messin, A. Browaeys, and P. Grangier, *Quantum interference between two single photons emitted by independently trapped atoms*, Nature, 440 (2006), pp. 779–782.

[15] I. Bloch, T. Hansch, and T. Esslinger, *Measurement of the spatial coherence of a trapped Bose gas at the phase transition*, Nature, 403 (2000), pp. 166–70.

[16] N. Bohr, *Can quantum-mechanical description of physical reality be considered complete?*, Physical review, 48 (1935), p. 696.

[17] M. Bonneau, *Atomic four-wave mixing in an optical lattice*, theses, Université Paris Sud - Paris XI, Dec. 2011.

[18] M. Bonneau, J. Ruaudel, R. Lopes, J.-C. Jaskula, A. Aspect, D. Boiron, and C. I. Westbrook, *Tunable source of correlated atom beams*, Phys. Rev. A, 87 (2013), p. 061603.

[19] E. M. Bookjans, C. D. Hamley, and M. S. Chapman, *Strong quantum spin correlations observed in atomic spin mixing*, Physical review letters, 107 (2011), p. 210406.

[20] Q. Bouton, R. Chang, A. L. Hoendervanger, F. Nogrette, A. Aspect, C. I. Westbrook, and D. Clément, *Fast production of Bose-Einstein condensates of metastable helium*, Physical Review A, 91 (2015), p. 061402(R).

[21] D. Bouwmeester, J.-W. Pan, K. Mattle, M. Eibl, H. Weinfurter, and A. Zeilinger, *Experimental quantum teleportation*, Nature, 390 (1997), pp. 575–579.

[22] A. Browaeys, *Piégeage magnétique d'un gaz d'hélium métastable: vers la condensation de bose-einstein*, PhD Thesis, (2000).

[23] N. Brunner, D. Cavalcanti, S. Pironio, V. Scarani, and S. Wehner, *Bell nonlocality*, Reviews of Modern Physics, 86 (2014), p. 419.

[24] L. F. Buchmann, G. M. Nikolopoulos, O. Zobay, and P. Lambropoulos, *Correlated directional atomic clouds via four-heterowave mixing*, Phys. Rev. A, 81 (2010), p. 031606.

[25] R. Bücker, J. Grond, S. Manz, T. Berrada, T. Betz, C. Koller, U. Hohenester, T. Schumm, A. Perrin, and J. Schmiedmayer, *Twin-atom beams*, Nature Physics, 7 (2011), pp. 608–611.

[26] R. Bücker, A. Perrin, S. Manz, T. Betz, C. Koller, T. Plisson, J. Rottmann, T. Schumm, and J. Schmiedmayer, *Single-particle-sensitive imaging of freely propagating ultracold atoms*, New Journal of Physics, 11 (2009), p. 103039.

[27] H. Buhrman, R. Cleve, S. Massar, and R. de Wolf, *Nonlocality and communication complexity*, Reviews of modern physics, 82 (2010), p. 665.

[28] S. Burger, F. S. Cataliotti, C. Fort, F. Minardi, M. Inguscio, M. L. Chiofalo, and M. P. Tosi, *Superfluid and dissipative dynamics of a bose-einstein condensate in a periodic optical potential*, Phys. Rev. Lett., 86 (2001), pp. 4447–4450.

[29] G. K. Campbell, J. Mun, M. Boyd, E. W. Streed, W. Ketterle, and D. E. Pritchard, *Parametric amplification of scattered atom pairs*, Phys. Rev. Lett., 96 (2006), p. 020406.

[30] R. A. Campos, B. E. Saleh, and M. C. Teich, *Quantum-mechanical lossless beam splitter: Su (2) symmetry and photon statistics*, Physical Review A, 40 (1989), p. 1371.

[31] Y. Castin and R. Dum, *Bose-einstein condensates in time dependent traps*, Phys. Rev. Lett., 77 (1996), pp. 5315–5319.

[32] S. Chelkowski and G. N. Gibson, *Adiabatic climbing of vibrational ladders using Raman transitions with a chirped pump laser*, Physical Review A, 52 (1995), pp. 0–3.

[33] K. S. Choi, *Coherent control of entanglement with atomic ensembles*, theses, California Institute of Technology, 2011.

[34] B. Christensen, K. McCusker, J. Altepeter, B. Calkins, T. Gerrits, A. Lita, A. Miller, L. Shalm, Y. Zhang, S. Nam, et al., *Detection-loophole-free test of quantum nonlocality, and applications*, Physical review letters, 111 (2013), p. 130406.

[35] J. F. Clauser and M. A. Horne, *Experimental consequences of objective local theories*, Physical review D, 10 (1974), p. 526.

[36] J. F. Clauser and A. Shimony, *Bell's theorem. experimental tests and implications*, Reports on Progress in Physics, 41 (1978), p. 1881.

[37] J. Coffey, *Who discovered helium?* http://www.universetoday.com/53563/who-discovered-helium/. Accessed: 2015-10-20.

[38] M. M. Cola and N. Piovella, *Theory of collective raman scattering from a bose-einstein condensate*, Physical Review A, 70 (2004), p. 045601.

[39] T. S. Cubitt, D. Leung, W. Matthews, and A. Winter, *Zero-error channel capacity and simulation assisted by non-local correlations*, Information Theory, IEEE Transactions on, 57 (2011), pp. 5509–5523.

[40] J. Dalibard, *Des cages de lumière pour les atomes: la physique des pièges et des réeseaux optiques*. Cours du Collège de France, 2013.

[41] R. Dall and A. Truscott, *Bose–einstein condensation of metastable helium in a bi-planar quadrupole ioffe configuration trap*, Optics Communications, 270 (2007), pp. 255–261.

[42] K. B. Davis, M.-O. Mewes, M. R. Andrews, N. Van Druten, D. Durfee, D. Kurn, and W. Ketterle, *Bose-einstein condensation in a gas of sodium atoms*, Physical review letters, 75 (1995), p. 3969.

[43] R. H. Dicke, *Coherence in spontaneous radiation processes*, 1954.

[44] F. P. Dos Santos, J. Léonard, J. Wang, C. Barrelet, F. Perales, E. Rasel, C. Unnikrishnan, M. Leduc, and C. Cohen-Tannoudji, *Bose-einstein condensation of metastable helium*, Physical Review Letters, 86 (2001), p. 3459.

[45] P. H. Eberhard, *Background level and counter efficiencies required for a loophole-free einstein-podolsky-rosen experiment*, Physical Review A, 47 (1993), p. R747.

[46] A. Einstein, *Quantentheorie des einatomigen idealen Gases*, Sitzungsberichte der Preußischen Akademie der Wissenschaften, Physikalisch-mathematische Klasse (1924), pp. 261–267.

[47] A. Einstein, B. Podolsky, and N. Rosen, *Can quantum-mechanical description of physical reality be considered complete?*, Phys. Rev., 47 (1935), pp. 777–780.

[48] A. K. Ekert, *Quantum cryptography based on bell's theorem*, Physical review letters, 67 (1991), p. 661.

[49] L. Fallani, L. De Sarlo, J. E. Lye, M. Modugno, R. Saers, C. Fort, and M. Inguscio, *Observation of dynamical instability for a bose-einstein condensate in a moving 1d optical lattice*, Phys. Rev. Lett., 93 (2004), p. 140406.

[50] A. J. Ferris, M. J. Davis, R. W. Geursen, P. B. Blakie, and A. C. Wilson, *Dynamical instabilities of bose-einstein condensates at the band edge in one-dimensional optical lattices*, Phys. Rev. A, 77 (2008), p. 012712.

[51] H. Gibbs, Q. Vrehen, and H. Hikspoors, *Single-pulse superfluorescence in cesium*, Physical Review Letters, 39 (1977), p. 547.

[52] M. Giustina, A. Mech, S. Ramelow, B. Wittmann, J. Kofler, J. Beyer, A. Lita, B. Calkins, T. Gerrits, S. W. Nam, et al., *Bell violation using entangled photons without the fair-sampling assumption*, Nature, 497 (2013), pp. 227–230.

[53] M. Giustina, M. A. Versteegh, S. Wengerowsky, J. Handsteiner, A. Hochrainer, K. Phelan, F. Steinlechner, J. Kofler, J.-Å. Larsson, C. Abellán, et al., *Significant-loophole-free test of bell's theorem with entangled photons*, Physical review letters, 115 (2015), p. 250401.

[54] R. J. Glauber, *The quantum theory of optical coherence*, Physical Review, 130 (1963), p. 2529.

[55] P. Grangier, G. Roger, and A. Aspect, *Experimental evidence for a photon anticorrelation effect on a beam splitter: A new light on single-photon interferences*, EPL (Europhysics Letters), 1 (1986), p. 173.

[56] J. A. Greenberg and D. J. Gauthier, *Steady-state, cavityless, multimode superradiance in a cold vapor*, Phys. Rev. A, 86 (2012), p. 013823.

[57] M. Greiner, C. Regal, J. Stewart, and D. Jin, *Probing pair-correlated fermionic atoms through correlations in atom shot noise*, Physical review letters, 94 (2005), p. 110401.

[58] R. Grimm, M. Weidemüller, and Y. B. Ovchinnikov, *Optical dipole traps for neutral atoms*, vol. 42 of Advances In Atomic, Molecular, and Optical Physics, Academic Press, 2000, pp. 95 – 170.

[59] C. Gross, H. Strobel, E. Nicklas, T. Zibold, N. Bar-Gill, G. Kurizki, and M. Oberthaler, *Atomic homodyne detection of continuous-variable entangled twin-atom states*, Nature, 480 (2011), pp. 219–223.

[60] M. Gross, C. Fabre, P. Pillet, and S. Haroche, *Observation of near-infrared dicke superradiance on cascading transitions in atomic sodium*, Physical Review Letters, 36 (1976), p. 1035.

[61] M. Gross and S. Haroche, *Superradiance: An essay on the theory of collective spontaneous emission*, Physics Reports, 93 (1982), pp. 301–396.

[62] G. Grynberg, A. Aspect, and C. Fabre, *Introduction to quantum optics: from the semi-classical approach to quantized light*, Cambridge Univ. Press, New York, NY, 2010.

[63] H. Haken, *Encyclopedia of physics, vol. xxv/2c*, 1970.

[64] R. Hambury Brown and R. Q. Twiss, *Correlation between photons in two coherent beams of light*, Journal of Astrophysics and Astronomy, 15 (1994), pp. 13–19.

[65] R. Hanbury Brown and R. Q. Twiss, *A Test of a New Type of Stellar Interferometer on Sirius*, Nature, 178 (1956), pp. 1046–1048.

[66] B. Hensen, H. Bernien, A. Dréau, A. Reiserer, N. Kalb, M. Blok, J. Ruitenberg, R. Vermeulen, R. Schouten, C. Abellán, et al., *Loophole-free bell inequality violation using electron spins separated by 1.3 kilometres*, Nature, 526 (2015), pp. 682–686.

[67] K. M. Hilligsøe and K. Mølmer, *Phase-matched four wave mixing and quantum beam splitting of matter waves in a periodic potential*, Phys. Rev. A, 71 (2005), p. 041602.

[68] S. Hodgman, R. Dall, A. Manning, K. Baldwin, and A. Truscott, *Direct measurement of long-range third-order coherence in bose-einstein condensates*, Science, 331 (2011), pp. 1046–1049.

[69] L. Hoendervanger, *A New Metastable Helium Machine : An Investigation into the Attributes of Trapping, Cooling and Detecting Metastable Helium*, theses, Institut d'Optique Graduate School, Oct. 2014.

[70] J. Hofmann, M. Krug, N. Ortegel, L. Gérard, M. Weber, W. Rosenfeld, and H. Weinfurter, *Heralded entanglement between widely separated atoms*, Science, 337 (2012), pp. 72–75.

[71] C. Hong, Z. Ou, and L. Mandel, *Measurement of subpicosecond time intervals between two photons by interference*, Physical Review Letters, 59 (1987), p. 2044.

[72] S. Inouye, A. Chikkatur, D. Stamper-Kurn, J. Stenger, D. Pritchard, and W. Ketterle, *Superradiant rayleigh scattering from a bose-einstein condensate*, Science, 285 (1999), pp. 571–574.

[73] T. S. Iskhakov, K. Y. Spasibko, M. V. Chekhova, and G. Leuchs, *Macroscopic hong–ou–mandel interference*, New Journal of Physics, 15 (2013), p. 093036.

[74] J.-C. Jaskula, *Création et étude de sources d'états non classiques pour l'optique atomique quantique*, PhD Thesis, (2010).

[75] J.-C. Jaskula, G. B. Partridge, M. Bonneau, R. Lopes, J. Ruaudel, D. Boiron, and C. I. Westbrook, *Acoustic analog to the dynamical casimir effect in a bose-einstein condensate*, Physical Review Letters, 109 (2012), p. 220401.

[76] T. Jeltes, J. M. McNamara, W. Hogervorst, W. Vassen, V. Krachmalnicoff, M. Schellekens, A. Perrin, H. Chang, D. Boiron, A. Aspect, and C. I. Westbrook, *Comparison of the Hanbury Brown-Twiss effect for bosons and fermions.*, Nature, 445 (2007), pp. 402–405.

[77] R. a. H. John F. Clauser, Michael A. Horne, Abner Shimony, *Proposed Experiment To Test Local Hidden-Variable Theories*, Phys. Rev. Lett., 23 (1969), pp. 880–884.

[78] P. L. Kapitza and P. A. M. Dirac, *The reflection of electrons from standing light waves*, Mathematical Proceedings of the Cambridge Philosophical Society, 29 (1933), pp. 297–300.

[79] A. Kaufman, B. Lester, M. Foss-Feig, M. Wall, A. Rey, and C. Regal, *Entangling two transportable neutral atoms via local spin exchange*, Nature, 527 (2015), pp. 208–211.

[80] A. Kaufman, B. Lester, C. Reynolds, M. Wall, M. Foss-Feig, K. Hazzard, A. Rey, and C. Regal, *Two-particle quantum interference in tunnel-coupled optical tweezers*, Science, 345 (2014), pp. 306–309.

[81] K. V. Kheruntsyan, J.-C. Jaskula, P. Deuar, M. Bonneau, G. B. Partridge, J. Ruaudel, R. Lopes, D. Boiron, and C. I. Westbrook, *Violation of the cauchy-schwarz inequality with matter waves*, Phys. Rev. Lett., 108 (2012), p. 260401.

[82] L. Landau and E. Lifshitz, *Mechanics*, Butterworth Heinemann, Butterworth-Heinemann, 1976.

[83] J.-Å. Larsson and R. D. Gill, *Bell's inequality and the coincidence-time loophole*, EPL (Europhysics Letters), 67 (2004), p. 707.

[84] V. Letokhov and S. Johansson, *Astrophysical lasers*, OUP Oxford, 2008.

[85] R. Lewis-Swan and K. Kheruntsyan, *Proposal for demonstrating the hong–ou–mandel effect with matter waves*, Nature communications, 5 (2014).

[86] R. J. Lewis-Swan and K. V. Kheruntsyan, *Proposal for a motional-state bell inequality test with ultracold atoms*, Phys. Rev. A, 91 (2015), p. 052114.

[87] R. Lopes, *An atomic Hong-Ou-Mandel experiment*, PhD Thesis, (2015).

[88] R. Lopes, A. Imanaliev, A. Aspect, M. Cheneau, D. Boiron, and C. I. Westbrook, *Atomic hong-ou-mandel experiment*, Nature, 520 (2015), pp. 66–68.

[89] R. Lopes, a. Imanaliev, M. Bonneau, J. Ruaudel, M. Cheneau, D. Boiron, and C. I. Westbrook, *Second-order coherence of superradiance from a Bose-Einstein condensate*, Physical Review A - Atomic, Molecular, and Optical Physics, 90 (2014), pp. 1–5.

[90] R. Loudon, *The Quantum Theory of Light*, Oxford University Press, 1992.

[91] B. Lücke, M. Scherer, J. Kruse, L. Pezzé, F. Deuretzbacher, P. Hyllus, J. Peise, W. Ertmer, J. Arlt, L. Santos, et al., *Twin matter waves for interferometry beyond the classical limit*, Science, 334 (2011), pp. 773–776.

[92] E. W. M. Born, *Optics*, Pergamon Oxford, 1980.

[93] L. Mandel and E. Wolf, *Optical Coherence and Quantum Optics*, Cambridge University Press, 1995. Cambridge Books Online.

[94] P. J. Martin, B. G. Oldaker, A. H. Miklich, and D. E. Pritchard, *Bragg scattering of atoms from a standing light wave*, Physical review letters, 60 (1988), p. 515.

[95] D. Matsukevich, P. Maunz, D. Moehring, S. Olmschenk, and C. Monroe, *Bell inequality violation with two remote atomic qubits*, Physical Review Letters, 100 (2008), p. 150404.

[96] C. Menotti, A. Smerzi, and A. Trombettoni, *Superfluid dynamics of a bose–einstein condensate in a periodic potential*, New Journal of Physics, 5 (2003), p. 112.

[97] S. Moal, M. Portier, J. Kim, J. Dugué, U. Rapol, M. Leduc, and C. Cohen-Tannoudji, *Accurate determination of the scattering length of metastable helium atoms using dark resonances between atoms and exotic molecules*, Physical review letters, 96 (2006), p. 023203.

[98] M. Modugno, C. Tozzo, and F. Dalfovo, *Role of transverse excitations in the instability of bose-einstein condensates moving in optical lattices*, Phys. Rev. A, 70 (2004), p. 043625.

[99] K. Moler, D. S. Weiss, M. Kasevich, and S. Chu, *Theoretical analysis of velocity-selective raman transitions*, Phys. Rev. A, 45 (1992), pp. 342–348.

[100] M. Moore and P. Meystre, *Theory of superradiant scattering of laser light from bose-einstein condensates*, Physical Review Letters, 83 (1999), p. 5202.

[101] A. Öttl, S. Ritter, M. Köhl, and T. Esslinger, *Correlations and counting statistics of an atom laser*, Phys. Rev. Lett., 95 (2005), p. 090404.

[102] Z. Ou and L. Mandel, *Violation of bell's inequality and classical probability in a two-photon correlation experiment*, Physical Review Letters, 61 (1988), p. 50.

[103] Z. Y. Ou and L. Mandel, *Observation of spatial quantum beating with separated photodetectors*, Physical Review Letters, 61 (1988), pp. 54–57.

[104] Z. Y. Ou, S. F. Pereira, H. J. Kimble, and K. C. Peng, *Realization of the einstein-podolsky-rosen paradox for continuous variables*, Phys. Rev. Lett., 68 (1992), pp. 3663–3666.

[105] G. B. Partridge, J.-C. Jaskula, M. Bonneau, D. Boiron, and C. I. Westbrook, *Bose-einstein condensation and spin mixtures of optically trapped metastable helium*, Physical Review A, 81 (2010), p. 053631.

[106] P. M. Pearle, *Hidden-variable example based upon data rejection*, Physical Review D, 2 (1970), p. 1418.

[107] K. Pearson, *Note on regression and inheritance in the case of two parents*, Proceedings of the Royal Society of London, 58 (1895), pp. 240–242.

[108] J. Pellegrino, R. Bourgain, S. Jennewein, Y. R. Sortais, A. Browaeys, S. Jenkins, and J. Ruostekoski, *Observation of suppression of light scattering induced by dipole-dipole interactions in a cold-atom ensemble*, Physical review letters, 113 (2014), p. 133602.

[109] R. Penrose, *On gravity's role in quantum state reduction*, General relativity and gravitation, 28 (1996), pp. 581–600.

[110] A. Perrin, H. Chang, V. Krachmalnicoff, M. Schellekens, D. Boiron, A. Aspect, and C. I. Westbrook, *Observation of atom pairs in spontaneous four-wave mixing of two colliding bose-einstein condensates*, Physical review letters, 99 (2007), p. 150405.

[111] C. Pethick and H. Smith, *Bose-Einstein Condensation in Dilute Gases*, Cambridge University Press, 2002.

[112] L. Pezzé and A. Smerzi, *Entanglement, nonlinear dynamics, and the heisenberg limit*, Physical review letters, 102 (2009), p. 100401.

[113] N. Piovella, M. Cola, and R. Bonifacio, *Quantum fluctuations and entanglement in the collective atomic recoil laser using a bose-einstein condensate*, Phys. Rev. A, 67 (2003), p. 013817.

[114] H. Pu, W. Zhang, and P. Meystre, *Wave mixing of optical pulses and bose-einstein condensates*, Phys. Rev. Lett., 91 (2003), p. 150407.

[115] J. M. Raimond, P. Goy, M. Gross, C. Fabre, and S. Haroche, *Statistics of millimeter-wave photons emitted by a rydberg-atom maser: An experimental study of fluctuations in single-mode superradiance*, Phys. Rev. Lett., 49 (1982), pp. 1924–1927.

[116] N. F. Ramsey, *A molecular beam resonance method with separated oscillating fields*, Phys. Rev., 78 (1950), pp. 695–699.

[117] J. Rarity and P. Tapster, *Experimental violation of Bell's inequality based on phase and momentum*, Physical Review Letters, 64 (1990), pp. 2495–2498.

[118] J. G. Rarity and P. R. Tapster, *Two-color photons and nonlocality in fourth-order interference*, Physical Review A, 41 (1990), pp. 5139–5146.

[119] M. F. Riedel, P. Böhi, Y. Li, T. W. Hänsch, A. Sinatra, and P. Treutlein, *Atom-chip-based generation of entanglement for quantum metrology*, Nature, 464 (2010), pp. 1170–1173.

[120] A. Robert, *Réalisation d'un condensat de bose-einstein d'atomes d'hélium métastable*, PhD Thesis, (2001).

[121] A. Robert, O. Sirjean, A. Browaeys, J. Poupard, S. Nowak, D. Boiron, C. I. Westbrook, and A. Aspect, *A bose-einstein condensate of metastable atoms*, Science, 292 (2001), pp. 461–464.

[122] A. T. Rosenberger and T. DeTemple, *Far-infrared superradiance in methyl fluoride*, Physical Review A, 24 (1981), p. 868.

[123] M. a. Rowe, D. Kielpinski, V. Meyer, C. a. Sackett, W. M. Itano, C. Monroe, and D. J. Wineland, *Experimental violation of a Bell's inequality with efficient detection.*, Nature, 409 (2001), pp. 791–794.

[124] J. Ruaudel, *Création et caractérisation d'une source ajustable de paires d'atomes corrélés*, PhD Thesis, (2013).

[125] H. Sakai, T. Saito, T. Ikeda, K. Itoh, T. Kawabata, H. Kuboki, Y. Maeda, N. Matsui, C. Rangacharyulu, M. Sasano, Y. Satou, K. Sekiguchi, K. Suda, A. Tamii, T. Uesaka, and K. Yako, *Spin correlations of strongly interacting massive fermion pairs as a test of bell's inequality*, Phys. Rev. Lett., 97 (2006), p. 150405.

[126] C. Santori, D. Fattal, J. Vučković, G. S. Solomon, and Y. Yamamoto, *Indistinguishable photons from a single-photon device*, Nature, 419 (2002), pp. 594–597.

[127] M. Schellekens, *L'effet Hanbury Brown et Twiss pour les atomes froids*, PhD Thesis, (2007).

[128] M. Schellekens, R. Hoppeler, a. Perrin, J. V. Gomes, D. Boiron, a. Aspect, and C. I. Westbrook, *Hanbury Brown Twiss effect for ultracold quantum gases.*, Science (New York, N.Y.), 310 (2005), pp. 648–651.

[129] D. Schneble, G. K. Campbell, E. W. Streed, M. Boyd, D. E. Pritchard, and W. Ketterle, *Raman amplification of matter waves*, Phys. Rev. A, 69 (2004), p. 041601.

[130] D. Schneble, Y. Torii, M. Boyd, E. W. Streed, D. E. Pritchard, and W. Ketterle, *The onset of matter-wave amplification in a superradiant bose-einstein condensate*, Science, 300 (2003), pp. 475–478.

[131] L. K. Shalm, E. Meyer-Scott, B. G. Christensen, P. Bierhorst, M. A. Wayne, M. J. Stevens, T. Gerrits, S. Glancy, D. R. Hamel, M. S. Allman, et al., *Strong loophole-free test of local realism*, Physical review letters, 115 (2015), p. 250402.

[132] J. F. Sherson, C. Weitenberg, M. Endres, M. Cheneau, I. Bloch, and S. Kuhr, *Single-atom-resolved fluorescence imaging of an atomic mott insulator*, Nature, 467 (2010), pp. 68–72.

[133] Y. H. Shih and C. O. Alley, *New Type of Einstein-Podolsky-Rosen-Bohm Experiment Using Pairs of Light Quanta Produced by Optical Parametric Down Conversion*, 1988.

[134] B. W. Shore, M. V. Gromovyy, L. P. Yatsenko, and V. I. Romanenko, *Simple mechanical analogs of rapid adiabatic passage in atomic physics*, American Journal of Physics, 77 (2009), pp. 1183–1194.

[135] C. Simon and W. T. Irvine, *Robust long-distance entanglement and a loophole-free bell test with ions and photons*, Physical review letters, 91 (2003), p. 110405.

[136] N. Skribanowitz, I. Herman, J. MacGillivray, and M. Feld, *Observation of dicke superradiance in optically pumped hf gas*, Physical Review Letters, 30 (1973), p. 309.

[137] K. Y. Spasibko, F. Töppel, T. S. Iskhakov, M. Stobińska, M. Chekhova, and G. Leuchs, *Interference of macroscopic beams on a beam splitter: phase uncertainty converted into photon-number uncertainty*, New Journal of Physics, 16 (2014), p. 013025.

[138] P. R. Tapster, J. G. Rarity, and P. C. M. Owens, *Violation of bell's inequality over 4 km of optical fiber*, Phys. Rev. Lett., 73 (1994), pp. 1923–1926.

[139] W. Tittel, J. Brendel, H. Zbinden, and N. Gisin, *Violation of bell inequalities by photons more than 10 km apart*, Phys. Rev. Lett., 81 (1998), pp. 3563–3566.

[140] N. V. Vitanov, T. Halfmann, B. W. Shore, and K. Bergmann, *Laser-induced population transfer by adiabatic passage techniques.*, Annual review of physical chemistry, 52 (2001), pp. 763–809.

[141] J. Vogels, K. Xu, and W. Ketterle, *Generation of macroscopic pair-correlated atomic beams by four-wave mixing in bose-einstein condensates*, Physical review letters, 89 (2002), p. 020401.

[142] D. Walls and G. Milburn, *Quantum Optics*, SpringerLink: Springer e-Books, Springer Berlin Heidelberg, 2008.

[143] T. Wasak, P. Szańkowski, P. Ziń, M. Trippenbach, and J. Chwedeńczuk, *Cauchy-schwarz inequality and particle entanglement*, Physical Review A, 90 (2014), p. 033616.

[144] G. Weihs, T. Jennewein, C. Simon, H. Weinfurter, and A. Zeilinger, *Violation of bell's inequality under strict einstein locality conditions*, Phys. Rev. Lett., 81 (1998), pp. 5039–5043.

[145] T. Wilk, A. Gaëtan, C. Evellin, J. Wolters, Y. Miroshnychenko, P. Grangier, and A. Browaeys, *Entanglement of two individual neutral atoms using rydberg blockade*, Physical Review Letters, 104 (2010), p. 010502.

[146] B. Wu and Q. Niu, *Landau and dynamical instabilities of the superflow of bose-einstein condensates in optical lattices*, Phys. Rev. A, 64 (2001), p. 061603.

[147] B. Wu and Q. Niu, *Superfluidity of bose–einstein condensate in an optical lattice: Landau–zener tunnelling and dynamical instability*, New Journal of Physics, 5 (2003), p. 104.

[148] Y. Yoshikawa, T. Sugiura, Y. Torii, and T. Kuga, *Observation of superradiant raman scattering in a bose-einstein condensate*, Phys. Rev. A, 69 (2004), p. 041603.

[149] M. Żukowski, A. Zeilinger, M. Horne, and A. Ekert, *"event-ready-detectors"bell experiment via entanglement swapping*, Physical Review Letters, 71 (1993), p. 4287.

université PARIS-SACLAY | ÉCOLE DOCTORALE Ondes et Matière (EDOM)

Title: Towards testing Bell's inequality using atoms correlated in momentum

Abstract:

This manuscript describes quantum atom optics experiments using metastable helium atoms with a single-atom momentum resolved detector.

In the first part of this manuscript, the second order correlation measurement of the superradiance from a metastable helium Bose-Einstein condensate is presented. The superradiance effect is the collective radiation of dense ensemble where a strong gain of the radiation is expected. We have shown the thermal like statistics of the emission even in the presence of the strong gain.

The next part of the manuscript is devoted to the quantum nonlocality test using a pair of atoms entangled in momentum. The protocol we came up with is inspired from the one of Rarity and Tapster with pairs of photons entangled in momentum. The essential ingredients of this protocol are the atomic pair produced by dynamical instability of the Bose-Einstein condensate in a moving optical lattice, the coherent control of the atomic pair by Bragg diffraction and the correlation measurement of the atoms in different output modes of the interferometric protocol. The experimental characterization and preparation of coherent control by Bragg diffraction are presented showing the proof of principle of such a protocol.

The last part of the manuscript discusses the realization of the atomic Hong-Ou-Mandel experiment using the same atomic pair with an atomic beamsplitter. The non-classical interference result of this experiment has opened an opportunity for us to realize Bell's inequality test with massive particles correlated in external degrees of freedom.

Keywords: Bose-Einstein condensate, superradiance, correlation, entanglement, atomic four-wave mixing, Bragg diffraction, Bell's inequality test, two-particle interference, indistinguishability

Titre: Vers la réalisation d'un test d'inégalité de Bell avec des atomes corrélés en impulsion

Résumé:

Ce manuscrit décrit des expériences d'optique atomique quantique utilisant un détecteur résolu en impulsions d'atomes uniques d'hélium métastable.

La première partie du manuscrit décrit la mesure de cohérence de deuxième ordre de la superradiance à partir d'un condensat de Bose-Einstein d'helium métastable. Bien que le condensat soit cohérent et le gain du processus de superradiance élevé, celle-ci montre toujours une statistique thermique comme celle de l'émission spontanée.

La suite du manuscrit est dédiée au test de la non localité d'une source atomique corrélée en impulsion. Le schéma du test s'inspire d'une réalisation faite par Rarity et Tapster sur des photons intriqués en impulsion. Les ingrédients principaux d'un tel schéma sont la source atomique générée par instabilité dynamique du condensat dans un réseau optique en mouvement, le contrôle cohérent des atomes par diffraction de Bragg et la mesure de la corrélation des atomes dans les différentes voies de sortie du schéma interférométrique. Un point clé est le contrôle et la manipulation de la phase des ondes atomiques. Le chapitre 3 décrit les tests sur le contrôle cohérent par diffraction de Bragg et leurs résultats encourageants.

La nature non classique de notre source atomique est démontrée par l'observation d'une interférence à deux particules en les envoyant sur une séparatrice atomique. Cet analogue atomique de l'expérience de Hong Ou et Mandel est le sujet du dernier chapitre de ce manuscrit. Le résultat de cette expérience ouvre la possibilité du test d'inégalité de Bell avec des particules massives corrélées sur des degrés de liberté externe.

Mots clés: condensat de Bose-Einstein, superradiance, corrélation, intrication, mélange à quatre ondes, diffraction de Bragg, inégalité de Bell, interférence a deux particules, indiscernabilité